2016

Natural Abundance 14N and 15N Solid-State NMR Studies of Organic, Biochemical, and Pharmaceutical Systems

Stanislav L. Veinberg
University of Windsor

Natural Abundance ^{14}N and ^{15}N Solid-State NMR Studies of Organic, Biochemical, and Pharmaceutical Systems

by

Stanislav L. Veinberg

A Dissertation
Submitted to the Faculty of Graduate Studies
through the Department of Chemistry and Biochemistry
in Partial Fulfilment of the Requirements for
the Degree of Doctor of Philosophy at the
University of Windsor

Windsor, Ontario, Canada
2016

“Natural Abundance ^{14}N and ^{15}N Solid-State NMR Studies of Organic, Biochemical, and Pharmaceutical Systems”

by

Stanislav L. Veinberg

APPROVED BY:

D. Bryce, External Examiner
University Of Ottawa

W. Kedzierski
Department of Physics

S. Johnson
Department of Chemistry & Biochemistry

S. Loeb
Department of Chemistry & Biochemistry

R. Schurko, Advisor
Department of Chemistry & Biochemistry

April 20, 2016

Declaration of Co-authorship / Previous Publications

This thesis is presented in manuscript format, as outlined in the guidelines set forth by the Faculty of Graduate Studies. Chapter 3 of this dissertation was published in a peer-reviewed journal where I was the primary author:

Chapter 3: Veinberg, S.L., Friedl, Z.W., Harris, K.J., O'Dell, L.A., and Schurko, R.W. Ultra-wideline ^{14}N Solid-State NMR as a Method of Differentiating Polymorphs: Glycine as a Case Study. *CrystEngComm.* **2015**, *17*, 5225–5236. DOI: 10.1039/C5CE00060B.

I am also the primary author on Chapters 2, 5, and 6, which are planned for submission for publication.

Chapter 4 of this dissertation was a joint effort (*vide infra*) and was published in a peer reviewed journal where I was the second author:

Chapter 4: Harris, K.J., Veinberg, S.L., Mireault, C.R., Lupulescu, A., Frydman, L., and Schurko, R.W. Rapid Acquisition of ^{14}N Solid-State NMR Spectra Using Broadband Cross Polarization. *Chem. Eur. J.* **2013**, *19*, 16469-16475. DOI: 10.1002/chem.201301862.

I certify that I have obtained a written permission from the copyright owner(s) to include the above published material(s) in my thesis. I certify that the above material describes work completed during my registration as a graduate student at the University of Windsor.

I acknowledge my supervisor, Professor Robert W. Schurko, as a co-author on this work (the dissertation), who made key contributions to writing and editing of all manuscripts. I hereby declare that this thesis incorporates material that is a result of joint research, as follows:

Chapter 2, "^{14}N Solid-State NMR of Amino Acids," includes contributions from Zachary W. Friedl, a former undergraduate student in our research group who assisted

with sample preparation, acquisition of NMR spectra, and DFT calculations; Austin W. Lindquist, an undergraduate student in our research group who assisted with computational data analysis and the preparation of tensor figures, and Brianna M. Kispal, a former undergraduate student in our research group who assisted in data organization. Kris J. Harris, a former post-doctoral fellow in our group, and Luke A. O'Dell assisted with the acquisition of high-field experiments.

Chapter 3, "Ultra-wideline ^{14}N Solid-State NMR as a Method for Differentiating Polymorphs: Glycine as a Case Study," includes contributions from Zachary W. Friedl, who assisted with the polymorph synthesis, sample preparation, acquisition of NMR spectra, and DFT calculations.

Chapter 4, "Rapid Acquisition of ^{14}N Solid-State NMR Spectra Using Broadband Cross Polarization," was a collaborative effort with Kristopher J. Harris. Christopher R. Mireault acquired the direct-excitation spectrum of isoxsuprine HCl. I performed the remainder of the data acquisition with occasional assistance from Kris J. Harris. I also performed the majority of data processing and prepared all of the figures for publication. I also made significant intellectual contributions during the writing and editing process. Although my contributions to this manuscript were equal to those of Kris J. Harris, assigning equal author contribution was not an available option during the submission process. In regard to this, I have obtained the appropriate permissions from all involved parties to use this publication in this dissertation.

Chapter 5, "Practical Considerations for the Acquisition of Ultra-Wideline ^{14}N NMR Spectra," has contributions from Austin W. Lindquist, and Michael J. Jaroszewicz,

a former M.Sc. student in our research group. Both assisted with the SIMPSON simulations.

Chapter 6, "Natural Abundance ^{14}N and ^{15}N Solid-State NMR of Pharmaceuticals and their Polymorphs," was a collaborative effort with Karen E. Johnston, a former post-doctoral fellow in our lab, and with Takeshi Kobayashi and Marek Pruski of the Ames Lab at Iowa State University. Takeshi Kobayashi assisted with the acquisition of the ^{1}H{^{15}N}idHETCOR spectra and their processing, and acquired the ^{15}N DNP spectra. Karen E. Johnston acquired the ^{1}H{^{15}N}idHETCOR spectra and assisted with the acquisition of the ^{14}N SSNMR powder patterns. Karen E. Johnston also made invaluable contributions to the writing of the manuscript. Christopher R. Mireault prepared the bupivacaine HCl polymorphs, Brianna M. Kispal assisted with data organization, and Michael J. Jaroszewicz provided intellectual contributions.

I am aware of the University of Windsor Senate Policy on Authorship and I affirm that I have acknowledged the contribution of other individuals to my thesis, and I have obtained permission from each of the co-authors to include the aforementioned material in my thesis. I certify that the previously mentioned material describes work completed during my registration as a graduate student at the University of Windsor.

I declare that, to the best of my knowledge, my thesis does not infringe upon anyone's copyright nor violate any proprietary rights and that any ideas, techniques, quotations, or any other material from the work of other people included in my thesis, published or otherwise, are fully acknowledged in accordance with the standard referencing practices. Furthermore, to the extent that I have included copyrighted material that surpasses the bounds of fair dealing within the meaning of the Canada

Copyright Act, I certify that I have obtained a written permission from the copyright owner(s) to include such material(s) in my thesis.

I declare that this is a true copy of my thesis, including any final revisions, as approved by my thesis committee and the Graduate Studies office, and that this thesis has not been submitted for a higher degree to any other University or Institution.

Abstract

Nitrogen is an important element in all areas of chemistry, biology, and materials science. However, it is challenging to probe directly with solid-state nuclear magnetic resonance (SSNMR). The commonly studied isotope, ^{15}N (nuclear spin, I, = ½), has a low natural abundance (0.36%); therefore, ^{15}N NMR experiments often require isotopically enriched samples. ^{14}N (I = 1) has a high natural abundance (99.64%) but is a quadrupolar nucleus. ^{14}N SSNMR spectra are generally very broad due to the moderate quadrupole moment of ^{14}N. Ultra-wideline (UW) ^{14}N SSNMR spectra have very low signal-to-noise, which complicates their acquisition; however, they are useful probes of molecular-level structure and dynamics, and do not require isotopic enrichment for their acquisition.

This dissertation focuses on developing and applying direct-detection techniques for the acquisition of UW ^{14}N SSNMR powder patterns. These techniques have been studied from both empirical and theoretical points of view and are facile to implement on modern NMR consoles.

First, we present a ^{14}N SSNMR study of sp^3-hybridized nitrogen moieties in amino acids and related derivatives. ^{14}N NMR powder patterns were acquired in relatively short experimental times using moderate field strengths (e.g., 9.4 T), and from these, the ^{14}N quadrupolar parameters were determined. The ^{14}N electric field gradient (EFG) tensors are extremely sensitive to intermolecular hydrogen-bonding, and in conjunction with plane-wave density functional theory calculations, correlations are found between these tensors and nitrogen structural environments. Second, ^{14}N SSNMR was applied for the differentiation of polymorphs of glycine and its HCl salt. We also

investigated the rotational dynamics of NH_3 groups, finding that the ^{14}N transverse relaxation is dependent upon motional variation with temperature and can be exploited to reduce the experimental times of CPMG-type ^{14}N NMR experiments. Third, we describe improvements in the efficiency of ^{14}N UW SSNMR experiments by utilizing broadband cross-polarization methods, improving the parameterization and execution of WURST pulses, and strategically considering the appearances of ^{14}N powder patterns. Finally, we present a preliminary investigation of the tandem use of directly-detected ^{14}N and indirectly-detected ^{15}N SSNMR for the characterization of active pharmaceutical ingredients and their polymorphs, without isotopic enrichment.

I would like to dedicate this work to my family and Maria for their continued support and encouragement during my graduate studies.

In Loving Memory of Lidia Veinberg
(1954.04.23 – 2015.10.01)

несмотря на то что ты больше не с нами,
ты всегда будеш оставаться в моём сердце

Acknowledgments

There are a large number of people to whom I am truly grateful for making this dissertation possible. First and foremost, I would like to thank Professor Robert Schurko for giving me the opportunity to work in his research group. Rob has been a superb supervisor and mentor and is responsible for my love of NMR. Rob has afforded me many opportunities to attend scientific conferences and work sabbaticals at state-of-the-art NMR facilities in North America, and these experiences will stay with me long after I have left his group.

I would also like to acknowledge members of the Schurko research group, past and present. In particular, I would like to thank two former post-docs: Karen Johnston and Kris Harris. Kris was my mentor when I was just starting in the lab; he taught me the basics of NMR experiments, as well as some more advanced things like pulse programming. Karen helped me mature into the NMR spectroscopist that I am today. Her organizational skills, attention to detail, and dedication are truly inspiring. I would also like to thank Aaron Rossini, Hiyam Hamaed, and Bryan Lucier for the knowledge that they imparted before graduating and moving on from the Schurko group. I would also like to thank many of the people I worked with over the years, including Marcel Hildebrand, Andrew Namespetra, Anthony Sandre, Valerie Seymour, and Alex Riedel. Special mentions go to Chris Mireault, Brianna Kispal, and Zachary Friedl, my ^{14}N comrades. I had the pleasure of supervising Brianna and Zach and have learned a lot in the process. Their assistance with organization and NMR experimentation is especially appreciated, and results of my joint work with them are described in Chapters 2, 3, and 6. I would also like to thank all current members of the Schurko group for the stimulating

discussions in the office, encouragement, willingness to proofread my work, and patience to sit through my "twenty-minute presentations." A big thank you goes out to Austin Lindquist for his assistance with more recent NMR projects and sorting out the massive table of contents of this dissertation. Thanks to David Hirsh and Chris O'Keefe for being great colleagues - I believe that we have all learned much from one another. Lastly, I would especially like to thank Michael Jaroszewicz for being the most hardcore Schurko group member that I have ever encountered; his dedication and willingness to help is insurmountable, and I appreciate all the hard work that he put in to our joint projects, especially in the time leading up to the submission of this dissertation.

In addition to the members of the Schurko group, there are many people at the University of Windsor whom I would also like to thank. I would like to thank Professors Stephen J. Loeb and Samuel A. Johnson for agreeing to be on my Ph.D. committee, for all of the fruitful discussions during our committee meetings, and for reading this dissertation. I would also like to thank the many graduate students in the Chemistry and Biochemistry department en masse for making these last six years great. I thank Matt Revington, our department NMR facility manager, who always makes sure that the NMR spectrometers remain operational, and for sharing his knowledge regarding the proper care of the magnets and procedures for cryogen fills: his coming in on a Saturday to do an emergency helium fill because our magnet dropped below 10% is still a vivid memory in my mind. I would also like to thank all of the university support staff who helped with various aspects of the research and performing all the "behind-the-scenes" tasks. I wish to thank to Joe Lichaa for his assistance with computer related issues, and Sinisa Jezdic who is always willing to fix our electronics, especially the low-γ box, which was crucial

for my NMR experiments. A huge thank you goes to Cathy Wilson, Marlene Bezaire, and Beth Kickham for all of their administrative work and for always being available to help. Thank you to Una Lee and Nedhal Al-Nidawy for letting me use their lab space, glassware, and chemicals for my attempts at doing "chemistry."

I would also like to acknowledge several collaborators abroad: Professor Marek Pruski and Dr. Takeshi Kobayashi (Ames Lab, Iowa State University, USA), Professor Lucio Frydman (Weizmann Institute, Israel), and especially Dr. Luke O'Dell (Deakin University, Australia) for all of his input, experimental assistance, and valuable discussion of ^{14}N solid-state NMR. I thank Victor Terskikh for all of his assistance with ultra-high field NMR experiments at the Canadian National Ultra-High Field Facility for Solids, as well as Zhehong Gan, Ivan Hung, and Peter Gor'kov at the National High Magnetic Field Laboratory in Tallahassee, Florida.

Finally, I would like to thank Natan Veinberg for being the best younger brother anyone could have hoped for and making things interesting; my parents, Leonid and Lidia Veinberg, for raising me to be the person I am today and always being there for me in times of need; as well as my extended family and friends for their support. A special mention goes to Shelly Gamon, who helped my mother during the direst of times and alleviated much of the pressure on me so that I was able to continue my studies. Lastly, I would like to thank Maria, my companion in life, for being there for me during the long nights of writing and experiments and for all of her love and support during the writing of this dissertation.

Table of Contents

List of Tables

List of Figures and Schemes

List of Abbreviations

BCP	Broadband Cross-polarization
BRAIN	BRoadband Adiabatic INversion
BRAIN-CP	BRoadband Adiabatic INversion Cross-Polarization
BRAIN-CP/WURST-CPMG	BRoadband Adiabatic INversion Cross-Polarization with WURST-CPMG
CASTEP	Cambridge serial total energy package
CP	Cross-polarization
CP/MAS	Cross-polarization magic-angle spinning
CPMG	Carr-Purcell Meiboom-Gill
CS	Chemical shift
CSA	Chemical shift anisotropy
CSD	Cambridge Structure Database
CT	Central transition
DE	Direct excitation
DEISM	Direct enhancement of integer spin magnetization
DFT	Density functional theory
DOR	Double rotation
EFG	Electric field gradient
FID	Free induction decay
FOQI	First-order quadrupolar interaction
FT	Fourier transform
GGA	Generalized gradient approximation

GIPAW	Gradient-including projector augmented wave algorithm
HE	Hahn-echo
HORROR	HOmonucleaR ROtary Resonance
i.d.	Inner diameter
idHETCOR	Indirectly detected HETeronuclear CORrelation
MAS	Magic-angle spinning
MQMAS	Multiple-quantum magic-angle spinning
MS	Magnetic Shielding
n.a.	Natural abundance
NMR	Nuclear magnetic resonance
NMS	Nuclear magnetic shielding
NQR	Nuclear Quadrupole Resonance
o.d.	Outer diameter
PAS	Principal axis system
ppm	Parts per million
pXRD	Powder X-ray diffraction
QI	Quadrupolar interaction
rf	Radiofrequency
rPBE	Revised Perdew, Burke, and Ernzerhof
S/N	Signal-to-noise
SHARCNET	Canadian Shared Hierarchical Academic Research Computing Network
SOQI	Second-order quadrupolar interaction

SPINAL	Small Phase INcremental ALternation
SSB	Spinning sideband
SSNMR	Solid-state nuclear magnetic resonance
ST	Satellite Transition
UW	Ultra-wideline
UWNMR	Ultra-wideline Nuclear Magnetic Resonance
VOCS	Variable Offset Cumulative Spectra
VT	Variable temperature
WCPMG	WURST-CPMG
WURST	Wideband Uniform Rate Smooth Truncation
XRD	X-ray Diffraction

List of Symbols

α	Spin-up state
a, b, c	Crystal lattice parameters
β	Spin-down state
B_0	Static external magnetic field
B_1	Applied oscillating magnetic field
B_{eff}	Effective magnetic field
B_{ind}	Induced magnetic field
B_{loc}	Local magnetic field at nucleus
C_Q	Quadrupolar coupling constant
ct	Contact time
Cu-K_α	Copper X-ray source
δ	Chemical shift
δ_{iso}	Isotropic chemical shift
$\delta_{11}, \delta_{22}, \delta_{33}$	Principal components of the CS tensor
Δ	Sweep range of the WURST pulse
dwp	Dwell time of the WURST pulse
dwp_{max}	Nyquist dwell time
e	Elementary charge
E_A	Activation energy
γ	Gyromagnetic ratio
h	Planck's constant
$\hbar$	Planck's constant in radians
η	Electric field gradient asymmetry parameter
$\mathbf{I}$	Nuclear spin angular momentum vector
I	Nuclear spin quantum number
κ	Skew
k	Boltzmann constant
λ	wavelength

$\mathbf{M}_0$	Net nuclear spin magnetization
m_I	Nuclear spin state quantum number
$\boldsymbol{\mu}$	Nuclear spin magnetic moment
μ_0	Vacuum permeability constant
ν_0	Larmor frequency (in MHz)
ν_Q	Quadrupolar frequency
ν_{rf}	Frequency of the rf pulse
ν_{rot}	Sample spinning rate (in Hz)
ν_{T_x}	Transmitter frequency (in MHz)
$\Delta\nu$	Frequency offset from the Larmor frequency (in kHz)
$\Delta\nu_{T_x}$	Transmitter frequency offset from the Larmor frequency (in kHz)
ν_{11}, ν_{22}, ν_{33}	Frequencies of the horn, shoulder, and foot discontinuities
N_α, N_β	Population of the α and β spin state, respectively
Ω	Span
ϕ	Phase
$P2_12_12_1$, $P2_1$	Space group designation
θ_p	Tip angle of the pulse
θ_R	Angle between rotor axis and $\mathbf{B}_0$
Q	Nuclear quadrupole moment
r	Distance between two atoms
R	Linear sweep rate of the WURST pulse
R_{DD}	Dipolar coupling constant
σ	Chemical/magnetic shielding
σ_{iso}	Isotropic chemical shielding
σ_{11}, σ_{22}, σ_{33}	Principal components of the MS tensor
$S_+(t)$	Sensitivity of the NMR signal
τ	Inter pulse delay
τ_{acq}	Acquisition time
τ_c	Correlation time

τ_{echo}	Spin-echo time
τ_o	Pre-exponential factor
τ_p	Pulse width
τ_{window}	Time to acquire the observable spin echo
T	Temperature
T_1	Longitudinal relaxation time constant
$T_{1\rho}$	Time constant for the decay of magnetization along the $\mathbf{B}_1$
T_2	Transverse relaxation time constant
T_2*	Transverse relaxation time constant, including effect from B_0 inhomogeneity
T_2^{eff}	Effective transverse relaxation time constant
T_{max}	Temperature where maximum ^{14}N NMR signal is observed
T_{RT}	Room temperature (*ca*. 25 °C)
$\ddot{\mathbf{V}}$	Electric Field Gradient tensor (EFG)
V_{11},V_{22}, V_{33}	Principal components of the EFG tensor
ω_0	Larmor frequency (in rad s^{-1})
ω_1	Nutation frequency of applied rf fields (in rad s^{-1})
ω_{T_x}	Frequency of applied rf fields (in rad s^{-1})

Chapter 1: Introduction

The contents of the following sections were derived from a number of sources which cover the theoretical aspects of NMR spectroscopy in various degrees of detail. The reader is referred to a series of excellent references for further information.[1–10]

1. Principles of NMR

The interaction of nuclear spins with an applied external magnetic field, $\mathbf{B}_0$ (the boldface denotes that the quantity is a vector), gives rise to the phenomenon of nuclear magnetic resonance (NMR). Nuclear spin angular momentum is an intrinsic property of nuclei; nuclei that do not possess an intrinsic spin (nuclear spin number, $I = 0$) are termed NMR inactive, while NMR-active nuclei may have half-integer ($I = 1/2, 3/2, 5/2$, etc.) or integer ($I = 1, 2, 3$, etc.) spins. The nuclear spin angular momentum, which is defined by the vector **I**, gives rise to a nuclear magnetic dipole moment, **μ**:

$$\boldsymbol{\mu} = \gamma \mathbf{I} \qquad [1.1]$$

The proportionality constant, γ, is known as the gyromagnetic ratio (units of rad T^{-1} s^{-1}). The sign of γ can be either positive or negative, which indicates that the direction of **μ** is aligned parallel or antiparallel to **I**, respectively. In NMR, the Larmor frequency, ω_0, is dependent upon γ and the magnitude of the applied external magnetic field:

$$\omega_0 = -\gamma \mathbf{B}_0 \qquad [1.2]$$

and describes the frequency of precession of the nucleus. In the following section, the interactions that give rise to unique NMR spectra are discussed.

1.1 NMR Interactions

All of the NMR interactions can be divided into two categories: external and internal. The external interactions include interactions of nuclear spins with $\mathbf{B}_0$, the external magnetic field, and with $\mathbf{B}_1$, the oscillating magnetic field which is induced by an applied radiofrequency (rf) pulse from the NMR coil. The internal interactions arise due to the magnetic and/or electronic environment in which the nucleus is located. The NMR Hamiltonian for a diamagnetic sample can be expressed as follows:[2,11,12]

$$\hat{\mathcal{H}}_{\mathrm{NMR}} = \hat{\mathcal{H}}_{\mathrm{Z}} + \hat{\mathcal{H}}_{\mathrm{rf}} + \hat{\mathcal{H}}_{\mathrm{Q}} + \hat{\mathcal{H}}_{\mathrm{CS}} + \hat{\mathcal{H}}_{\mathrm{DD}} + \hat{\mathcal{H}}_{\mathrm{J}} \qquad [1.3]$$

Where $\hat{\mathcal{H}}_{\mathrm{Z}}$, $\hat{\mathcal{H}}_{\mathrm{rf}}$, $\hat{\mathcal{H}}_{\mathrm{Q}}$, $\hat{\mathcal{H}}_{\mathrm{CS}}$, $\hat{\mathcal{H}}_{\mathrm{DD}}$, $\hat{\mathcal{H}}_{\mathrm{J}}$ are the Zeeman, rf, quadrupolar interaction (QI), nuclear magnetic shielding (NMS / MS), direct (dipolar) spin-spin coupling, and indirect (*J*) spin-spin coupling Hamiltonians, respectively. All of the interactions are discussed in detail below, with the exception of *J*-coupling, which does not play a major role in any of the projects discussed herein.

1.1.1 External Interactions

1.1.1.1 Zeeman Interaction

The Zeeman interaction is the interaction between a nuclear spin and an external magnetic field, $\mathbf{B}_0$, whose orientation is conventionally described along an arbitrary z-axis ($\mathbf{B}_0 = [0, 0, B_0]$). The Zeeman Hamiltonian is given as:

$$\hat{\mathcal{H}}_{\mathrm{Z}} = \gamma \hbar B_0 \hat{I}_{\mathrm{z}} \qquad [1.4]$$

where $\hbar$ is Planck's constant per radian (1.054571×10^{-34} kg m^2 s^{-1} rad^{-1}) and $\hat{I}_{\mathrm{z}}$ is the spin angular momentum operator which describes the projection of the nuclear spin angular momentum along the *z*-axis.

According to the classical picture of a magnetic dipole that is placed in an external magnetic field, the energy depends on the relative orientation of $\boldsymbol{\mu}$ to $\mathbf{B}_0$:

$$E = -\boldsymbol{\mu} \cdot B_0 = -\mu B_0 \cos(\theta) \qquad [1.5]$$

where θ is the angle in radians between $\boldsymbol{\mu}$ and $\mathbf{B}_0$. Thus, when $\boldsymbol{\mu}$ is aligned parallel with $\mathbf{B}_0$ ($\theta = 0$), this is the most energetically favourable orientation (i.e., lowest energy), whereas the anti-parallel orientation ($\theta = \pi$) is the most energetically unfavourable.

Unlike the classical picture in which $\boldsymbol{\mu}$ can take on any orientation from 0 to π radians, when a nucleus is placed in an external magnetic field, the orientations of $\boldsymbol{\mu}$ are quantized, because the spin angular momentum can only take on discrete values. The number of discrete energy levels that a nucleus of spin I can assume is $2I + 1$; each is associated with a unique quantum number m_I, where $m_I = +I, +I - 1, \ldots, -I$. The presence of the external magnetic field breaks the degeneracy of the m_I spin states, and their energy levels are described according to:

$$E_{m_I} = -m_I \hbar \gamma B_0 = -m_I \hbar \omega_0 \qquad [1.6]$$

An energy level diagram of the Zeeman interaction for a spin-1/2 nucleus with a positive gyromagnetic ratio is illustrated in **Figure 1.1**. The two spin states ($m_I = +1/2$ and $m_I = -1/2$, also known as α and β) represent nuclear spins which are precessing in counterclockwise and clockwise directions about $\mathbf{B}_0$ (the precession of the β spin can equivalently be described as counterclockwise, but with an orientation opposite to the direction of $\mathbf{B}_0$).[3,13] The nuclear spins in both orientations precess over a conical path, having a fixed angle between the external magnetic field and the nuclear spin angular momentum vector. The energy difference between the m_I spin states is therefore:

$$\Delta E = \hbar\omega_0 \qquad [1.7]$$

NMR is a very insensitive spectroscopic technique in terms of observable signal. This is due to the small energy differences between the m_I spin states, and the very small differences between the populations of the ensembles of spins in these states. For a typical NMR experiment, the energy of the Zeeman interaction is much smaller than the magnitude of the thermal energy (kT, where k is the Boltzmann constant (1.38065×10^{-23} J K^{-1}) and T is the temperature in Kelvin). For an ensemble of spins in a bulk sample, the ratio of spin populations in the α and β spin states is given by the Boltzmann distribution:

$$\frac{N_\alpha}{N_\beta} = e^{\frac{\Delta E}{kT}} = e^{\frac{\hbar\gamma B_0}{kT}} \qquad [1.8]$$

where N_α and N_β are the populations of the lower and higher energy spin states, respectively. For an ensemble of ^{1}H spins (I = 1/2, γ = 267.513×10^6 rad T^{-1} s^{-1} or

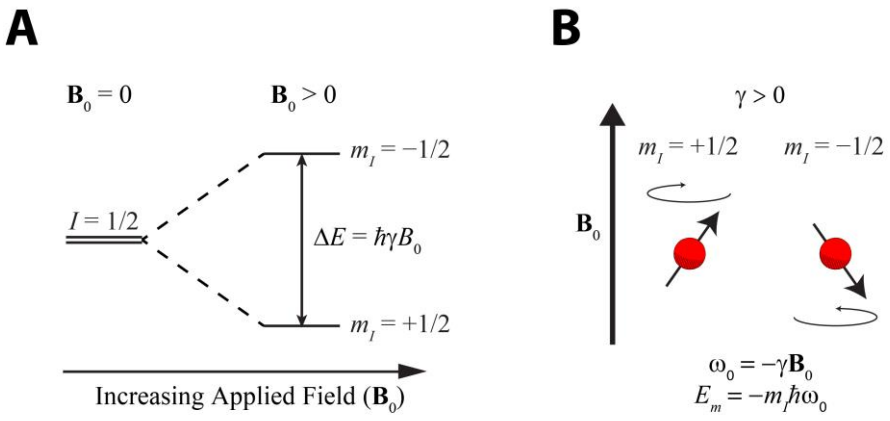

Figure 1.1. (A) The Zeeman interaction splits the degenerate energy levels of a spin-1/2 nucleus in the presence of an external magnetic field, $\mathbf{B}_0$. (B) Depiction of the nuclear spin angular momentum precessing about $\mathbf{B}_0$ for a nucleus with a positive value of γ.

42.576 MHz T^{-1}) in an applied magnetic field of 9.4 T and 298 K, the ratio N_α/N_β is equal to 1.000064456, which is a difference of only 0.0072%.

Despite the small difference in populations of the magnetic spin states, the excess spins in the α spin state result in a net bulk macroscopic magnetization, **M**, which is parallel to $\mathbf{B}_0$. It is this bulk magnetization that eventually leads to the NMR signal (*vide infra*). The NMR signal, $S_+(t)$, is proportional to:

$$S_+(t) \propto \frac{N\gamma^3\hbar^2{B_0}^2}{4kT} \qquad [1.9]$$

where N is the total number of NMR active spins ($N_\alpha + N_\beta$) in the sample. Clearly, higher magnetic fields are useful for increasing the NMR signal. In addition, increasing the number of spins (i.e., considerations of natural abundance and/or isotopic enrichment), using a nuclide with a higher value of γ (e.g., ^{35}Cl vs. ^{37}Cl), and/or conducting experiments at lower temperatures (as permissible) are all important for designing an NMR experiment that maximizes signal.

1.1.1.2 Radiofrequency Interaction

After a sample has been placed in the external magnetic field, $\mathbf{B}_0$, and the bulk magnetization, **M**, reaches an equilibrium state (as dictated by relaxation properties of the nucleus, *vide infra*), the NMR signal is not immediately detected. This is because **M** is aligned parallel to $\mathbf{B}_0$, and its presence cannot easily be observed with an induction coil with its axis oriented along the direction of $\mathbf{B}_0$; hence, it is necessary to orient **M** at a direction perpendicular to $\mathbf{B}_0$. This is achieved with the use of pulse of finite duration (τ_p), which oscillates at a particular transmitter frequency (ω_{T_x}, generally set to be equal to or near ω_0). The rf pulse is generated by passing alternating current through a

solenoid, which is oriented such that it generates a small oscillating field, $\mathbf{B}_1$, along its axis, which is oriented perpendicular to $\mathbf{B}_0$. The radiofrequency interaction (rf) describes what effect an applied rf field ($\mathbf{B}_1$) has on **M**, and is described by the Hamiltonian:[14]

$$\hat{\mathcal{H}}_{\text{rf}} = -\gamma B_1(t)\cos[\omega_{T_{\text{x}}}(t) + \phi]\mathbf{I}_{\text{x}} \qquad [1.10]$$

where $\omega_{T_{\text{x}}}$ is the radiofrequency of the pulse and ϕ is the phase.

The magnitude of B_1 is proportional to the power that is passed through the NMR coil; higher powers yield larger B_1 fields. In order to quantify the magnitude of the $\mathbf{B}_1$ field, B_1, a simple relationship describing the nutation frequency, ω_1, of the pulse is used:

$$\omega_1 = -\gamma B_1 \qquad [1.11]$$

The nutation frequency describes the rate at which magnetization precesses about $\mathbf{B}_1$ when it is applied on resonance (i.e., when $\omega_{T_{\text{x}}} = \omega_0$).

In order to understand why it is possible to rotate **M** with a very small $\mathbf{B}_1$ field (which is on the order of 10^4–10^5 times smaller than the magnitude of $\mathbf{B}_0$), the rotating frame model is applied. The rotating frame is a reference frame that rotates about the direction of $\mathbf{B}_0$ (z-axis) with an angular frequency of $\omega_{T_{\text{x}}}$. The new axes of this frame are denoted x' and y'. Hence, if a $\mathbf{B}_1$ field oscillating at $\omega_{T_{\text{x}}}$ is applied along an arbitrary axis of the lab frame, this component will appear to be stationary in the new rotating frame. The position of $\mathbf{B}_1$ in the rotating frame is set by choosing the appropriate reference phase;[3,6] most commonly, $\mathbf{B}_1$ is applied along the x', y', $-x'$, and $-y'$ axes of the rotating frame. In the rotating frame, the α and β spins that are precessing about $\mathbf{B}_0$ appear to be stationary if $\omega_0 = \omega_{T_{\text{x}}}$, as if the $\mathbf{B}_0$ field has completely disappeared (**Figure 1.2**). In this case, **M** precesses about $\mathbf{B}_1$ for as long as the rf pulse is applied (relaxation effects are

neglected here). If the pulse is applied for an interval known as the *pulse width*, τ_p, **M** rotates through the tip angle, θ_{rf}, according to:

$$\theta_{rf} = \tau_p \gamma B_1 = \tau_p \omega_1 \qquad [1.12]$$

When τ_p is chosen such that $\theta_{rf} = \pi/2$ rad, **M** is rotated into the *xy*-plane, which is a condition known as *saturation*, where the populations of the α and β spin states are equal. After a $\pi/2$ pulse, this new *transverse magnetization* precesses about $\mathbf{B}_0$, and induces a current in the same coil that was used to tip the magnetization in the first place. The induced signal in the coil is known as the *free precession signal*, or more commonly, the *free induction decay* (FID), since relaxation effects cause a gradual decay of the signal,

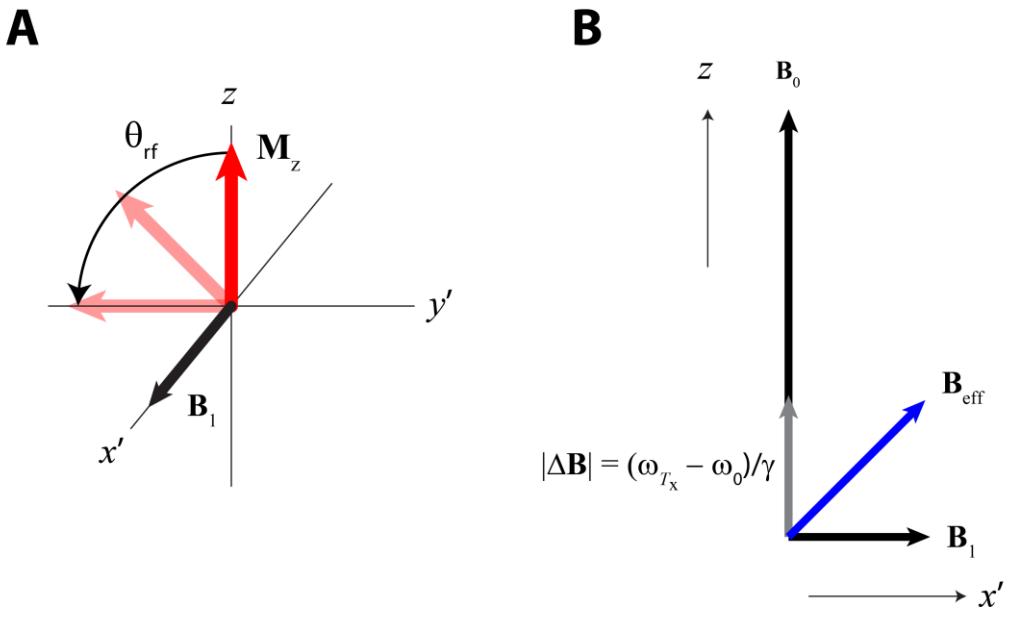

Figure 1.2. (A) Pictorial representation of a pulse, $\mathbf{B}_1$, applied on-resonance. $\mathbf{B}_1$ appears stationary along the *x*′-axis of a frame rotating at a frequency ω_0. Bulk magnetization, $\mathbf{M}_z$, precesses about the applied field and is rotated towards the *x*′*y*′-plane. (B) Application of a pulse at a frequency, ω_{T_x}, which differs from the Larmor frequency (i.e., $\Delta\omega = \omega_{T_x} - \omega_0$), results in two components of the applied rf field: one along the *x*′-axis and the other along the *z*-axis (having magnitude ΔB). The vector sum of $\mathbf{B}_1$ and $\Delta\mathbf{B}$ produces an effective $\mathbf{B}_1$ field ($\mathbf{B}_{eff}$) capable of rotating $\mathbf{M}_z$.

(*vide infra*). In order to efficiently tip **M** into the *xy*-plane, pulses have to be calibrated by (i) varying the pulse length (τ_p) while maintaining a constant power, or (ii) by maintaining a constant pulse length while varying the power. In both methods, maximum NMR signal indicates that a $\pi/2$ pulse has been calibrated. If the nutation frequency and tip angles for the $\pi/2$ pulse are known, they can be used to make a π pulse, which tips **M** by 180^o; this creates the condition known as *inversion*, where the populations of the α and β spin states are opposite to what they are at thermal equilibrium.

The above discussion focuses on the effects of $\mathbf{B}_1$ fields that are applied on-resonance (i.e., $\Delta\omega = \omega_{Tx} - \omega_0 = 0$). In most cases, especially in the case of spectra with multiple peaks and/or broad powder patterns, pulses are not applied exactly on resonance. To understand what happens in these off-resonance situations, the effective field is defined as:

$$\mathbf{B}_{\text{eff}} = (\mathbf{B}_0 - \omega_{T_x}/\gamma)\mathbf{z} + (\mathbf{B}_1/2)\mathbf{x}' \qquad [1.13]$$

where **z** and **x′** are unit vectors along the *z*- and *x*-axes of the rotating frame. If the $\mathbf{B}_1$ field is applied at a ω_{T_x} that is very far away from resonance, i.e., $(\mathbf{B}_0 - \omega_{T_x}/\gamma) >> \mathbf{B}_1$, then the $\mathbf{B}_{\text{eff}} \approx (\mathbf{B}_0 - \omega_{T_x}/\gamma)$, and there is no effect on the bulk magnetization. However, if $\mathbf{B}_1$ is applied at a ω_{T_x} closer to ω_0, then $(\mathbf{B}_0 - \omega_{T_x}/\gamma) << \mathbf{B}_1$ and $\mathbf{B}_{\text{eff}} \approx \mathbf{B}_1/2$, and there is a stationary effective field capable of rotating **M**. In such cases, there are two components of the applied rf field: one along the *x′*-axis and the other along the *z*-axis; the latter has a magnitude equal to $\Delta B = (\omega_{T_x} - \omega_0)/\gamma$. The magnitude of $\mathbf{B}_{\text{eff}}$ in this case is given by:

$$B_{\text{eff}} = \left(B_1^2 + \Delta B^2\right)^{1/2} \qquad [1.14]$$

Therefore, peaks at different frequency positions actually rotate at slightly different frequencies, depending on their distance from ω_{T_x}. This is the origin of *phase errors* in spectra, which can be corrected with *first-order phasing*.

1.1.2 Relaxation Processes

Although relaxation processes are not discussed in great detail in this dissertation, it is important to mention the two underlying relaxation processes in NMR. The *longitudinal relaxation*, T_1, is the relaxation process that describes the return of magnetization to its thermal equilibrium along the $\mathbf{B}_0$-axis (**Figure 1.3A**), according to:

$$M_z = M_0 \left(1 - e^{-\frac{t}{T_1}}\right) \qquad [1.15]$$

where M_z is the magnitude of the magnetization along the *z* axis, and M_0 is the magnitude of the equilibrium magnetization. Before commencing the application of pulses to create transverse magnetization, a waiting period known as the *recycle delay* is allowed to pass, in order to allow the magnetization to obtain a state of thermal equilibrium (complete thermal equilibrium occurs at $5T_1$). The T_1 of the nucleus depends upon fluctuating magnetic fields near the nucleus; in particular, magnetic fields that fluctuate at a rate near the Larmor frequency cause efficient T_1 relaxation. The T_1 can be dependent upon the nucleus, sample, and temperature, and can range from as short as μs to as long as hours or days; most commonly, it is found to range from ms to s in the solid state.

The *transverse relaxation*, T_2, is the relaxation process that describes the decoherence of precessing macroscopic magnetization in the transverse (*xy*) plane. After **M** is tipped into the *xy*-plane by an rf pulse, and the rf pulse is turned off, the presence of $\mathbf{B}_0$ causes the magnetization to start precessing in the *xy*-plane. The decoherence of magnetization in the *xy*-plane is brought about by both fluctuating magnetic fields and static magnetic fields (so-called non-secular and secular effects, respectively). Different components of the magnetization start to precess at slightly faster and slower frequencies, and decoherence continues until there is no coherent magnetization vector in the

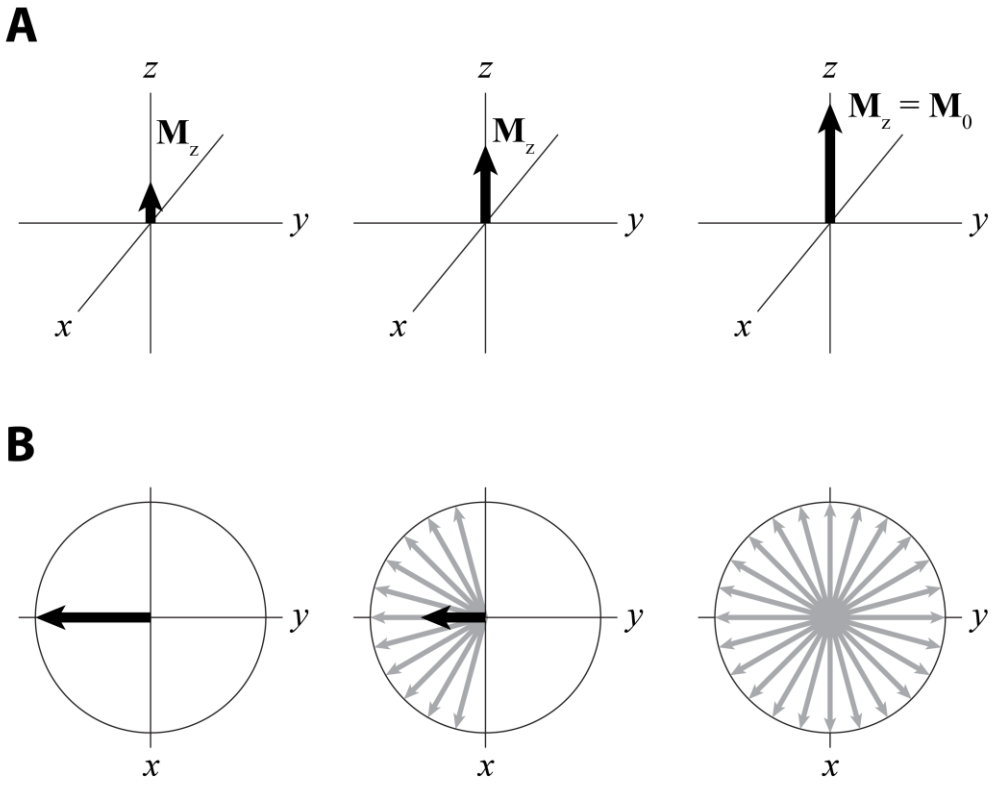

Figure 1.3. (A) The T_1 relaxation process showing the gradual build-up of magnetization along the z-axis. (B) The T_2 relaxation process showing the eventual decoherence of the magnetization in the *xy*-plane. The black vector represents the net magnetization, and the grey vectors represent individual isochromats with distinct precession frequencies.

transverse plane (**Figure 1.3B**). The decoherence of magnetization in the transverse plane can be described by $M_0\exp(-t/T_2)$, which means that more than 99% of the magnetization is incoherent after a time interval of $3T_2$.

1.1.3. Internal Interactions

1.1.3.1 Quadrupolar Nuclei and the Quadrupolar Interaction

Nuclides that have $I > 1/2$ possess nuclear quadrupole moments, Q, which result from an aspherical distribution of positive nuclear charge.[1,15] The quadrupolar interaction (QI) is the interaction of Q with the electric field gradient (EFG) at the nucleus. Nuclei that are surrounded by non-spherically symmetric (i.e., non-tetrahedral, non-cubic) distributions of charges and electron densities experience a non-zero EFG.[16,17] The EFGs with their origin at the nucleus are described by a symmetric (e.g., $V_{ij} = V_{ji}$), second-rank tensor, $\ddot{\mathbf{V}}$:

$$\ddot{\mathbf{V}} = \begin{bmatrix} V_{xx} & V_{xy} & V_{xz} \\ V_{yx} & V_{yy} & V_{yz} \\ V_{zy} & V_{zy} & V_{zz} \end{bmatrix} \qquad [1.16]$$

where the nine elements of the matrix correspond to EFG components oriented in some arbitrary reference frame.[18] The EFG tensor can be diagonalized into its principal axis system (PAS):[9]

$$\ddot{\mathbf{V}}^{\mathbf{PAS}} = \begin{bmatrix} V_{11} & 0 & 0 \\ 0 & V_{22} & 0 \\ 0 & 0 & V_{33} \end{bmatrix} \qquad [1.17]$$

where $|V_{11}| \leq |V_{22}| \leq |V_{33}|$. The EFG tensor is traceless (i.e., $V_{11} + V_{22} + V_{33} = 0$); therefore, it is often described by two parameters. The first is the *quadrupolar coupling constant*, C_Q (units of Hz):

$$C_Q = \frac{eqeQ}{h} = \frac{eQV_{33}}{h} \qquad [1.18]$$

which describes the magnitude of the quadrupolar interaction ($eq = V_{33}$, the largest component of the EFG tensor). The second parameter used to describe the EFG tensor is the *asymmetry parameter*, η_Q (dimensionless, $0 \leq \eta_Q \leq 1$):

$$\eta_Q = \frac{(V_{11} - V_{22})}{V_{33}} \qquad [1.19]$$

which describes the degree of axial symmetry of the EFG tensor. When $\eta_Q = 0$, $V_{11} = V_{22}$, and the EFG tensor has axial symmetry. At the other extreme, when $\eta_Q = 1$, $|V_{22}|$ and $|V_{33}|$ are equivalent (N.B., V_{11} and V_{22} have opposite signs to V_{33}). The Hamiltonian describing the quadrupolar interaction is:[9]

$$\hat{\mathcal{H}}_Q = \frac{eQ}{2I(2I-1)\hbar}\mathbf{I}\cdot\ddot{\mathbf{V}}\cdot\mathbf{I} \qquad [1.20]$$

The quadrupolar Hamiltonian can be expanded using perturbation theory:

$$\hat{\mathcal{H}}_Q = \hat{\mathcal{H}}_Q^{[1]} + \hat{\mathcal{H}}_Q^{[2]} + \cdots \qquad [1.21]$$

Although the QI may be expanded to even higher orders, generally only the first- and second-order terms of the quadrupolar interaction (FOQI and SOQI, respectively) have influences on the NMR powder patterns.[3] The energies for the spin states can be described by the sums of the energies associated with the interactions according to:[9]

$$E_m = E_{Z,m} + E_{Q,m}^{[1]} + E_{Q,m}^{[2]} \qquad [1.22]$$

where E_m is the total energy for a given spin state m, $E_{Z,m}$ is the energy of the Zeeman interaction, and $E^{[1]}_{Q,m}$ and $E^{[2]}_{Q,m}$ are the energy corrections associated with the FOQI and SOQI, respectively. The formula describing the energy correction to spin state m due to the FOQI is given by:[9,19,20]

$$E^{[1]}_{Q,m}=\frac{e^2qQ}{4I(2I-1)}[3m^2-I(I+1)]\cdot F(\theta,\phi) \qquad [1.23]$$

and $F(\theta, \phi)$ is:

$$F(\theta,\phi)=\frac{1}{2}\left[(3\cos^2\theta-1)+\frac{1}{2}\eta_Q\sin^2\theta\cos2\phi\right] \qquad [1.24]$$

where θ and ϕ are polar angles describing the orientation of the PAS of the EFG tensor with respect to the B_0 (θ is the angle between V_{33} and B_0). The energy correction due to the SOQI is similarly described by:[9,19,20]

$$E^{[2]}_{Q,m}=\left(\frac{e^2qQ}{4I(2I-1)}\right)^2\frac{m}{\omega_0}\cdot F_2(\theta,\phi,m,I) \qquad [1.25]$$

and $F_2(\theta, \phi, m, I)$ is:

$$\begin{aligned}F_2(\theta,\phi,m,I)=[&-\frac{1}{5}(I(I+1)-3m^2)\left(3+\eta_Q^2\right)+\frac{1}{28}(8(I(I+1)-12m^2\\&-3\left[\left(\eta_Q^2-3\right)(3\cos^2\theta-1)+6\eta_Q\sin^2\theta\cos2\phi\right]\\&+\frac{1}{8}(18(I(I+1)-34m^2-5)\left[\frac{1}{140}(18+\eta_Q^2)(35\cos^4\theta-30\cos^2\theta+3\right]\\&\times\frac{3}{7}\eta_Q^2\sin^2\theta(7\cos^2\theta-1)\cos2\phi+\frac{1}{4}\sin^4\theta\cos4\phi]\end{aligned} \qquad [1.26]$$

Figure 1.4 depicts how the FOQI and SOQI perturb the energies of the Zeeman spin states for a spin-1 nucleus.

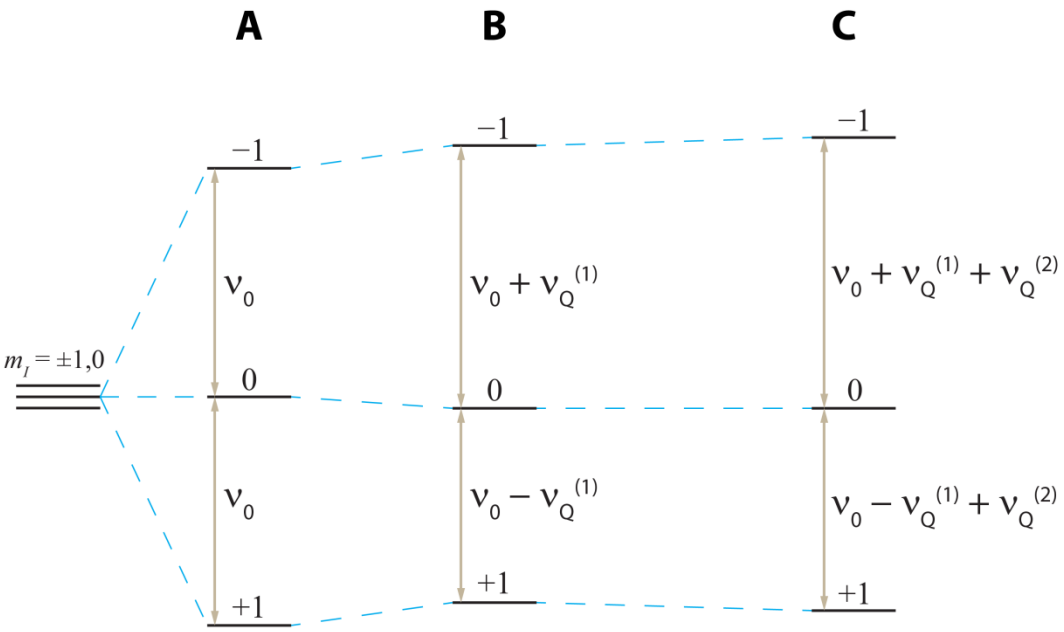

Figure 1.4. Schematic spin-1 energy level diagram showing the perturbations to the ^{14}N fundamental transitions (+1 ↔ 0 and 0 ↔ −1) under the influence of the (A) Zeeman, (B) first- and (C) second-order quadrupolar interactions. Note that the perturbations to the energy levels due to the SOQI are exaggerated compared to those of the Zeeman and FOQI.

The selection rule for allowed NMR transitions is $\Delta m = \pm 1$. The transition from $m = +1/2$ to $m = -1/2$ is known as the *central transition*. Any other transitions that satisfy the selection rule are known as satellite transitions (STs). From equation [1.23], it can be shown that for a spin-1 system all three spin states are perturbed by the FOQI (the $m = +1$ and $m = -1$ spin states are perturbed in the same direction, while the $m = 0$ spin state is perturbed in the opposite direction), resulting in two allowed fundamental ($\Delta m = \pm 1$) NMR transitions: +1 ↔ 0 and 0 ↔ −1. SSNMR spectra of spin-1 nuclides like ^{2}H, ^{6}Li, and ^{14}N in powdered, microcrystalline samples, which are only affected by the FOQI, yield a powder pattern known as a *Pake doublet*, which is mirror-symmetric about the Larmor frequency. This distinct appearance is caused by the overlapping patterns of the

two fundamental transitions (**Figure 1.5**). This characteristic pattern has discontinuities occurring at specific frequencies that occur for crystallite orientations in which V_{11}, V_{22}, or V_{33}, are parallel to B_0; they are related to the quadrupolar parameters according to:

$$\nu_{11} = \pm \frac{3}{8} C_Q(1 - \eta_Q) \qquad [1.24a]$$

$$\nu_{22} = \pm \frac{3}{8} C_Q(1 + \eta_Q) \qquad [1.24b]$$

$$\nu_{33} = \pm \frac{3}{4} C_Q \qquad [1.24c]$$

The discontinuities at ν_{11}, ν_{22}, and ν_{33} are referred to as the "horns," "shoulders," and "feet" of the powder pattern, respectively. Therefore, the positions of the discontinuities are also related to η_Q:

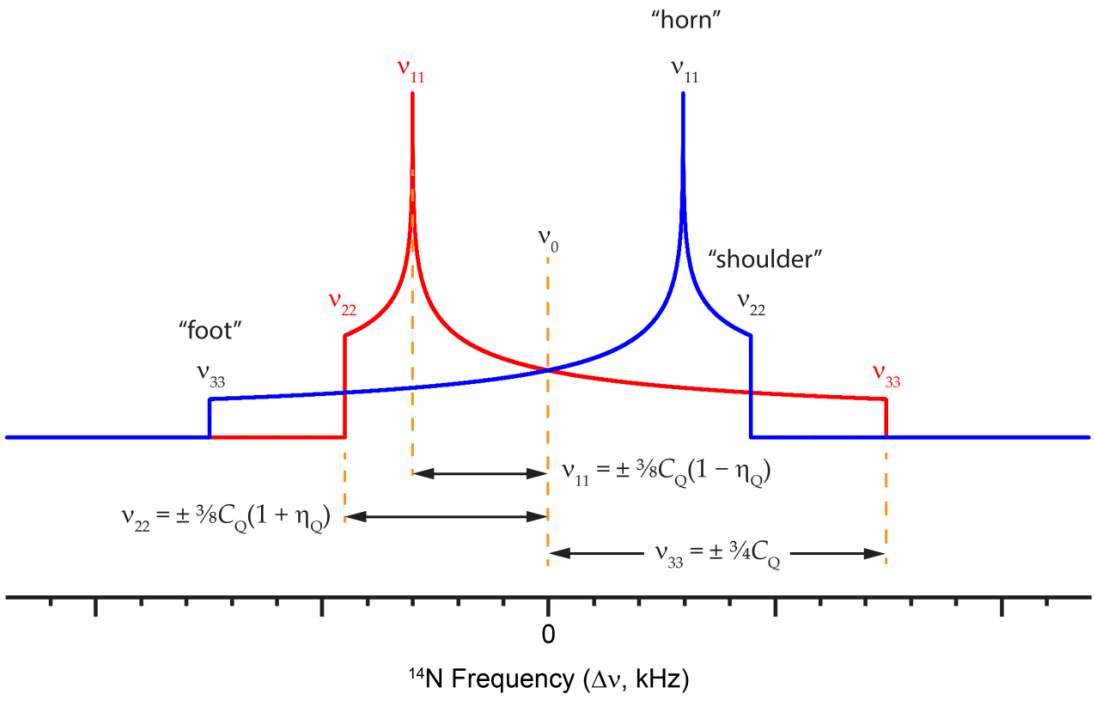

Figure 1.5. The underlying powder patterns for the two fundamental transitions, +1 ↔ 0 (red trace) and 0 ↔ −1 (blue trace) that make up the *Pake doublet* pattern observed in ^{14}N SSNMR powder patterns that are dominated by the FOQI.

$$\eta_Q = \frac{(\nu_{11} - \nu_{22})}{\nu_{33}} \qquad [1.25]$$

^{14}N SSNMR powder patterns with different values of C_Q and η_Q are shown in **Figure 1.6**. The breadth of the powder pattern depends on C_Q, while the separation of the horn and shoulder discontinuities is determined by η_Q.

When the magnitude of the QI becomes large (i.e., $C_Q \gtrsim 0.1\nu_0$),[21,22] the SOQI makes significant contributions to the ^{14}N SSNMR powder pattern. In the case of spin-1, the SOQI perturbs only the +1 and −1 spin states (in opposite directions), which breaks the mirror symmetry of the Pake doublet. The effects of the SOQI on the ^{14}N powder

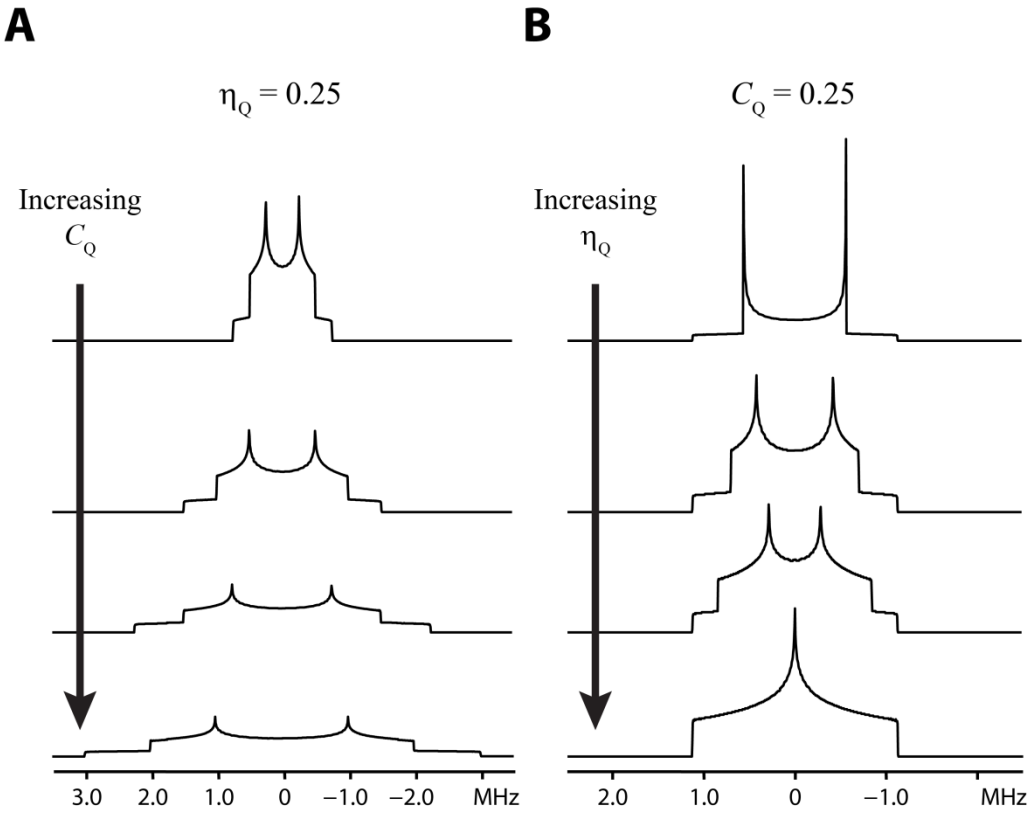

Figure 1.6. Variation in the shapes of ^{14}N powder patterns, when (A) changing the quadrupolar coupling constant, C_Q, with a constant value of η_Q = 0.25 and (B) changing the asymmetry parameter, η_Q, with a constant value of C_Q = 1 MHz. In (A), C_Q increases from 1 to 4 MHz in increments of 1 MHz. In (B), η_Q increases from 0 to 1 in increments of 0.25.

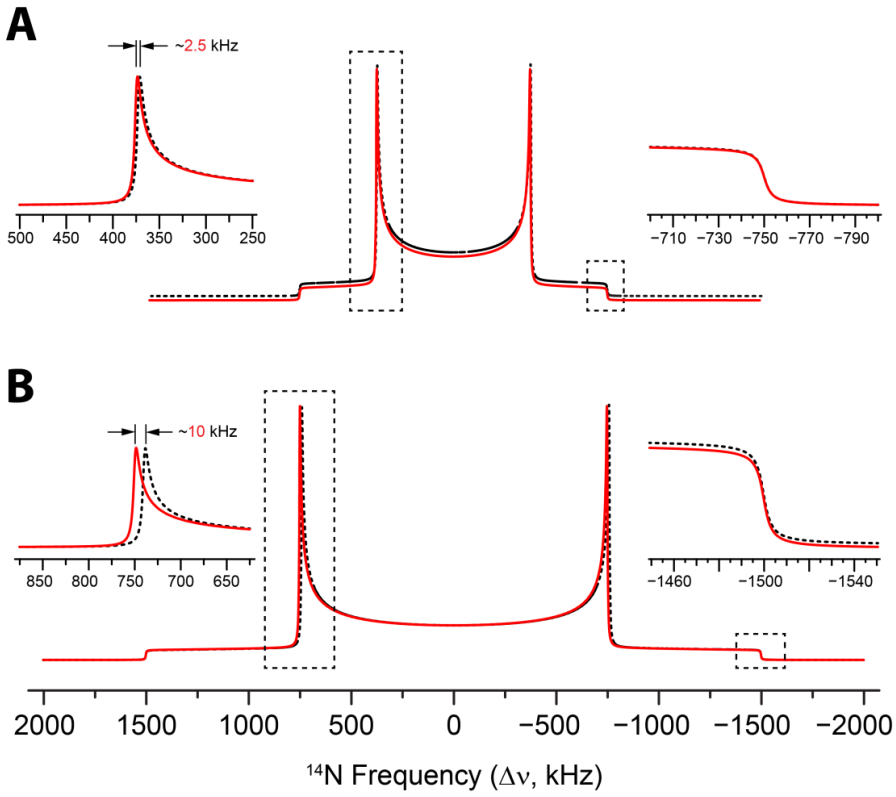

Figure 1.7. Analytical simulations of FOQI-dominated ^{14}N powder patterns with (**A**) C_Q = 1 MHz and η_Q = 0.00 and (**B**) C_Q = 2 MHz and η_Q = 0.00. The black and red simulations are without and with inclusion of the effects of the SOQI, respectively. The insets are expansions of the horn and foot discontinuities. For C_Q values of 1 and 2 MHz, the frequency of the horn discontinuities shift by 2.5 and 10 kHz, respectively, when the SOQI is included.

pattern are depicted in **Figure 1.7**.

In this dissertation, most of the systems that are investigated with ^{14}N SSNMR have $C_Q(^{14}N)$ values in the range of $0.8 \leq |C_Q| \leq 1.5$ MHz. Their powder patterns are dominated by the FOQI, and contributions from the SOQI (and other NMR interactions, *vide infra*) are insignificant and may be safely disregarded.

1.1.3.2 Magnetic Shielding and Chemical Shifts

If a molecule is placed into an external magnetic field, $\mathbf{B}_0$, small local fields, $\mathbf{B}_{ind}$, are induced in the molecule that decrease or increase the local net magnetic fields at each

nucleus, $\mathbf{B}_{loc}$. These effects are known as *nuclear magnetic shielding* (NMS) or *magnetic shielding* (MS). If $B_{loc} < B_0$, the nucleus is said to be shielded, and if $B_{loc} > B_0$, the nucleus is said to be deshielded. The shielding and deshielding of the nucleus leads to deviations from the Larmor frequency; thus, equation [1.2] for a nucleus affected by both the Zeeman and nuclear magnetic shielding interactions can be written as:

$$\omega_0 = -\gamma(B_0 + B_{ind}) \qquad [1.26]$$

What makes chemical shielding so invaluable for structural characterization is that the magnitude and sign of B_{ind} are dependent on both the chemical structure and orientation of the molecule with respect to $\mathbf{B}_0$. The Hamiltonian that is used to describe the MS has the form:[12]

$$\hat{\mathcal{H}}_{MS} = \gamma\hbar\hat{\mathbf{I}}\ddot{\sigma}\mathbf{B}_0 \qquad [1.27]$$

where $\ddot{\sigma}$ is the magnetic shielding tensor, which is a second-rank tensor:

$$\ddot{\sigma} = \begin{bmatrix} \sigma_{xx} & \sigma_{xy} & \sigma_{xz} \\ \sigma_{yx} & \sigma_{yy} & \sigma_{yz} \\ \sigma_{zy} & \sigma_{zy} & \sigma_{zz} \end{bmatrix} \qquad [1.28]$$

The MS tensor is asymmetric (i.e., $\sigma_{ij} \neq \sigma_{ji}$), but may be decomposed into a sum of two tensors consisting of symmetric and anti-symmetric matrix elements. Although only the symmetric component of the MS tensor makes a contribution to the observable NMR spectrum, both symmetric and anti-symmetric components play a role in nuclear spin relaxation.[23] The symmetric component of the MS tensor may be diagonalized and expressed in its PAS as:

$$\ddot{\sigma}^{PAS} = \begin{bmatrix} \sigma_{11} & 0 & 0 \\ 0 & \sigma_{22} & 0 \\ 0 & 0 & \sigma_{33} \end{bmatrix} \qquad [1.29]$$

where the principal axis components follow the convention $\sigma_{11} \leq \sigma_{22} \leq \sigma_{33}$. Unlike the EFG tensor, the MS tensor is not traceless (i.e., $\sigma_{11} + \sigma_{22} + \sigma_{33} \neq 0$).

In solution NMR, the sharp peak that is observed in the NMR spectrum is the result of rapid molecular tumbling that spatially averages the MS tensor, such that an isotropic magnetic shielding value is observed, $\sigma_{iso} = (\sigma_{11} + \sigma_{22} + \sigma_{33})/3$. Since magnetic shielding is reported relative to the shielding of a bare nucleus, and it is impractical to measure the NMR spectrum of a bare nucleus, it is convenient to utilize chemical shift (δ) and the chemical shift tensor (CS). The chemical shift value is determined by comparison of the experimentally determined resonant frequency to an accepted resonant frequency of a reference compound according to:[24]

$$\delta = \frac{\omega_{sample} - \omega_{reference}}{\omega_{reference}} \qquad [1.30]$$

where ω_{sample} and $\omega_{reference}$ are the frequencies of the experimental signal and the reference signal, respectively. δ is measured in parts per million (ppm), meaning that chemical shifts and their differences (i.e., between references and samples) are the same, regardless of the external magnetic field strength. Chemical shift values are related to magnetic shielding according to:[24]

$$\delta = \frac{\sigma_{reference} - \sigma_{sample}}{1 - \sigma_{reference}} \approx \sigma_{reference} - \sigma_{sample} \qquad [1.31]$$

Since the MS and CS values are easily interconvertible, it follows that the established conventions for MS are transferable to CS (but with opposite signs, i.e., $\delta_{11} \geq \delta_{22} \geq \delta_{33}$).

The CS tensor is often described with other sets of parameters, all of which distinguish the isotropic chemical shift from the chemical shift anisotropy (CSA).[9,25,26]

The Herzfeld-Berger convention uses (i) the isotropic chemical shift, δ_{iso}, which indicates the centre of gravity of the distribution of possible chemical shifts, ($\delta_{iso} = (\delta_{11} + \delta_{22} + \delta_{33})/3$) (ii) the span, Ω, which is the separation between the components indicating lowest (δ_{11}) and highest (δ_{33}) shielding ($\Omega = \delta_{11} - \delta_{33}$), and (iii) the skew, κ, which is a measure of the axial symmetry of the CS tensor:

$$\kappa = \frac{3(\delta_{22} - \delta_{iso})}{\Omega} \qquad [1.32]$$

where κ varies from −1 to +1. When $\kappa = \pm 1$, the CS tensor is axially symmetric. The Haeberlen convention can also be used to described CSA and the CS tensor[27] but it is not applied in this work.

The entire nitrogen chemical shift range spans roughly 900 ppm (if paramagnetic shifts are considered, the range is 1300 ppm).[28] By comparison, typical ^{14}N UW SSNMR powder patterns reported in this dissertation span *ca*. 62000 ppm (at 9.4 T). In all instances, the effects of the nitrogen CS tensor can be neglected; however, for the ^{15}N NMR spectra presented herein, the nitrogen chemical shifts are of great importance (*vide infra*).

1.1.3.3 Euler Angles

It is noted that the relative orientation of the EFG and CS tensors can have a profound effect on the powder patterns of quadrupolar nuclei, especially when the effects of the QI and CSA are of comparable magnitude.[29,30] The angles used to describe the relative orientation of the EFG and CS tensors are known as the *Euler angles*, α, β, and γ. As mentioned, the contribution of the nitrogen CSA can be neglected for the ^{14}N powder patterns reported in this dissertation, and hence, the Euler angles need not be considered.

1.1.3.4 Direct Dipolar Interaction

The magnetic dipole moments of two nuclear spins have a mutual through-space interaction, known as the *direct dipolar interaction*. The dipolar Hamiltonian that is used to describe the interaction between two spins, *I* and *S*, is:[9,11,31]

$$\hat{\mathcal{H}}_{DD} = \mathbf{I} \cdot \ddot{\mathbf{D}} \cdot \mathbf{S} \qquad [1.33]$$

The dipolar interaction tensor, $\ddot{\mathbf{D}}$, is described by a symmetric and traceless tensor. The dipolar Hamiltonian may be expanded to:

$$\hat{\mathcal{H}}_{DD} = R_{DD}\left[\mathbf{I} \cdot \mathbf{S} - \frac{3(\mathbf{I} \cdot \mathbf{r})(\mathbf{S} \cdot \mathbf{r})}{r^2}\right] \qquad [1.34]$$

where **r** is the internuclear vector and *r* is the internuclear distance. The term R_{DD}, known as the dipolar coupling constant is defined as:

$$R_{DD} = \left(\frac{\mu_0}{4\pi}\right)\left(\frac{\gamma_I \gamma_S \hbar^2}{\langle r^3 \rangle}\right) \qquad [1.35]$$

where μ_0 is the permeability of free space. It is clear from equation [1.35] that the magnitude of the direct dipolar interaction drops off precipitously as the distance between two nuclear spins is increased (due to the r^{-3} dependence). This Hamiltonian can be further expanded into the so-called *dipolar alphabet* Hamiltonian, which is comprised of terms with zero-, single- and double-quantum spin operators (only the single-quantum terms make secular contributions to NMR spectra in solids, while all terms can influence the contributions of the dipolar interaction to both longitudinal and transverse relaxation).[20]

Molecules undergoing rapid tumbling (i.e., in solution or gas phases) show no evidence of shifts or splittings arising from dipolar coupling, though the relaxation of the spin system is often dominated by dipolar interactions. However, the effects of homo-

and heteronuclear dipolar coupling (for both spin-1/2 and quadrupolar nuclei) can have adverse effects on SSNMR spectra, producing a complex variety of patterns.

The dipolar couplings that are of primary concern in this thesis are those involving the heteronuclear ^{1}H-^{14}N and ^{1}H-^{15}N spin pairs. For an N-H distance of 1.00 Å, which is a typical bond length in a RNH_3^+ moiety, the $R_{DD}(^{1}H\text{-}^{14}N)$ and $R_{DD}(^{1}H\text{-}^{15}N)$ are 8.7 and −12.2 kHz, respectively. The relatively small magnitudes of the ^{1}H-^{14}N dipolar coupling have little impact on ultra wideline (UW) ^{14}N SSNMR spectra, and no secular effects are generally visible (note that high-power ^{1}H decoupling fields of $\nu_2(^{1}H)$ = 30 kHz or greater are enough to partially, or completely, remove these effects). However, the ^{1}H-^{14}N dipolar couplings can affect the transverse relaxation of the ^{14}N nuclei, which can severely impact the acquisition of ^{14}N UW SSNMR spectra using the methodologies that are outlined in **Section 1.2.2**.

1.2 Solid-State NMR Techniques

1.2.1 Magic-Angle Spinning

Magic-angle spinning (MAS) is perhaps the most widely used technique in SSNMR. To first-order, NMR interactions have a $(3\cos^2\theta - 1)$ term that describes their orientation dependence (recall θ is the angle between $\mathbf{B}_0$ and the largest component of the interaction tensor). As discussed for the dipolar interaction, rapid molecular tumbling (i.e., small molecules in gas or liquid phases) reorients the NMR interaction tensors such that all values of θ are sampled on a rapid time scale (i.e., *correlation times*, τ_c, on the order of 10^{-11} to 10^{-12} s), which serves to average the NMR interactions to zero (i.e., quadrupolar and dipolar interactions) or to their isotropic values (i.e., chemical shifts and

indirect spin-spin couplings). In the solid state, molecules do not experience this rapid molecular tumbling; therefore, the anisotropic interactions are not averaged, which results in broad powder patterns and decreased S/N due to the dispersal of signal intensity over wide frequency ranges.

MAS can be used to achieve isotropic averaging of the NMR interactions by orienting the sample (contained within a rotor) such that its rotational axis is at the magic angle, 54.74°, with respect to the direction of $\mathbf{B}_0$, and spinning rapidly about this axis. The expectation value for the geometrical term, $\langle 3\cos^2\theta - 1 \rangle$, can be set to zero by considering the relative orientations of the reference frames of the NMR interaction, rotor, and magnetic field:[9]

$$\langle 3\cos^2\theta - 1 \rangle = \frac{1}{2}(3\cos^2\theta_R - 1)(3\cos^2\beta - 1) \qquad [1.36]$$

where θ_R is the angle between $\mathbf{B}_0$ and the rotor axis, and β is the angle between the largest principal tensor component of the NMR interaction tensor with respect to the rotor axis (**Figure 1.8**). Setting θ_R to 54.74° makes the right-hand side of eq. [1.36] equal to zero; this averages the expectation value on the left-hand side, meaning that it is possible to average the geometrical terms responsible for first-order anisotropic broadening to zero. To fully average a first-order anisotropic interaction of a single nucleus (i.e., to obtain a spectrum with a single peak, as would be observed in solution), the MAS spinning frequency must exceed the frequency distribution of the interaction. Advancements in probe technologies have allowed the development of NMR probes cable of reaching MAS rates in excess of 100 kHz (*ca*. 6 million revolutions per minute).[32–35]

For most ^{14}N SSNMR spectra, the magnitude of the broadening resulting from the FOQI far exceeds any reasonable MAS rate that can currently be achieved, so ^{14}N MAS

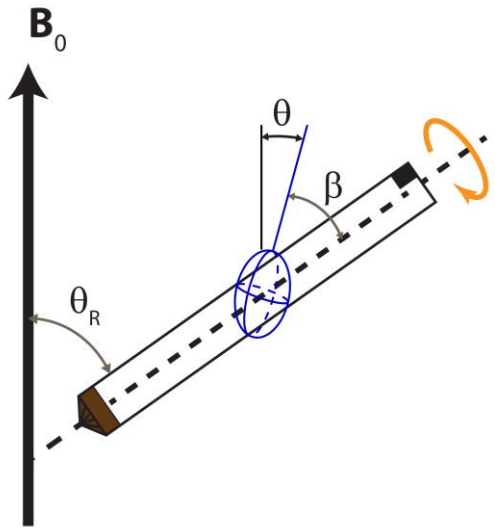

Figure. 1.8. Graphical depiction of the orientation of an NMR rotor with respect to $\mathbf{B}_0$. θ_R is the rotor angle (adjusted by the user), but is most commonly set to the magic angle, 54.74°. The ellipsoid represents one NMR-interaction-tensor orientation and its orientation with respect to $\mathbf{B}_0$ (described by the angle θ) and the rotor axis (described by the angle β).

cannot be used to entirely average this interaction. If anisotropic NMR interactions are not completely averaged with MAS, the result is an NMR spectrum exhibiting *spinning sidebands*, which occur at regular intervals (equal to the spinning rate) from the central isotropic centreband. Further complications arise for powder patterns displaying the effects of the SOQI, since second-order effects cannot be completely averaged by spinning at the magic angle, no matter how fast the sample is spun. In order to average second-order effects, the sample can be spun at two angles simultaneously (e.g., θ_1 = 54.74° and θ_2 = 30.56°), which requires specialized techniques and hardware (i.e., double-rotation MAS, DOR).[36] Alternatively, researchers have used manipulation of multiple quantum coherences in two-dimensional experiments to provide averaging of

second-order effects; in particular, the multiple-quantum MAS (MQMAS) experiment has found much use for acquiring spectra free of second-order effects.[37,38]

Although researchers have successfully demonstrated the acquisition of broad ^{14}N powder patterns with the use of MAS, the experiments required probes with extremely stable spinning speeds (less than ±1 Hz) and a precisely tuned magic angle (less than ±0.01°).[39–41] Due to the hardware requirements and extremely long experiments (e.g., in excess of 40 hours per experiment), this methodology has not become commonplace. All ^{14}N powder patterns described in this dissertation have therefore been acquired under static conditions (ν_{rot} = 0 Hz). *Chapter 6* of this dissertation is the only chapter in which the use of MAS is discussed.

1.2.2 Bloch decay vs. Hahn echo vs. CPMG

The simplest NMR experiment is the Bloch decay experiment. In its simplest form, this experiment features a single $\pi/2$ pulse, followed by an acquisition period. After the rf pulse has been applied, a short waiting period is necessary to allow for any remaining power in the circuit to dissipate and for the receiver to turn on and equilibrate, before the NMR signal can be detected. Failure to allow for a short dead time (τ_{dead}) results in interference in the FID, which is often termed as *pulse breakthrough*. This can be problematic for the acquisition of SSNMR spectra, since the FIDs decay very quickly due to the effects of anisotropic NMR interactions which result in inhomogeneously broadened powder patterns. The effects of this inhomogeneous broadening are akin to the T_2* effects on linewidths observed in solution NMR spectra, except that in this case, broadening arises from the inhomogeneity in the external magnetic field. The unfortunate consequence of this is that the NMR signal might be totally or partially

decayed before it can be detected by the receiver (**Figure 1.9A**). One possible way to detect the NMR signal is to create a "spin-echo" with the use of the Hahn-echo pulse sequence.

The Hahn-echo pulse sequence is expressed in the form $\{(\pi/2)_x - \tau_1 - \pi_y - \tau_2 - \text{acquire}\}$, where τ_1 and τ_2 are inter-pulse delays, and the subscripts indicate the phases of the pulses, which correspond to the x' and y' axes of the rotating frame (**Figure 1.9B**). The first $\pi/2$ pulse rotates the magnetization into the transverse plane; this is followed by an evolution period, τ_1. Then, a π pulse is applied to refocus the magnetization that is dephasing as the result of inhomogeneous broadening. After a second time interval, τ_2, the magnetization refocuses, forming a *spin echo* or *Hahn echo.* The values of τ_1 and τ_2 can be selected to allow for the collection of either half of the echo or the full echo.

The Carr-Purcell Meiboom-Gill (CPMG) pulse sequence features continued

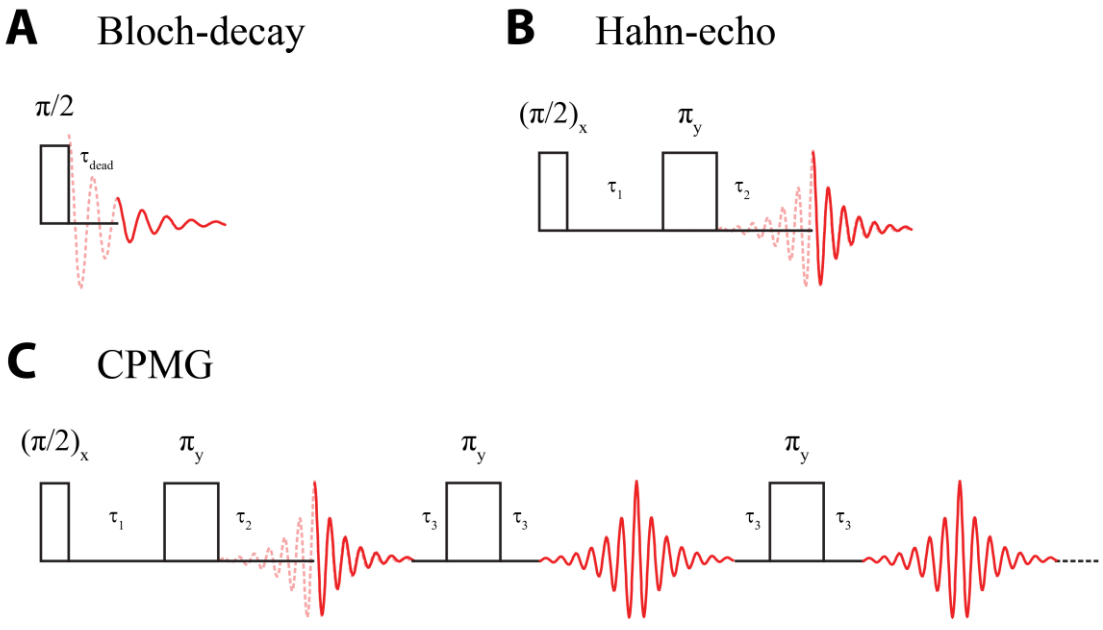

Figure. 1.9. Schematic representations of (A) Bloch-decay, (B) Hahn-echo, and (C) CPMG pulse sequences.

application of π refocusing pulses after the initial π pulse,[42–45] interspersed with acquisition windows (**Figure 1.9C**). The resulting FID consists of a train of echoes whose decay is dependent on T_2 (or an effective T_2, T_2^{eff}, when decoupling is applied in double-resonance experiments). The decays of the individual echoes are still largely governed by the T_2* effects arising from inhomogeneous broadening. The collection of many echoes in a single FID results in significant S/N gains over conventional Hahn-echo and Bloch decay experiments. The FID may be processed by simple Fourier transformation, resulting in a frequency spectrum consisting of "spikelets," whose outer manifold will trace out the overall powder pattern. Conversely, the CPMG echoes may be shifted and co-added to form a single high-intensity echo, which when Fourier transformed, results in a standard powder pattern. Powder patterns processed using the latter method are referred to as 'echo-coadded spectra.'

In solid-state NMR experiments, CPMG-style pulse sequences are generally parameterized to maximize the S/N (by collecting as many echoes as possible), while retaining a high degree of resolution so that important spectral features may be accurately located (i.e., discontinuities). There are numerous considerations for successfully conducting CPMG-style experiments, including the parameterization of inter-echo delays and concomitant spikelet spacings; the reader is referred to an excellent review of the practical aspects of CPMG NMR by Hung and Gan.[46]

1.2.3 WURST-CPMG

All of the rf pulses discussed to this point are conventional rectangular pulses that are short (on the order of μs), monochromatic (single transmitter frequency), and of constant phase. Such pulses are crucial in most NMR experiments, since they are generally capable of uniformly exciting relatively broad spectral regions. However, rectangular pulses which are high in power and short in duration are not effective for the uniform excitation patterns with breadths of 250 kHz or greater (especially with larger coil sizes from 2.5 mm inner diameter or greater). In addition, the repeated application of high power pulses can put severe stress on the NMR hardware, especially when cross polarization (CP, *vide infra*) sequences are used, which can feature simultaneous pulses on two channels for tens of ms.

In 1995, Kupče and Freeman published an article describing a frequency-swept pulse which has the characteristics of being Wideband, Uniform-Rate, and having Smooth Truncation (WURST),[47] whose amplitude and phase profiles are depicted in **Figure 1.10**. WURST pulses are utilized for the irradiation of broad spectral regions using low rf fields at constant transmitter frequencies; the broad excitation is made possible by quadratic modulation of the phase of the WURST pulse, which results in a virtual frequency sweep. This virtual frequency sweep generates an effective magnetic field, $\mathbf{B}_{\text{eff}}$, that slowly rotates magnetization from the *z*-axis for the purposes of creating transverse or inverted magnetization. These pulses, which are sometimes referred to as "chirped" pulses, have found many uses in solution-state NMR for broadband decoupling, excitation and signal suppression.[48]

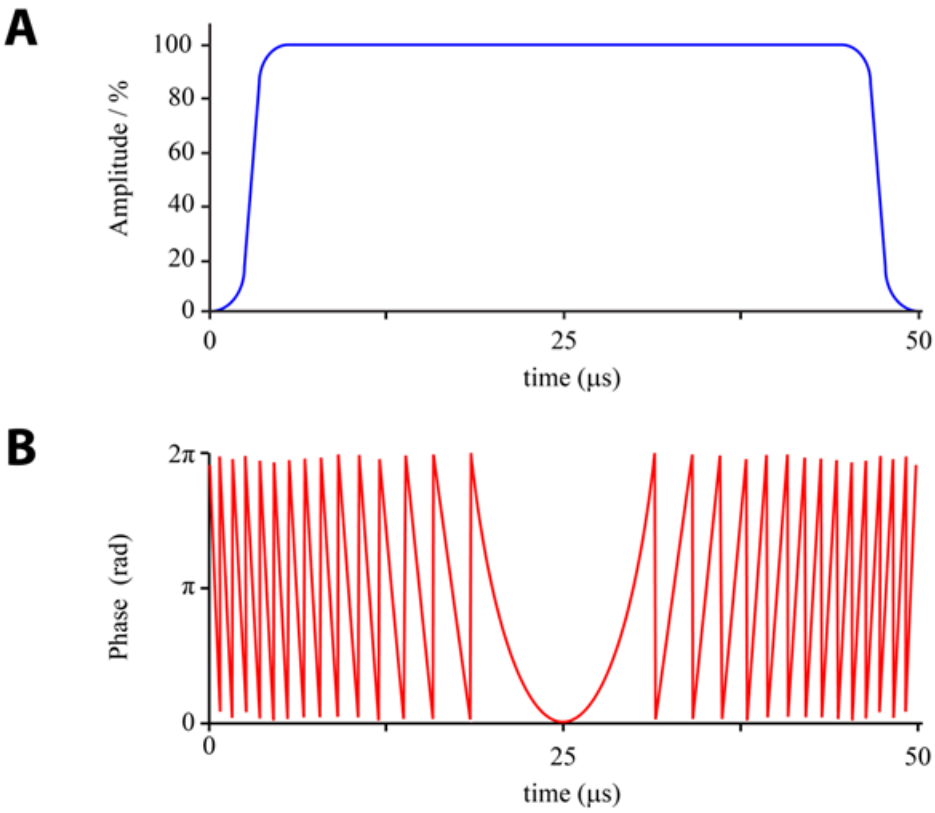

Figure. 1.10. (A) Amplitude and (B) phase profiles of a wideband, uniform-rate, smooth truncation (WURST) pulse.

In 2007, Bhattacharyya and Frydman demonstrated the use of WURST pulses in a Hahn echo-like pulse sequence, for the purposes of exciting central-transition powder patterns of quadrupolar nuclei spanning hundreds of kHz in breadth.[49] In 2008, O'Dell and Schurko demonstrated that the WURST pulses may be implemented in the framework of a CPMG pulse sequence, providing the benefits of broadband excitation (WURST) and T_2-based signal enhancement (CPMG).[50]

The WURST-CPMG pulse sequence (**Figure 1.11**) has two identical WURST pulses; the first pulse is the excitation pulse (similar to the $\pi/2$ pulse in the CPMG pulse sequence), while the second and subsequent pulses are used for refocusing of the magnetization in the transverse plane. This pulse sequence has been widely used for the

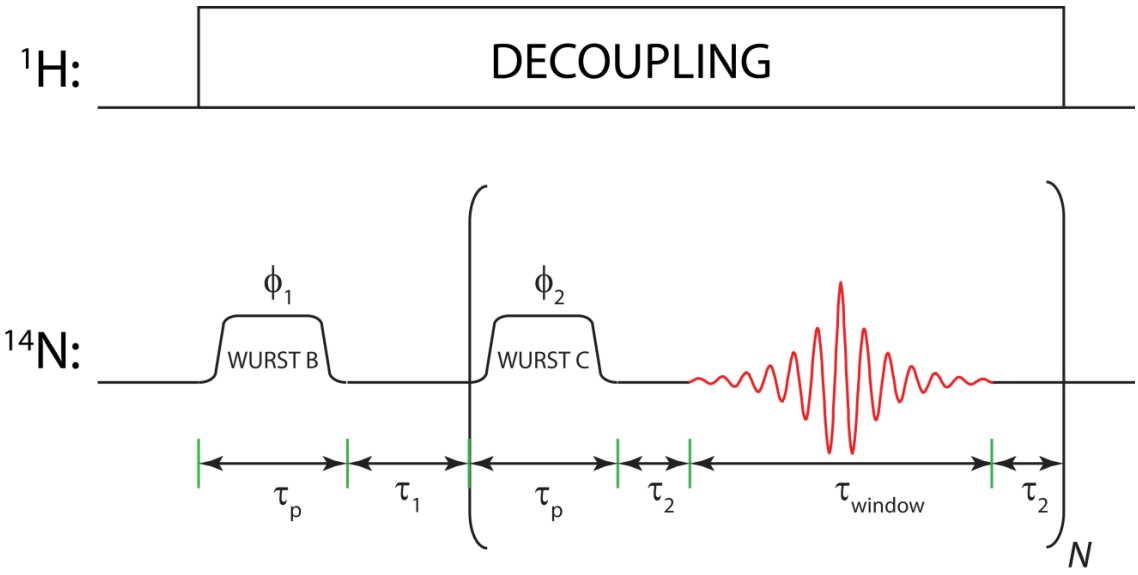

Figure 1.11. Schematic representation of the WURST-CPMG pulse sequence. The WURST pulses, denoted WURST-B and WURST-C, are identical. WURST-B is used for excitation while WURST-C is used for refocusing.

acquisition of NMR spectra with broad patterns arising from anisotropic quadrupolar and chemical shift interactions.[51,52] The excitation breadths that can be achieved with the WURST pulses are dependent on the parameterization of the pulses and is discussed in further detail in Chapter 5, along with their use in maximizing the efficiency of the acquisition of ^{14}N UW SSNMR powder patterns.

1.2.4 Frequency-Stepped Acquisition of Broad Powder Patterns

The SSNMR powder patterns discussed herein typically have breadths on the order of 1 to 2 MHz. Despite the broad excitation bandwidths afforded by WURST pulses, the breadths of the powder patterns may still exceed the excitation and detection bandwidths of the most NMR probes, meaning that only portions of the overall patterns can be excited in a single experiment at a single transmitter frequency. In such cases, it is possible to use the variable-offset cumulative spectroscopy (VOCS) or frequency-stepped

acquisition method,[53–55] where individual sub-spectra are acquired by stepping the transmitted frequency in even increments across the breadth of the entire pattern (**Figure 1.12**). The sub-spectra are then combined to form the total spectrum via co-addition or skyline projection.

There are two considerations for acquiring frequency-stepped spectra: (i) the separation between subsequent transmitter frequencies has to be chosen such that there is sufficient overlap between the adjacent sub-spectra (transmitter steps that are too far apart may result in undersampling of the overall spectrum, while transmitter steps that are too close together result in oversampling of the spectrum and unnecessarily long experiments). The choice of transmitter separation is often determined empirically for a given excitation profile, after observation of excitation breadths and pattern shapes from a single experiment. (ii) For frequency-stepped acquisition using CPMG-style pulse sequences, such as WURST-CPMG, the transmitter steps should be multiple integers of the spikelet separation, in order aid in the co-addition/projection of individual sub-spectra (this is only strictly necessary if the spectra are processed to yield spikelets in the frequency domain). The use of the frequency-stepped method with the WURST-CPMG pulse sequence allows for a substantial reduction in the number of sub-spectra that need to be acquired, thereby reducing overall experimental time, and in some cases, allowing access to broad patterns (e.g., 5 MHz or greater) that cannot be acquired by any other set of methods.

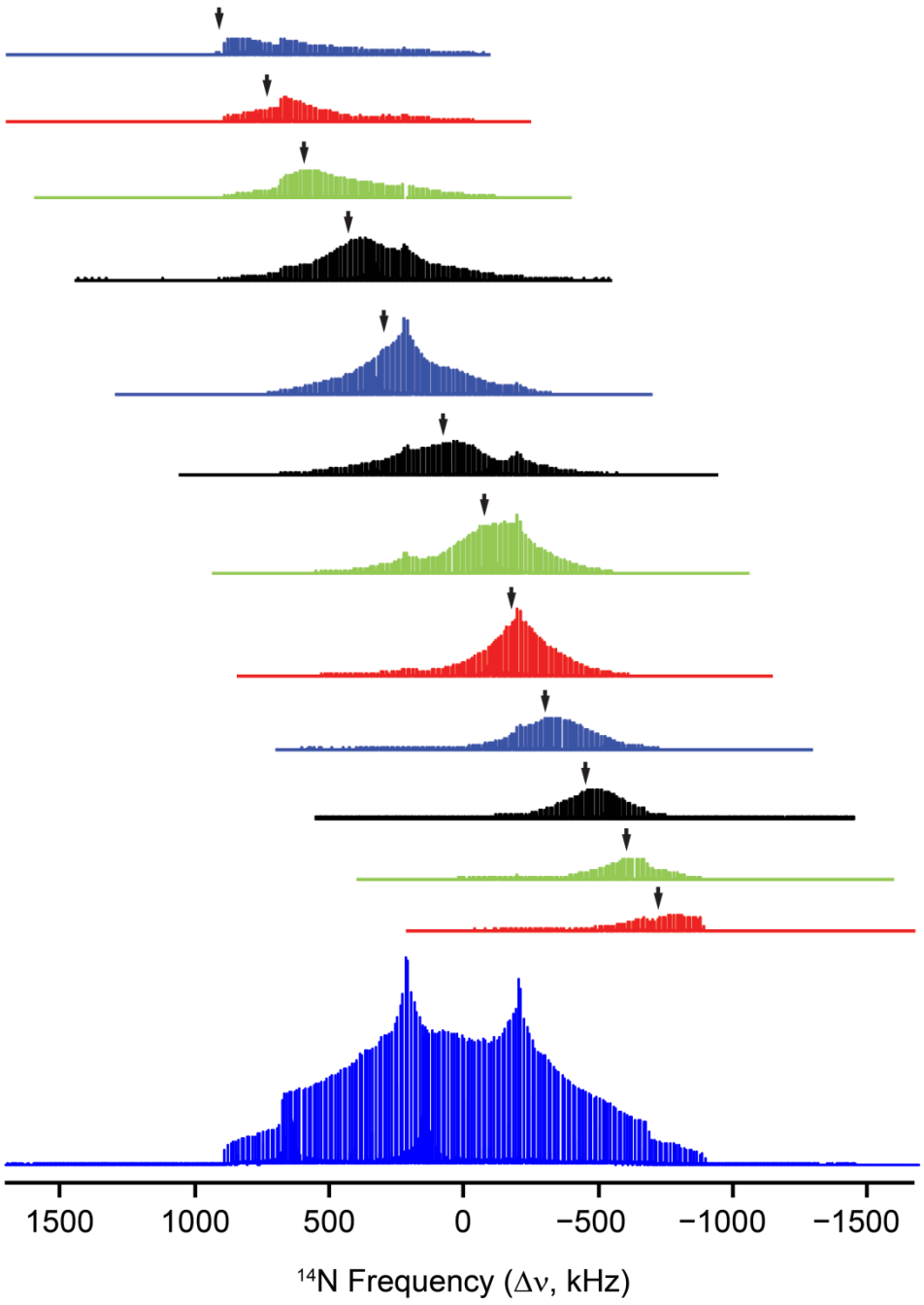

Figure 1.12. ^{14}N WURST-CPMG sub-spectra of α-glycine acquired via the frequency-stepped acquisition method. The transmitter frequency ($\Delta\nu_{T_X}$) of each sub-spectrum is denoted by the arrow. The total spectrum is produced by co-addition of the sub-spectra.

1.2.5 Cross-Polarization

Cross-polarization is one of the most widely used techniques in SSNMR. This technique involves the transfer of spin polarization from *abundant*, high-γ nuclides (e.g., ^{1}H and ^{19}F are the most common) to lower-γ nuclei (e.g., ^{13}C, ^{14}N and ^{15}N), which are often referred to as *dilute nuclides*. The abundant and dilute nuclides are normally denoted as *I* and *S*. This transfer of polarization is achieved with the use of the CP pulse sequence shown in **Figure 1.13**.[56–58] A π/2 pulse is applied (along the *x*-axis) to tip the spin polarization of the *I* nucleus into the *xy*-plane (along the –*y*-axis). Spin-locking pulses (along the *y*-axis) are then applied on both *I* and *S* channels. In order to achieve polarization transfer, the power of the spin-locking pulses must be chosen such that they satisfy the Hartmann-Hahn condition:[59,60]

$$\omega_{1I} = \omega_{1S} \qquad [1.37]$$

$$\gamma_I B_{1I} = \gamma_S B_{1S} \qquad [1.38]$$

where ω_{1I} and ω_{1S} are the nutation rates on the **I** and **S** channels, respectively. The Hartmann-Hahn condition can vary depending on the spins of *I* and *S*,[61,62] and whether the experiment is conducted upon a static sample or under the conditions of MAS.[56–58] The time that the spin-locking pulse is applied for is called the contact time (*ct*), the duration of which can vary, depending on the identity of the spin pair and the specific chemistry of the system. After the polarization has been transferred to the S nuclei, since it is already in the *xy*-plane, it can be detected without any additional rf pulses.

The use of CP yields a potential signal enhancement on the ratio of the gyromagnetic ratios of the nuclei that are involved in the process; for the two nuclei discussed in this dissertation, this maximum theoretical signal enhancements are 9.86 and

13.84, for ^{15}N and ^{14}N, respectively. Additionally, since no excitation pulses are applied on the *S* channel, the repetition rate of the experiment depends on the T_1 relaxation time of the *I* nuclei. For many spin-1/2 nuclides in organic, inorganic, biological and organometallic systems, such as ^{13}C, ^{15}N and ^{31}P, the $T_1(^1\text{H})$ is often much shorter than that of the *S* nuclides, which results in shorter recycle delays and substantial reductions in experimental times. For quadrupolar nuclides like ^{14}N, the $T_1(^1\text{H})$ is often much longer than the $T_1(^{14}\text{N})$, and experimental times are not reduced from decreased recycle delays (though the regular advantages of CP are still in play).

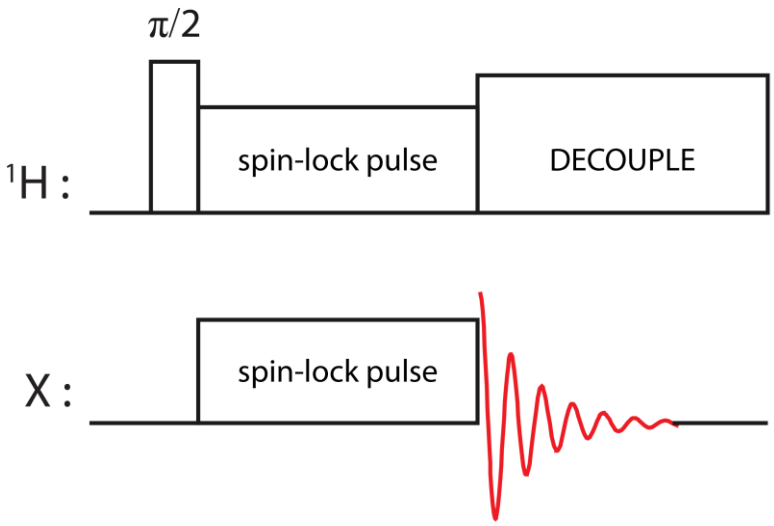

Figure 1.13. Schematic representation of the conventional CP pulse sequence.

1.2.6 BRoadband Adiabatic INversion Cross-Polarization

Conventional CP sequences, like the one shown in **Figure 1.13**, are only capable of transferring polarization over a limited frequency range of the *S* channel, even under conditions of MAS. Such techniques are extremely limited for the excitation of UW SSNMR powder patterns, the application of conventional CP systems results in sub-

spectra with high S/N but very limited excitation bandwidths. This may necessitate the collection of many sub-spectra (using frequency-stepping) in order to obtain the full UW powder pattern.

The use of a WURST pulse for spin-locking on the *S* channel has recently been proposed by Harris *et al.*[63] in order to achieve cross polarization over broadband frequencies. This new pulse sequence, BRoadband Adiabatic INversion Cross-Polarization (BRAIN-CP) can be combined with the WURST-CPMG pulse sequence, which results in a fully broadband CP experiment which has the benefits of both high S/N from the CP process and T_2-dependent echo collection, as well as broad excitation and refocusing due to the use of WURST pulses. The BRAIN-CP/WURST-CPMG pulse sequence (BCP for brevity) is depicted in **Figure 1.14**. There are several key differences that distinguish BRAIN-CP from conventional CP: (i) the spin-locking pulse on the *S* channel is a frequency-swept WURST pulse, (ii) for a given crystallite in the powder pattern, the Hartmann-Hahn condition does not occur for the entire duration of the CT, but rather, for at least two crystallite orientations, and (iii) the BCP process inverts spin polarization along the $-z$ axis; therefore, a conversion pulse is necessary to rotate this magnetization into the *xy*-plane for detection.

The application of the BRAIN-CP/WURST-CPMG pulse sequence to spin-1 nuclei is demonstrated in *Chapters 2* and *4* of this dissertation. To date, one limitation of the BRAIN-CP/WURST-CPMG pulse sequence is the inability to utilize it in conjunction with MAS, though an exploratory study by our group has been published,[64] and further work is currently underway.

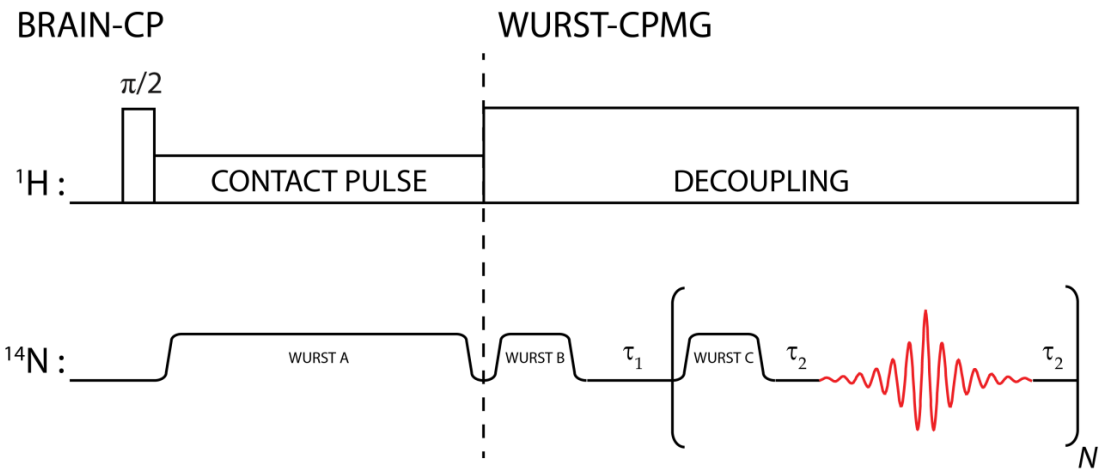

Figure 1.14. Schematic representation of the BRAIN-CP/WURST-CPMG pulse sequence. The two portions of the pulse sequence are separated by a vertical dashed line. In the BRAIN-CP portion, WURST-A is a distinct WURST pulse designed for broadband adiabatic inversion. In the WURST-CPMG portion, WURST-B and WURST-C are identical WURST pulses used for broadband conversion and refocusing, respectively.

1.2.7 Minimizing the Times of ^{14}N SSNMR Experiments

The ^{14}N powder patterns discussed herein are very broad (1 to 2.25 MHz) and generally have low S/N. Clearly, the aforementioned WURST-CPMG, BCP and frequency-stepped methods are all useful for their spectral acquisition. Further steps can be taken to reduce experimental time, while not compromising the information that can be extracted from these spectra. One of these steps is called spectral mirroring, in which only half of the total ^{14}N powder pattern is acquired (either the high- or low-frequency half, depending upon probe tuning conditions), and the other half is produced by mirroring about the ^{14}N Larmor frequency (N.B., mirroring during processing is largely done for aesthetic purposes, and to keep the traditional Pake doublet appearance of the ^{14}N pattern; in fact, only half of the ^{14}N pattern needs to be displayed, see *Chapter 5*). ^{14}N powder patterns arising from C_Q values between 0.5 and 2.25 MHz are dominated by the FOQI, and are mirror-symmetric about the ^{14}N Larmor frequency. It is only

necessary to acquire the entire powder pattern in cases where (i) the C_Q value is very small (i.e., $C_Q \precsim 0.5$ MHz) and the effects of nitrogen CSA contributions are apparent or (ii) the C_Q value is very large (i.e., $C_Q \gtrsim 2$ MHz) and the effects of the SOQI are manifested in the spectrum. This method allows for the collection of a diminished number of sub-spectra, and reduces the overall acquisition time by a factor of two.

Another benefit of mirroring becomes apparent if the NMR hardware has different tuning characteristics for frequencies above or below the ^{14}N Larmor frequency (i.e., tuning range limitations, power handling, etc.). Half of the ^{14}N powder pattern may be acquired using the hardware configuration that produces the best result, which allows avoiding hardware related distortions in the spectrum.

Finally, quadrupolar parameters are extracted from ^{14}N powder patterns solely on the basis of the positions of the discontinuities; this suggests that it is possible to further reduce the number of sub-spectra needed to obtain this information, via targeted spectral acquisitions. This is discussed in Chapter 5 of this dissertation.

1.2.8 Direct vs. Indirect Detection

The NMR methods discussed to this point are classified as *direct detection* methods, in which the NMR signals are observed on the channel corresponding to the *S* nucleus. In contrast to this, it is possible to *indirectly detect* the NMR signal which arises from the *S* nucleus by observing its influences on the NMR signal of the *I* nucleus (i.e., ^{1}H).[65,66] There can be a significant gain in sensitivity by detecting the signal from the **I** nuclei, due to their higher natural abundance and higher γ. Indirect detection experiments can be conducted on spin pairs that are directly dipolar or indirectly spin-spin coupled.

The indirect detection of ^{14}N has been highlighted extensively by Cavadini *et al.*,[67–69] Ulzega,[70] and others.[71–73] Solid-state NMR investigations of ^{15}N via indirect detection have included organic-inorganic hybrid materials,[74] isotopically enriched proteins,[75] and peptides.[76,77] In this thesis, the indirectly detected heteronuclear correlation (idHETCOR) experiment[76,78,79] is utilized for the acquisition of ^{15}N-^{1}H correlation spectra on samples without isotopic enrichment of ^{15}N.

Indirect detection solution NMR experiments involving ^{1}H, ^{13}C, and ^{15}N have been successful, largely due to the narrow ^{1}H resonance linewidths that are present in solution, which yield high resolution and good separation of cross-peaks. In the solid state, the ^{1}H resonances are severely broadened due to the homonuclear coupling of protons, which limits the resolution of indirect-detection methods. With the advent of ultra-fast MAS probes capable of achieving stable MAS rates in excess of 40 kHz, the breadths of proton resonances can now be significantly reduced, which clears the way for indirect detection techniques.[78]

In this dissertation, the idHETCOR pulse sequence that is utilized (**Figure 1.15**) is a modification of a sequence proposed by Ishii and Tycko.[76,78] The experiment commences with $^{1}\text{H} \rightarrow {}^{15}\text{N}$ CP transfer, followed by a t_1 period during which ^{15}N magnetization evolves in the presence of heteronuclear ^{1}H decoupling (SPINAL-64[80]). Any residual ^{1}H magnetization remaining after the evolution period is eliminated using rotary resonance recoupling by a pair of long pulses with orthogonal phases,[79,81] whose RF amplitudes satisfied the HORROR condition $\nu_{RF}(^{1}\text{H}) = \nu_{rot}/2$. The ^{1}H magnetization is detected following the final $^{15}\text{N} \rightarrow {}^{1}\text{H}$ CP transfer, this time under heteronuclear ^{15}N SPINAL-64 decoupling. The evolution period, t_1, is incremented in even steps that are

multiples of the MAS rate. The resulting two-dimensional spectrum consists of a ^{1}H chemical shift spectrum in the direct dimension (*x*-axis), a ^{15}N chemical shift spectrum in the indirect dimension (*y*-axis), and cross-peaks that correspond to dipolar correlations between ^{1}H and ^{15}N. The idHETCOR experiments discussed in this dissertation have been acquired on natural abundance samples without any isotopic enrichment.

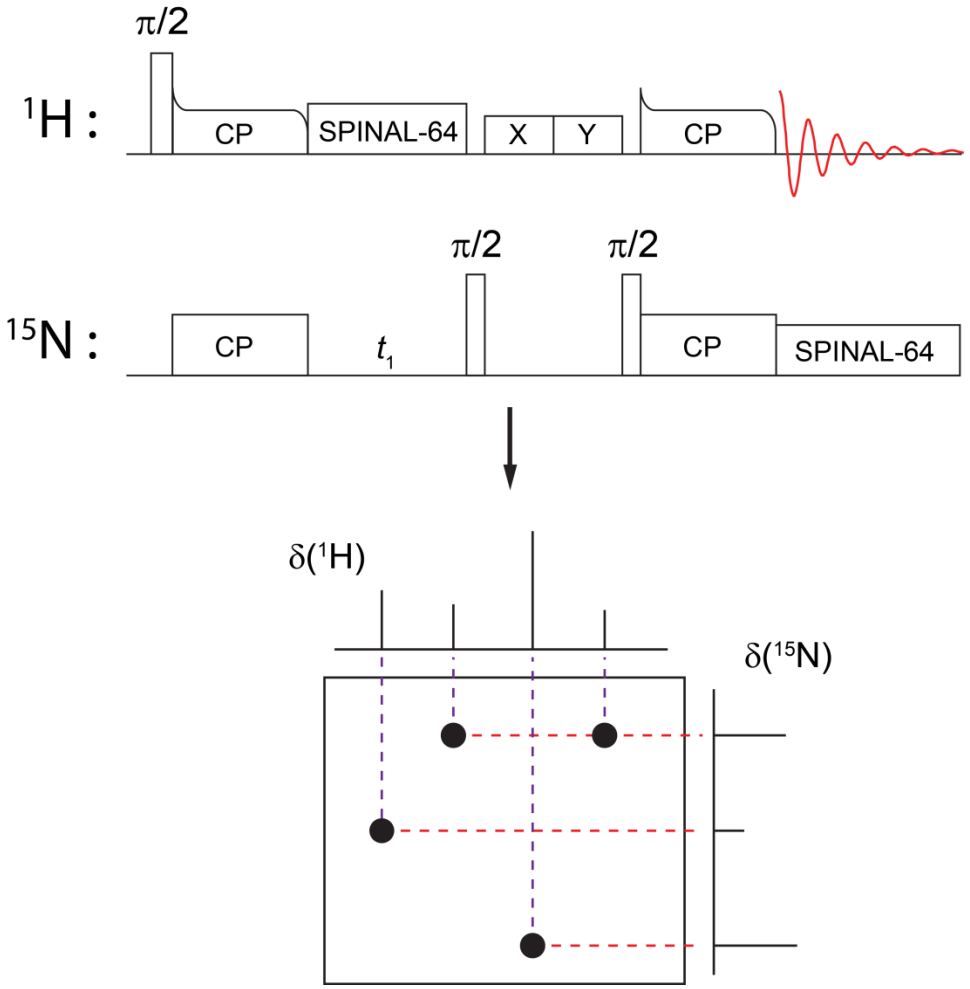

Figure 1.15. Schematic representation of the ^{1}H{^{15}N} idHETCOR pulse sequence.

1.2.9 Ab initio calculations

One of the major challenges for first principles quantum-chemical theories is the accurate calculation of NMR interaction tensor parameters.[18,82] These calculations allow for the correlation of MS and EFG interaction tensor parameters and orientations with differences and changes in molecular-level structure, bonding, and dynamics. This in turn allows for the exploration of the origin of NMR interactions, and the potential to solve structures and propose the rational synthesis and design of new molecules and materials. One of our particular interests is the orientations of NMR interaction tensors, which are normally only experimentally available from single-crystal NMR studies (which are rare), or by inference from symmetry and local geometry. Modern quantum chemistry computational packages are capable of providing reliable information on tensor parameters and orientations, which in turn, aids in our understanding of the NMR-structure relationships outlined above.

Density functional theory (DFT), which is currently the predominant method for solid state quantum chemical computations, exploits the principle that the electronic properties of a system may be determined from the total electronic energy of that system, and that the ground-state electronic energy is described solely as a function of the spatially-dependent electron density. It is possible to calculate physical properties such as electrical properties (e.g., dielectrics), magnetic properties (e.g., MS tensors), elastic constants (e.g., lattice parameters), and phonons, all by calculating second-order energies with respect to perturbations of electric and magnetic fields or atomic coordinates. Therefore, by accurately calculating the ground-state electronic energy of a system, it is feasible to calculate the NMR interaction tensors (i.e., EFG tensors, which are dependent

only upon the ground state, and MS tensors, which require accurate treatment of the excited states).

There are many DFT-based computational packages available for calculating NMR tensor parameters; however, the nitrogen-containing solids discussed herein are all crystalline and have highly periodic structures. Therefore, their NMR interactions cannot be accurately calculated from computational packages that utilize models featuring isolated single molecules (i.e., so-called "gas-phase" calculations). Although calculations on cluster models of increasing size have been shown to improve the accuracy of the calculated NMR parameters, they still lack the accuracy provided by the CASTEP[83] and NMR CASTEP[84] packages.[85] One key difference between the CASTEP computational packages in comparison to computational methods such as Gaussian[86] and Amsterdam Density Functional (ADF)[87] is the utilization of gauge-including projector augmented-wave (GIPAW) calculations in the former.[88] GIPAW calculations employ plane-wave basis sets that satisfy periodic boundary conditions and are particularly suitable for compounds that have long-range periodic structures. Due to the periodic nature of crystals, the potential at a given point in space satisfies Bloch's theorem: $V(\mathbf{r} + \mathbf{L}) = V(\mathbf{r})$, where $V(\mathbf{r})$ is the potential at point $\mathbf{r}$, and $V(\mathbf{r} + \mathbf{L})$ is the potential at a point $\mathbf{r}$ displaced by a vector, $\mathbf{L}$, (representing a translation of the lattice); hence, the computation can be conducted upon the simplest repeating unit of the crystal structure, the unit cell, without the need to build large cluster models. The use of pseudopotentials further allows CASTEP and NMR CASTEP to simplify the complex effects of the motions of core (i.e., non-valence) electrons of the atom, in order to reduce computational times. As such, the CASTEP and NMR CASTEP packages are useful for DFT calculations on a wide range

of systems, including crystalline materials, amorphous solids, liquids, surfaces, and even metals.

Many of the nitrogen-containing solids described herein feature intermolecular hydrogen-bonding as an essential component of their structures; therefore, comparison of ^{14}N NMR EFG tensors obtained from experiment and theory is extremely valuable for studying intermolecular hydrogen bonding, as shown in *Chapters 2, 3* and *6*.

1.3 Context of the Research

Nitrogen is ubiquitous in chemistry, biology, and materials science. ^{15}N (I = ½) solid-state NMR (SSNMR) is widely used for the molecular-level characterization of nitrogen-containing compounds; however, ^{15}N has a low natural abundance (0.37%), which generally necessitates isotopic enrichment; this can be expensive, synthetically challenging, and/or restrict the experimentalist to the study of only systems which can be isotopically enriched. By contrast, ^{14}N is 99.63% naturally abundant; however, there are significantly fewer ^{14}N SSNMR studies reported in the literature, since ^{14}N is a quadrupolar nucleus (I = 1), with a moderate quadrupole moment (Q = 20.44 mbarn) and a low gyromagnetic ratio ($\gamma(^{14}\mathrm{N})$ = 1.934 × 10^7 rad T^{-1} s^{-1}). ^{14}N SSNMR spectra typically exhibit severe inhomogeneous broadening arising from the first-order quadrupolar interaction (FOQI), for almost all ^{14}N nuclei except those in environments with highly spherical distributions of ground-state electron density. These patterns are difficult to acquire due to their very low S/N ratios, which arise from the combination of wide spectral breadths and low experimental Larmor frequencies.

Many recent advances for enhancing S/N in UW SSNMR spectra show promise for enabling routine acquisition of ^{14}N SSNMR spectra, including broadband excitation pulses, CPMG-type sequences, strategic acquisition methods, and the increasing availability of state-of-the-art hardware (e.g., high magnetic fields, low-gamma probes, and dynamic nuclear polarization (DNP) NMR spectrometers). All of these innovations are crucial for the development of ^{14}N SSNMR spectroscopy for probing important aspects of organic and inorganic solids, such as hydrogen-bonding and polymorphism, as well as molecular dynamics and relaxation processes.[40,41,89–92] The primary foci of this dissertation are (i) to develop methodologies for easily and rapidly acquiring ^{14}N SSNMR utilizing pulse sequences designed for UW NMR patterns, (ii) to apply these methods for the characterization of a wide range of nitrogen-containing systems, and (iii) to explore the relationships between ^{14}N EFG tensor parameters and molecular structure and dynamics.

Chapter 2 of this dissertation focuses on a ^{14}N SSNMR study of sp^3-hybridized nitrogen moieties of amino acids. The amino acid systems were chosen due to their central importance to many areas of chemistry and biochemistry, as well as because (i) they are readily available, inexpensive and facile to prepare in pure forms (including deuterated species), (ii) they contain pseudo-tetrahedral (i.e., RNH_3^+ or $RR'NH_2^+$) nitrogen moieties, which have ^{14}N UW SSNMR powder patterns that can be acquired in reasonable time frames using moderate magnetic field strengths (e.g., 9.4 T), and (iii) they provide a large data set of quadrupolar parameters from structural homologues which will allow for continued investigation of the relationships between local molecular structure, intermolecular interactions (i.e., hydrogen bonding) and the ^{14}N EFG tensor.

In Chapter 3, ^{14}N UW SSNMR is applied for the differentiation of three polymorphs of glycine and its HCl salt derivative. The polymorphs are successfully differentiated based on the ^{14}N quadrupolar parameters, as well as the ^{14}N relaxation characteristics (i.e., $T_2^{\text{eff}}(^{14}\text{N})$. A brief investigation into the dynamics of the rotating NH_3 groups in these samples is also undertaken, and these results are exploited in an effort to reduce the experimental times of ^{14}N UW SSNMR experiments.

Chapters 4 and 5 focus on increasing experimental efficiency of and reducing the time required to acquire ^{14}N UW SSNMR powder patterns. The application of broadband CP, in the form of the BRAIN-CP/WURST-CPMG pulse sequence, is explored in Chapter 4. The enhancements in the S/N of the ^{14}N NMR spectra are found to be between four and ten times, which, in some cases, allow for the acquisition of ^{14}N powder patterns that would be prohibitive with the use of direct-excitation NMR methods, due to the extremely long experimental times. In Chapter 5, the parameterization of the WURST-CPMG pulse sequence, as it is applied in ^{14}N UW SSNMR experiments, is systematically investigated in two parts: (i) the design of the WURST pulse is explored and practical guidelines are established for efficient acquisition of ^{14}N UW SSNMR powder patterns, and (ii) practical considerations for the use of CPMG refocusing for maximizing both S/N and resolution in ^{14}N SSNMR powder patterns. The fundamental appearance of ^{14}N powder patterns is also explored, and a strategy is developed that allows for the measurement of the ^{14}N quadrupolar parameters from only two sub-spectra acquired at strategically located transmitter frequencies.

Finally, in Chapter 6, a preliminary investigation of the use of natural abundance ^{14}N and ^{15}N SSNMR methods (WURST-CPMG and BRAIN-CP/WURST-CPMG and

$^{1}H\{^{15}N\}$ idHETCOR, for ^{14}N and ^{15}N respectively) in tandem for the study of active pharmaceutical ingredients (APIs) and their polymorphs is presented. The acquisition of NMR spectra of both NMR isotopes permits the collection of quadrupolar and CS parameters that aid in polymorph differentiation, identification of impurity phases, and perhaps even structural prediction.

1.4 Bibliography

(1) Slichter, C. P. *Principles of Magnetic Resonance*; 3rd ed.; New York, 1990.

(2) Mehring, M. *Principles of High Resolution NMR in Solids*; 2nd ed.; Springer-Verlag, 1983.

(3) Levitt, M. H. *Spin Dynamics: Basics of Nuclear Magnetic Resonance*; 2nd ed.; John Wiley & Sons, Ltd.: Chichester, England, 2008.

(4) Keeler, J. *Understanding NMR Spectroscopy*; John Wiley & Sons: Chichester, 2005.

(5) Schmidt-Rohr, K.; Spiess, H. W. *Multidimensional Solid-State NMR and Polymers*; Academic Press: San Diego, 1994.

(6) Fukushima, E.; Roeder, S. B. W. *Experimental Pulse NMR - A Nuts and Bolts Approach*; Addison-Wesley Publishing Company, Inc.: Reading, Massachusetts, 1981.

(7) Abragam, A.; Goldman, M. *Nuclear Magnetism: order and disorder*; Clarendon Press: Oxford, 1982.

(8) Fyfe, C. A. *Solid State NMR for Chemists*; C.F.C. Press: Guelph, 1983.

(9) Duer, M. J. *Introduction to Solid-State NMR Spectroscopy*; Wiley-Blackwell, 2004.

(10) Stejskal, E. O.; Memory, J. D. *High Resolution NMR in the Solid State*; Oxford

University Press: New York, 1994.

(11) Cowan, B. *Nuclear Magnetic Resonance and Relaxation*; Cambridge University Press: Cambridge, 1997.

(12) Haeberlen, U. *High Resolution NMR in Solids: Selective Averaging*; Academic Press, Inc.: New York, 1976.

(13) Levitt, M. H. *J. Magn. Reson.* **1997**, *126*, 164.

(14) Harris, R. K. *Nuclear Magnetic Resonance Spectroscopy*; 1986.

(15) Lucken, E. A. C. *Nuclear Quadrupole Coupling Constants*; Academic Press: London, 1969.

(16) Akitt, J. W.; McDonald, W. S. *J. Magn. Reson.* **1984**, *58*, 401.

(17) Knop, O.; Palmer, E. M.; Robinson, R. W. *Acta Crystallogr. Sect. A* **1975**, *31*, 19.

(18) Autschbach, J.; Zheng, S.; Schurko, R. W. *Concepts Magn. Reson. Part A* **2010**, *36A*, 84.

(19) Cohen, M. H.; Reif, F. In *Solid State Physics*; Seitz, F., Ed.; Academic Press: New York, 1957; pp. 321–438.

(20) Abragam, A. In *The Principles of Nuclear Magnetic Resonance*; Claredon Press: Oxford, 1983; p. Chapter VII.

(21) Bain, A. D. *Mol. Phys.* **2003**, *101*, 3163.

(22) Bain, A. D.; Khasawneh, M. *Concepts Magn. Reson. Part A Bridg. Educ. Res.* **2004**, *22*, 69.

(23) Anet, F. A. L.; O'Leary, D. J. *Concepts Magn. Reson.* **1991**, *3*, 193.

(24) Emsley, J. W.; Feeney, J.; Sutcliffe, L. H. *High Resolution Nuclear Magnetic Resonance Spectroscopy*; Vot 1.; 1965.

(25) Dye, J. L.; Ellaboudy, A. S.; Kim, J. *Pract. Spectrosc.* **1991**, *11*, 217.

(26) Herzfeld, J.; Berger, A. E. *J. Chem. Phys.* **1980**, *73*, 6021.

(27) Harris, R. K.; Becker, E. D.; De Menezes, S. M. C.; Granger, P.; Hoffman, R. E.; Zilm, K. W. *Pure Appl. Chem.* **2008**, *80*, 59.

(28) Marburger, S. P.; Fung, B. M.; Khitrin, A. K. *J. Magn. Reson.* **2002**, *154*, 205.

(29) Power, W. P.; Wasylishen, R. E.; Mooibroek, S.; Pettitt, B. A.; Danchura, W. *J. Phys. Chem.* **1990**, *94*, 591.

(30) Cheng, J. T.; Edwards, J. C.; Ellis, P. D. *J. Phys. Chem.* **1990**, *94*, 553.

(31) Wasylishen, R. E. *Encyclopedia of Nuclear Magnetic Resonance*; Grant, D. M.; Harris, R. K., Eds.; Wiley: New York, 1996.

(32) Agarwal, V.; Penzel, S.; Szekely, K.; Cadalbert, R.; Testori, E.; Oss, A.; Past, J.; Samoson, A.; Ernst, M.; Böckmann, A.; Meier, B. H. *Angew. Chem. Int. Ed. Engl.* **2014**, *53*, 12253.

(33) Nishiyama, Y.; Kobayashi, T.; Malon, M.; Singappuli-Arachchige, D.; Slowing, I. I.; Pruski, M. *Solid State Nucl. Magn. Reson.* **2015**, *66*, 56.

(34) Pandey, M. K.; Nishiyama, Y. *Solid State Nucl. Magn. Reson.* **2015**, *70*, 15.

(35) Qi, Y.; Malon, M.; Martineau, C.; Taulelle, F.; Nishiyama, Y. *J. Magn. Reson.* **2014**, *239*, 75.

(36) Samoson, A.; Lippmaa, E.; Pines, A. *Mol. Phys.* **1988**, *65*, 1013.

(37) Frydman, L.; Harwood, J. S. *J. Am. Chem. Soc.* **1995**, *117*, 5367.

(38) Medek, A.; Harwood, J. S.; Frydman, L. *J. Am. Chem. Soc.* **1995**, *117*, 12779.

(39) Giavani, T.; Bildsøe, H.; Skibsted, J.; Jakobsen, H. J. *Chem. Phys. Lett.* **2003**, *377*, 426.

(40) Giavani, T.; Bildsøe, H.; Skibsted, J.; Jakobsen, H. J. *J. Magn. Reson.* **2004**, *166*, 262.

(41) Zhou, B.; Giavani, T.; Bildsøe, H.; Skibsted, J.; Jakobsen, H. J. *Chem. Phys. Lett.* **2005**, *402*, 133.

(42) Larsen, F. H.; Jakobsen, H. J.; Ellis, P. D.; Nielsen, N. C. *J. Phys. Chem. A* **1997**, *101*, 8597.

(43) Siegel, R.; Nakashima, T. T.; Wasylishen, R. E. *J. Phys. Chem. B* **2004**, *108*, 2218.

(44) Siegel, R.; Nakashima, T. T.; Wasylishen, R. E. *Concepts Magn. Reson. Part A* **2005**, *26A*, 47.

(45) Lipton, A. S.; Sears, J. A.; Ellis, P. D. *J. Magn. Reson.* **2001**, *151*, 48.

(46) Hung, I.; Gan, Z. *J. Magn. Reson.* **2010**, *204*, 256.

(47) Kupče, Ē.; Freeman, R. *J. Magn. Reson. Ser. A* **1995**, *115*, 273.

(48) Garwood, M.; DelaBarre, L. *J. Magn. Reson.* **2001**, *153*, 155.

(49) Bhattacharyya, R.; Frydman, L. *J. Chem. Phys.* **2007**, *127*, 1.

(50) O'Dell, L. A.; Schurko, R. W. *Chem. Phys. Lett.* **2008**, *464*, 97.

(51) Schurko, R. W. Acquisition of Wideline Solid-State NMR Spectra of Quadrupolar Nuclei. *Encyclopedia of Magnetic Resonance*, 2012.

(52) Schurko, R. W. *Acc. Chem. Res.* **2013**, *46*, 1985.

(53) Massiot, D.; Farnan, I.; Gautier, N.; Trumeau, D.; Trokiner, A.; Coutures, J. P. *Solid State Nucl. Magn. Reson.* **1995**, *4*, 241.

(54) Medek, A.; Frydman, V.; Frydman, L. *J. Phys. Chem.* **1999**, *103*, 4830.

(55) Tang, J. A.; Masuda, J. D.; Boyle, T. J.; Schurko, R. W. *ChemPhysChem* **2006**, *7*, 117.

(56) Pines, A.; Gibby, M. G.; Waugh, J. S. *Chem. Phys. Lett.* **1972**, *15*, 373.

(57) Gibby, M. G.; Griffin, R. G.; Pines, A.; Waugh, J. S. *Chem. Phys. Lett.* **1972**, *17*,

80.

(58) Pines, A.; Gibby, M. G.; Waugh, J. S. *J. Chem. Phys.* **1972**, *56*, 1776.

(59) Hartmann, S. R.; Hahn, E. L. *Phys. Rev.* **1962**, *128*, 2042.

(60) Levitt, M. H.; Suter, D.; Ernst, R. R. *J. Chem. Phys.* **1986**, *84*, 4243.

(61) Vega, A. J. *J. Magn. Reson.* **1992**, *96*, 50.

(62) Vega, a J. *Solid State Nucl. Magn. Reson.* **1992**, *1*, 17.

(63) Harris, K. J.; Lupulescu, A.; Lucier, B. E. G.; Frydman, L.; Schurko, R. W. *J. Magn. Reson.* **2012**, *224*, 38.

(64) Wi, S.; Gan, Z.; Schurko, R.; Frydman, L. *J. Chem. Phys.* **2015**, *142*.

(65) Maudsley, A. A.; Müller, L.; Ernst, R. R. *J. Magn. Reson.* **1977**, *28*, 463.

(66) Maudsley, A. A.; Ernst, R. R. *Chem. Phys. Lett.* **1977**, *50*, 368.

(67) Cavadini, S.; Antonijevic, S.; Lupulescu, A.; Bodenhausen, G. *J. Magn. Reson.* **2006**, *182*, 168.

(68) Cavadini, S.; Antonijevic, S.; Lupulescu, A.; Bodenhausen, G. *ChemPhysChem* **2007**, *8*, 1363.

(69) Cavadini, S.; Vitzthum, V.; Ulzega, S.; Abraham, A.; Bodenhausen, G. *J. Magn. Reson.* **2010**, *202*, 57.

(70) Ulzega, S. *Chimia (Aarau).* **2010**, *64*, 157.

(71) Gan, Z.; Amoureux, J.-P.; Trébosc, J. *Chem. Phys. Lett.* **2007**, *435*, 163.

(72) Shen, M.; Trébosc, J.; O'Dell, L. A.; Lafon, O.; Pourpoint, F.; Hu, B.; Chen, Q.; Amoureux, J. *J. Magn. Reson.* **2015**, *258*, 86.

(73) Antonijevic, S.; Halpern-Manners, N. *Solid State Nucl. Magn. Reson.* **2008**, *33*, 82.

(74) Mao, K.; Wiench, J. W.; Lin, V. S.-Y.; Pruski, M. *J. Magn. Reson.* **2009**, *196*, 92.

(75) Paulson, E. K.; Morcombe, C. R.; Gaponenko, V.; Dancheck, B.; Byrd, R. A.; Zilm, K. W. *J. Am. Chem. Soc.* **2003**, *125*, 15831.

(76) Althaus, S. M.; Mao, K.; Stringer, J. A.; Kobayashi, T.; Pruski, M. *Solid State Nucl. Magn. Reson.* **2014**, *57-58*, 17.

(77) Pawlak, T.; Paluch, P.; Trzeciak-Karlikowska, K.; Jeziorna, A.; Potrzebowski, M. J. *CrystEngComm* **2013**, *15*, 8680.

(78) Ishii, Y.; Tycko, R. *J. Magn. Reson.* **2000**, *142*, 199.

(79) Ishii, Y.; Yesinowski, J. P.; Tycko, R. *J. Am. Chem. Soc.* **2001**, *123*, 2921.

(80) Fung, B. M.; Khitrin, A. K.; Ermolaev, K. *J. Magn. Reson.* **2000**, *142*, 97.

(81) Oas, T. G.; Griffin, R. G.; Levitt, M. H. *J. Chem. Phys.* **1988**, *89*, 692.

(82) Kaupp, M.; Bühl, M.; Malkin, V. G. *Calculation of NMR and EPR Parameters*; Wiley-VCH Verlag GmbH & Co. KGaA: Weinheim, FRG, 2004.

(83) Clark, S. J.; Segall, M. D.; Pickard, C. J.; Hasnip, P. J.; Probert, M. I. J.; Refson, K.; Payne, M. C. *Zeitschrift für Krist.* **2005**, *220*, 567.

(84) Profeta, M.; Mauri, F.; Pickard, C. J. *J. Am. Chem. Soc.* **2003**, *125*, 541.

(85) O'Dell, L. A.; Schurko, R. W. *Phys. Chem. Chem. Phys.* **2009**, *11*, 7069.

(86) Frisch, M. J.; Trucks, G. W.; Schlegel, H. B.; Scuseria, G. E.; Robb, M. A.; Cheeseman, J. R.; Scalmani, G.; Barone, V.; Mennucci, B.; Petersson, G. A.; Nakatsuji, H.; Caricato, M.; Li, X.; Hratchian, H. P.; Izmaylov, A. F.; Bloino, J.; Zheng, G.; Sonnenberg, J. L.; Hada, M.; Ehara, M.; Toyota, K.; Fukuda, R.; Hasegawa, J.; Ishida, M.; Nakajima, T.; Honda, Y.; Kitao, O.; Nakai, H.; Vreven, T.; Montgomery Jr., J. A.; Peralta, J. E.; Ogliaro, F.; Bearpark, M. J.; Heyd, J.; Brothers, E. N.; Kudin, K. N.; Staroverov, V. N.; Kobayashi, R.; Normand, J.; Raghavachari, K.; Rendell, A. P.; Burant, J. C.; Iyengar, S. S.; Tomasi, J.; Cossi, M.; Rega, N.; Millam, N. J.; Klene, M.; Knox, J. E.; Cross, J. B.; Bakken, V.; Adamo, C.; Jaramillo, J.; Gomperts, R.; Stratmann, R. E.; Yazyev, O.; Austin, A.

J.; Cammi, R.; Pomelli, C.; Ochterski, J. W.; Martin, R. L.; Morokuma, K.; Zakrzewski, V. G.; Voth, G. A.; Salvador, P.; Dannenberg, J. J.; Dapprich, S.; Daniels, A. D.; Farkas, Ö.; Foresman, J. B.; Ortiz, J. V; Cioslowski, J.; Fox, D. J. Gaussian 09, 2009.

(87) te Velde, G.; Bickelhaupt, F. M.; Baerends, E. J.; Fonseca Guerra, C.; van Gisbergen, S. J. A.; Snijders, J. G.; Ziegler, T. *J. Comput. Chem.* **2001**, *22*, 931.

(88) Bonhomme, C.; Gervais, C.; Babonneau, F.; Coelho, C.; Pourpoint, F.; Azaïs, T.; Ashbrook, S. E.; Griffin, J. M.; Yates, J. R.; Mauri, F.; Pickard, C. J. *Chem. Rev.* **2012**, *112*, 5733.

(89) O'Dell, L. A.; Schurko, R. W.; Harris, K. J.; Autschbach, J.; Ratcliffe, C. I. *J. Am. Chem. Soc.* **2011**, *133*, 527.

(90) Elmi, F.; Hadipour, N. L. *J. Phys. Chem. A* **2005**, *109*, 1729.

(91) Veinberg, S. L.; Friedl, Z. W.; Harris, K. J.; O'Dell, L. A.; Schurko, R. W. *CrystEngComm* **2015**, *17*, 5225.

(92) Xu, J.; Lucier, B. E. G.; Sinelnikov, R.; Terskikh, V. V.; Staroverov, V. N.; Huang, Y. *Chem. Eur. J.* **2015**, *21*, 14348.

Chapter 2: ^{14}N Solid-State NMR of Amino Acids

2.1 Overview

^{14}N ultra-wideline solid-state NMR (UW SSNMR) spectra have been obtained for sixteen naturally occurring amino acids and four related derivatives. Spectra with high signal-to-noise ratios and minimal distortions were acquired within relatively short timeframes using the WURST-CPMG (wideband uniform-rate smooth-truncation) pulse sequence and frequency-stepped acquisitions. Our measurements focus upon obtaining ^{14}N NMR spectra of pseudo-tetrahedral moieties (i.e., RNH_3^+ and $RR'NH_2^+$), which have C_Q values ranging from 0.8 to 1.5 MHz, and powder pattern breadths of 1.20 to 2.25 MHz. The quadrupolar parameters extracted from these spectra, in concert with plane-wave density function theory (DFT) calculations of ^{14}N EFG tensor parameters and orientations, allow for the grouping of the moieties into three structural categories according to the values of the quadrupolar asymmetry parameter, η_Q: low ($\eta_Q < 0.3$), intermediate ($0.31 \leq \eta_Q \leq 0.7$), and high ($\eta_Q > 0.71$). For the RNH_3^+ moieties, those in the low-η_Q category have little variation in their N-H bond lengths resulting from uniform intermolecular hydrogen-bonding arrangements, whereas those in the intermediate-η_Q category have greater N-H bond length variation due to non-uniform interactions. Strategies for decreasing experimental acquisition times are discussed, including the use of deuteration, high-power ^{1}H decoupling, spectral mirroring and processing strategies, ultra-high magnetic fields (i.e., 21.1 T), and broadband adiabatic inversion cross-polarization (BRAIN-CP) methods. The impact of dynamic rotations of the NH_3 groups, their variation with temperature, and their influence on effective transverse relaxation rates and spectral quality, are all considered. This set of methodologies permits for rapid

acquisition of directly-detected ^{14}N SSNMR spectra that cannot be matched by any other methods proposed to date. The relative ease with which spectra can be acquired and the extreme sensitivity of the ^{14}N EFG tensors to variation in hydrogen bonding suggest that ^{14}N SSNMR will have great value for characterization of structure and dynamical motions in wide range of nitrogen-containing organic solids.

2.2 Introduction

Nitrogen, the seventh most abundant element, is ubiquitous in important compounds in chemistry, biology, and materials science. Structural studies of nitrogen-containing compounds using ^{15}N (I = ½) solid-state nuclear magnetic resonance (SSNMR) dominate the literature, despite its extremely low natural abundance (0.37%), which generally necessitates isotopic enrichment, and relatively low gyromagnetic ratio ($\gamma(^{15}\mathrm{N}) = -2.712 \times 10^7$ rad T^{-1} s^{-1}), which places ^{15}N at the lower end of the tuning range of most commercial NMR probes. By contrast, there are significantly fewer studies that focus on ^{14}N (I = 1), even though it is 99.63% naturally abundant. This is because ^{14}N is a quadrupolar nucleus with a moderate quadrupole moment (Q = 20.44 mbarn) and a low gyromagnetic ratio ($\gamma(^{14}\mathrm{N}) = 1.934 \times 10^7$ rad T^{-1} s^{-1}). ^{14}N SSNMR experiments have been traditionally avoided for two main reasons: (i) the integer spin and moderate Q of ^{14}N result in severe inhomogeneous broadening of ^{14}N SSNMR powder patterns for all but the most spherically-symmetric nitrogen environments, due to the first-order quadrupolar interaction (FOQI), and (ii) to a lesser extent, its low γ causes the ^{14}N Larmor frequency, $\nu_0(^{14}\mathrm{N})$, to lie outside the tuning range of most commercial NMR probes.

Typical ^{14}N SSNMR powder patterns often have breadths ranging from hundreds of kHz to several MHz. Pseudo-tetrahedral sp^3-hybridized nitrogen environments (i.e., $RR'R''NH^+$, $RR'NH_2^+$, or RNH_3^+), which are of central interest to the current work, have breadths ranging from 1.0 to 2.25 MHz.[1,2] Many other types of nitrogen environments that are planar or linear have even wider pattern breadths due to increased quadrupolar interactions (*vide infra*). These *ultra-wideline* (UW) ^{14}N powder patterns result in very low signal-to-noise (S/N) ratios due to the distribution of the signal intensity over broad frequency ranges.[2–4] Despite these seemingly unfavourable NMR properties, recently introduced methods for enhancing S/N in ^{14}N UW SSNMR spectra show promise for enabling more routine investigations of structural features like hydrogen-bonding and polymorphism, as well as molecular dynamics and relaxation processes, in a wide variety of nitrogen-containing systems.[5–11]

The electric field gradients (EFGs) at the ^{14}N nucleus are described with a second-rank tensor that is traceless and symmetric, having three principal components: V_{11}, V_{22}, and V_{33} ($|V_{11}| \leq |V_{22}| \leq |V_{33}|$). The interaction of the ^{14}N nuclear quadrupole moment, Q, with these EFGs is known as the quadrupolar interaction. Typically, experimental measurements of the quadrupolar interaction report the quadrupolar coupling constant, C_Q, (in MHz) and the asymmetry parameter, η_Q (dimensionless, $0 \leq \eta_Q \leq 1$):

$$C_Q = \frac{eQV_{33}}{h} \qquad [2.1]$$

$$\eta_Q = \frac{(V_{11} - V_{22})}{V_{33}} \qquad [2.2]$$

^{14}N powder patterns resulting from $C_Q(^{14}N)$ values greater than ca. 0.8 MHz are dominated by the FOQI and have a characteristic Pake doublet shape. The powder

patterns have discontinuities at frequencies that correspond to specific orientations of the principal components of the EFG tensor with respect to the external magnetic field. To first order, when V_{11}, V_{22}, or V_{33} are parallel to B_0:

$$\nu_{11} = \pm \frac{3}{8} C_Q(1 - \eta_Q) \quad [2.3a]$$

$$\nu_{22} = \pm \frac{3}{8} C_Q(1 + \eta_Q) \quad [2.3b]$$

$$\nu_{33} = \pm \frac{3}{4} C_Q \quad [2.3c]$$

The discontinuities at ν_{11}, ν_{22}, and ν_{33} are often referred to as the "horns", "shoulders", and "feet" of the powder pattern, respectively (**Scheme 2.1**). The separation of the feet is a measure of the breadth of the ^{14}N powder patterns, and is proportional to C_Q (breadth = $\nu_{33} - (-\nu_{33}) = (3/2)C_Q$), while the separation of the horn and shoulder depends on the axial symmetry of the ^{14}N EFG tensor. If the FOQI is dominant, the powder patterns are mirror symmetric about the chemical shift/Larmor frequency for any spin-1 nuclide. For ^{14}N SSNMR spectra arising from a $C_Q \gtrsim 0.8$ MHz at moderate to high magnetic field strengths, which is the case for all of the systems investigated herein, the effects of the second-order quadrupolar interaction (SOQI) and the nitrogen chemical shielding anisotropy (CSA) can be neglected, due to the much smaller magnitudes of these interactions (see **Appendix A, Figure A1,** for further discussion).[9]

A number of methods have been explored for the acquisition of ^{14}N SSNMR spectra, including direct observation of ^{14}N NMR signals from single crystals,[12] anisotropically oriented samples,[13,14] overtone ^{14}N NMR spectroscopy,[15–17] and ^{14}N magic-angle spinning (MAS) NMR using probes with precisely tuned rotor angles,[9] slow spinning speeds,[18] and specialized pulse sequences.[19] Nuclear quadrupole resonance

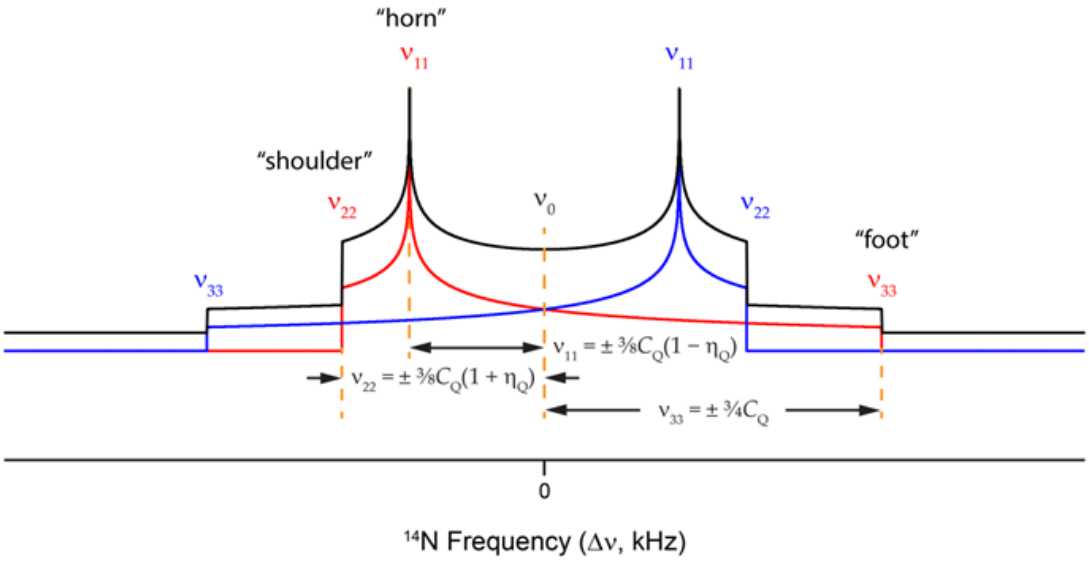

Scheme 2.1. An idealized ^{14}N SSNMR powder pattern that is dominated by the FOQI. The powder patterns corresponding to the two underlying fundamental transitions and the frequencies of their discontinuities are indicated in blue ($0 \leftrightarrow -1$) and red ($+1 \leftrightarrow 0$).

(NQR) has also been widely used to investigate many types of nitrogen systems.[1] Attempts have also been made to investigate ^{14}N via residual dipolar coupling observed in the NMR spectra of heteronuclear dipolar coupled spin-½ nuclei (e.g., ^{13}C); as well as using indirect detection methods involving ^{1}H-^{14}N spin-spin correlations.[20–26] While the latter have gained some popularity, none of the direct detection techniques have achieved regular use, due to limits on the nature of the samples which can be studied, or the need for sophisticated hardware and/or probes.[2] For further details on both direct and indirect excitation and detection of ^{14}N SSNMR spectra, we refer the reader to several excellent reviews.[2,27,28]

Our group has proposed a methodology for the acquisition of UW SSNMR spectra that has been successful for studying both spin-½ and quadrupolar nuclei (including ^{14}N).[5,7,11,29–31] This methodology consists of three components:[3,4] (i) utilizing WURST (Wideband, Uniform Rate, and Smooth Truncation) pulses[32,33] for uniform excitation of

broad powder patterns,[34] (ii) using the WURST pulses in a CPMG-like sequence for T_2-based signal enhancement (i.e., the WURST-CPMG pulse sequence[30]), and (iii) acquiring sub-spectra at evenly spaced transmitter increments across the breadth of the powder pattern (i.e., the variable offset cumulative spectrum (VOCS) or frequency-stepped method).[35–37] We have also demonstrated that WURST pulses may be utilized for broadband cross-polarization (BCP) from spin-½ nuclides (e.g., ^{1}H) to less receptive nuclei (both spin-½ and quadrupolar) under static (i.e., ν_{rot} = 0 kHz) conditions,[38] and have successfully applied this approach in the acquisition of several ^{14}N UW SSNMR powder patterns of nitrogen-containing compounds.[39]

In this work, we conduct a comprehensive study on seventeen naturally occurring amino acids and some related derivatives (**Scheme 2.2**, **Table 2.1**) with the use of direct-excitation and direct-detection ^{14}N SSNMR using the WURST-CPMG pulse sequence. The amino acid systems were chosen due to their central importance to many areas of chemistry and biochemistry, as well as because (i) they are readily available, inexpensive and facile to prepare in pure forms (including deuterated species), (ii) they contain pseudo-tetrahedral (i.e., RNH_3^+ or $RR'NH_2^+$) nitrogen moieties, which have ^{14}N UW SSNMR powder patterns that can be acquired in reasonable time frames at moderate magnetic field strengths (e.g., 9.4 T), and (iii) they provide a large data set of quadrupolar data from structural homologues, which will allow for continued investigation of the relationships between local molecular structure, intermolecular interactions (i.e., hydrogen bonding) and the ^{14}N EFG tensor. Herein, we present a comprehensive investigation on the following facets of ^{14}N SSNMR of amino acids: (i) the feasibility of ^{14}N SSNMR experiments for the study of amino acids in reasonable experimental time

frames, (ii) the relationships between molecular geometry and the ^{14}N EFG tensor parameters and orientations, using a combination of experimental evidence and quantum chemical calculations, (iii) several experimental considerations for improving the acquisition of ^{14}N powder patterns (i.e., deuteration, variable temperature NMR, high magnetic field strengths), and (iv) the use of ^{14}N SSNMR for differentiating multiple magnetically inequivalent nitrogen environments in the same compound, as well as in polymorphs.

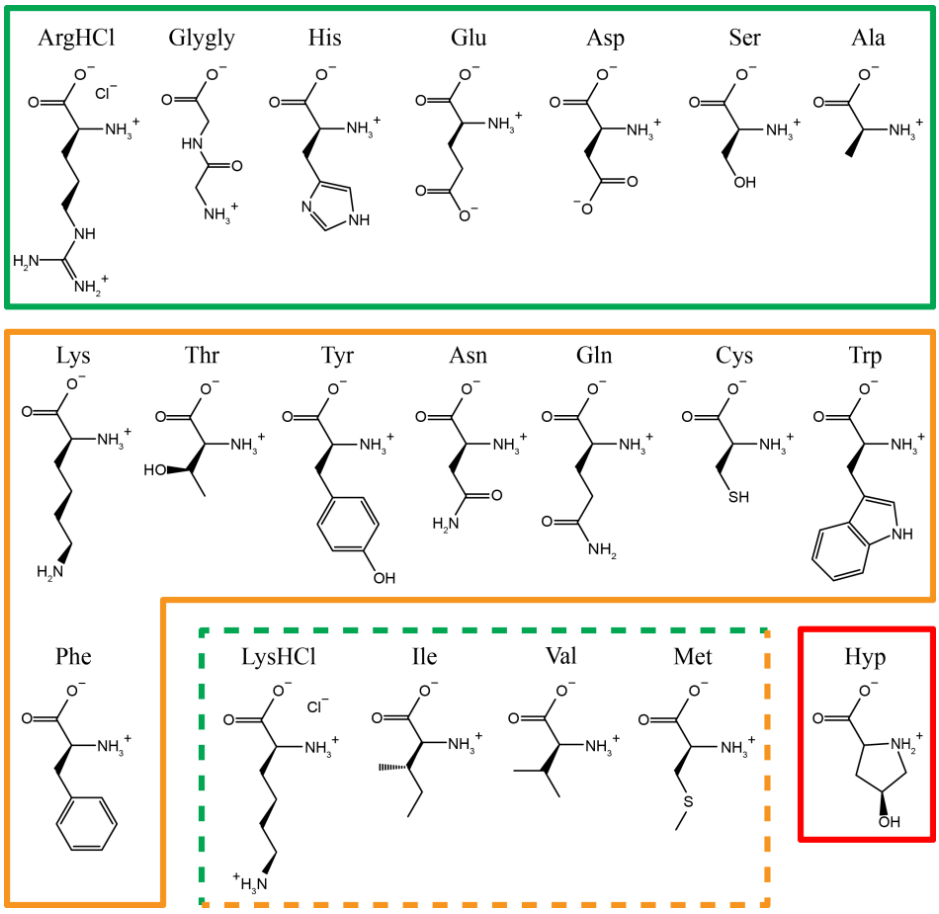

Scheme 2.2. The zwitterionic forms of the amino acids and related derivatives investigated in this study. Grouping is based on the value of η_Q (green outline: $0 \leq \eta_Q \leq 0.30$, orange outline: $0.31 \leq \eta_Q \leq 0.70$, red outline: $0.71 \leq \eta_Q \leq 1$). The amino acids enclosed in the box with green and orange dashed boundaries feature two nitrogen sites, one with $0 \leq \eta_Q \leq 0.30$ and the other with $0.31 \leq \eta_Q \leq 0.70$.

2.3 Experimental Methods

2.3.1 Samples

Samples of the crystalline amino acids and their HCl salts (excepting the few special cases discussed below) were obtained from Sigma-Aldrich and used without further purification. High purity B-histidine was purchased from Fluka Analytical (Sigma-Aldrich Co.) and used without further purification. In some cases, samples were recrystallized from $D_2O(\ell)$ in order to alter ^{14}N relaxation characteristics and to improve spectra acquisition (*vide infra*). See **Table 2.1** for a full listing of all the samples discussed in this chapter. Sample purity was confirmed by powder XRD (pXRD, supplementary information, **Figures A2** and **A3**).

2.3.2 Powder XRD experiments

pXRD patterns were collected using a D8 DISCOVER X-ray diffractometer equipped with an Oxford Cryosystems 700 Cryostream Plus Cooler. A Cu-K_α (λ = 1.54184 Å) radiation source with a Bruker AXS HI-STAR area detector using the General Area Detector Diffraction Systems (GADDS) software package was used. Powder diffraction patterns were simulated with the PowderCell software package.[40]

2.3.3 Direct-Excitation (DE) NMR experiments

The majority of the spectra reported herein were acquired on a Varian InfinityPlus spectrometer equipped with a wide-bore 9.4 T magnet using Larmor frequencies of 399.73 MHz and 28.89 MHz for ^1H and ^{14}N, respectively. A 5.0 mm static HX probe was used for all experiments, with a Varian/Chemagnetics low-γ tuning box on the ^{14}N

channel. For lysine HCl, *L*-tyrosine, *L*-valine, and deuterated *L*-valine-d_3, the ^{14}N powder patterns were acquired using the same field strength with a Bruker Avance III HD spectrometer (following a console upgrade from the older Varian/Agilent system mentioned above). Spectra were referenced against a sample of solid NH_4Cl (δ_{iso} = 0 ppm), although chemical shifts are not reported due to large uncertainties in their measurements (*vide infra*). High-field NMR experiments were acquired at the National Ultrahigh-field NMR Facility for Solids in Ottawa, Canada using a Bruker Avance II spectrometer equipped with a wide-bore 21.1 T magnet ($\nu_0(^1H)$ = 900.00 MHz, $\nu_0(^{14}N)$ = 65.03 MHz) and a home-built 7.0 mm HX static probe.

All DE ^{14}N SSNMR spectra were acquired with the WURST-CPMG (WCPMG) pulse sequence,[30] along with the frequency-stepped acquisition method (also known as the variable-offset cumulative spectra, or VOCS).[35–37] Individual sub-spectra were acquired at evenly spaced transmitter frequencies that were chosen such that (i) they are integer multiples of the CPMG spikelet spacing and (ii) the overlap between the individual sub-spectra is optimized to yield undistorted spectra.[41] Only one half of the ^{14}N powder pattern is acquired in each case, with the other half the pattern produced by reflection about the Larmor frequency. This is because the ^{14}N Pake doublet is symmetric to first order, and the quadrupolar parameters can be determined from the positions of two discontinuities on either side of the pattern.[2]

Complete ^{14}N SSNMR spectra were assembled (*vide infra*) from two to fourteen sub-spectra, which were acquired using ^{14}N pulse delays ranging from 0.5 to 10 seconds, resulting in total experimental acquisition times ranging from 0.3 – 16 hours. 50, 75, or 100 μs WURST-80 pulses[32] with a sweep range of 450 kHz – 3.0 MHz and *ca*. 30 kHz rf

power were applied in all experiments, along with a continuous-wave ^{1}H decoupling field of *ca*. 40 – 60 kHz over the duration of each scan.[31] The sweep direction of the WURST pulse was set to move outwards from the ^{14}N Larmor frequency, which has been reported as a means of maximizing the direct enhancement of integer spin magnetization (DEISM) effect.[41] **Tables A1** and **A2** (**Appendix A**) show complete lists of acquisition parameters. For each sub-spectrum, the individual echoes in the CPMG echo train were co-added to yield one high-intensity echo, followed by Gaussian broadening, zero-filling, Fourier-transformation, and magnitude processing. Sub-spectra were then co-added using the NUTS software (Acorn NMR). ^{14}N SSNMR powder patterns were simulated using the WSolids1 program.[42]

2.3.4 Variable-Temperature (VT) NMR experiments

^{14}N SSNMR spectra of *L*-aspartic acid, *L*-phenylalanine, *L*-tyrosine, *L*-valine, and deuterated *L*-valine-d_3 were acquired at multiple temperatures ranging from −87.5 °C to +181.2 °C with the use of a Varian VT upper stack and nitrogen gas. Temperatures were calibrated on the basis of static ^{207}Pb NMR of crystalline $Pb(NO_3)_2$ as described by Bielecki *et al*.[43]

2.3.5 Broadband Adiabatic Inversion Cross-Polarization (BRAIN-CP) NMR experiments

A spectrum of *L*-tyrosine was also acquired with the use of the BRAIN-CP[38] pulse sequence. The polarization transfer and refocusing pulses in the BRAIN-CP pulse sequence were carefully calibrated to ensure that polarization was only transferred to one

of the fundamental transitions for each crystallite in the low-frequency half of the Pake doublet.[39] A complete list of experimental parameters is given in **Table A4**.

2.3.6 Ab initio calculations

Plane-wave density functional theory (DFT) calculations of the ^{14}N EFG tensors were performed using the CASTEP NMR program[44] in the Materials Studio 5.0 environment on a Dell Studio XPS 435T/9000 with a single Intel Core i7 920 processor and 8 GB of DDR3 RAM. High-performance cluster computing was also utilized using the Canadian Shared Hierarchical Academic Research Computing Network (SHARCNET). 'On the fly' ^{14}N pseudopotentials were used for the EFG calculations, with a plane wave basis set cut-off of 610 eV and a fine *k*-point set (2 x 2 x 4). The revised Perdew, Burke and Ernzerhof (rPBE) functional was used in the generalized gradient approximation (GGA) for the exchange correlation energy. Where appropriate, geometry optimizations of hydrogen atom positions were carried out using the Broyden-Fletcher-Goldfarb-Shanno optimization algorithm,[45] while holding fixed the positions of all other heavier atoms and lattice parameters. Crystal structures for all of the compounds were obtained from the literature (see **Appendix A**, **List A1** for the corresponding crystal structure references).

2.4 Results and Discussion

Almost all amino acids, in their zwitterionic or cationic forms, possess "pseudo-tetrahedral" ammonium moieties (**Scheme 2.2**); the two types investigated herein are of the forms RNH_3^+ and $RR'NH_2^+$. Most of the ammonium nitrogens have values of C_Q

grouped within a small range from 1.01 to 1.25 MHz (**Table 2.1**). By contrast, there is much greater variation in the values of η_Q; hence, the amino acids can be grouped by η_Q: low (0.00 to 0.30), intermediate (0.31 – 0.70), and high (0.71 – 1.00). Amino acids in these groupings with single magnetically distinct ^{14}N sites are discussed in sections 3.3, 3.4, and 3.5, respectively. Samples that have multiple RNH_3^+ moieties giving rise to overlapping ^{14}N NMR patterns are discussed in section 3.6. Strategies for enhancing the S/N in ^{14}N SSNMR spectra are discussed in section 3.7, while the application of ^{14}N SSNMR for the differentiation of polymorphs is discussed in section 3.8.

2.4.1 Ab initio calculations

Quantum chemical calculations of the ^{14}N EFG tensor parameters were conducted on a series of model systems based on the amino acid crystal structures, in order to aid in the spectral fitting and extraction of the ^{14}N quadrupolar parameters from the ^{14}N powder patterns, and also to investigate the relationships between the quadrupolar parameters, EFG tensor orientations, and crystal structures. Due to the highly periodic nature of these systems and the prevalence of intermolecular hydrogen bonding, extended crystal structures have to be considered in order to obtain accurate ^{14}N EFG tensor predictions;[31] hence, all of the calculations were conducted using CASTEP and NMR CASTEP.[44,46] **Table 2.1** summarizes the results of the EFG tensor calculations and experimentally observed values; where applicable, values previously reported in the literature are also listed. **Figures 2.1A** and **2.1B** are plots of the correlations between calculated and experimentally obtained values of C_Q and η_Q, respectively, which are found to be in reasonably good agreement. It is noted that crystal structures for some of the amino acids

Table 2.1. Experimental and theoretical ^{14}N quadrupolar parameters.

		Experimental		Plane-wave DFT (CASTEP)		Literature Values[†]	
		$\lvert C_Q\rvert$/MHz[a]	η_Q[b]	C_Q/MHz	η_Q	$\lvert C_Q\rvert$/MHz	η_Q
Ala *[,c]		1.15(2)[d]	0.24(2)	1.204	0.26	1.14 [9]	0.24 [9]
ArgHCl		1.14(2)	0.06(2)	1.248	0.06		
Asn		1.24(1)	0.50(1)	1.316	0.48	1.299 [1]	0.477 [1]
Asp		1.21(2)	0.17(2)	1.338	0.16	1.287 [1]	0.149 [1]
Cys *[,c]		1.18(1)	0.51(1)	1.289	0.50	1.22 [9]	0.50 [9]
Glu-β *[,c]		1.06(1)	0.17(1)	1.127	0.15	1.115 [1]	0.154 [1]
Gln *		1.10(1)	0.50(1)	1.132	0.51		
Glygly *[,c]		1.44(2)	0.12(2)	1.453	0.10	1.28 [1]	0.41 [1]
A-His *[,c]		1.23(2)	0.19(2)	1.252	0.12	1.22 [16]	0.15 [16]
B-His		1.22(2)	0.20(2)	1.279	0.13	1.305 [1]	0.143 [1]
Hyp-d_2 *		1.20(1)	0.92(2)	−1.281	0.92	1.279 [1]	0.910 [1]
Ile-d_3	Site 1	1.14(2)	0.30(2)	1.218	0.45	1.16 [9]	0.29 [9]
	Site 2	1.18(2)	0.11(2)	1.255	0.17	1.20 [9]	0.11 [9]
Lys		1.11(2)	0.29(2)	-	-		
LysHCl	Site 1	1.09(2)	0.30(2)	1.212	0.33		
	Site 2	1.02(2)	0.26(2)	1.151	0.10		
Met	Site 1	1.22(2)	0.42(2)	1.246	0.52	1.22 [9]	0.37 [9]
	Site 2	1.17(2)	0.19(2)	1.220	0.13	1.16 [9]	0.17 [9]
Phe		1.25(3)	0.55(3)	1.285	0.52	1.363 [1]	0.580 [1]
Ser		1.15(1)	0.18(1)	1.174	0.11	1.17 [9]	0.17 [9]
Thr *[,c]		1.10(1)	0.38(1)	1.130	0.39	1.158 [1]	0.361 [1]
Trp	Site 1	1.21(2)	0.52(2)	1.320 [#]	0.531 [#]	1.270 [1]	0.550 [1]
	Site 2	1.2(2)	0.4(2)	1.275 [#]	0.665 [#]		
Tyr		1.00(1)	0.44(2)	1.054	0.46	1.078 [1]	0.414 [1]
Val		1.17(2)	0.18(2)	1.247	0.17	1.17 [9]	0.17 [9]
Val-d_3	Site 1	1.11(2)	0.34(3)	1.198	0.46	1.19 [9]	0.25 [9]
	Site 2	1.15(2)	0.18(2)	1.247	0.17	1.17 [9]	0.17 [9]
Leu-d_3 [e]	Site 1	1.14(2)	0.30(2)	1.230	0.38	1.19 [9]	0.33 [9]
	Site 2	1.12(1)	0.08(1)	1.170	0.11	1.13 [9]	0.08 [9]
Pro [e]		1.47(1)	0.98(2)	−1.73	0.95	1.623 [1]	0.955 [1]

* Calculations on models based on neutron structures. All remaining models are based on X-ray crystal structures. [a] $C_Q = eQV_{33}/h$. Note that the sign of C_Q cannot be determined from ^{14}N SSNMR spectra. [b] $\eta_Q = (V_{11} - V_{22})/V_{33}$. [c] EFG tensor calculations without prior geometry optimization of the H atom positions. [d] Uncertainty is reported to the last decimal place. [e] Experimental parameters are reported in reference 31. [†] Superscripted numbers correspond to the reference numbers in the bibliography. [#] Average of eight values (see text for details).

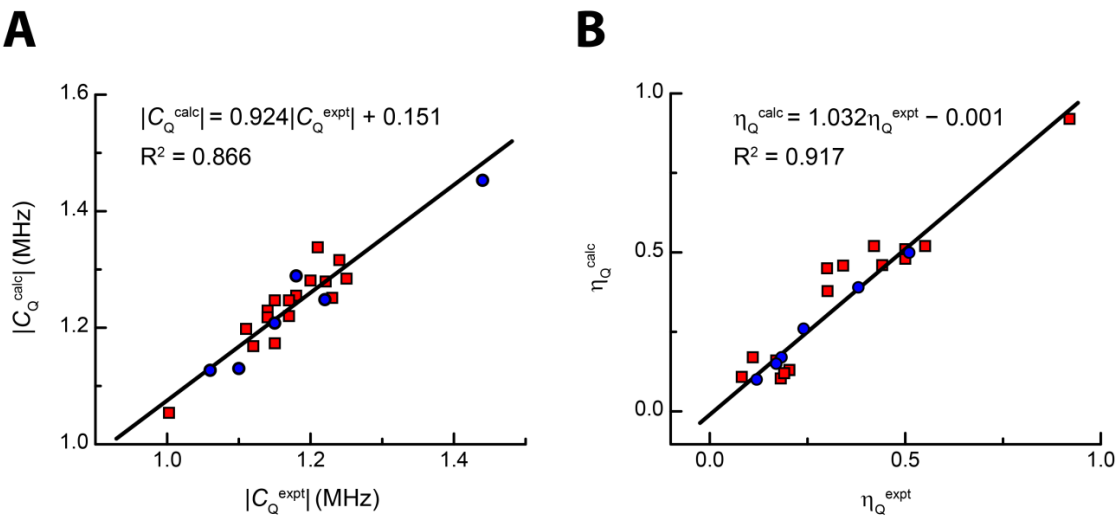

Figure 2.1. Graphs of calculated (DFT) vs. experimental values of (A) C_Q and (B) η_Q. Models used in these calculations are based on crystal structures obtained with X-ray (red squares) and neutron (blue circles) diffraction. Uncertainties in the experimental values are reported in **Table 2.1**.

are determined via neutron diffraction methods, while others are from X-ray diffraction techniques. DFT calculations of ^{14}N EFG tensors on model systems based on the former yield good agreement with experiment without optimizing the hydrogen atom positions, while those based on the latter required geometry optimization of the hydrogen atoms prior to calculation of the EFG tensors. The orientations of ^{14}N EFG tensors for three representative cases of pseudo-tetrahedral nitrogen moieties are shown in **Figure 2.2**. For RNH_3^+ nitrogen moieties (e.g., **Figures 2.2A** and **2.2B**), V_{33} is oriented coincident or nearly coincident with the C-N bond.[31,47,48] It is well known that EFG tensor parameters and orientations are dependent upon local symmetry. For an axially symmetric EFG tensor ($\eta_Q = 0$), V_{33} is oriented along a rotation axis of C_n symmetry (where $n \geq 3$). None of the RNH_3^+ moieties have perfect C_3 rotational axes; however, in instances where the N-H bond lengths are similar, η_Q is found to be ≤ 0.30 and the EFG tensor is oriented such that the angle $\measuredangle V_{33}$-N-C $\lesssim 3°$ (i.e., V_{33} is oriented along or nearly

along the N-C bond). When there is greater variation in the N-H bond distances (e.g., arising from a non-uniform arrangement of intermolecular hydrogen bonds, **Table A6**), η_Q is found to be between 0.31 and 0.70, and $\measuredangle V_{33}$-N-C $\gtrsim 3°$. In this work, these ranges are referred to as "low-η_Q" and "intermediate-η_Q," respectively. For $RR'NH_2^+$ moieties, there are no rotational axes with C_3 or pseudo-C_3 symmetries. As a result, the ^{14}N EFG tensors are oriented very differently (**Figure 2.2C**), and the η_Q values are closer to unity, meaning that V_{11} is the distinct principal component, and that V_{22} and V_{33} are similar in magnitude (but opposite in sign). These ^{14}N EFG tensors generally have V_{11} oriented in the H-N-H plane and nearly bisecting the H-N-H angle, while V_{33} is nearly perpendicular to the R-N-R′ plane. Herein, values of $0.71 \leq \eta_Q \leq 1.0$ are referred to as "high-η_Q".

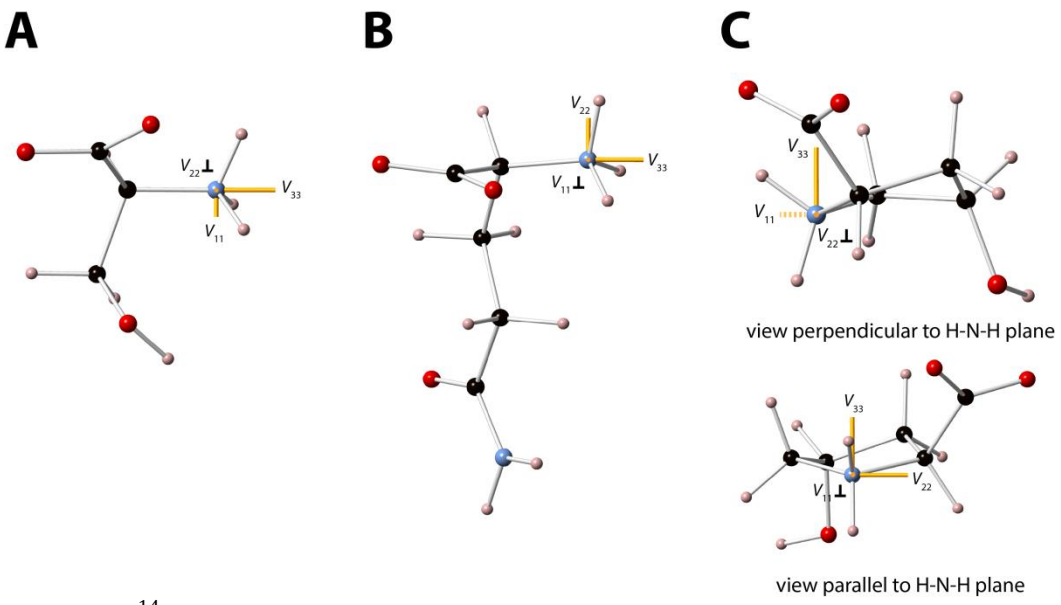

Figure 2.2. ^{14}N EFG tensor orientations for moieties with (A) a low-η_Q EFG tensor (represented by **ser**), (B) an intermediate-η_Q EFG tensor (represented by **gln**), and (C) a high-η_Q EFG tensor (represented by **hyp**). For the low-η_Q EFG tensor, $|V_{11}| \approx |V_{22}|$ and V_{33} is nearly coincident with the C-N bond. When η_Q is intermediate, all three principal axis components have different magnitudes and V_{33} is tilted away from the C-N bond, but still points in the general direction of the C atom. For the high-η_Q EFG tensor, $|V_{22}| \approx |V_{33}|$ and V_{11} lies in the H-N-H plane and approximately bisects the H-N-H angle.

2.4.2 General comments regarding ^{14}N SSNMR

Before discussion of the details of the ^{14}N SSNMR spectra presented in **Figures. 2.4-2.11**, a few general remarks must be made on their acquisition and appearance:

1. Generally, powder patterns corresponding to pseudo-tetrahedral (e.g., RNH_3^+, $RR'NH_2^+$, $RR'R''NH^+$) moieties are relatively easy to acquire, due to the reduced ^{14}N EFGs in these environments.[49–51] Pyramidal and/or planar (e.g., RNH_2 and R=NH) nitrogen moieties are associated with large C_Q values (i.e., > 2.5 MHz), which result in extremely broad ^{14}N SSNMR powder patterns (i.e., > 3.75 MHz in breadth). These patterns are less easily observed due to their low intensities. In some of the spectra shown in this work, there is weak underlying signal intensity from these broad patterns that can be safely neglected for the purposes of determining C_Q and η_Q from the much narrower patterns corresponding to pseudo-tetrahedral sites. It is possible, with specialized experimental set-ups and/or higher magnetic fields, to acquire spectra of ^{14}N sites with large C_Q values (though some of these experiments may require very long acquisition periods). For instance, ^{14}N SSNMR powder patterns have been acquired (using the VOCS method)[35–37] of nitrogen moieties with C_Q > 1.5 MHz with the use of an ultra-high magnetic field (i.e., 21.1 T).[5,52] For the samples discussed herein, it is advantageous to detect signals arising only from the ^{14}N nuclei in pseudo-tetrahedral environments, since their powder patterns act as spectral fingerprints of each amino acid.

2. For the majority of the samples, ^{14}N SSNMR spectra were acquired within a time frame of 3.0 to 7.5 hours under the following conditions: 9.4 T, room temperature, and using direct excitation (i.e., WCPMG) on the ^{14}N channel (these conditions hold for all samples discussed below, unless mentioned otherwise, see **Table A1**). The ^{14}N static

UW NMR experiments discussed herein are much shorter than corresponding ^{14}N MAS NMR experiments, which typically take upwards of 40 hours.[9] For certain samples, different strategies had to be adopted for enhancing the signal intensity in their ^{14}N SSNMR spectra, including the use of deuterated samples, variable-temperature experiments, ^{1}H-^{14}N broadband cross polarization (BCP), and ultra-high field acquisitions (*vide infra*).

3. High-power CW ^{1}H decoupling was applied during the acquisition period of every ^{14}N experiment. Generally, this only partially removes the contribution of the ^{14}N-^{1}H dipolar coupling mechanism to the transverse relaxation (T_2), due to limitations in the amount of power than can be applied on the ^{1}H channels of our probes. Hence, the ^{14}N transverse relaxation time constant, which determines the decay of the signal in the CPMG FIDs is not the true T_2, but rather an *effective* T_2 (i.e., $T_2^{\text{eff}}(^{14}\text{N})$).

4. ^{14}N SSNMR powder patterns are dominated by the FOQI, with insignificant contributions from either the SOQI or nitrogen CSA when $0.5 \leq C_Q \leq 2.0$ MHz (**Figure A1**). In such cases, determination of the quadrupolar parameters is possible via measurement of the positions of any two of the three spectral discontinuities, since their frequencies (the "horn", "shoulder", and "foot") are related to the C_Q and η_Q values to first order (**Figure A4**).

5. Most of the ^{14}N powder patterns shown in this work have been "mirrored," meaning that only half of the powder pattern was acquired (either the high- or low-frequency half, depending upon probe tuning conditions). Since the C_Q and η_Q values can be determined from measurement of only two discontinuities, it is not necessary to acquire the entire pattern from end to end; however, the patterns are displayed in

traditional Pake doublet format by reflection through a point corresponding to the ^{14}N Larmor frequency, $\nu_0(^{14}N)$, largely for aesthetic purposes (**Figure A5**). It is noted that the entire nitrogen chemical shift range for pseudo-tetrahedral moieties in amino acids is ca. 30 ppm (ca. 850-900 Hz), and consideration of isotropic shifts can be neglected for mirroring and simulating patterns. It is only necessary to acquire the entire powder pattern in cases where (i) the C_Q value is very small and nitrogen CSA contributions are prevalent or (ii) the C_Q value is very large and the effects of the SOQI are manifested in the spectrum.

In each section that follows, the ^{14}N NMR spectra and the relevant quadrupolar parameters for each system are discussed. In addition, challenges with acquiring and simulating ^{14}N SSNMR spectra are considered, along with suggestions for methodologies aimed at the acquisition of spectra with high S/N and minimal distortions.

2.4.3 Nitrogen moieties with low-η_Q ^{14}N EFG tensors

The amino acids discussed in this section have RNH_3^+ groups with pseudo-C_3 rotational axes, due to sets of N-H bond lengths which are similar to one another (**Table A6**), and values of η_Q in the range of 0.0 to 0.30. These low-η_Q EFG tensors are indicative of uniform sets of N-H bond lengths, which undoubtedly arise from correspondingly uniform sets of intermolecular NH···O hydrogen bond interactions. In all of the ^{14}N NMR powder patterns, the discontinuities corresponding to V_{11} and V_{22} are closely spaced, but are resolvable in most cases.

A good starting point is *L*-serine (**ser**), which has a single ammonium moiety in its zwitterionic form. The ^{14}N SSNMR powder pattern of **ser** is shown in **Figure 2.3A**.

The ^{14}N quadrupolar parameters were measured to be C_Q = 1.15 MHz and η_Q = 0.18, in good agreement with values reported previously by Giavanni *et al.*[9] and Werner-Zwanziger *et al.*[53] from ^{14}N MAS NMR and ^{14}N SQUID NQR experiments, respectively. Glutamic acid-β (**glu-β**) is similar, in that all of the discontinuities are clearly resolved in the spectrum (**Figure 2.3B**), from which the ^{14}N quadrupolar parameters were determined to be C_Q = 1.06 MHz and η_Q = 0.17, in close agreement with previous NQR data.[54]

L-alanine (**ala**) also has a single ammonium moiety in the unit cell. Its ^{14}N SSNMR spectrum (**Figure 2.3C**) has low S/N near the foot discontinuity, which is a common occurrence in many UW powder patterns acquired with CPMG methods where there are few crystallites giving rise to observable S/N.[2] Nonetheless, the horn and

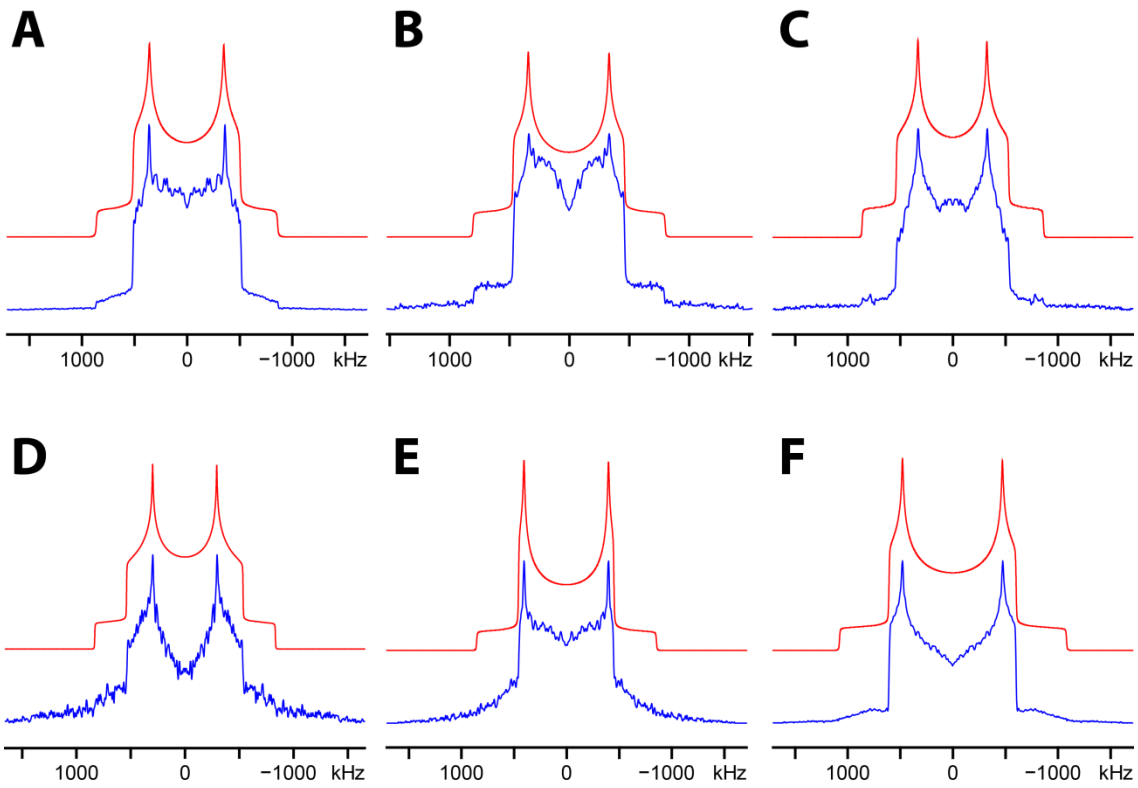

Figure 2.3. ^{14}N SSNMR powder patterns of (A) **ser**, (B) **glu-β**, (C) **ala**, (D) **lys**, (E) **argHCl**, and (F) **glygly** acquired using WCPMG at 9.4 T (blue) and associated spectral simulations (red).

shoulder discontinuities are clearly visible, allowing for measurement of C_Q = 1.15 MHz and η_Q = 0.24.[9,55] The value of η_Q is slightly higher than those of most of the species discussed in this section, and reflects some variance across the set of N-H bond lengths arising from greater variation in intermolecular hydrogen bonding distances.

L-lysine (**lys**), *L*-arginine HCl (**argHCl**), and glycylglycine (**glygly**) have multiple nitrogen environments (e.g., pseudo-tetrahedral RNH_3^+ moieties, a planar RR′NH moiety in **glygly** and **argHCl**, as well as pyramidal (RNH_2) and planar (R=NH) moieties in **argHCl**). **Lys** and **glygly** have similar hydrogen-bonding arrangements to that described for **ser** (*vide supra*). We attempted to acquire a ^{14}N powder pattern of *L*-arginine (**arg**) but were unsuccessful due to the lack of a pseudo-tetrahedral nitrogen moiety. Although **arg** is zwitterionic in the solid state, the hydrogen atom resides on one of the nitrogen atoms in the tail functionality rather than forming the RNH_3^+ moiety; all of the C_Q values were calculated to be > 3 MHz. For this reason, we chose to study **argHCl**, since the presence of the additional H^+ from the HCl results in a positively charged RNH_3^+ moiety. **ArgHCl** is the first cationic amino acid discussed herein, and features one NH···Cl and two NH···O hydrogen bonds (each chloride ion makes two short H···Cl contacts, i.e., < 2.2 Å);[56] however, the N-H bonds have similar distances. The ^{14}N SSNMR powder patterns for all three samples (**Figures 2.3D-F**) only show evidence of signal arising from the RNH_3^+ moieties. In each case, only two of the three discontinuities are observed in the ^{14}N patterns due to low signal intensity in the foot regions; again, this is enough for the accurate determination of C_Q and η_Q. The ^{14}N quadrupolar parameters reported herein are generally in good agreement with previously reported values for all samples

(**Table 2.1**);[1,9] the most evident discrepancy is **glygly**; however, our NMR CASTEP calculations corroborate our experimental values (*vide supra*).

2.4.4 Nitrogen moieties with intermediate-η_Q ^{14}N EFG tensors

Several samples that have ^{14}N EFG tensors with intermediate values of η_Q (0.31 – 0.70) are discussed in this section. The experimentally determined η_Q values range from 0.38 to 0.54, which results in ^{14}N powder patterns with clearly resolved frequencies for the horn, shoulder, and foot discontinuities, since all three principal components of the ^{14}N EFG tensor have unique magnitudes.

^{14}N SSNMR powder patterns of *L*-glutamine (**gln**), *L*-threonine (**thr**), *L*-cysteine (**cys**), *L*-asparagine (**asn**), and *L*-tryptophan (**trp**), and their corresponding simulations are shown in **Figures 2.4A-E**, respectively. For the first four compounds, the three discontinuities are clearly resolved in each spectrum, though the signal intensities in the foot regions are lower than predicted by simulations (in some cases, this can be caused by T_2 anisotropy, which is the variation of the T_2 or T_2^{eff} associated with NMR signals arising from different crystallite orientations).[11] Each of these compounds has a single magnetically distinct ^{14}N site which results in a unique powder pattern corresponding to the RNH_3^+ moiety. As in the case of the low-η_Q systems, no additional signal intensity is observed for other nitrogen sites (i.e., in **gln** and **asn**).

The spectrum of **trp** is more complex, in that two discontinuities are observed in the horn region, there may be at least two overlapping discontinuities in the shoulder, and the foot has very low S/N, making it difficult to detect the presence of multiple patterns in this region. This spectrum indicates the presence of two distinct ^{14}N powder patterns,

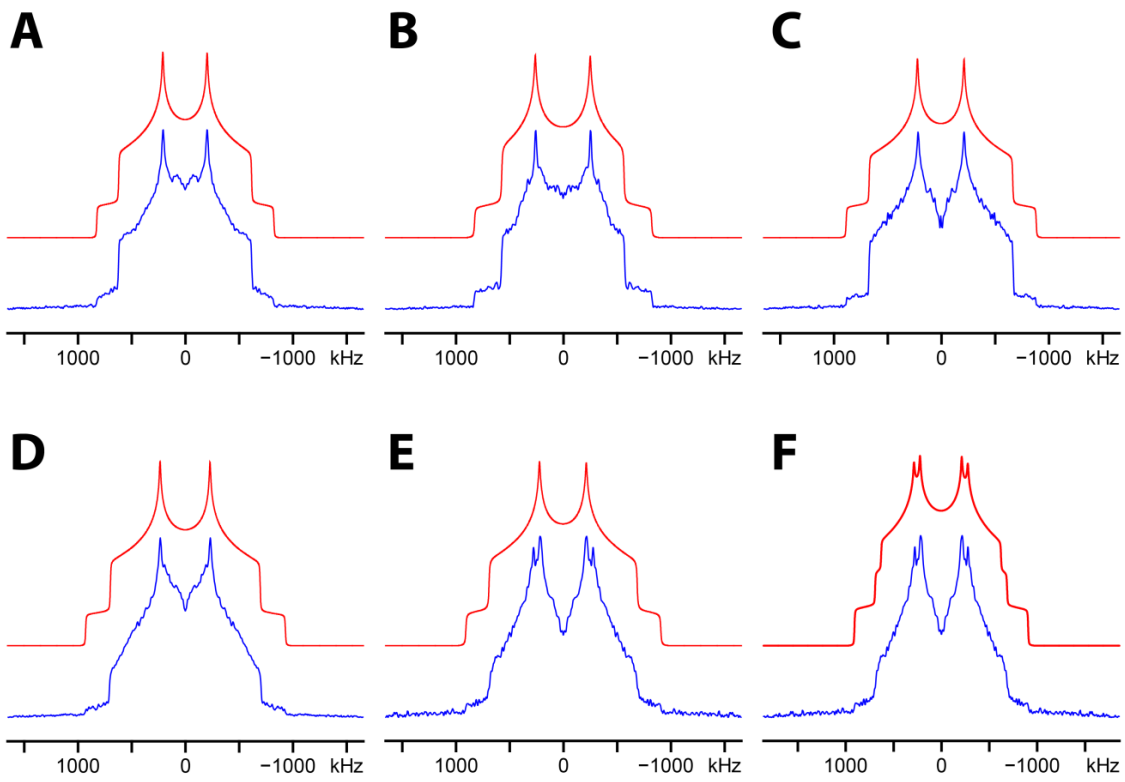

Figure 2.4. ^{14}N SSNMR powder patterns of (A) **gln**, (B) **thr**, (C) **cys**, (D) **asn**, (E) **trp** acquired using WCPMG at 9.4 T (blue) and associated spectral simulations (red). In (F), a two-site fit for **trp** is proposed.

which would imply the existence of two magnetically distinct ^{14}N sites (this result was confirmed with additional ^{14}N SSNMR data acquired at 21.1 T, **Figure A6A**). It is unlikely that one of these sites can be attributed to the nitrogen in the indole ring, as the C_Q for this site would be expected to be on the order of 3 MHz (as indicated by our own CASTEP calculations (**Table A5**) and previous ^{14}N NQR measurements).[1]

From a simulation of the powder pattern using a single ^{14}N site, the ^{14}N quadrupolar parameters are C_Q = 1.21 MHz and η_Q = 0.52, which are in good agreement with previously reported NQR values.[1] Based on the additional features in the ^{14}N powder pattern, a two-site fit has been attempted (**Figure 2.4F**) and the quadrupolar

parameters of the second nitrogen site are C_Q = 1.2(1) MHz and η_Q = 0.35(10) (for deconvolution, see **Figure A6B**). It is possible that the two ^{14}N patterns are the result of some sort of dynamical motion which is present at room temperature but not at 77 K (the temperature at which the NQR experiments were conducted). The most recent single-crystal structure of **trp** was solved by Görbitz *et al.*,[57] who found that there are 16 crystallographically distinct molecules in the unit cell. Our NMR CASTEP calculations predict that there are two sets of structurally distinct RNH_3^+ nitrogen sites: one set is predicted to have $\eta_Q \cong 0.66$ with a standard deviation of 0.01, while the other set is predicted to have $\eta_Q \cong 0.53$ with a standard deviation of 0.02. Although the agreement between the NMR CASTEP values and the experimental values is not perfect, both our experimental data and ^{14}N EFG tensor calculations confirm the presence of two distinct groups of nitrogen sites. It is possible that this data may aid in providing further refinement of the structure of **trp**.

All of these amino acids have crystal structures which indicate a higher degree of variation in the N-H bond lengths of the RNH_3^+ group in comparison to those discussed in the low-η_Q section above (**Table A6**); this results from variance in the H···O bond distances (i.e., hydrogen bond strengths). It is clear, from comparison of the systems with low- and intermediate-η_Q ^{14}N EFG tensors, that increased uniformity of N-H and H···O bond distances corresponds to increasingly axially symmetric (low-η_Q) EFG tensors. This trend is similar for analogous systems discussed below in sections 3.5-3.8. The values of C_Q remain in a relatively small range, since V_{33} is still closely aligned to the C-N bond direction of the RNH_3^+ group in all of these systems (though $\measuredangle V_{33}$-C-N increases for intermediate-η_Q systems, see **Figure 2.2** and **Table A6**). Clearly, the

asymmetry parameter could be very valuable for identifying discrepancies in hydrogen atom positions of amino groups in crystal structures for which neutron data is not available, while also providing a unique probe of hydrogen-bonding interactions.

2.4.5 Nitrogen moieties with high-η_Q ^{14}N EFG tensors

The only naturally occurring amino acid lacking the pseudo-tetrahedral RNH_3^+ moiety is proline (**pro**), which has a single pseudo-tetrahedral $R'R''NH_2^+$ moiety (and its structure has only one crystallographically distinct nitrogen site in the unit cell). Since we have already undertaken an investigation of **pro** with ^{14}N SSNMR,[31] we elected to examine 4-hydroxy-*L*-proline (**hyp**) in this study. Quadrupolar coupling constants for this type of moiety fall in the 0.8 – 1.5 MHz range (for **pro** and **hyp**, C_Q = 1.47 and 1.20 MHz, respectively);[1,9,31,39] however, their η_Q values are generally higher than 0.71 (η_Q = 0.92 and 0.98 for **pro** and **hyp**, respectively), which reflects the absence of a higher-order rotation axis (e.g., C_3 or pseudo-C_3).

It was not possible to obtain a high-quality ^{14}N NMR spectrum of **hyp** at 9.4 T in a reasonable timeframe, due to a short $T_2^{eff}(^{14}N)$ and reduced number of CPMG echoes (we note that previously reported experiments on **pro** took ca. 27 hours at 9.4 T).[31] Hence, **hyp** was recrystallized from $D_2O(\ell)$ in order to deuterate the $RR'NH_2^+$ moiety, which reduces the contributions of the ^{14}N-^{1}H dipolar coupling to $T_2^{eff}(^{14}N)$, and in turn, yields longer echo trains (and higher S/N) from CPMG-style experiments (**Figure A7**). The ^{14}N SSNMR powder pattern of **hyp-*d*$_2$** (**Figure 2.5A**) took nearly 16 hours to acquire at 9.4 T; however, acquisition of this spectrum with the use of an ultra-high magnetic field (i.e., 21.1 T) required only 3 hours of acquisition time (**Figure 2.5B**). The full ^{14}N

powder pattern was obtained at 21.1 T with the acquisition of only two sub-spectra with transmitter offsets 400 kHz apart (at 9.4 T, four sub-spectra were collected with transmitter offsets of 200 kHz). This is due to the much higher S/N attainable at 21.1 T, as well as the lower *Q*-value of the probe on this instrument, which permits broader excitation and detection bandwidths. The distinct probe characteristics at each field results in some noticeable differences in the appearances of these ^{14}N patterns; however, they have the same discontinuity positions and breadths at both fields (in units of Hz) since they are dominated by the FOQI, which has no magnetic field dependence.

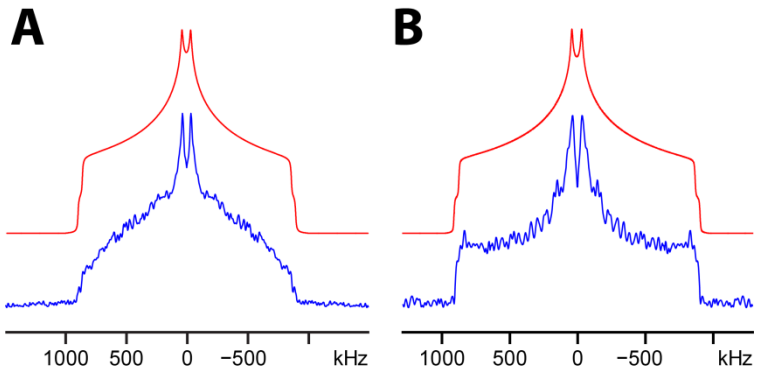

Figure 2.5. ^{14}N SSNMR powder patterns of **hyp-*d*$_2$** at (A) 9.4 T and (B) 21.1 T acquired with the use of WCPMG (blue) and associated spectral simulations (red).

2.4.6 Amino Acids with Multiple ^{14}N Patterns Arising from RNH_3^+ Moieties

The amino acids *L*-methionine (**met**), *L*-leucine (**leu**), *L*-isoleucine (**ile**), and *L*-valine (**val**) all have two chemically and magnetically distinct ^{14}N nuclei in RNH_3^+ moieties; they are all classified as hydrophobic, and none possess an aromatic functionality, as noted by Dalhus and Görbitz in their crystallographic investigation of these amino acids.[58–60] These same authors commented on the existence of alternating

layers of hydrophilic and hydrophobic regions in the crystal structure, which gives rise to two distinct molecules in the asymmetric unit. They also demonstrated that all of the compounds crystallize in the same monoclinic space group ($P2_1$) and that they possess similar bonding arrangements (*vide infra*).

In some cases, it is possible to distinguish distinct ^{14}N UW SSNMR patterns arising from magnetically non-equivalent ^{14}N sites, provided that the values of C_Q and/or η_Q are different enough.[2,5,9,31] In other cases, unfortunate overlaps of key discontinuities from each unique pattern or low S/N in key portions of the patterns can make spectral assignment very difficult (though it may be possible to differentiate such patterns using relaxation-assisted separation (RAS) techniques, as suggested by Frydman *et al.*).[61]

We start our investigation on an amino acid with two magnetically distinct nitrogen sites in the molecule (i.e., **lysHCl**) and then move on to investigate several amino acids with magnetically distinct nitrogen sites in the unit cell. **Figure 2.6** shows ^{14}N SSNMR spectra of three different AA samples, each with two overlapping ^{14}N powder patterns arising from magnetically non-equivalent nitrogen environments, and their accompanying two-site simulations (deconvolutions are shown in **Figure A8**). Spectral assignments can be aided by (i) theoretically calculated ^{14}N quadrupolar parameters (i.e., NMR CASTEP) and (ii) the use of variation in T_2^{eff}(^{14}N) characteristics and/or ^{1}H-^{14}N CP efficiencies ("spectral editing" techniques); we focus on the use of the former herein.

LysHCl, the HCl salt of **lys**, has two chemically distinct nitrogen moieties: an RNH_3^+ nitrogen attached to the α-carbon and an RNH_3^+ nitrogen in the amino acid tail. Despite the overlapping horns, the presence of multiple shoulder and foot discontinuities

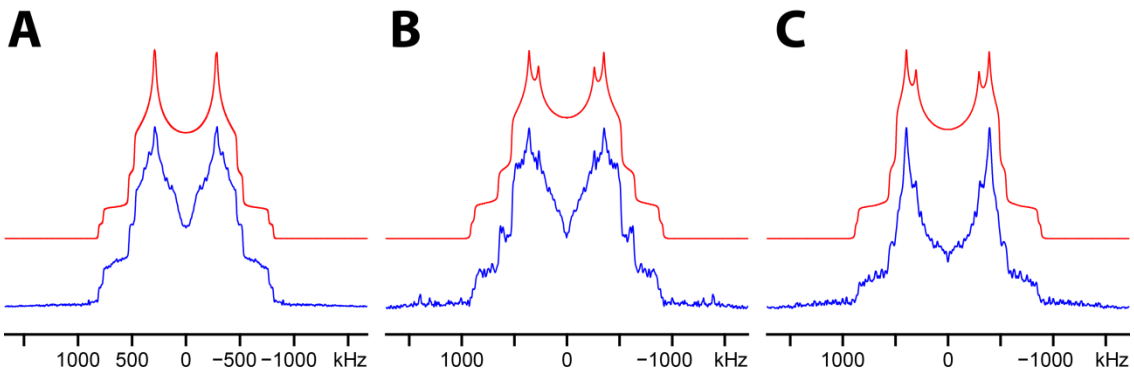

Figure 2.6. ^{14}N SSNMR powder patterns of (A) **lysHCl**, (B) **met**, and (C) **ile-*d*$_3$** acquired using WCPMG at 9.4 T (blue) and associated two-site simulations (red).

(**Figure 2.6A**) allowed us to fit the powder pattern using two ^{14}N sites with values of C_Q = 1.09 MHz and C_Q = 1.02 MHz and η_Q = 0.30 and η_Q = 0.26 for sites 1 and 2, respectively. Herein, we designate the nitrogen site with the higher η_Q value as site 1, while the other site is designated as site 2. The ^{14}N NMR spectrum of **met** (**Figure 2.6B**) clearly reveals multiple horn, shoulder, and foot discontinuities that are simulated with two ^{14}N sites: C_Q = 1.22 MHz and C_Q = 1.17 MHz, and η_Q = 0.42 and η_Q = 0.19, respectively.

Our research group has previously investigated **leu**;[31] here we report the quadrupolar parameters in **Table 2.1** and include **leu** in our subsequent discussion (*vide infra*). *L*-Isoleucine (**ile**), a structural isomer of *L*-leucine (**leu**), is one of two amino acids that have a chiral side chain (the other is threonine, **thr**). Four stereoisomers of **ile** exist; however, the form discussed herein is the naturally occurring (2S,3S) stereoisomer, as confirmed by pXRD (**Figure A2**). ^{14}N WCPMG NMR experiments conducted on **ile** result in short CPMG echo trains due to very short T_2^{eff}(^{14}N) constants, even with high-power ^{1}H decoupling (similar to the observations made for **leu**).[31] However, the ^{14}N SSNMR powder pattern of the deuterated form, **ile-*d*$_3$**, has high S/N and reveals multiple

horn, shoulder, and foot discontinuities (**Figure 2.6C**). A two-site simulation of the powder pattern yields C_Q = 1.14 MHz and C_Q = 1.18 MHz and η_Q = 0.30 and η_Q = 0.11, for sites 1 and 2, respectively.

L-valine (**val**) has a single type of nitrogen within the molecular unit, but when crystallized in its zwitterionic form, there are two crystallographically distinct nitrogen sites in the unit cell; hence, one would expect the observation of two distinct ^{14}N powder patterns (our DFT calculations confirm this, **Table A5**). The ^{14}N spectrum of **val** is indicative of a single ^{14}N site with very well resolved discontinuities (**Figure 2.7A**). The spectrum was simulated using C_Q = 1.17 MHz and η_Q = 0.18. This means that either there are two sites with almost identical quadrupolar parameters which yield overlapping patterns, or that one of the powder patterns is distinct, but is not resolved due to a short $T_2^{eff}(^{14}N)$.

In order to resolve patterns arising from the magnetically distinct ^{14}N sites, **val** was recrystallized from $D_2O(\ell)$, with the hope of increasing $T_2^{eff}(^{14}N)$ for both sites and obtaining a WCPMG spectrum with higher S/N and showing both overlapping spectra. The ^{14}N SSNMR powder pattern of **val-d_3** (**Figure 2.7B**) has additional features in the horn, shoulder, and foot regions. These additional features allowed us to fit the powder pattern using two distinct ^{14}N sites with C_Q = 1.11 MHz and η_Q = 0.34 (site 1), and C_Q = 1.15 MHz and η_Q = 0.18 (site 2). Clearly, the two ^{14}N sites have very different quadrupolar parameters, and deuteration aids in enhancing the signal of the intermediate-η_Q pattern in this case.

For the four amino acids discussed in this section (i.e., **met**, **leu**, **ile**, and **val**), the similarities in bonding result in compounds that each have one nitrogen site with a low

η_Q value and the other with a moderate η_Q value. Using the geometry optimized structures from CASTEP, we observed that for the ^{14}N moieties with low η_Q values, the N-H bond lengths are all similar and range from 1.046 – 1.054 Å, while for those with intermediate η_Q values, the N-H bond lengths are much more varied and range from 1.039 – 1.069 Å. The complete list of bond lengths can be found in **Table A7**.

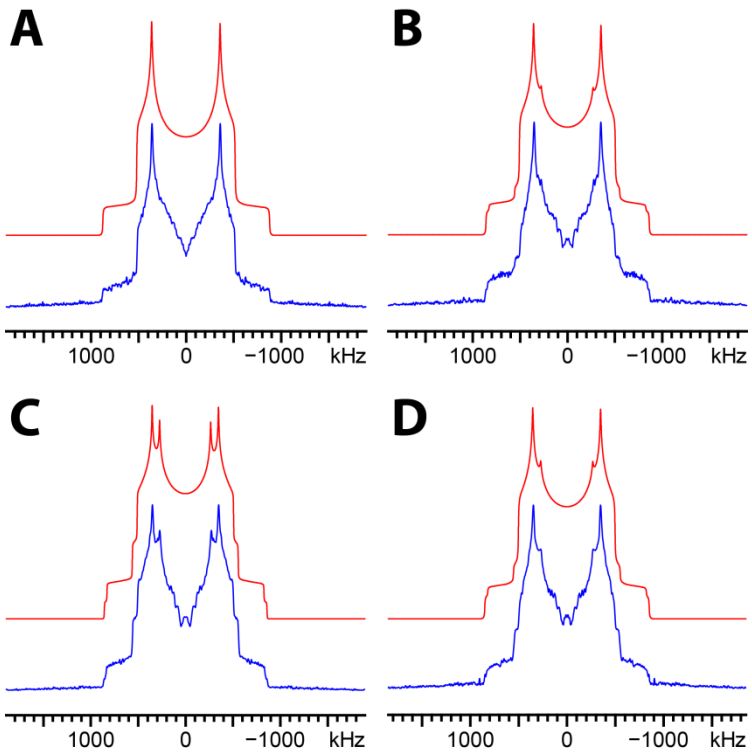

Figure 2.7. ^{14}N SSNMR powder patterns of (A) **val**, (B) **val-*d*$_3$**, (C) **val** acquired at T_{max} = 130 °C, and (D) **val-*d*$_3$** acquired at T_{max} = 100 °C using WCPMG at 9.4 T (blue) and associated spectral simulations (red).

2.4.7 Strategies for Enhancing S/N in ^{14}N SSNMR spectra

Some of the amino acids are not particularly responsive to CPMG-type experiments, due to the influences of ^{1}H-^{14}N dipolar coupling on the T_2^{eff}(^{14}N). As described above for **hyp**, **ile** and **val**, one possible means of increasing T_2^{eff}(^{14}N) is by deuterating the ammonium moieties; however, in some cases, this selective deuteration

(when possible) is still not enough to allow for the collection of a significant number of CPMG echoes, possibly due to strong heteronuclear dipolar couplings with protons from other functional groups, and/or dynamical molecular motions which may impact the $T_2^{eff}(^{14}N)$ behaviour. Several other means of increasing S/N in the ^{14}N SSNMR spectra of ammonium moieties are: (i) conducting experiments over a range of temperatures, (ii) using broadband ^{1}H-^{14}N cross polarization (BCP), and/or (iii) ultra-high magnetic fields (i.e., 21.1 T). In this section, ^{14}N SSNMR experiments on unresponsive systems (e.g., **asp**, and **phe**) are discussed, along with strategies for improving S/N and decreasing experimental times.

We have previously observed that the $T_2^{eff}(^{14}N)$ can be extremely sensitive to temperature, and may have a correlation with the energy barrier to rotation of the NH_3 groups.[47] The ^{14}N S/N ratio is temperature dependent: a relationship between T_{max} (the temperature at which the highest ^{14}N S/N is observed) and the energy barrier for rotation of the NH_3 group seems to exist. The threefold-jump motion that amine groups undergo can be modeled by a single-energy activation model described by the Arrhenius equation:[62,63]

$$\tau_c = \tau_o \exp\left(\frac{E_A}{RT}\right) \qquad [2.4]$$

where τ_c is the correlation time, τ_o is the pre-exponential factor, E_A is the energy barrier for free rotation of the amine group, R is the gas constant, and T is the temperature. As demonstrated previously,[47] with the use of activation energies determined by Andrews *et al.*,[62,64–66] it is possible to estimate the temperature at which the various amino acids will have the same correlation time, and ideally, similar ^{14}N relaxation characteristics (i.e., $T_2^{eff}(^{14}N)$). Previously, we used the α-polymorph of glycine as our reference compound,

since at room temperature, the $T_2^{eff}(^{14}N)$ is found to be at its maximum, which allows for a long train of CPMG echoes to be acquired.

The first sample to be discussed in this section is **val**, which has two ^{14}N RNH_3^+ sites, and required deuteration to obtain high quality ^{14}N NMR spectra (*vide supra*). The rotational barrier in **val** is higher than in α-glycine (E_A = 37.4 kJ/mol vs. E_A = 21.7 kJ/mol, respectively);[65,67] therefore, at room temperature, the τ_c for NH_3 rotation is lower for **val** at room temperature than for **α-gly**. The Arrhenius equation predicts that the τ_c for **val** at 151 °C is equal to that of **α-gly** at room temperature. Hence, as the temperature of **val** is increased, the τ_c is expected to increase, and a longer train of CPMG echoes is expected to be observed in the ^{14}N FID. Individual sub-spectra of **val** at temperatures ranging from −81 to +172 °C shows the temperature dependence of the ^{14}N NMR signal resulting from an increased $T_2^{eff}(^{14}N)$ (**Figure A9A**). The sub-spectrum with the highest ^{14}N S/N (roughly two times that of the room temperature spectrum, T_{RT}) occurs at a temperature of 130 °C (T_{max}), about 20 °C lower than that predicted by the Arrhenius equation. We note that discrepancies in the temperature values may arise from several factors, including the accuracy of T_{max} of α-gly (which is the basis of our calculations), the large temperature increments that we used, as well as the fact that there may not be an exact correspondence between the ^1H relaxation measurements of Andrew *et al.*,[62,65,68] our $T_2^{eff}(^{14}N)$ values, and the magnitudes of the rotational barriers. Nonetheless, we were able to acquire a ^{14}N powder pattern of **val** at T_{max} with nearly the same integrated signal intensity as the T_{RT} spectrum in approximately half of the experimental time (**Figure 2.7C**). Unlike the T_{RT} spectrum, discontinuities arising from the two ^{14}N patterns are clearly discernable: the quadrupolar parameters are easily determined, and found to be

similar to those measured at T_{RT} (within experimental error), with C_Q = 1.11 MHz and η_Q = 0.35 (site 1) and C_Q = 1.15 MHz and η_Q = 0.19 (site 2). This is also consistent with the previous observation that temperature variation does not have a significant effect on the ^{14}N quadrupolar parameters, since the increased rate of rotational motion does not result in significant averaging of any of the components of the ^{14}N EFG tensor.[47]

Since the $T_2^{eff}(^{14}N)$ is clearly influenced by both deuteration and temperature, the effects of temperature on deuterated **val-*d*$_3$** were investigated. The individual ^{14}N sub-spectra of **val-*d*$_3$** were acquired over a temperature range from 0 to 150 °C (**Figure A9B**). The S/N in each spectrum appears to be relatively constant from 25 ^{o}C to 150 °C – very different behaviour than that observed for non-deuterated **val**. Clearly, the rotation of the ND_3 group does not have a major influence on $T_2^{eff}(^{14}N)$ in contrast to NH_3 rotation; this may be due to: (i) reduction of the magnitude of the fluctuating magnetic fields due to the absence of large ^{14}N-^{1}H dipolar couplings by deuteration, and/or (ii) change in the activation energy for rotation due to deuteration. We are currently investigating the underlying mechanisms of relaxation which influence ^{14}N SSNMR patterns of RNH_3^+ moieties, and how they are influenced by deuterium exchange and variation in temperature; this will be the subject of a future publication.

Our attempts at acquiring a room-temperature spectrum of *L*-aspartic acid (**asp**) were hindered by a short $T_2^{eff}(^{14}N)$, which resulted in a sub-spectrum with low S/N, even after two hours of acquisition (see **Figure A10**). However, a ^{14}N powder pattern of **asp** was acquired in less than an hour at T_{max} = 108 °C (**Figure 2.8A**); from this, values of C_Q = 1.21 MHz and η_Q = 0.17 were measured. The rotational barrier in **asp** (E_A = 29.8 kJ/mol)[68] is higher than that of α-glycine, but lower than that of **val**; this T_{max}

corresponds reasonably well with the predicted temperature of 90 °C, where the correlation time of **asp** matches that of **α-gly** at T_{RT}.

The ^{14}N powder pattern of *L*-phenylalanine (**phe**) could not be acquired at T_{RT} in any sort of reasonable timeframe and attempts to deuterate the sample via recrystallization from $D_2O(\ell)$ were unsuccessful. However, the ^{14}N powder pattern could be acquired at T_{max} = 171 °C (**Figure 2.8B**). Again, despite poor S/N in the foot region of the pattern, the values of C_Q = 1.25 MHz and η_Q = 0.55 were easily determined.

The ^{14}N powder pattern of *L*-tyrosine (**tyr)** has clearly resolved discontinuities,

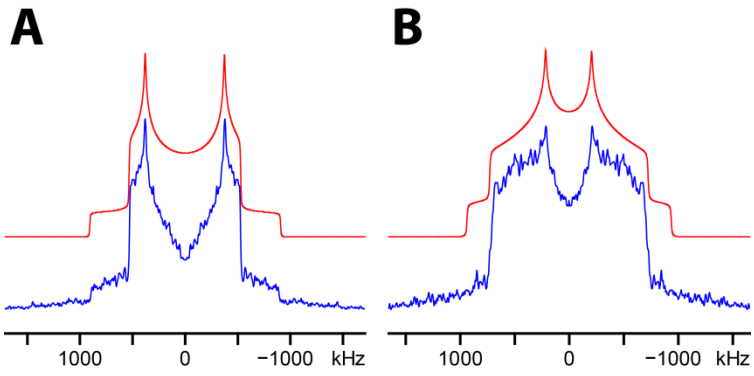

Figure 2.8. ^{14}N SSNMR powder patterns of (A) **asp** (acquired at T_{max} = 108 °C) and (B) **phe** (acquired at T_{max} = 171 °C) acquired using WCPMG at 9.4 T (blue) and associated spectral simulations (red).

from which quadrupolar parameters are measured as C_Q = 1.00 MHz and η_Q = 0.44 (**Figure 2.9A**). Although we were able to acquire the ^{14}N powder pattern in *ca*. 5 hours and it has clearly resolved discontinuities, the S/N is not optimal due to efficient $T_2^{eff}(^{14}N)$ relaxation. Attempts to deuterate the sample were unsuccessful; however, subjecting the sample to ^{14}N VT experiments yielded favourable results. **Figure 2.9B** shows the ^{14}N powder pattern acquired at T_{max} = 171 °C in only 1.7 hours. The

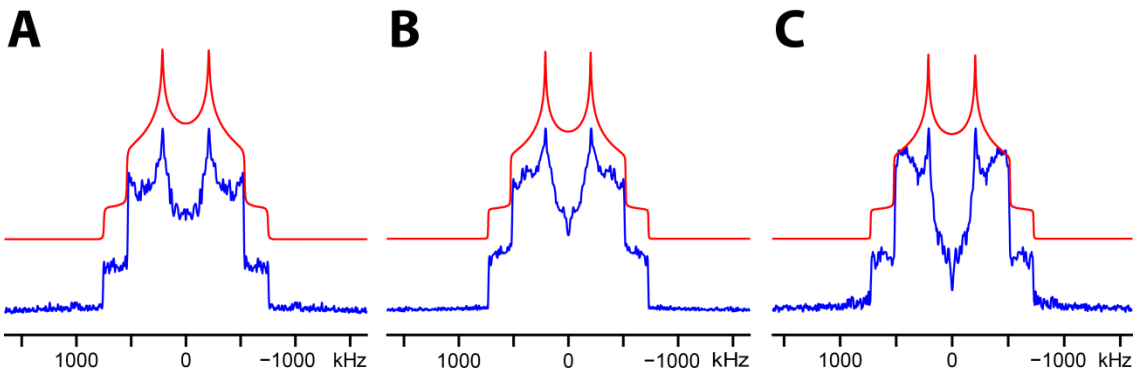

Figure 2.9. ^{14}N SSNMR powder patterns of (A) **tyr** acquired using WCPMG at T_{RT}, (B) **tyr** acquired using WCPMG at T_{max} = 171 °C, and (C) **tyr** acquired with BCP at T_{max} = 171 °C at 9.4 T (blue) and associated spectral simulations (red). The experiments in A), B), and C) required 5, 1.7, and 0.5 hours of acquisition, respectively.

quadrupolar parameters, C_Q = 0.98 MHz and η_Q = 0.44, are within the limits of the experimental uncertainties of those determined at T_{RT}.

The $T_2^{eff}(^{14}N)$ is not the only relaxation time constant that changes appreciably with temperature. Andrews *et al*. determined the activation energies for amine group rotation by observing variations in $T_1(^1H)$ with temperature.[62,64,68] The T_{max} reported herein for **tyr** does not correspond precisely to the temperature at which Andrews *et al.* report their $T_1(^1H)$ minimum (T_{max} = 171 °C vs. $T_1(^1H)_{min}$ = 126 °C [68]). Of course, the main reason for this is that there are different interactions and timescales contributing to $T_2^{eff}(^{14}N)$ and $T_1(^1H)$ relaxation. For **tyr**, the $T_1(^1H)$ (estimated indirectly from ^{1}H pulse delay = $5T_1$) at room temperature was determined to be > 10 s, while at T_{max}, it was estimated to be ca. 0.5 s (**Figure A11**).

The shorter $T_1(^1H)$, and correspondingly shorter ^{1}H recycle delay at T_{max}, allowed us to explore the possibility of using broadband CP to further boost the S/N of the ^{14}N spectra. This is not feasible at room temperature due to the short $T_2^{eff}(^{14}N)$ and the long ^{1}H recycle delay (> 60 s). With the use of the BRAIN-CP/WCPMG pulse sequence,[38] the

^{14}N SSNMR powder pattern of **tyr** was acquired at T_{max} and took only 0.5 hours (**Figure 2.9C**) – significantly faster than the corresponding WCPMG spectrum at T_{RT}. We note that the CP efficiency seems to vary across the breadth of the powder pattern, leading to some distortions. Nonetheless, all of the discontinuities are still discernable and the quadrupolar parameters are determined as C_Q = 0.97 MHz and η_Q = 0.43. Using individual sub-spectra acquired with identical acquisition parameters, the spectra acquired with DE and BCP methods at T_{max} have ca. 2.5 and 5.0 times the S/N of the spectrum acquired at T_{RT} using DE (**Figure A12**). This set of data nicely illustrates that in certain cases, the combination of VT with BCP clearly allows for reduction of experimental times, while retaining the ability to accurately determine the ^{14}N quadrupolar parameters.

Lastly, conducting DE ^{14}N SSNMR experiments at ultra-high magnetic field strengths (i.e., 21.1 T) allows for the rapid acquisition of the ^{14}N powder patterns. Complete spectra (without "mirroring") of **ser**, **tyr**, **thr**, and **gln** (**Figure 2.10**) were all acquired in less than two hours each (as opposed to *ca*. 5 hours each for the mirrored spectra at 9.4 T). All of the spectra have clearly resolved discontinuities; the ^{14}N quadrupolar parameters can be accurately extracted and are in agreement with those determined at 9.4 T (recall that on the Hz scale, FOQI dominated spectra remain unchanged with magnetic field). The combination of ^{14}N VT, BCP, and ultra-high magnetic fields has the potential to decrease the ^{14}N experimental times for pseudo-tetrahedral nitrogen moieties even further, as well as permitting the investigation of nitrogen environments associated with larger C_Q values (i.e., planar, pyramidal, and linear).

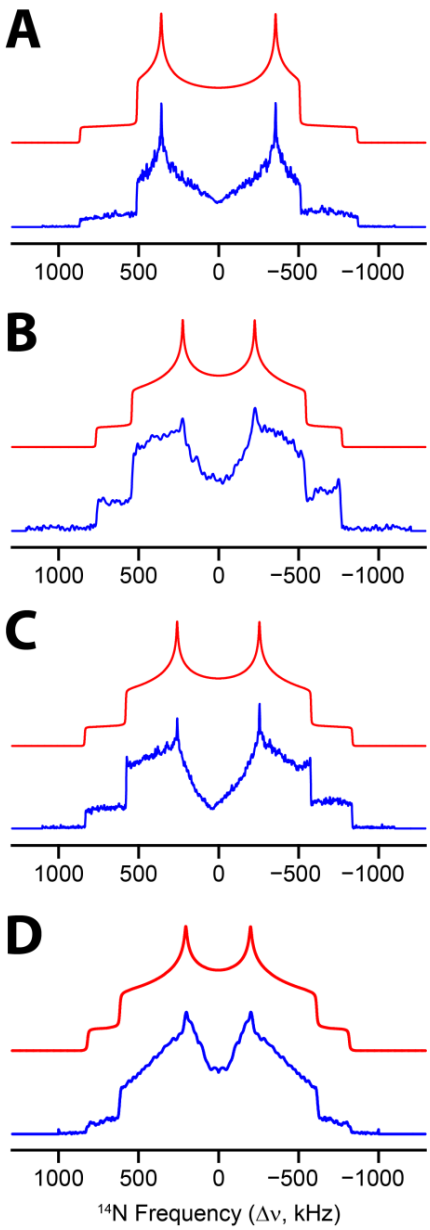

Figure 2.10. ^{14}N SSNMR powder patterns of (A) **ser**, (B) **tyr**, (C) **thr**, and (D) **gln** acquired using WCPMG at 21.1 T (blue) and associated spectral simulations (red).

2.4.8 Polymorph differentiation of A- and B-histidine

The sensitivity of the ^{14}N EFG tensor to small structural differences in the ammonium moieties makes ^{14}N SSNMR a good candidate for polymorph differentiation. In particular, in cases where the nitrogen atom has directly bound hydrogen atoms, minute variations in hydrogen bonding most often result in unique ^{14}N EFG parameters. Several cases of polymorph differentiation using ^{14}N nuclear quadrupole resonance (NQR) have been reported in the literature,[69–75] and we have previously demonstrated the use of ^{14}N UW SSNMR to differentiate polymorphs of glycine and various active pharmaceutical ingredients based on (i) unique sets of quadrupolar parameters and (ii) variation in $T_2^{\text{eff}}(^{14}\text{N})$ relaxation constants.[47,76]

L-histidine has two polymorphic forms at room temperature; A-histidine (**A-his**) has an orthorhombic unit cell with $P2_12_12_1$ and a = 5.175(6) Å, b = 7.315(8) Å, c = 18.75(2) Å, while B-histidine (**B-his**) has a monoclinic unit cell with $P2_1$ and a = 5.166(6) Å, b = 7.385(5) Å, and c = 9.465(4) Å. Both polymorphs have one unique pseudo-tetrahedral nitrogen moiety. Their corresponding ^{14}N SSNMR powder patterns are shown in **Figures 2.11A** and **2.11B**, respectively. Spectral simulation of the powder patterns reveals that **A-his** has C_Q = 1.19 MHz and η_Q = 0.16, while **B-his** has C_Q = 1.23 MHz and η_Q = 0.19. The slight variation in the quadrupolar parameters for the two polymorphs is attributed to the variation in the N-H bond lengths for the two samples caused by different degrees of H-bonding. Surprisingly, the ^{14}N EFG tensor parameters of these polymorphs are very similar, despite clear differences in the local hydrogen-bonding arrangements at their RNH_3^+ groups (**Table A6**). The polymorphs can also be distinguished by a difference in the $T_2^{\text{eff}}(^{14}\text{N})$ relaxation behaviour, which results in

different S/N ratios for their respective spectra (the ratio of S/N of A-his to B-his is approximately 0.6). The T_2^{eff} values at the horn discontinuity of both samples were measured to be 7(3) ms and 24(4) ms for **A-** and **B-his**, respectively (**Figure A13**). The potential of using ^{14}N relaxation characteristics to differentiate polymorphs improves the value of ^{14}N SSNMR for such purposes. Work is currently underway in on our laboratory in applying ^{14}N UW SSNMR experiments under a variety of conditions (VT, BCP, higher fields, etc.) for differentiation of polymorphs of amino acids, as well as a variety of nitrogen-containing organic molecules such as active pharmaceutical ingredients.

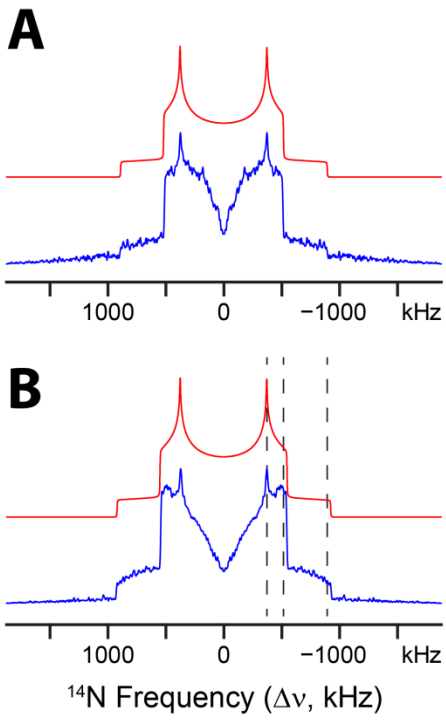

Figure 2.11. ^{14}N SSNMR powder patterns of (A) **A-his** and (B) **B-his** acquired using WCPMG at 9.4 T (blue) and associated spectral simulations (red). Dashed lines correspond to discontinuities of the spectrum of **A-his**.

2.5. Conclusions and Outlook

^{14}N UW SSNMR powder patterns of nearly all of the *L*-amino acids and several derivatives have been acquired in relatively short experimental times with the use of the WCPMG and BCP pulse sequences. Since all of the samples have sp^3 hybridized nitrogen moieties (i.e., RNH_3^+ and $RR'NH_2^+$), the C_Q values for all of the samples fall in the range $0.8 \leq |C_Q| \leq 1.5$ MHz. Variation in η_Q and consideration of plane-wave DFT calculations of ^{14}N EFG tensor parameters and orientations allow for the grouping of these moieties into three general categories: RNH_3^+ moieties were found to possess low ($\eta_Q < 0.3$) and intermediate ($0.31 \leq \eta_Q \leq 0.7$) values of η_Q; nitrogen sites with low η_Q values have N-H bond lengths that are all approximately equal in length (indicating either a complete lack of H-bonding or nearly identical hydrogen bonding environments for all three N-H bonds), while intermediate-η_Q values are observed for nitrogen environments having greater variation in N-H bond lengths resulting from non-uniform hydrogen bonding arrangements. Nitrogen moieties with $RR'NH_2^+$ geometries consistently have high-η_Q values, due to the absence of a C_3 or pseudo-C_3 symmetry axis. Based on this work, we are currently exploring pathways for rapid acquisition of broader ^{14}N patterns arising from nitrogen environments of planar, pyramidal and linear geometries.

The use of high-power ^{1}H decoupling, deuteration, and/or variable temperature NMR aided the acquisition of ^{14}N powder patterns by increasing the effective transverse relaxation time, $T_2^{eff}(^{14}N)$, which allows for the collection of more echoes using CPMG methods. NMR CASTEP calculations of ^{14}N EFG tensor parameters that account for the extended crystal structures with the use of periodic boundary conditions were found to be in good agreement with the experimentally determined ^{14}N quadrupolar parameters. The

use of ^{14}N SSNMR for the differentiation of two polymorphs of *L*-histidine demonstrated that differentiation may be achieved with the use of the quadrupolar parameters, as well as $T_2^{eff}(^{14}N)$, which can be determined from the FIDs of individual sub-spectra. We have also briefly discussed the dynamics of the NH_3 group and the effects of temperature variation on its rate of rotational motion, and how these impact the S/N in their ^{14}N SSNMR powder patterns. More work is currently underway in our laboratory to clearly elucidate the relaxation mechanisms responsible for this behaviour.

The sensitivity of the ^{14}N EFG tensor to variations in intermolecular hydrogen bonding arrangements may be of particular value in the emerging area of NMR crystallography,[77] where structural predictions can be made with the use of computational methods including the *ab initio* random structural searching (AIRSS) algorithm[78–81] and other algorithms.[82–84] Accurately measured ^{14}N quadrupolar parameters and theoretical ^{14}N EFG tensors obtained from models that have been structurally refined should lend much insight into hydrogen bonding, intermolecular interactions and crystal structure packing in a wide range of solid organic compounds. We hope that the work detailed herein encourages other researchers to consider the use of ^{14}N UW SSNMR methods as part of their spectroscopic toolbox for the characterization of molecular-level structure and dynamics in nitrogen-containing systems.

2.6 Bibliography

(1) Edmonds, D. T. *Phys. Rep.* **1977**, *29*, 233.

(2) O'Dell, L. A. *Prog. Nucl. Magn. Reson. Spectrosc.* **2011**, *59*, 295.

(3) Schurko, R. W. Acquisition of Wideline Solid-State NMR Spectra of Quadrupolar Nuclei. *Encyclopedia of Magnetic Resonance*, 2012.

(4) Schurko, R. W. *Acc. Chem. Res.* **2013**, *46*, 1985.

(5) O'Dell, L. A.; Schurko, R. W.; Harris, K. J.; Autschbach, J.; Ratcliffe, C. I. *J. Am. Chem. Soc.* **2011**, *133*, 527.

(6) Elmi, F.; Hadipour, N. L. *J. Phys. Chem. A* **2005**, *109*, 1729.

(7) Veinberg, S. L.; Friedl, Z. W.; Harris, K. J.; O'Dell, L. A.; Schurko, R. W. *CrystEngComm* **2015**, *17*, 5225.

(8) Xu, J.; Lucier, B. E. G.; Sinelnikov, R.; Terskikh, V. V.; Staroverov, V. N.; Huang, Y. *Chem. Eur. J.* **2015**, *21*, 14348.

(9) Giavani, T.; Bildsøe, H.; Skibsted, J.; Jakobsen, H. J. *J. Magn. Reson.* **2004**, *166*, 262.

(10) Zhou, B.; Giavani, T.; Bildsøe, H.; Skibsted, J.; Jakobsen, H. J. *Chem. Phys. Lett.* **2005**, *402*, 133.

(11) O'Dell, L. A.; Ratcliffe, C. I. *Chem. Commun.* **2010**, *46*, 6774.

(12) Whitehouse, B. A.; Ray, J. D.; Royer, D. J. *J. Magn. Reson.* **1969**, *1*, 311.

(13) Hilbers, C. W.; Maclean, C. *Mol. Phys.* **1969**, *16*, 275.

(14) Yannoni, C. S. *J. Chem. Phys.* **1970**, *52*, 2005.

(15) Tycko, R.; Opella, S. J. *J. Chem. Phys.* **1987**, *86*, 1761.

(16) O'Dell, L. A.; Brinkmann, A. *J. Chem. Phys.* **2013**, *138*, 064201.

(17) O'Dell, L. A.; He, R.; Pandohee, J. *CrystEngComm* **2013**, *15*, 8657.

(18) Hill, E. A.; Yesinowski, J. P. *J. Chem. Phys.* **1997**, *106*, 8650.

(19) Hill, E. A.; Yesinowski, J. P. *J. Chem. Phys.* **1997**, *107*, 346.

(20) Harris, R. K.; Olivieri, A. C. *Prog. Nucl. Magn. Reson. Spectrosc.* **1992**, *24*, 435.

(21) Cavadini, S.; Abraham, A.; Bodenhausen, G. *J. Magn. Reson.* **2008**, *190*, 160.

(22) Cavadini, S.; Vitzthum, V.; Ulzega, S.; Abraham, A.; Bodenhausen, G. *J. Magn. Reson.* **2010**, *202*, 57.

(23) Tatton, A. S.; Pham, T. N.; Vogt, F. G.; Iuga, D.; Edwards, A. J.; Brown, S. P.

Mol. Pharm. **2013**, *10*, 999.

(24) Shen, M.; Trébosc, J.; Lafon, O.; Pourpoint, F.; Hu, B.; Chen, Q.; Amoureux, J.-P. *J. Magn. Reson.* **2014**, *245*, 38.

(25) Pandey, M. K.; Nishiyama, Y. *Solid State Nucl. Magn. Reson.* **2015**, *70*, 15.

(26) Reddy, G. N. M.; Marsh, A.; Davis, J. T.; Masiero, S.; Brown, S. P. *Cryst. Growth Des.* **2015**, *15*, 5945.

(27) O'Dell, L. A. *Annu. Reports NMR Spectrosc.* **2015**, *86*, 211.

(28) Cavadini, S. *Prog. Nucl. Magn. Reson. Spectrosc.* **2010**, *56*, 46.

(29) MacGregor, A. W.; O'Dell, L. A.; Schurko, R. W. *J. Magn. Reson.* **2011**, *208*, 103.

(30) O'Dell, L. A.; Schurko, R. W. *Chem. Phys. Lett.* **2008**, *464*, 97.

(31) O'Dell, L. A.; Schurko, R. W. *Phys. Chem. Chem. Phys.* **2009**, *11*, 7069.

(32) Kupče, Ē.; Freeman, R. *J. Magn. Reson. Ser. A* **1995**, *115*, 273.

(33) O'Dell, L. A. *Solid State Nucl. Magn. Reson.* **2013**, *55-56*, 28.

(34) Bhattacharyya, R.; Frydman, L. *J. Chem. Phys.* **2007**, *127*, 1.

(35) Massiot, D.; Farnan, I.; Gautier, N.; Trumeau, D.; Trokiner, A.; Coutures, J. P. *Solid State Nucl. Magn. Reson.* **1995**, *4*, 241.

(36) Medek, A.; Frydman, V.; Frydman, L. *J. Phys. Chem.* **1999**, *103*, 4830.

(37) Tang, J. A.; Masuda, J. D.; Boyle, T. J.; Schurko, R. W. *ChemPhysChem* **2006**, *7*, 117.

(38) Harris, K. J.; Lupulescu, A.; Lucier, B. E. G.; Frydman, L.; Schurko, R. W. *J. Magn. Reson.* **2012**, *224*, 38.

(39) Harris, K. J.; Veinberg, S. L.; Mireault, C. R.; Lupulescu, A.; Frydman, L.; Schurko, R. W. *Chem. Eur. J.* **2013**, *19*, 16469.

(40) Kraus, W.; Nolze, G. PowderCell, 2000.

(41) O'Dell, L. A.; Schurko, R. W. *J. Am. Chem. Soc.* **2009**, *131*, 6658.

(42) Eichele, K.; Wasylishen, R. E. WSolids, 2000.

(43) Bielecki, A.; Burum, D. P. *J. Magn. Reson. Ser. A* **1995**, *116*, 215.

(44) Clark, S. J.; Segall, M. D.; Pickard, C. J.; Hasnip, P. J.; Probert, M. I. J.; Refson, K.; Payne, M. C. *Zeitschrift für Krist.* **2005**, *220*, 567.

(45) Mauri, F.; Pfrommer, B. G.; Louie, S. G. *Phys. Rev. Lett.* **1996**, *77*, 5300.

(46) Profeta, M.; Mauri, F.; Pickard, C. J. *J. Am. Chem. Soc.* **2003**, *125*, 541.

(47) Veinberg, S. L.; Friedl, Z. W.; Harris, K. J.; O'Dell, L. A.; Schurko, R. W. *CrystEngComm* **2015**, 17.

(48) Edmonds, D. T.; Hunt, M. J.; Mackay, A. L. *J. Magn. Reson.* **1973**, *9*, 66.

(49) Akitt, J. W.; McDonald, W. S. *J. Magn. Reson.* **1984**, *58*, 401.

(50) Knop, O.; Palmer, E. M.; Robinson, R. W. *Acta Crystallogr. Sect. A* **1975**, *31*, 19.

(51) Autschbach, J.; Zheng, S.; Schurko, R. W. *Concepts Magn. Reson. Part A* **2010**, *36A*, 84.

(52) Viger-Gravel, J.; Korobkov, I.; Bryce, D. L. *Cryst. Growth Des.* **2011**, *11*, 4984.

(53) Werner-Zwanziger, U.; Ziegeweid, M.; Black, B.; Pines, A. *Z. Naturforsch* **1994**, *49a*, 1188.

(54) Hunt, M. J. *J. Magn. Reson.* **1974**, *15*, 113.

(55) Andersson, L.-O.; Gourdji, M.; Guibé, L.; Proctor, W. G. *C. R. Acad. Sci.* **1968**, *267*, 803.

(56) Desiraju, G.; Steiner, T. *The Weak Hydrogen Bond*; Oxford University Press, 2001.

(57) Görbitz, C. H.; Törnroos, K. W.; Day, G. M. *Acta Crystallogr. Sect. B Struct. Sci.* **2012**, *68*, 549.

(58) Dalhus, B.; Görbitz, C. H. *Acta Chem. Scand.* **1996**, *50*, 544.

(59) Görbitz, C. H.; Dalhus, B. *Acta Crystallogr. Sect. C Cryst. Struct. Commun.* **1996**, *52*, 1464.

(60) Görbitz, C. H.; Dalhus, B. *Acta Crystallogr. Sect. C Cryst. Struct. Commun.* **1996**, *52*, 1754.

(61) Lupulescu, A.; Kotecha, M.; Frydman, L. *J. Am. Chem. Soc.* **2003**, *125*, 3376.

(62) Andrew, E. R.; Hinshaw, W. S.; Hutchins, M. G.; Sjöblom, R. O. I. *Mol. Phys.* **1976**, *32*, 795.

(63) Kinsey, R. A.; Kintanar, A.; Oldfield, E. *J. Biol. Chem.* **1981**, *256*, 9028.

(64) Andrew, E. R.; Hinshaw, W. S.; Hutchins, M. G. *J. Magn. Reson.* **1974**, *15*, 196.

(65) Andrew, E. R.; Hinshaw, W. S.; Hutchins, M. G.; Sjöblom, R. O. I. *Mol. Phys.* **1977**, *34*, 1695.

(66) Andrew, E. R.; Green, T. J.; Hoch, M. J. R. *J. Magn. Reson.* **1978**, *29*, 331.

(67) Taylor, R. E.; Dybowski, C. *J. Mol. Struct.* **2008**, *889*, 376.

(68) Andrew, E. R.; Hinshaw, W. S.; Hutchins, M. G.; Sjöblom, R. O. I. *Mol. Phys.* **1976**, *31*, 1479.

(69) Blinc, R.; Seliger, J.; Zidanšek, A.; Žagar, V.; Milia, F.; Robert, H. *Solid State Nucl. Magn. Reson.* **2006**, *30*, 61.

(70) Seliger, J. *Acta Chim. Slov.* **2011**, *58*, 471.

(71) Seliger, J.; Žagar, V.; Latosińska, J. N. *Phys. Chem. Chem. Phys.* **2010**, *12*, 13007.

(72) Balchin, E.; Malcolme-Lawes, D. J.; Poplett, I. J. F.; Rowe, M. D.; Smith, J. A. S.; Pearce, G. E. S.; Wren, S. A. C. *Anal. Chem.* **2005**, *77*, 3925.

(73) Lavrič, Z.; Pirnat, J.; Lužnik, J.; Puc, U.; Trontelj, Z.; Srčič, S. *J. Pharm. Sci.* **2015**, *104*, 1909.

(74) Lužnik, J.; Pirnat, J.; Jazbinšek, V.; Lavrič, Z.; Zagar, V.; Srčič, S.; Seliger, J.; Trontelj, Z. *J. Pharm. Sci.* **2014**, *103*, 2704.

(75) Seliger, J.; Žagar, V. *Solid State Nucl. Magn. Reson.* **2012**, *47-48*, 47.

(76) Veinberg, S. L.; Johnston, K. E.; Jaroszewicz, M. J.; Kispal, B. M.; Mireault, C. R.; Kobayashi, T.; Pruski, M.; Schurko, R. W. *Chem. Sci.* **2016**, *submitted*.

(77) *NMR Crystallography*; Harris, R. K.; Wasylishen, R. E.; Duer, M. J., Eds.; John Wiley & Sons, Ltd.: Chichester, U.K., 2009.

(78) Baias, M.; Widdifield, C. M.; Dumez, J.-N.; Thompson, H. P. G.; Cooper, T. G.; Salager, E.; Bassil, S.; Stein, R. S.; Lesage, A.; Day, G. M.; Emsley, L. *Phys. Chem. Chem. Phys.* **2013**, *15*, 8069.

(79) Malone, B. D.; Cohen, M. L. *Phys. Rev. B - Condens. Matter Mater. Phys.* **2012**, *85*, 1.

(80) Morris, A. J.; Grey, C. P.; Needs, R. J.; Pickard, C. J. *Phys. Rev. B* **2011**, *84*.

(81) Pickard, C. J.; Needs, R. J. *J. Phys. Condens. Matter* **2011**, *23*, 053201.

(82) Dračínský, M.; Hodgkinson, P. *CrystEngComm* **2013**, *15*, 8705.

(83) Rossi, G.; Ferrando, R. *J. Phys. Condens. Matter* **2009**, *21*, 084208.

(84) Schön, J. C.; Doll, K.; Jansen, M. *Phys. Status Solidi Basic Res.* **2010**, *247*, 23.

Chapter 3: Ultra-wideline ^{14}N Solid-State NMR as a Method for Differentiating Polymorphs: Glycine as a Case Study

3.1 Overview

Nitrogen-14 solid-state NMR (SSNMR) is utilized to differentiate three polymorphic forms and a hydrochloride (HCl) salt of the amino acid glycine. The ^{14}N quadrupolar interaction is shown to be very sensitive to variations in the local electric field gradients (EFGs) about the ^{14}N nucleus; hence, differentiation of the samples is accomplished through determination of the quadrupolar parameters C_Q and η_Q, which are obtained from analytical simulations of the ^{14}N SSNMR powder patterns of stationary samples (*i.e.*, static NMR spectra, ν_{rot} = 0 Hz). Additionally, differentiation of the polymorphs is also possible via the measurement of ^{14}N effective transverse relaxation time constants, $T_2^{eff}(^{14}N)$. Plane-wave density functional theory (DFT) calculations, which exploit the periodicity of crystal lattices, are utilized to confirm the experimentally-determined quadrupolar parameters as well as to determine the orientation of the ^{14}N EFG tensors in the molecular frame. Several signal-enhancement techniques are also discussed to help improve the sensitivity of the ^{14}N SSNMR acquisition method, including the use of selective deuteration, the application of the BRoadband Adiabatic INversion Cross-Polarization (BRAIN-CP) technique, and the use of variable-temperature (VT) experiments. Finally, we examine several cases where ^{14}N VT experiments employing Carr-Purcell-Meiboom-Gill (CPMG) refocusing are used to approximate the rotational energy barriers for RNH_3^+ groups.

3.2 Introduction

Although glycine is the simplest of the standard, naturally occurring amino acids, it has a complex series of solid-state structures. Three distinct polymorphs exist at ambient conditions (*i.e.*, α, β, and γ). All forms are zwitterionic in the solid state ($H_3N^+CH_2COO^-$) and polymorphism arises from different modes of hydrogen-bonding (H-bonding) due to the disparate arrangements of the molecules in the unit cell.[1,2] The polymorphs have been studied by numerous spectroscopic techniques, including X-ray diffraction,[3–5] thermodynamic studies,[6,7] and ^{1}H and ^{13}C NMR,[8–12] to name a few. Unfortunately, ^{1}H and ^{13}C SSNMR are not always reliable for differentiating polymorphs, as demonstrated by Taylor and Dybowski in their multinuclear SSNMR of glycine.[10]

Nitrogen SSNMR is capable of detecting the subtle changes in the local nitrogen environments that result from different degrees of hydrogen-bonding in several amino acids and more complicated polypeptide systems.[13–19] Nitrogen has two NMR-active nuclides, ^{14}N (nuclear spin, I = 1) and ^{15}N (I = ½). ^{15}N NMR is much more prevalent because of the relatively narrow peaks and high resolution chemical shift information it can provide; however, ^{15}N has a very low natural abundance (0.37%), requiring that most samples be isotopically enriched, which may be expensive and synthetically challenging. There are several reports describing the use of ^{15}N SSNMR to investigate polymorphism in amino acids: some groups have reported the use of ^{15}N SSNMR to investigate tautomerism[20,21] and polymorphism[22] in histidine, several others have successfully used ^{15}N SSNMR to investigate polymorphism in fully ^{15}N-labelled biological systems,[17–19] and still others have investigated polymorphs of glycine,[22,23] and glycine bound to a silica

surface.[23,24] Although ^{15}N SSNMR spectra are sensitive to the protonation state of the nitrogen atom, this sensitivity is reduced when the compounds have the same charge (as is the case with polymorphs), in that the nitrogen chemical shifts are very similar and differ only by a few ppm. Nitrogen-14 on the other hand is 99.63% naturally abundant but has a lower gyromagnetic ratio (*i.e.*, $\gamma(^{14}\text{N}) = 1.93 \times 10^7$ rad T^{-1} s^{-1} *vs.* $\gamma(^{15}\text{N}) = -2.71 \times 10^7$ rad T^{-1} s^{-1}).[25,26] Nitrogen-14 SSNMR is largely avoided because of (i) its low Larmor frequencies, which often require specialized probes and/or tuning equipment, and (ii) the fact that ^{14}N has a nuclear spin of 1 with a moderate ^{14}N quadrupole moment (Q = 20.44 x 10^{-31} m^2),[25] which results in inhomogeneously broadened powder patterns that typically span hundreds of kHz to several MHz. This pattern broadening arises from the quadrupolar interaction (QI), which is the interaction between the quadrupolar nucleus (*i.e.*, $I > ½$) and the surrounding EFGs. In particular, the first-order quadrupolar interaction (FOQI) dominates the appearance of ^{14}N SSNMR spectra, and its orientation dependence results in a typical Pake doublet pattern for $I = 1$ nuclei, from which the quadrupolar coupling constant and quadrupolar asymmetry parameter, denoted C_Q, and η_Q, respectively, can easily be determined (see **Table 3.1** for formal definitions). The entire nitrogen chemical shift range spans *ca*. 1300 ppm;[27] hence, the effects of nitrogen chemical shifts, including chemical shift anisotropies (CSAs) are rarely detected in static ultra-wideline (UW – spectral breadths exceeding more than 250 kHz)[28] ^{14}N SSNMR spectra. In cases where the ^{14}N spectra are narrow due to very small quadrupolar coupling constants (*i.e.*, samples with high Platonic symmetry), it is possible to extract both the quadrupolar parameters and the CSA.[29–31] Although it is possible to acquire UW ^{14}N SSNMR spectra under conditions of magic-angle spinning in order to observe the

simultaneous effects of the CSA and the first- and second-order quadrupolar interactions, long acquisition times (*ca*. 44 – 88 hours) and very stable spinning speeds (*i.e.*, specialized probes) are required for such experiments.[13]

For most nitrogen-containing structural motifs, the local bonding environment and symmetry produce large electric field gradients (EFGs) at the ^{14}N nuclei which give rise to large FOQIs, which in turn broaden most ^{14}N NMR powder patterns beyond the excitation bandwidths of most high-power rectangular pulses. Recently, our research group has demonstrated that pulse sequences incorporating broadband frequency-swept pulses can be used to efficiently acquire ^{14}N SSNMR spectra of such systems.[14,15,32] We note that standard rectangular pulses are suitable for cases in which the nitrogen environments have high spherical or Platonic symmetry, and correspondingly small quadrupolar coupling constants and a narrow powder patterns.[33] Frequency-swept Wideband, Uniform Rate, Smooth Truncated (WURST)[34,35] pulses, in conjunction with the Carr-Purcell Meiboom-Gill (CPMG) refocusing protocol,[36] have been demonstrated to be effective for acquiring ^{14}N SSNMR spectra at moderate and high magnetic fields (*i.e.*, 9.4 to 21.1 T).[14–16] However, in many cases, even the broadband excitation afforded by the WURST pulses is not sufficient to completely excite the entire powder pattern in a single experiment. Therefore, ^{14}N SSNMR spectra are often acquired by stepping the transmitter frequency in even increments across the breadth of the powder pattern (this is the so-called variable-offset cumulative spectra (VOCS) method).[37,38] Fortunately, given the symmetric nature of the ^{14}N Pake doublet powder patterns to first order, it is possible to reduce experimental time by acquiring only half of the ^{14}N powder pattern (and constructing the other half by reflection, if desired; see the experimental section for

details).[15,39] For an account of the progress in ^{14}N SSNMR, we refer the readers to a review article published in 2011 by O'Dell L. A.[16]

In this work, we demonstrate that UW ^{14}N SSNMR can be used to differentiate between three polymorphic forms of glycine (*i.e.*, α, β, and γ), as well as an HCl salt derivative. Although α-glycine has previously been studied by ^{14}N SSNMR by our group[14,40] and others,[13,41,42] its ^{14}N SSNMR spectra can be acquired with great rapidity, making it useful for comparison to its known polymorphs and salts. We also demonstrate that the polymorphs may be differentiated via the measurement of the effective ^{14}N transverse relaxation time constant, $T_2^{\text{eff}}(^{14}\text{N})$. The ^{14}N EFG tensor parameters of the polymorphic phases are correlated to their crystal structures *via* the use of plane-wave DFT calculations. We also discuss how the unique structural and dynamical properties of the RNH_3^+ moieties, which are common in many nitrogen-containing compounds, can be exploited to enhance signal-to-noise (S/N), improve spectral quality, and reduce experimental times. The sensitivity of ^{14}N SSNMR may prove particularly useful for the study of more industrially interesting systems such as active pharmaceutical ingredients (APIs) and other organic and inorganic molecules of interest.

3.3 Experimental Methods

3.3.1 Sample preparation

Samples of α-glycine, γ-glycine, and glycine HCl were obtained from Sigma Aldrich and used without further purification. High purity samples of β-glycine were prepared by the method described by Boldyreva *et al.*[1] A deuterated sample of γ-glycine

was prepared by the method described by Harris *et al*.[43] The phase purities of all samples were confirmed by powder X-ray Diffraction (pXRD) (**Appendix B**, **Figure B1**).

3.3.2 Powder XRD experiments

Diffraction patterns for all the samples were collected using a D8 DISCOVER X-ray diffractometer equipped with an Oxford Cryosystems 700 Cryostream Plus Cooler. A Cu-K_α (λ = 1.54056 Å) radiation source with a Bruker AXS HI-STAR area detector running under the General Area Detector Diffraction Systems (GADDS) was used. Powder patterns were simulated with the PowderCell software package.[44]

3.3.3 Direct-Excitation (DE) NMR experiments

All spectra were acquired using a Varian InfinityPlus spectrometer equipped with a wide-bore 9.4 T magnet using Larmor frequencies of 399.73 MHz and 28.875 MHz for ^{1}H and ^{14}N, respectively. A Chemagnetics 5.0 mm static double-resonance HX probe was used for all experiments, equipped with a Varian/Chemagnetics low-γ tuning box on the ^{14}N channel. Spectra were referenced against a sample of solid NH_4Cl (δ_{iso} = 39.3 ppm),[45] although chemical shifts are not reported due to large uncertainties in their measurements (*vide infra*).

Due to the large breadths of the ^{14}N NMR powder patterns, the WURST-CPMG pulse sequence[46] was used for DE ^{14}N NMR experiments, as previously described elsewhere.[16,20,38] WURST-80[34] pulses 50 μs in length were linearly swept from low to high frequency covering a total range of 2 MHz and having a maximum amplitude of ν_1 = 30 kHz. Continuous wave (CW) ^{1}H decoupling with ν_2 = 40 kHz was applied during

the duration of each scan.[14,47,48] With our current low-γ probe circuit configuration, we are restricted to an upper maximum of *ca*. 40 kHz for proton decoupling power, which means that for some samples it is not possible to fully decouple the ^{14}N-^{1}H heteronuclear dipolar interactions.

Individual sub-spectra were acquired at evenly-spaced transmitter frequencies, which were chosen such that (i) they are integer multiples of the CPMG spikelet spacing, and (ii) the overlap between the individual sub-spectra is optimized to yield undistorted spectra.[38] Each sub-spectrum was zero-filled, apodized, Fourier transformed, and magnitude processed. Only the high-frequency sides of the ^{14}N powder patterns were acquired, with the low frequency sides of the patterns produced by reflection (since the ^{14}N Pake doublet is symmetric about the isotropic chemical shift to first order).[15,16] **Table B1** (**Appendix B**) shows a complete list of acquisition parameters. ^{14}N SSNMR powder patterns were simulated using the WSolids1 program.[49]

3.3.4 Variable-Temperature (VT) NMR experiments

^{14}N WURST-CPMG spectra of non-deuterated α- and γ-glycine were acquired at multiple temperatures ranging from −88 °C to +181 °C with a Varian VT upper stack and nitrogen gas heat exchanger. Temperatures were calibrated using the ^{207}Pb isotropic shift of solid $Pb(NO_3)$, as suggested by Bielecki and Burum.[50] We refer the readers to **Tables B2** and **B3** for detailed lists of temperatures and acquisition parameters.

3.3.5 BRoadband Adiabatic Inversion Cross-Polarization (BRAIN-CP) NMR experiments

A ^{14}N SSNMR spectrum of glycine HCl was acquired using the BRAIN-CP/WCPMG[51] pulse sequence in order to compare the performances of DE and cross-polarization (CP) pulse sequences. The frequency sweep range of the X-channel (X = ^{14}N) contact pulse was set to ensure that abundant ^{1}H spin-polarization was transferred predominantly to the +1 → 0 fundamental transition.[40] A 16-step phase cycle was employed to remove zero-quantum coherences (arising from thermal polarization) so that the WCPMG refocusing pulses only refocused the polarization resulting from the CP process.[40] For a complete list of experimental parameters, please refer to **Tables B4** and **B5**.

3.3.6 Ab initio calculations

Plane-wave density functional theory (DFT) calculations of the ^{14}N EFG tensors were performed using the CASTEP NMR program[52] in the Materials Studio 5.0 software suite on a Dell Studio XPS 435T/9000 with a single Intel Core i7 920 processor and 8 GB of DDR3 RAM. "On the fly" ^{14}N pseudopotentials were used for these calculations, with a plane-wave basis set cut-off of 610 eV and a fine *k*-point set (2 x 2 x 4). The revised Perdew, Burke and Ernzerhof (rPBE) functional was used in the generalized gradient approximation (GGA) for the exchange correlation energy. For all of the crystal structures, geometry optimizations of the hydrogen atom positions were carried out, while holding fixed the positions of all other heavier atoms and lattice parameters.

Crystal structures for α-glycine, β-glycine, γ-glycine, and glycine HCl were obtained from the Cambridge Structural Database (CSD).[3,4,52,53]

3.4 Results and Discussion

3.4.1 ^{14}N SSNMR spectra of the different forms of glycine: direct-excitation experiments

In this section, a brief discussion of the ^{14}N SSNMR spectra of the various forms of glycine is presented. In all cases, the S/N ratio for each spectrum is high enough that two of the three discontinuities associated with the principal components of the ^{14}N EFG tensor can be observed. The outermost discontinuities, which correspond to the largest component of the EFG tensor, V_{33}, are hard to clearly discern in certain cases. Fortunately, only two of the three discontinuities need to be resolved to accurately obtain the quadrupolar parameters (this is because the EFG tensor is traceless, *i.e.*, $V_{33} = -(V_{11} + V_{22})$.[16] Due to variations in the longitudinal relaxation time constant, $T_1(^{14}\text{N})$, and the effective transverse relaxation time constant, $T_2^{\text{eff}}(^{14}\text{N})$, the acquisition times vary for each sample (*vide infra*). We note that the terminology "effective $T_2(^{14}\text{N})$" or "$T_2^{\text{eff}}(^{14}\text{N})$" is used to describe transverse relaxation, due to the partial or complete absence of contributions to relaxation from ^{14}N-^{1}H dipolar coupling resulting from the application of high-power ^{1}H decoupling. **Table 3.1** shows the values of C_Q, η_Q, and $T_2^{\text{eff}}(^{14}\text{N})$ at room temperature (*i.e.*, 20 ^{o}C) for the aforementioned compounds.

Table 3.1. ^{14}N quadrupolar parameters obtained from solid-state NMR spectra and plane-wave DFT calculations and experimental $T_2^{eff}(^{14}N)$ constants.

	Experimental [a]		Plane-wave DFT (unoptimized) [b]		Plane-wave DFT (H optimized) [c]		$T_2^{eff}(^{14}N)$ (ms)[d]
	C_Q (MHz)	η_Q	C_Q (MHz)	η_Q	C_Q (MHz)	η_Q	
α-glycine	1.19(2)[e]	0.52(2)	1.23	0.55	1.23	0.62	54(14)
β-glycine	1.26(3)	0.42(3)	1.63	0.25	1.31	0.54	12(1)
γ-glycine	1.19(4)	0.38(4)	1.28	0.42	1.26	0.41	25(4)
γ-glycine-ND_3^+	1.19(2)	0.37(2)	–	–	–	–	24(3)
glycine HCl	1.16(2)	0.17(2)	1.20	0.16	1.14	0.22	40(10)

[a] The EFG tensor is defined by three principal components ordered such that $|V_{11}| \leq |V_{22}| \leq |V_{33}|$ and $V_{11} + V_{22} + V_{33} = 0$. The quadrupolar parameters are described by $C_Q = eQV_{33}/h$ and $\eta_Q = (V_{11} - V_{22})/V_{33}$, where $0 \leq \eta_Q \leq 1.0$. [b] EFG tensor calculations without prior geometry optimization of the H atom positions. [c] EFG tensor calculations after the H atom positions were optimized. [d] ^{14}N FIDs were acquired at a transmitter frequency of 29.175 MHz, a temperature of 20 °C, and identical ^{1}H decoupling rf fields. [e] Uncertainty is reported to the last decimal place.

3.4.1.1 α-, β-, and γ-glycine

The ^{14}N NMR powder pattern for α-glycine (**Figure 3.1A**) has high S/N, and the discontinuities arising from all three principal axes of the EFG tensor are clearly visible. Analytical simulation of this spectrum yields C_Q = 1.19 ± 0.02 MHz and η_Q = 0.52 ± 0.02, in close agreement with previously obtained results.[13,14] The ^{14}N NMR powder pattern for β-glycine (**Figure 3.1B**) also has high S/N, although it required a significantly longer acquisition time than that of α-glycine (*i.e.*, *ca*. 7.6 hours for the former vs. 0.5 hours for the latter). Comparing the free induction decays (FIDs), which were acquired with identical ^{1}H decoupling fields, reveals that the ^{14}N nuclei in β-glycine have a shorter $T_2^{eff}(^{14}N)$ value than those in α-glycine, resulting in the collection of fewer spin echoes and thereby necessitating a larger number of scans to obtain a spectrum with comparable

S/N (**Table B1**). A more detailed discussion of the measurement of $T_2^{eff}(^{14}N)$ is presented below.

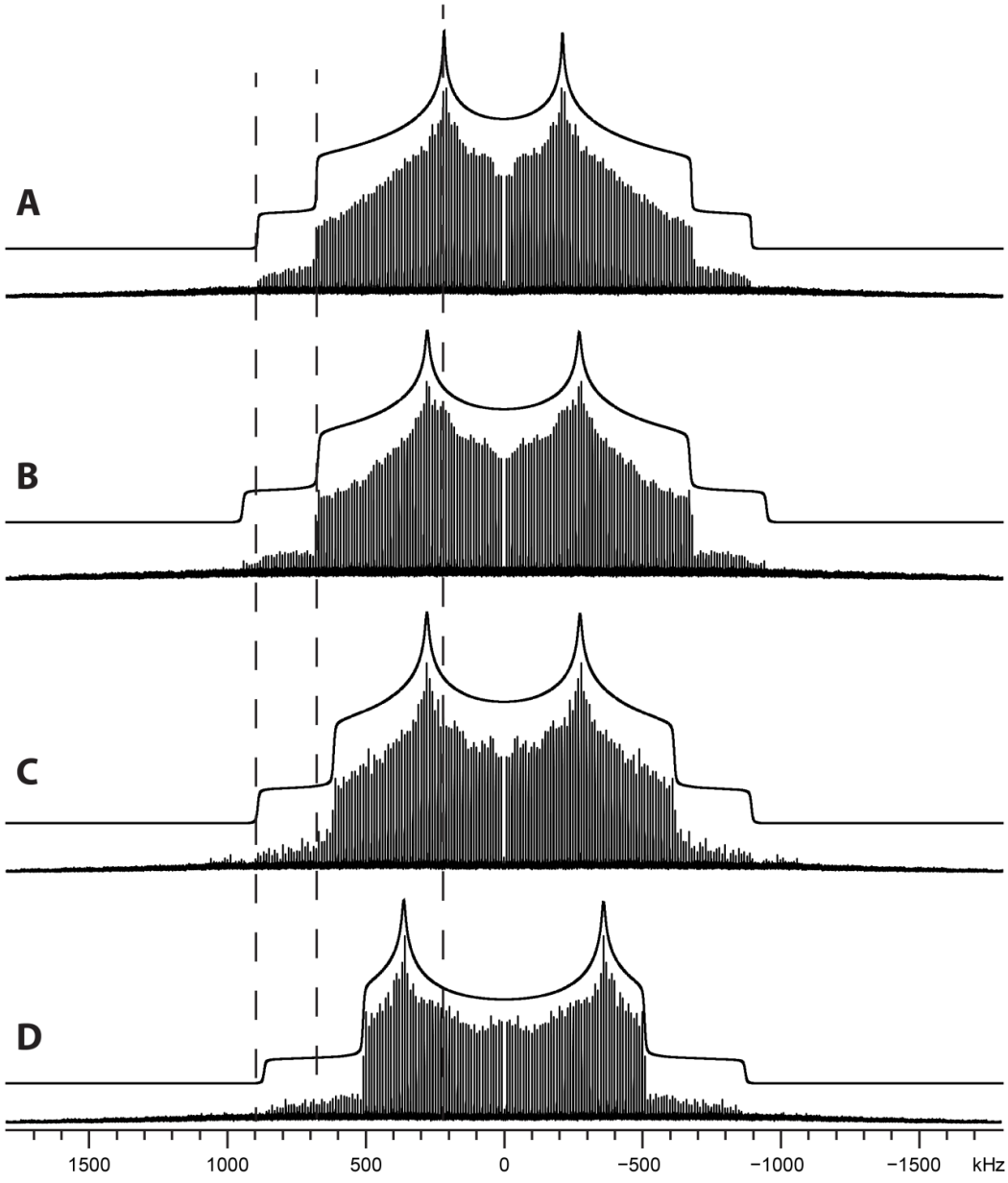

Figure 3.1. ^{14}N SSNMR spectra acquired using the WURST-CPMG pulse sequence at 9.4 T for (A) α-glycine, (B) β-glycine, (C) γ-glycine and (D) glycine HCl. The vertical dashed lines mark the positions of the discontinuities (horns, shoulders, and feet) of the α-glycine powder pattern.

The discontinuities in the spectrum of β-glycine are distinct from those in the spectrum of α-glycine, indicating that each sample is characterized by a unique set of quadrupolar parameters. Indeed, analytical simulation of the spectrum of β-glycine yields C_Q = 1.26 ± 0.03 MHz and η_Q = 0.42 ± 0.03. The ^{14}N NMR spectrum for the third polymorph, γ-glycine, is shown in **Figure 3.1C**. During acquisition of the sub-spectra of γ-glycine, acoustic ringing was observed in the FIDs (**Figure B2**). The acoustic ringing likely arises from the piezoelectric nature of this sample, as described in previous publications.[1,5,54–58] Due to the semi-coherent nature of the ringing, its distorting effect can eventually be reduced with the use of signal averaging (complete averaging requires a large number of scans). Nonetheless, the "horn" and "shoulder" discontinuities are still clearly resolved, and analytical simulations of the powder pattern yield C_Q = 1.19 ± 0.04 MHz and η_Q = 0.38 ± 0.04. Although the value of C_Q is the same as that of α-glycine, the powder patterns are distinct in terms of the locations of the "horn" and "shoulder" discontinuities arising from their different η_Q values. Similar to the observation made for β-glycine, the FIDs of γ-glycine are associated with $T_2^{eff}(^{14}N)$ values that differ from those observed for both α- and β-glycine (*vide infra*).

The $T_2^{eff}(^{14}N)$ constants can be measured by fitting the CPMG echo trains with a first-order exponential decay function; however, we note that the $T_2^{eff}(^{14}N)$ values must be measured for individual sub-spectra (*i.e.*, from FIDs acquired at single transmitter frequencies). For a transmitter frequency of 29.175 MHz, and a ^{1}H decoupling field of ν_2 = 40 kHz, the $T_2^{eff}(^{14}N)$ values are measured to be 54 ± 14, 12 ± 0.6, and 25 ± 3.7 ms for α-, β-, and γ-glycine, respectively (**Figure B3**). The $T_2^{eff}(^{14}N)$ constant for the β-glycine sample is the shortest (corresponding to the most rapid decay of the echo train),

suggesting that there are larger contributions to transverse relaxation from heteronuclear ^{14}N-^{1}H dipolar couplings than in the cases of the α- and γ-glycine samples. This assumption is reasonable, since the values of C_Q are similar for all three compounds, meaning that it is unlikely to be much variation in the quadrupolar contributions to transverse relaxation. An interesting implication of this result is that it may be possible to differentiate polymorphs of some samples solely on the basis of the T_2 relaxation characteristics without having to acquire the entire ^{14}N powder pattern, which may be of use for discriminating systems which possess similar quadrupolar parameters, or possess ^{14}N patterns that are simply too broad to acquire in their entirety.

3.4.1.2 Glycine HCl

Although glycine HCl is a distinct chemical compound, it is of interest to see whether its ^{14}N quadrupolar parameters differ from those of the free-base glycine polymorphs. This of course could have great relevance in the characterization and differentiation of a variety of organic free-base compounds and their corresponding HCl salts, including amino acids, pharmaceuticals and numerous other systems. The ^{14}N NMR powder pattern for glycine HCl (**Figure 3.1D**) has comparable S/N to the powder pattern of α-glycine, with all of the discontinuities clearly resolved. The slightly lower signal intensity of the glycine HCl spectrum compared to that of α-glycine mainly arises from the shorter CPMG echo train (*i.e.*, shorter T_2^{eff}(^{14}N), **Table 3.1**) of the former. The quadrupolar parameters are C_Q = 1.16 ± 0.02 MHz and η_Q = 0.17 ± 0.02. Again, C_Q is very similar to that of α- and γ-glycine; however, its distinct η_Q value leads to a powder pattern that is easily distinguishable.

3.4.1.3 Correlation of ^{14}N NMR data to molecular structure

All of the ^{14}N NMR spectra presented above are associated with pseudo-tetrahedral nitrogen environments (*i.e.*, RNH_3^+, where R denotes the rest of the amino acid). In an idealized "gas phase" system, this moiety most often possesses a C_3 rotation axis along the C-N bond, which results in an axially symmetric ^{14}N EFG tensor ($\eta_Q = 0$) with the principal component of largest absolute magnitude, V_{33}, aligned directly along this axis. However, the systems studied herein do not possess perfect C_3 rotational axes due to intermolecular interactions in the solid state involving the NH_3 group (*i.e.*, hydrogen bonding); hence, the ^{14}N EFG tensors do not have perfect axial symmetry (*i.e.*, $V_{11} \neq V_{22}$ and $\eta_Q \neq 0$). In every case, the V_{33} component is still expected to align along, or close to, the direction of the C-N bond.

Plane-wave DFT calculations have been carried out to correlate the local structures of the nitrogen environments with experimentally-obtained ^{14}N quadrupolar parameters (**Table 3.1**). Plane-wave calculations are suitable for crystalline systems where intermolecular interactions may influence the EFG tensor components and orientations, since the extended crystal lattice is taken into account.[14,59,60] In all of the cases examined herein, the theoretically predicted ^{14}N quadrupolar parameters closely match the experimental data. For the structure obtained using an X-ray source (*i.e.*, β-glycine[4]), the prediction of quadrupolar parameters is improved if the EFG calculations are conducted after the proton positions have been optimized (the positions of the heavier atoms and lattice parameters were held constant). For structures obtained using a neutron source (*i.e.*, α-glycine,[3] γ-glycine,[52] and glycine HCl[53]), the values of C_Q and η_Q are predicted accurately whether or not the proton positions are geometry optimized.

The theoretically predicted ^{14}N EFG tensor orientations for all four systems are shown in **Figure 3.2**. In each case, V_{33} is oriented nearly along the C-N bond, as discussed above. In all cases, the sign of C_Q is predicted to be positive (**Table 3.1**), as expected.[15,61] Although the sign of C_Q cannot be determined experimentally from ^{14}N SSNMR spectra, it has been measured to be positive from the measurement of ^{13}C-^{14}N residual dipolar couplings in the ^{13}C SSNMR spectrum of α-glycine,[62] as well as from ^{14}N nuclear quadrupole resonance (NQR) experiments of other crystalline amino acids.[63,64]

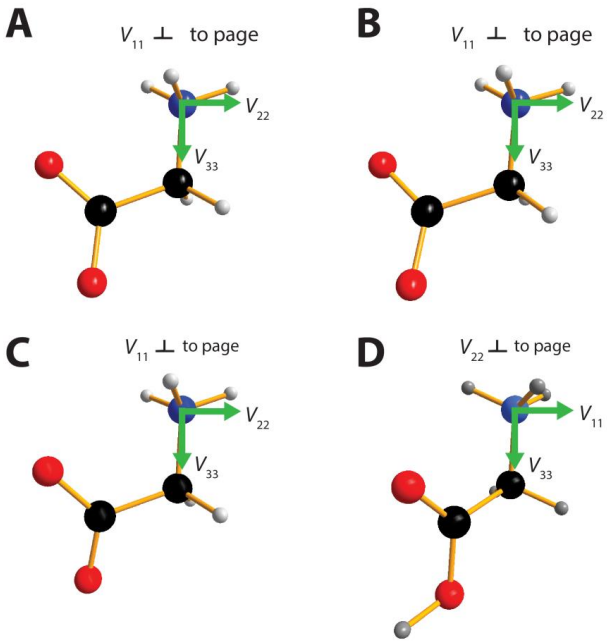

Figure 3.2. ^{14}N EFG tensor orientations in (A) α-glycine, (B) β-glycine, (C) γ-glycine and (D) glycine HCl.

In order to correlate the calculation results to known crystal structures, we restrict our discussion to α-glycine, γ-glycine, and glycine HCl. If one considers the lengths of the N-H bonds in the three samples (**Table B6**), it is evident that glycine HCl has the shortest N-H bonds (*i.e.*, all of the N-H bonds are < 1.4 Å), suggesting that the amount of

hydrogen-bonding with neighbouring molecules is very limited, resulting in a nearly axially symmetric EFG tensor (*i.e.*, $\eta_Q \approx 0$). Both α- and γ-glycine have one or more N-H bonds that are clearly affected by H-bonding (*i.e.*, N-H bond length > 1.5 Å), thereby resulting in an EFG tensor that is less axially symmetric with an intermediate η_Q value (*i.e.*, $\eta_Q \approx 0.5$).

Finally, some brief comments must be made on motional effects on the ^{14}N EFG tensors. This has been recently studied in a number of ^{14}N SSNMR experiments on a variety of different structural moieties.[14,47,65] Despite the fact that NH_3 groups are known to undergo a three-fold-jump motion about the C-N bond in the solid state,[66–68] the magnitude of V_{33} should not be substantially influenced by the motion, since V_{33} is oriented along or near the C-N bond. In addition, V_{11} and V_{22} do not show any evidence of averaging due to the motion, even at higher temperatures where rotational rates are expected to increase (*vide infra*).

3.4.2 Improving the efficiency of ^{14}N SSNMR experiments

The two NMR interactions that make the most significant contributions to nuclear magnetic relaxation processes in ^{14}N SSNMR experiments are the ^{14}N quadrupolar and ^{14}N-^{1}H direct dipolar interactions. Due to the strong dipolar couplings that arise from the short N-H bonds, both the longitudinal and transverse relaxation times are expected to be dominated by the ^{14}N-^{1}H dipolar coupling mechanism, the latter results in short CPMG echo trains and reduced S/N. Ideally, it is desirable to acquire ^{14}N CPMG NMR spectra of such systems with as high a ^{1}H decoupling power as possible, in order to maximize the effective $T_2(^{14}N)$ (*vide supra*). We remind the reader that with the low-γ configuration of

our probe, the ^{1}H decoupling rf is limited to a maximum of *ca*. 40 kHz. It is noted that during the course of this study, we have investigated a variety of schemes to increase the efficiency of ^{1}H decoupling; however, no one decoupling scheme has been found to be more efficient (a full discussion of ^{1}H decoupling and the impacts on UW NMR experiments is beyond the scope of the current work, and further work on this issue is currently underway in our laboratory).

Since we cannot resort to simply using the highest ^{1}H decoupling fields possible as the sole means of acquiring higher quality ^{14}N SSNMR spectra, alternatives must be considered. Hence, in this section, we discuss several techniques that improve the efficiency of ^{14}N UW SSNMR experiments by increasing the S/N ratio and the spectral quality through the combined use of high-power ^{1}H decoupling, deuteration, broadband cross-polarization (BCP), and VT NMR.

3.4.2.1 ^{1}H decoupling and deuteration

By using CW ^{1}H decoupling to attenuate or eliminate the impact of relaxation arising from heteronuclear ^{14}N-^{1}H dipolar coupling during the acquisition of a ^{14}N FID, the number of spin echoes that form (and thus the resulting S/N of the Fourier-transformed spectrum) can be controlled (**Figure B4**). As described in previous works, the more spin echoes that compose a CPMG echo train, the higher the S/N of the resulting spectrum.[69–71] An alternative to using high-power ^{1}H decoupling to average heteronuclear ^{14}N-^{1}H dipolar couplings is to recrystallize the amino acids from an exchanging deuterated solvent (*e.g.,* D_2O). Exchanging nitrogen-bound protons for deuterons can decrease or eliminate (depending on the degree of exchange) the contribution of the ^{14}N-^{1}H dipolar coupling mechanism to the T_2 relaxation of the ^{14}N

nucleus,[14] since the gyromagnetic ratio of ^{2}H is significantly lower than that of ^{1}H ($\gamma(^{2}H)$ = 4.1 x 10^{7} rad T^{-1} s^{-1} *vs.* $\gamma(^{1}H)$ = 26.7 x 10^{7} rad T^{-1} s^{-1}). We note that due to the non-trivial synthesis of β-glycine, the instability of its solid form, and several failed attempts to deuterate the sample, the effects of deuterium labelling were not studied for the β-glycine polymorph. In addition, all of our attempts to recrystallize α-glycine from D_2O (*l*) have resulted in the formation of γ-glycine-ND_3^+.

Figure 3.3 provides a comparison of the ^{14}N powder patterns of γ-glycine-ND_3^+ and its non-deuterated counterpart, γ-glycine. The powder pattern of γ-glycine-ND_3^+ (**Figure 3.3A**) has the appearance of a nearly ideal ^{14}N SSNMR spectrum, with discontinuities that are very well-defined, especially in the "foot" region. The corresponding analytical simulation is the red trace in **Figure 3.3**. The quadrupolar parameters are C_Q = 1.19 ± 0.02 MHz and η_Q = 0.37 ± 0.02 and have smaller uncertainties compared to those of the non-deuterated sample of γ-glycine (*vide supra*). We note that even with deuteration, proton decoupling is still required to obtain high quality spectra, since other nearby protons (which do not exchange) can impact the transverse relaxation and therefore reduce the number of spin echoes that form in the CPMG echo train. Measurement of the $T_2^{eff}(^{14}N)$ constant in the sample of γ-glycine-ND_3^+ yielded 24 ± 3 ms, which within the level of uncertainty is equal to the T_2^{eff} value of the non-deuterated γ-glycine polymorph (T_2^{eff} = 25 ± 4 ms). As a result, the overall S/N of the spectrum is comparable to that observed for γ-glycine. The comparable $T_2^{eff}(^{14}N)$ value for the deuterated sample is a puzzling result, since it contradicts previous findings which show that deuteration of a nitrogen environment often increases the $T_2^{eff}(^{14}N)$ time constant.[14,16,40] It is possible that ^{14}N-^{1}H dipolar coupling involving the

proximate CH_2 protons makes a major contribution to the $T_2^{eff}(^{14}N)$; this could be due to the rapid rotational motion of the NH_3 group (*vide infra*). However, this is unlikely because comparison of ^{14}N SSNMR sub-spectra for α-glycine and α-glycine-D_5 reveals that their $T_2^{eff}(^{14}N)$ values are the same within uncertainty (**Figure 3.4**). Interestingly, no ringing was observed in the FID of γ-glycine-ND_3^+, unlike the corresponding FID of non-deuterated γ-glycine (**Figure B2**). We are currently investigating this phenomenon in greater detail.

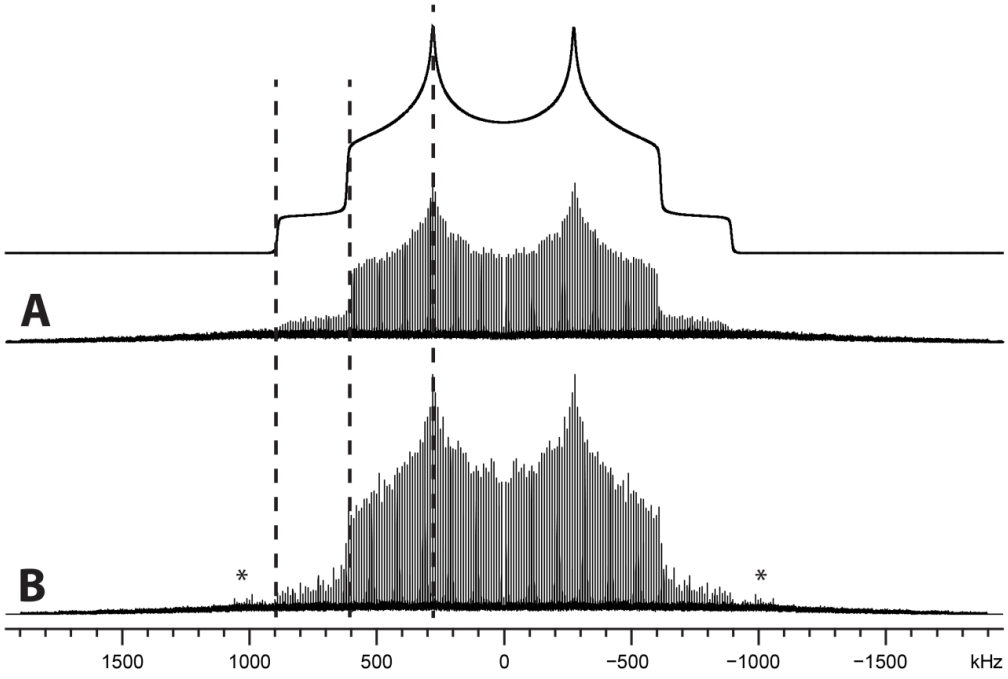

Figure 3.3. ^{14}N WURST-CPMG powder patterns of (A) γ-glycine-ND_3^+ and (B) γ-glycine-NH_3^+ and corresponding analytical simulation (red trace, C_Q = 1.19 ± 0.02 MHz and η_Q = 0.38 ± 0.02). The vertical dashed lines mark the positions of the discontinuities (horns, shoulders and feet) of the γ-glycine-ND_3^+ powder pattern. * ^{14}N NMR signal arising from the piezoelectric response of the sample due to RF irradiation.

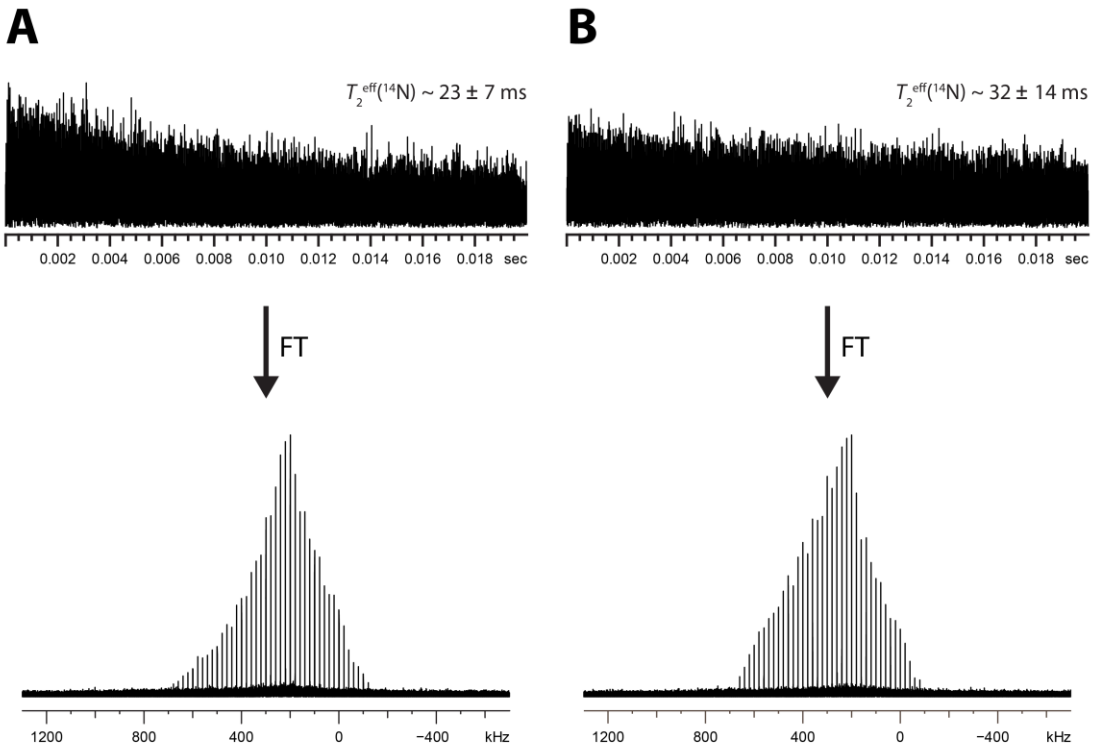

Figure 3.4. Comparison of ^{14}N FIDs and corresponding Fourier-transformed sub-spectra for (a) α-glycine and (b) α-glycine-d_5, acquired with the same experimental parameters. The $T_2^{eff}(^{14}N)$ values for α-glycine and α-glycine-d_5 were measured to be 23 ± 7 ms and 32 ± 14 ms, respectively. The high degree of uncertainty in the measurement of $T_2^{eff}(^{14}N)$ is the result of the low intensity of the individual spin-echoes in the FIDs.

3.4.2.2 Broadband Cross-Polarization (BCP)

Our group has recently published work demonstrating the ability of using cross-polarization over a broad frequency range.[40,51,72] The use of the BRoadband Adiabatic INversion Cross-Polarization (BRAIN-CP) pulse sequence provides all the advantages of regular CP experiments (*i.e.*, enhancement based on the ratio of the γ's, recycle delays that depend on the $T_1(^1H)$ constants, etc.), as well as the added benefit of a broad CP excitation profile, all of which lead to decreased experimental times. The benefits of BRAIN-CP for ^{14}N SSNMR have previously been demonstrated by our group with the

use of a sample of α-glycine and several pharmaceutical compounds.[40] In fact, α-glycine is an excellent ^{14}N NMR setup standard for both direct-excitation and CP experiments. We have investigated the effectiveness of BRAIN-CP for the acquisition of ^{14}N SSNMR spectra of β-glycine, γ-glycine and glycine HCl.

Figure 3.5A shows a comparison of individual sub-spectra of glycine HCl acquired with WURST-CPMG and BRAIN-CP/WURST-CPMG at the same transmitter frequency. For brevity, these direct-excitation and broadband cross-polarization experiments will be referred to as DE and BCP, respectively. The DE and BCP experiments were conducted with almost identical parameters, including the overall number of scans. The BCP sub-spectrum acquired at a transmitter frequency of 29.225 MHz has approximately 6.5 times the S/N of the corresponding DE sub-spectrum. **Figure 3.5B** shows a comparison of the ^{14}N powder patterns of glycine HCl acquired with both BCP and DE. It is evident that under the same experimental conditions, the signal intensity of the BCP spectrum is far better than that of the DE spectrum; in particular, the outer "foot" discontinuity is clearly visible in the BCP spectrum.

BCP experiments were also attempted on both β- and γ-glycine; however, they were unsuccessful. This could be due to several factors including poor CP transfer efficiency, short $T_{1\rho}$'s (both ^{1}H and ^{14}N) of the samples, efficient cross-relaxation, etc. We attempted ^{1}H-^{14}N BCP experiments on γ-glycine at a higher temperature (*i.e.*, T_{max} = 92 °C, *vide infra*) in order to see if the CP process differs with changes in the dynamical motions of the NH_3 moieties; however, spectra of adequate S/N could still not be obtained. It is clearly of interest to continue investigating the dependence of the CP mechanism on ^{1}H-^{14}N cross relaxation and the motion of the RNH_3^+ moieties (*vide infra*),

since this may enable the use of BCP experiments for a wider range of samples and different modes of polymorph differentiation; however, detailed investigation of these factors is beyond the scope of the current work.

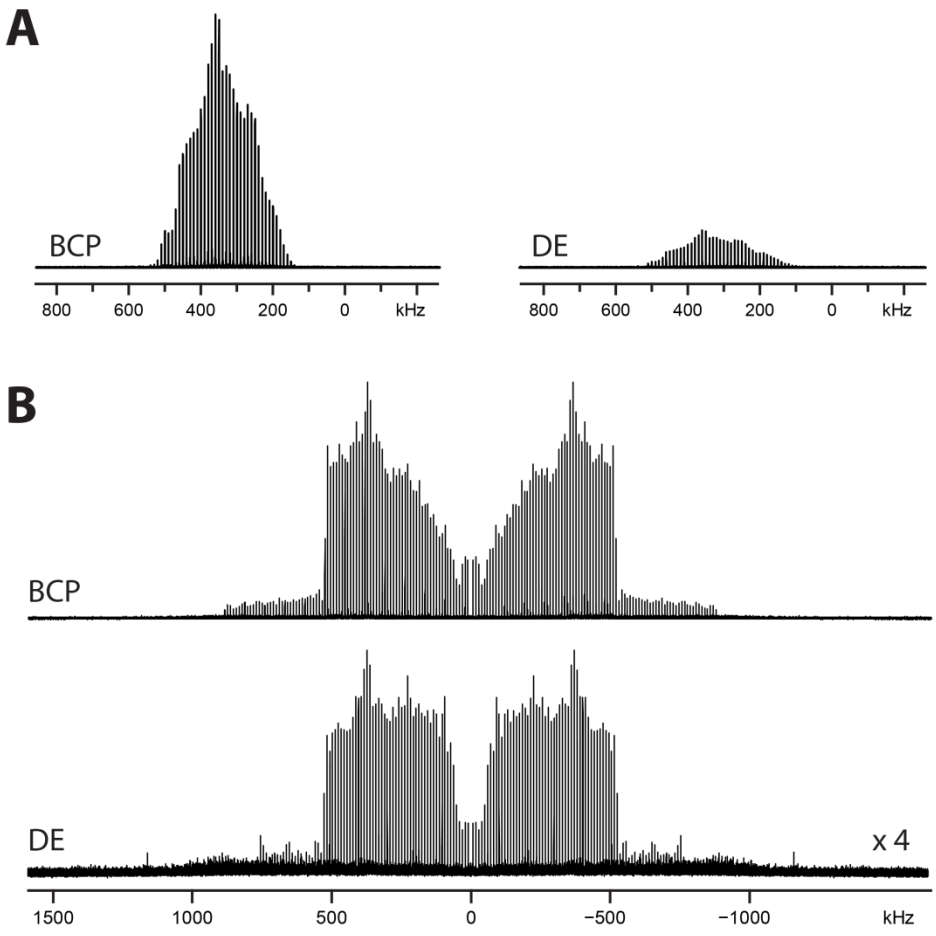

Figure 3.5. (A) Comparison of the individual sub-spectra of glycine HCl acquired with BCP and DE methods with similar acquisition parameters. The average enhancement in S/N is approximately 6.6 times for the BCP spectrum (**Table B8**). (B) Comparison of the entire ^{14}N SSNMR spectra of glycine HCl acquired with BCP and DE methods. Vertical dashed lines mark the edges of the "foot" discontinuity.

In cases where BCP experiments can be conducted and the CP conditions are favourable, high S/N spectra may be acquired in shorter experimental times than their DE counterparts. A second advantage of using BRAIN-CP to acquire ^{14}N SSNMR powder patterns is that due to the added S/N that results in many cases, ^{14}N powder patterns with high C_Q values (*i.e.*, C_Q > 1.6 MHz) may now be acquired at moderate magnetic field strengths (*i.e.*, 9.4 T), a practice which, to the best of our knowledge, has been limited to ultrahigh-field NMR (*i.e.*, 21.1 T),[15,16] ^{14}N overtone spectroscopy,[73–75] single-crystal NMR,[76] and NQR.[77–83]

3.4.2.3 Variable-temperature (VT) ^{14}N NMR experiments

One of the factors that influences the sensitivity of NMR experiments is temperature. The most obvious influence of temperature is the enhancement of S/N which is generally observed for spectra acquired at lower temperatures, due to modifications of the spin populations described by the Boltzmann equation. However, motional effects on relaxation can have a major impact on S/N and resolution. For instance, it has been shown that for a methyl group that undergoes rotational motions (*i.e.*, three-fold rotation) in the solid state, the relaxation characteristics of the ^{1}H and ^{13}C nuclides (*i.e.*, T_1's and T_2's) can be altered by changing the temperature.[84] Exploiting temperature-dependent relaxation characteristics can result in decreased experimental times and/or lend insight into dynamical processes at the molecular level.[47,65,85–88] In this section, we briefly discuss the effect of variation in temperature on the acquisition of ^{14}N SSNMR powder patterns; this was achieved with a series of sub-spectra of α-glycine, γ-

glycine, and glycine HCl acquired at temperatures ranging from −88 °C to +181 °C. We note that due to the unstable nature of β-glycine, VT ^{14}N SSNMR experiments were not attempted for this sample.

For α-glycine (**Figure 3.6A**), we observed that the ^{14}N sub-spectrum with maximum S/N occurs at a sample temperature of *ca*. 20 °C, with the S/N decreasing as the temperature is ramped away from 20 °C in either direction. For the rest of our discussion, we introduce the variable T_{max} to denote the *sample temperature at which we observe the maximum S/N ratio*. For γ-glycine (**Figure 3.6B**), we note that $T_{max} \approx 92$ °C, and the S/N appears to be roughly 25% higher than the room temperature (*i.e.*, 20 °C) sub-spectrum. For glycine HCl (**Figure 3.6C**), we found that $T_{max} \approx 2$ °C. Since the S/N of ^{14}N WCPMG SSNMR powder patterns is largely dependent on the $T_2^{eff}(^{14}N)$, it is clear that the variation of temperature serves to shorten or lengthen $T_2^{eff}(^{14}N)$, resulting in fewer or more spin echoes, respectively, in the CPMG echo train (**Figure B5**). The behaviour of the ^{14}N echo trains throughout the temperature range suggests that the ^{14}N-^{1}H dipolar coupling mechanism is likely a combination of two components: a static component (secular) and a dynamic component (non-secular). Using α-glycine as an example (**Figure 3.6A**), as the temperature is decreased below T_{max} = 20 °C (*e.g.*, T = −43 °C), the rotational rate of the NH_3 group is decreased and the secular component dominates the relaxation. Conversely, if the temperature is increased above T_{max} (*e.g.*, T = 92 °C), the NH_3 group rotates at a more rapid rate and the non-secular component dominates the relaxation. At T_{max}, neither relaxation mechanism is overly dominant, resulting in the most inefficient (longest) $T_2^{eff}(^{14}N)$ relaxation, and accordingly, the highest S/N in the corresponding CPMG spectra.

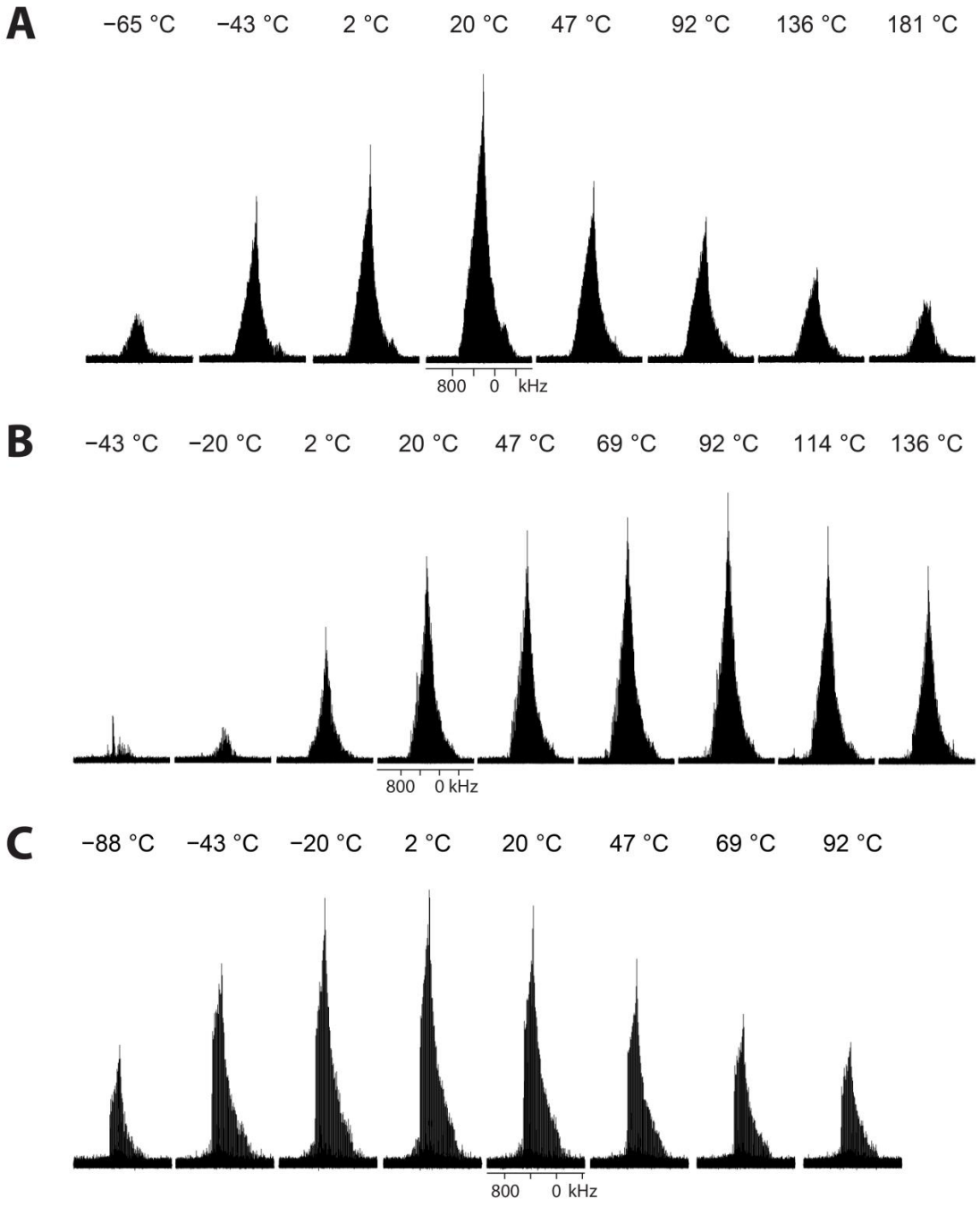

Figure 3.5. Temperature dependence of ^{14}N SSNMR signal intensity in the temperature range of −88 to +181 °C for (A) α-glycine, (B) γ-glycine, and (C) glycine HCl.

The rotational motion of NH_3 groups of solid amino acids has been investigated with both ^{1}H and ^{2}H SSNMR; in some cases, it is possible to calculate the rotational activation barriers for this motion based on NMR measurements.[43,66,68] The rotational motion is described as a three-fold-jump; the barrier to this rotation is given by the Arrhenius equation for a single-energy activation model:[87]

$$\tau_c = \tau_o e^{\left(\frac{E_A}{RT}\right)} \quad [3.1]$$

where τ_c is the correlation time, τ_o is the pre-exponential factor (infinite-temperature correlation time), E_A is the rotational barrier energy, R is the gas constant, and T is the temperature. The rotational barrier for α-glycine has been previously calculated to be 21.7 kJ mol^{-1},[10] while the rotational barrier for γ-glycine has been measured as 28.6 kJ mol^{-1}.[12] Based on these known activation energies and a τ_o value which is equal to 0.7×10^{-14} s,[10,12] the correlation times, τ_c, at room temperature (*i.e.*, 20 °C) are calculated to be 0.05 ns and 0.87 ns for α- and γ-glycine, respectively. The correlation times at T_{max} for α- and γ-glycine are calculated to be 0.05 ns and 0.08 ns, respectively. Thus, it would appear that at T_{max}, the correlation times for the two samples become similar, further suggesting that the rate at which the NH_3 group is rotating causes variation in the $T_2^{eff}(^{14}N)$.

To the best of our knowledge, the NH_3 rotational barrier of glycine HCl has not been reported in the literature. From our ^{14}N VT SSNMR experiments, with the use of finer temperature steps in the range of −16 °C to 20 °C (**Figure B6**), we have observed that T_{max} is approximately −11 °C (unlike the 2 °C which we observed with a coarser temperature increment, **Figure 3.5C**). By assuming that the correlation time of the NH_3 rotation would have to be similar, or equivalent, to that of α-glycine (*i.e.*, τ_c = 0.05 ns),

and keeping τ_o equivalent to that of α-glycine ($\tau_o = 0.7 \times 10^{-14}$ s for α-glycine and γ-glycine),[10,12] the rotational barrier for the NH_3 group in glycine HCl is calculated to be 19.4 kJ mol^{-1}.

Full ^{14}N SSNMR spectra of both α-glycine and γ-glycine were acquired at room temperature (*i.e.*, 20 °C) as well as an alternate temperature (*i.e.*, −43 and 92 °C for α-glycine and γ-glycine, respectively) and the quadrupolar parameters remain unchanged (**Figure 3.6**). The invariance of the quadrupolar parameters within the investigated temperature range can be attributed to the geometry of the nitrogen moiety, as discussed above (again, we note that drastic changes in η_Q would be indicative of a major structural change and/or phase transition). While the measurement of $T_2^{eff}(^{14}N)$ constants gives insight into rotational barriers and rates of motion, it may also serve to enable

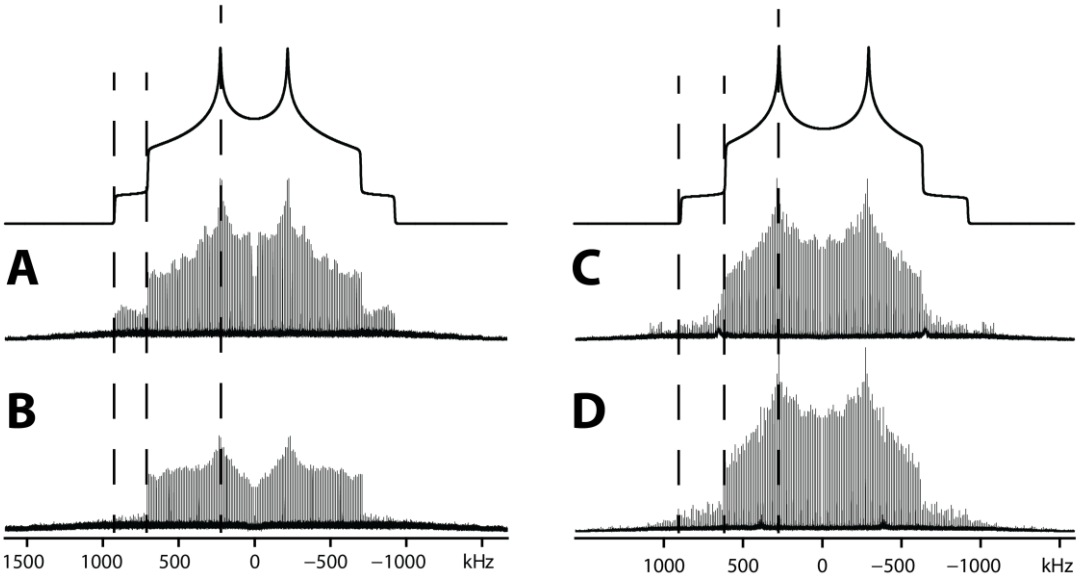

Figure 3.6. ^{14}N NMR powder patterns of α-glycine at (A) 20 °C and (B) −43 °C, and corresponding analytical simulation (C_Q = 1.19 ± 0.02 MHz and η_Q = 0.52 ± 0.02). Spectra of γ-glycine at (C) 20 °C and (D) 92 °C and corresponding analytical simulation (C_Q = 1.19 ± 0.04 MHz and η_Q = 0.38 ± 0.04). Relative positions of the discontinuities are shown by vertical dashed lines. * ^{14}N NMR signal arising from piezoelectric response of sample due to rf irradiation.

differentiation of subtly different polymorphic forms, or perhaps the discovery of new polymorphs, on the basis of disparate $T_2^{eff}(^{14}N)$ constants over a wide range of temperatures.

3.5 Conclusions

In this work, we have demonstrated the effectiveness of ^{14}N SSNMR for differentiating between polymorphic forms of glycine, as well as its HCl salt derivative. Differentiation is achieved by determining and comparing the quadrupolar parameters, C_Q and η_Q, without the need for chemical shift information. We note that differentiating the various forms of glycine can be achieved by comparing not only their respective quadrupolar parameters, but also by comparing their $T_2^{eff}(^{14}N)$ constants. Since this methodology could be used for a wide range of organic solids which feature RNH_3 moieties, including solids which may be disordered and unamenable to characterization via X-ray methods, we have also discussed several methods for improving the acquisition of ^{14}N SSNMR powder patterns. High-power ^{1}H decoupling is an effective means of increasing S/N; however, the limit to what power can be used depends upon the hardware available and the nature of the samples being investigated. Hence, ^{1}H decoupling is best utilized with any or a combination of RNH_3 group deuteration and variable temperature acquisition (for minimization of $T_2^{eff}(^{14}N)$ and maximization of S/N), as well as broadband CP (where appropriate). We have also briefly highlighted the dynamical motion of the NH_3 group and its variation with temperature, and how this impacts S/N in ^{14}N CPMG and ^{1}H-^{14}N CP NMR spectra. More work is needed to clearly elucidate the relaxation mechanisms at play in both of these cases. In addition, we have utilized plane-

wave DFT calculations to accurately predict the ^{14}N EFG tensor components by taking into account the periodic nature exhibited by crystals.

We hope that this work inspires other researchers to utilize ^{14}N SSNMR as an additional tool in their spectroscopic toolbox for the study of nitrogen-containing systems of varying complexity. One such area that has immense potential that we are currently investigating is polymorph differentiation of nitrogen-containing HCl pharmaceutical compounds. It is clear that the sets of different secular and non-secular ^{14}N NMR parameters that can be measured with relatively ease should be very useful for polymorph recognition and discovery, the identification of impurity phases or phase transitions, and perhaps even the differentiation of distinct chemical forms of both crystalline and amorphous pharmaceuticals, including free-base organic molecules, organic salts and co-crystalline species.

3.6 Bibliography

(1) Drebushchak, V. A.; Kovalevskaya, Y. A.; Paukov, I. E.; Boldyreva, E. V. *J. Therm. Anal. Calorim.* **2003**, *74*, 109–120.

(2) Kozhin, V. M. *Kristallografiya* **1978**, *23*, 1211–1215.

(3) Power, L. F.; Turner, K. E.; Moore, F. H. *Acta Crystallogr. Sect. B Struct. Crystallogr. Cryst. Chem.* **1976**, *32*, 11–16.

(4) Drebushchak, T. N.; Boldyreva, E. V.; Shutova, E. S. *Acta Crystallogr. Sect. E Struct. Reports Online* **2002**, *58*, o634–o636.

(5) Iitaka, Y. *Acta Crystallogr.* **1961**, *14*, 1–10.

(6) Boldyreva, E. V.; Drebushchak, V. A.; Drebushchak, T. N.; Paukov, I. E.; Kovalevskaya, Y. A.; Shutova, E. S. *J. Therm. Anal. Calorim.* **2003**, *73*, 409–418.

(7) Boldyreva, E. V.; Drebushchak, V. A.; Drebushchak, T. N.; Paukov, I. E.; Kovalevskaya, Y. A.; Shutova, E. S. *J. Therm. Anal. Calorim.* **2003**, *73*, 419–428.

(8) Taylor, R. E. *Concepts Magn. Reson. Part A Bridg. Educ. Res.* **2004**, *22*, 79–89.

(9) Drebushchak, I. V.; Kozlova, S. G.; Semenov, A. R.; Boldyreva, E. V. *J. Mol. Struct.* **2008**, *885*, 176–178.

(10) Taylor, R. E.; Dybowski, C. *J. Mol. Struct.* **2008**, *889*, 376–382.

(11) Yamada, K.; Shimizu, T.; Yamazaki, T.; Sato, A. *Chem. Lett.* **2008**, *37*, 472–473.

(12) Andrew, E. R.; Hinshaw, W. S.; Hutchins, M. G.; Sjöblom, R. O. I. *Mol. Phys.* **1976**, *31*, 1479–1488.

(13) Giavani, T.; Bildsøe, H.; Skibsted, J.; Jakobsen, H. J. *J. Magn. Reson.* **2004**, *166*, 262–272.

(14) O'Dell, L. A.; Schurko, R. W. *Phys. Chem. Chem. Phys.* **2009**, *11*, 7069–7077.

(15) O'Dell, L. A.; Schurko, R. W.; Harris, K. J.; Autschbach, J.; Ratcliffe, C. I. *J. Am. Chem. Soc.* **2011**, *133*, 527–546.

(16) O'Dell, L. A. *Prog. Nucl. Magn. Reson. Spectrosc.* **2011**, *59*, 295–318.

(17) Dos, A.; Schimming, V.; Tosoni, S.; Limbach, H.-H. *J. Phys. Chem. B* **2008**, *112*, 15604–15615.

(18) Apperley, D. C.; Markwell, A. F.; Harris, R. K.; Hodgkinson, P. *Magn. Reson. Chem.* **2012**, *50*, 680–690.

(19) Schmidt, H. L. F.; Sperling, L. J.; Gao, Y. G.; Wylie, B. J.; Boettcher, J. M.; Wilson, S. R.; Rienstra, C. M. *J. Phys. Chem. B* **2007**, *111*, 14362–14369.

(20) Li, S.; Hong, M. *J. Am. Chem. Soc.* **2011**, *133*, 1534–1544.

(21) Kolehmainen, E.; Ośmiałowski, B. *Int. Rev. Phys. Chem.* **2012**, *31*, 1–63.

(22) Kimura, H.; Nakamura, K.; Eguchi, A.; Sugisawa, H.; Deguchi, K.; Ebisawa, K.; Suzuki, E. I.; Shoji, A. *J. Mol. Struct.* **1998**, *447*, 247–255.

(23) Lopes, I.; Piao, L.; Stievano, L.; Lambert, J. F. *J. Phys. Chem. C* **2009**, *113*, 18163–18172.

(24) Ben Shir, I.; Kababya, S.; Schmidt, A. *J. Phys. Chem. C* **2012**, *116*, 9691–9702.

(25) Pyykkö, P. *Mol. Phys.* **2001**, *99*, 1617–1629.

(26) Harris, R. K.; Becker, E. D.; Cabral de Menezes, S. M.; Goodfellow, R.; Granger, P. *Solid State Nucl. Magn. Reson.* **2002**, *22*, 458–483.

(27) Marburger, S. P.; Fung, B. M.; Khitrin, A. K. *J. Magn. Reson.* **2002**, *154*, 205–209.

(28) Schurko, R. W. *Acc. Chem. Res.* **2013**, *46*, 1985–1995.

(29) Giavani, T.; Johannsen, K.; Jacobsen, C. J. H.; Blom, N.; Bildsøe, H.; Skibsted, J.; Jakobsen, H. J. *Solid State Nucl. Magn. Reson.* **2003**, *24*, 218–235.

(30) Hove, A. R.; Bildsøe, H.; Skibsted, J.; Brorson, M.; Jakobsen, H. J. *Inorg. Chem.* **2006**, *45*, 10873–10881.

(31) Jakobsen, H. J.; Hove, A. R.; Hazell, R. G.; Bildsøe, H.; Skibsted, J. *Magn. Reson. Chem.* **2006**, *44*, 348–356.

(32) O'Dell, L. A.; Harris, K. J.; Schurko, R. W. *J. Magn. Reson.* **2010**, *203*, 156–166.

(33) Rothgeb, T. M.; Oldfield, E. *J. Biol. Chem.* **1981**, *256*, 6004–6009.

(34) Kupče, Ē.; Freeman, R. *J. Magn. Reson. Ser. A* **1995**, *115*, 273–276.

(35) O'Dell, L. A. *Solid State Nucl. Magn. Reson.* **2013**, *55-56*, 28–41.

(36) Meiboom, S.; Gill, D. *Rev. Sci. Instrum.* **1958**, *29*, 688.

(37) Massiot, D.; Farnan, I.; Gautier, N.; Trumeau, D.; Trokiner, A.; Coutures, J. P. *Solid State Nucl. Magn. Reson.* **1995**, *4*, 241–248.

(38) Tang, J. A.; Masuda, J. D.; Boyle, T. J.; Schurko, R. W. *ChemPhysChem* **2006**, *7*, 117–130.

(39) O'Dell, L. A.; Rossini, A. J.; Schurko, R. W. *Chem. Phys. Lett.* **2009**, *468*, 330–335.

(40) Harris, K. J.; Veinberg, S. L.; Mireault, C. R.; Lupulescu, A.; Frydman, L.; Schurko, R. W. *Chem. Eur. J.* **2013**, *19*, 16469–16475.

(41) Andersson, L.-O.; Gourdji, M.; Guibé, L.; Proctor, W. G. *C. R. Acad. Sci.* **1968**,

267, 803.

(42) Haberkorn. R. A.; Stark, R. E.; Van Willigen, H.; Griffin, R. G. *J. Am. Chem. Soc.* **1981**, *103*, 2534–2539.

(43) Aliev, A. E.; Mann, S. E.; Rahman, A. S.; McMillan, P. F.; Corà, F.; Iuga, D.; Hughes, C. E.; Harris, K. D. M. *J. Phys. Chem. A* **2011**, *115*, 12201–12211.

(44) Nolze, G.; Kraus, W. *Powder Diffr.* **1998**, *13*, 256–259.

(45) Bertani, P.; Raya, J.; Bechinger, B. *Solid State Nucl. Magn. Reson.* **2014**, *61-62*, 15–18.

(46) O'Dell, L. A.; Schurko, R. W. *Chem. Phys. Lett.* **2008**, *464*, 97–102.

(47) O'Dell, L. A.; Schurko, R. W. *J. Am. Chem. Soc.* **2009**, *131*, 6658–6659.

(48) Bhattacharyya, R.; Frydman, L. *J. Chem. Phys.* **2007**, *127*, 1–8.

(49) Eichele, K. WSolids1 — Solid State NMR Simulations, 2013.

(50) Bielecki, A.; Burum, D. P. *J. Magn. Reson. Ser. A* **1995**, *116*, 215–220.

(51) Harris, K. J.; Lupulescu, A.; Lucier, B. E. G.; Frydman, L.; Schurko, R. W. *J. Magn. Reson.* **2012**, *224*, 38–47.

(52) Kvick, Å.; Canning, W. M.; Koetzle, T. F.; Williams, G. J. B. *Acta Crystallogr. Sect. B-Structural Sci.* **1980**, *36*, 115–120.

(53) Al-Karaghouli, A. R.; Cole, F. E.; Lehmann, M. S.; Miskell, C. F.; Verbist, J. J.; Koetzle, T. F. *J. Chem. Phys.* **1975**, *63*, 1360.

(54) Iitaka, Y. *Acta Crystallogr.* **1958**, *11*, 225–226.

(55) Hughes, D. .; Pandey, L. *J. Magn. Reson.* **1984**, *56*, 428–442.

(56) Man, P. P. *Solid State Nucl. Magn. Reson.* **1992**, *1*, 149–158.

(57) Lemanov, V. V.; Popov, S. N. *Phys. Solid State* **1998**, *40*, 991–994.

(58) Ashok Kumar, R.; Ezhil Vizhi, R.; Vijayan, N.; Rajan Babu, D. *Phys. B Condens. Matter* **2011**, *406*, 2594–2600.

(59) Milman, V.; Winkler, B.; White, J.; Pickard, C. J.; Payne, M. C.; Akhmatskaya, E. V; Nobes, R. H. *Int. J. Quantum Chem.* **2000**, *77*, 895–910.

(60) Strohmeier, M.; Stueber, D.; Grant, D. M. *J. Phys. Chem. A* **2003**, *107*, 7629–7642.

(61) Gervais, C.; Dupree, R.; Pike, K. J.; Bonhomme, C.; Profeta, M.; Pickard, C. J.; Mauri, F. *J. Phys. Chem. A* **2005**, *109*, 6960–6969.

(62) Harris, R. K.; Olivieri, A. C. *Prog. Nucl. Magn. Reson. Spectrosc.* **1992**, *24*, 435–456.

(63) Edmonds, D. T.; Hunt, M. J.; Mackay, A. L. *J. Magn. Reson.* **1973**, *9*, 66–74.

(64) Edmonds, D. T.; Summers, C. P. *J. Magn. Reson.* **1973**, *12*, 134–142.

(65) O'Dell, L. A.; Ratcliffe, C. I. *Chem. Commun.* **2010**, *46*, 6774–6776.

(66) Andrew, E. R.; Hinshaw, W. S.; Hutchins, M. G. *J. Magn. Reson.* **1974**, *15*, 196–200.

(67) Andrew, E. R.; Hinshaw, W. S.; Hutchins, M. G.; Sjöblom, R. O. I. *Mol. Phys.* **1976**, *32*, 795–806.

(68) Andrew, E. R.; Hinshaw, W. S.; Hutchins, M. G.; Sjöblom, R. O. I. *Mol. Phys.* **1977**, *34*, 1695–1706.

(69) Schurko, R. W.; Hung, I.; Widdifield, C. M. *Chem. Phys. Lett.* **2003**, *379*, 1–10.

(70) Hung, I.; Gan, Z. *J. Magn. Reson.* **2010**, *204*, 256–265.

(71) Dey, K. K.; Ash, J. T.; Trease, N. M.; Grandinetti, P. J. *J. Chem. Phys.* **2010**, *133*, 054501.

(72) Lucier, B. E. G.; Johnston, K. E.; Xu, W.; Hanson, J. C.; Senanayake, S. D.; Yao, S.; Bourassa, M. W.; Srebro, M.; Autschbach, J.; Schurko, R. W. *J. Am. Chem. Soc.* **2014**, *136*, 1333–1351.

(73) O'Dell, L. A.; He, R.; Pandohee, J. *CrystEngComm* **2013**, *15*, 8657.

(74) O'Dell, L. A.; Ratcliffe, C. I. *Chem. Phys. Lett.* **2011**, *514*, 168–173.

(75) Rossini, A. J.; Emsley, L.; O'Dell, L. A. *Phys. Chem. Chem. Phys.* **2014**, *16*, 12890–12899.

(76) Stark, R. E.; Haberkorn. R. A.; Griffin, R. G. *J. Chem. Phys.* **1978**, *68*, 1996.

(77) Blinc, R.; Mali, M.; Osredkar, R.; Prelesnik, A.; Seliger, J.; Zupančič, I.; Ehrenberg, L. *J. Chem. Phys.* **1972**, *57*, 5087–5093.

(78) Werner-Zwanziger, U.; Ziegeweid, M.; Black, B.; Pines, A. *Z. Naturforsch* **1994**, *49a*, 1188–1192.

(79) Balchin, E.; Malcolme-Lawes, D. J.; Poplett, I. J. F.; Rowe, M. D.; Smith, J. A. S.; Pearce, G. E. S.; Wren, S. A. C. *Anal. Chem.* **2005**, *77*, 3925–3930.

(80) Shinohara, J.; Kobayashi, K.; Sato-Akaba, H.; Itozaki, H. *Solid State Nucl. Magn. Reson.* **2011**, *40*, 121–125.

(81) Latosińska, J. N.; Latosińska, M.; Seliger, J.; Žagar, V. *Eur. J. Pharm. Sci.* **2012**, *47*, 97–107.

(82) Seliger, J.; Žagar, V. *Magn. Reson. Chem.* **2008**, *46*, 58–62.

(83) Seliger, J.; Žagar, V. *J. Phys. Chem. A* **2010**, *114*, 12083–12087.

(84) Horsewill, A. J. *Prog. Nucl. Magn. Reson. Spectrosc.* **1999**, *35*, 359–389.

(85) Schmidt-Rohr, K.; Kulik, A. *Macromolecules* **1994**, *27*, 4733–4745.

(86) Vukotic, V. N.; Harris, K. J.; Zhu, K.; Schurko, R. W.; Loeb, S. J. *Nat. Chem.* **2012**, *4*, 456–460.

(87) Kinsey, R. A.; Kintanar, A.; Oldfield, E. *J. Biol. Chem.* **1981**, *256*, 9028–9036.

(88) Nicholson, L. K.; Kay, L. E.; Baldisseri, D. M.; Arango, J.; Young, P. E.; Bax, A.; Torchia, D. A. *Biochemistry* **1992**, *31*, 5253–5263.

Chapter 4: Rapid Acquisition of ^{14}N Solid-State NMR Spectra Using Broadband Cross Polarization

4.1 Overview

Nitrogen is an element of utmost importance in chemistry, biology and materials science. Of its two NMR-active isotopes, ^{14}N and ^{15}N, solid-state NMR (SSNMR) experiments are rarely conducted upon the former, due to its low gyromagnetic ratio (γ) and broad powder patterns arising from first-order quadrupolar interactions. In this work, we propose a methodology for the rapid acquisition of high quality ^{14}N SSNMR spectra that is easy to implement, and can be used for a variety of nitrogen-containing systems. We demonstrate that it is possible to dramatically enhance ^{14}N NMR signal in spectra of stationary, polycrystalline samples (i.e., amino acids and active pharmaceutical ingredients) via broadband cross polarization (CP) from abundant nuclei (i.e., ^{1}H). The **BR**oadband **A**diabatic **IN**version **C**ross-**P**olarization (**BRAIN-CP**) pulse sequence is combined with other elements for efficient acquisition of ultra-wideline SSNMR spectra, including wideband uniform-rate smooth-truncation (**WURST**) pulses for broadband refocusing, Carr-Purcell Meiboom-Gill (**CPMG**) echo trains for T_2-driven S/N enhancement, and frequency-stepped acquisitions. The feasibility of utilizing the BRAIN-CP/WURST-CPMG sequence is tested for ^{14}N, with special consideration given to (i) spin-locking integer spin nuclei while maintaining adiabatic polarization transfer, and (ii) the effects of broadband polarization transfer on the overlapping satellite transition patterns. The BRAIN-CP experiments are shown to provide increases in signal-to-noise ranging from four to ten times and reductions of experimental times from one to two orders of magnitude compared to analogous experiments where ^{14}N nuclei are

directly excited. Furthermore, patterns acquired with this method are generally more uniform than those acquired with direct excitation methods. We also discuss the proposed method and its potential for probing a variety of chemically distinct nitrogen environments.

4.2 Introduction

Nitrogen is of great importance in all areas of chemistry and biochemistry. Solid-state NMR (SSNMR) has been used to probe nitrogen sites for over fifty years, with the overwhelming majority of experiments being conducted upon the spin-½ ^{15}N nucleus. The low natural abundance and low gyromagnetic ratio of ^{15}N require, in almost every case, that samples be isotopically enriched to permit the acquisition of high quality spectra within reasonable time frames. There are very few ^{14}N (spin-1) SSNMR studies by comparison, owing to its even lower gyromagnetic ratio and nuclear quadrupole moment ($Q = 20.44 \times 10^{-21}$ m^2). In particular, this latter property of ^{14}N is troublesome for SSNMR experimentation, as the first-order quadrupolar interaction causes extreme broadening of ^{14}N SSNMR powder patterns in cases where an aspherical ground-state electronic environment causes a sizeable electric field gradient (EFG) at the ^{14}N nucleus.

A number of methods have been explored for the acquisition of ^{14}N SSNMR spectra, including direct observation of ^{14}N NMR signals from single crystals[1] and anisotropically oriented samples,[2,3] overtone ^{14}N NMR,[4–6] ^{14}N magic-angle spinning (MAS) NMR using probes with precisely tuned rotor angles[7,8] slow spinning and specialized pulse sequences,[9,10] or indirect detection.[11] However, due to requirements of such experiments on the nature of the sample, type of nitrogen environment or technical

difficulties with hardware or pulse sequences, none have become widely adopted. There has also been much effort put into the indirect observation of ^{14}N signals via spin-coupled spin-½ nuclei (e.g., ^{13}C).[11] For further details on direct excitation and detection of ^{14}N SSNMR spectra, we refer the reader to a recent thorough review on the subject.[12]

We have proposed a methodology for the acquisition of ultra-wideline (UW) SSNMR spectra that has been successful in examining both spin-½ and quadrupolar nuclei.[13,14] This methodology comprises three components: (i) stepping the transmitter in even increments across the breadth of the powder pattern and acquiring sub-spectra at each point (i.e., the variable offset cumulative spectrum (VOCS) or "piecewise" method, as outlined by the research groups of Massiot[15] and Frydman[16]), (ii) using CPMG echo trains for enhancing the S/N[17] (i.e., as described for half-integer spin quadrupolar nuclei by Larsen et al.),[18,19] and (iii) utilizing WURST (Wideband, Uniform Rate, and Smooth Truncation) pulses[20] for uniform excitation of broad powder patterns.[21] The WURST-CPMG pulse sequence has been demonstrated to work for a variety of spin-½[22,23] and quadrupolar nuclei,[13,14] and is effective for the rapid acquisition of ^{14}N UW SSNMR spectra for a variety of nitrogen-containing structural moieties.[24–26] The quadrupolar parameters extracted from the UW SSNMR spectra are extremely sensitive reporters on the local nitrogen environments via measurement of the ^{14}N EFG tensor.[27,28] The quadrupolar coupling constant, C_Q, is associated with the spherical symmetry of the ground-state electron density about the quadrupolar nucleus (i.e., as the spherical symmetry is reduced, the absolute magnitude of C_Q becomes larger). The asymmetry parameter, η_Q, describes the axial symmetry of the EFG tensor, and often, the degree of axial symmetry of the local bonding environment. For example, RNH_3^+ groups that are

involved in hydrogen bonding typically have moderate values of η_Q (e.g., ca. 0.35 – 0.65), whereas those that are not have values of η_Q near zero (i.e., ca. 0.0 – 0.2, axially or near-axially symmetric EFG tensors, with $V_{11} = V_{22}$ or $V_{11} \approx V_{22}$, respectively). It has also been demonstrated recently that ^{14}N powder patterns can be sensitive to molecular motion.[26] While the information content of ^{14}N SSNMR spectra is high, there are certain types of nitrogen sites that are not amenable to WURST-CPMG ^{14}N direct excitation (DE) experiments, most often due to lengthy longitudinal (T_1) or very short transverse (T_2) ^{14}N relaxation times, low nitrogen weight percentage or combinations of these factors.

One possible solution for dealing with the aforementioned long T_1 relaxation times and natural low-γ limitations is the utilization of cross polarization (CP),[29] which would (i) enhance the ^{14}N NMR signal via transfer of the larger polarization of abundant, high-γ nuclei such as protons and (ii) make the experiment reliant on the ^{1}H T_1's, which are often much shorter than the ^{14}N T_1's. ^{1}H-^{14}N CP experiments have been conducted almost exclusively on single crystals and oriented samples (both standard and overtone experiments),[4,30–34] with very few examples of applications to polycrystalline samples.[35,36] However, a major limitation in conducting CP experiments on UW SSNMR patterns is their narrow excitation bandwidths, which are restricted by the effective bandwidth of the ^{14}N spin-locking pulse and tolerances to offsets from the Hartmann-Hahn matching condition. Even when applying very high power levels (e.g., 300 W or more) to a probe with a 5 mm coil, we have found that typical excitation bandwidths on the ^{14}N channel range from 20 kHz to 50 kHz. The number of sub-spectra that must be acquired to map out ^{14}N powder patterns that are several hundred kHz to a couple of

MHz broad is therefore so large that the CP experiment is inefficient in comparison to the broadband DE WURST-CPMG experiment. NMR probes with smaller coil diameters would enable somewhat larger CP excitation bandwidths through higher spin-lock power levels, but the reduced sample volume and difficulties in satisfying the Hartmann-Hahn match over a large bandwidth prevents this approach from reaching the efficiency of the WURST-CPMG method. Furthermore, the high power levels utilized in conventional CP experiments must often be applied during the very long contact times expected for a low-γ nucleus like ^{14}N, which puts the probe at increased risk for arcing and potential damage.

Recently, we have demonstrated a method for using frequency-swept adiabatic inversion pulses for broadband CP to spin-½ nuclei with anisotropically broadened powder patterns.[37] Dubbed the BRAIN-CP (BRoadband Adiabatic INversion Cross Polarization) pulse sequence, it can be used with WURST-CPMG echo trains to produce broadband excitation and yield UW SSNMR spectra with very high S/N. A key advantage of this sequence, aside from its broadband excitation capability, is the ability to perform efficient CP at low radio frequency (rf) power levels, making this pulse sequence especially attractive for use in NMR experiments on low-γ nuclei such as ^{14}N.

Herein, we demonstrate a method for using the BRAIN-CP/WURST-CPMG pulse sequence (**Scheme 4.1**) for the acquisition of high-quality ^{14}N UW SSNMR spectra, and show results for four samples featuring different types of nitrogen structural motifs (RNH_3^+, aromatic R_3N^+, $RN_2H_2^+$ and R_3NH^+, **Scheme 4.2**), including one amino acid and three active pharmaceutical ingredients (APIs). The viability and practicality of the BRAIN-CP method is tested, and shown to yield spectra with S/N enhancements of four to ten times compared to those obtained via analogous DE ^{14}N WURST-CPMG

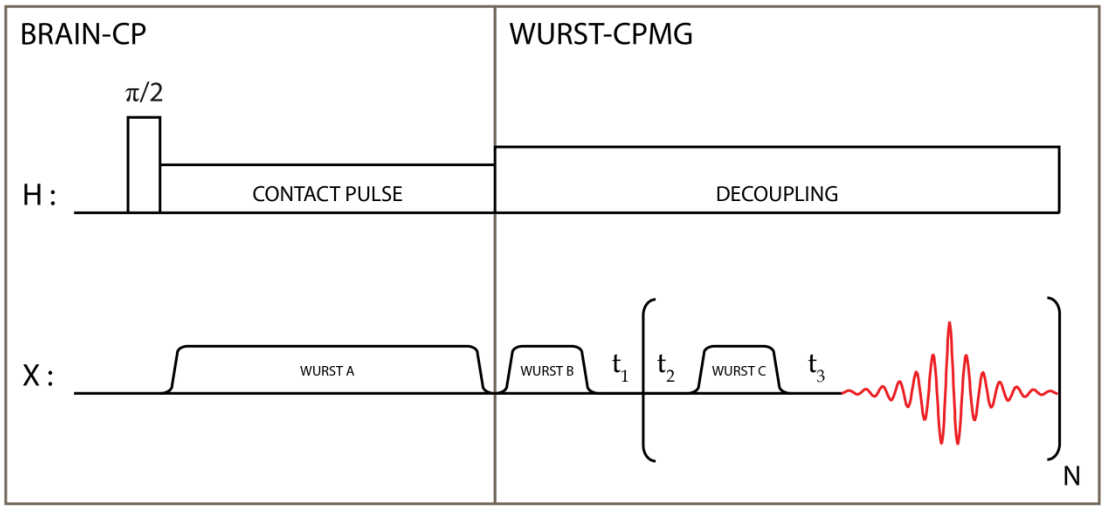

Scheme 4.1: The BRAIN-CP/WURST-CPMG pulse sequence. The left-hand portion of the sequence is BRAIN-CP, which features a frequency-swept WURST-A pulse that fulfills both polarization transfer conditions and an adiabatic storage of the ensuing polarization along –*z*, for a wide range of offsets. The right-hand portion of the sequence is WURST-CPMG, which uses the WURST-B pulse for rotation of the polarization into the transverse plane while WURST-C pulses are used for continued refocusing of the spin polarization.

experiments with identical CPMG parameters. Spectra acquired with DE and CP methods are compared for each sample, and show an exquisite sensitivity to the different nitrogen environments. Finally, we discuss the potential of this robust and widely-applicable CP experiment for opening up nitrogen SSNMR for routine use on organic, biological and inorganic samples through observation of 99.6% abundant ^{14}N nuclei, without the need for costly ^{15}N isotopic labeling.

4.3 Experimental

4.3.1 Chemicals

Samples (see **Scheme 4.2**) of α-glycine, trigonelline HCl and buflomedil HCl were purchased from Sigma Aldrich and used without further purification. Isoxsuprine

HCl was purchased from Sigma Aldrich and recrystallized from $D_2O(l)$. Samples were powdered and packed into shortened glass NMR tubes (outer diameter, o.d. = 5 mm).

4.3.2 NMR Spectroscopy

^{14}N SSNMR experiments were carried out on a Varian Infinity+ 400 MHz (9.4 T) spectrometer with $\nu_0(^{14}N)$ = 28.9 MHz, equipped with a Varian/Chemagnetics 5.0 mm

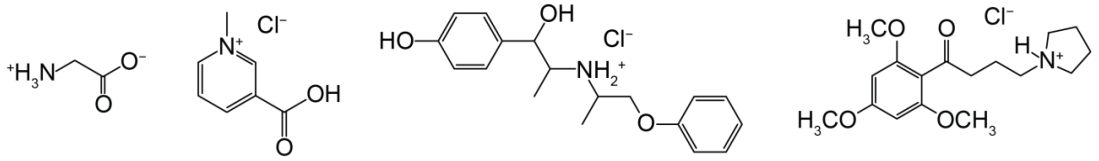

Scheme 4.2: The four nitrogen-containing compounds discussed in this work; from left to right: α-glycine, trigonelline HCl, isoxsuprine HCl and buflomedil HCl.

double-resonance non-spinning HX probe and a low-gamma tuning accessory. A sample of $NH_4Cl(s)$ was used to calibrate the rf power on the ^{14}N channel, as well as to reference the ^{14}N chemical shifts (δ_{iso} = 0 ppm); however, due to the enormous breadths of the ^{14}N patterns, chemical shifts are not reported, as they have very large uncertainties. This is because the breadths of the quadrupolar patterns discussed herein range from 800 kHz to well over 2 MHz; by comparison, the range of known nitrogen chemical shifts for organic compounds spans about 1300 ppm (ca. 3600 Hz with ν_0 = 28.12 MHz at 9.4 T), which represents less than 0.5% of the breadth of the narrowest ^{14}N patterns herein.

For experiments involving direct excitation of the ^{14}N nuclei, the WURST-CPMG pulse sequence[13] was applied using eight-step phase cycling and frequency-swept WURST-80 pulses[20] of equal amplitude and length for excitation and refocusing. ^{1}H-^{14}N

CP NMR experiments were conducted with the BRAIN-CP/WURST-CPMG pulse sequence (**Scheme 4.1**). The WURST-A pulse is the contact/inversion pulse, which is applied on the ^{14}N channel simultaneously with a conventional rectangular spin-lock pulse on the ^{1}H channel. The WURST-B and WURST-C pulses are utilized in the CPMG portion of the sequence for excitation and refocusing, respectively. 10 to 12.5 ms WURST-80 pulses with an rf field of 22 kHz were swept over 350 to 500 kHz in a linear fashion for implementing the CP portion of the experiment, and 50 μs WURST-80 pulses swept over 400 kHz were used for conversion and refocusing. In all cases, high-power ^{1}H decoupling was applied, with typical decoupling fields of ca. 40 kHz. All of the spectra presented herein are the best results (highest S/N) after optimizations of CPMG parameters, Hartmann-Hahn matching conditions and contact times. We note that in the event of very short effective T_2 values, BRAIN-CP may be combined with a simple WURST-echo experiment to obtain a single spin-echo FID. A two-step phase cycle of the ^{1}H spin lock pulse was used to alternate the generated polarization of the X nucleus between the positive and negative *z* axes, in order to ensure that only X polarization resulting from CP transfer is observed.[37] We note that after extensive testing of BRAIN-CP with multiple samples and sets of parameters, that *glycine* is an excellent set-up sample for those interested in initiating trials of this pulse sequence for use with ^{14}N. Experimental parameters are provided in **Appendix C**, **Tables C1** and **C2**. These should enable easy set-up of glycine (and a number of other samples) on NMR spectrometers of any field strength. The only parameters that require careful optimization are the rf fields for the Hartmann-Hahn matching condition and the sweep widths for the contact and

refocusing pulses (fortunately, the acquisition of high quality spectra is quite insensitive to missets in the latter parameters).

Due to the large breadths of the ^{14}N powder patterns and the limited excitation bandwidths associated with the WURST-80 pulses, all spectra herein were acquired using the variable-offset cumulative spectrum (VOCS) method.[15] The transmitter frequency was stepped in even increments across the pattern, with frequency increments equal to an integer multiple of the spikelet spacings arising from the CPMG portion of the pulse sequence.[38] Individual free-induction decays (FIDs) were transformed to produce sub-spectra, which were skyline projected or co-added to produce the total spectra. For all cases but α-glycine, only one half of the overall Pake doublet was acquired in both the DE and CP experiments. Under the assumption of a dominant first-order quadrupolar interaction, the total Pake doublet has mirror symmetry, and can be produced by "reflection" or "mirroring" of the high-frequency portion of the pattern about the predicted isotropic chemical shift, as discussed previously.[27] The positions of the three discontinuities in each half of the Pake doublet (i.e., the "foot", "shoulder" and "horn") depend directly on the values of C_Q and η_Q. Analytical simulations of idealized ^{14}N powder patterns were performed using the WSOLIDS software package.[39]

4.4 Results and Discussion

4.4.1 General observations

We begin this analysis with a comparison of ^{14}N UW SSNMR spectra acquired with direct excitation followed by the WURST-CPMG pulse sequence, against sets collected using cross polarization via the BRAIN-CP/WURST-CPMG pulse sequence. For brevity, we designate these experiments and corresponding spectra as direct

excitation (DE) and broadband cross polarization (BCP), respectively. Close examination of the BCP sequence reveals two distinct sections (**Scheme 4.1**). The BRAIN-CP section of the pulse sequence features a 90^{o} pulse on the ^{1}H channel followed by a spin-locking pulse, exactly as in a conventional CP experiment. On the X channel, by contrast, the counterpart contact pulse is an amplitude- and phase-modulated WURST-80 pulse[20] (labeled "WURST A"), which by linearly sweeping over a range of frequency offsets serves to (i) fulfill Hartmann-Hahn's polarization transfer conditions sequentially over a wide range over a broadband frequency range, and (ii) to "lock" the enhanced X spin-packets after their polarization transfer has been affected, performing on them an effective adiabatic sweep that ultimately enables their storage along the $-z$ direction at the end of the pulse. The portion of the sequence that follows utilizes the "WURST B" pulse to rotate this spin polarization from the $-z$-axis to the transverse plane, where it can be detected and/or further manipulated. A train of "WURST C" pulses act as a CPMG-like train, that refocuses the dephasing of these severely inhomogeneously broadened resonances to yield a time-domain FID consisting of spin echoes, the length of which depends on the effective T_2 of the nucleus under observation. In all cases, relatively low ^{1}H power levels during the contact time were used to achieve efficient BCP; however, comparatively higher ^{1}H decoupling fields (ca. 40 kHz) were used and found to be necessary[25] for reducing the contribution of ^{1}H-^{14}N dipolar relaxation to the effective $T_2(^{14}N)$, thereby increasing the number of echoes in the CPMG echo train and maximizing the S/N (see **Table C2** for details). Interestingly, the low rf fields available on the X (^{14}N) channel did not hinder us from achieving the Hartmann-Hahn matching

conditions, owing to the increase in nutation rates endowed by the frequency-swept WURST A pulse.

In order to make quantitative S/N assessments, we compare single sub-spectra acquired with DE and BCP methods featuring the same number of scans and identical experimental parameters in the WURST-CPMG portions of the pulse sequences. Single sub-spectra are used for these comparisons as opposed to the full- or half-Pake patterns, since the acquisition of the latter using DE methods is normally prohibitive in terms of long experimental times for most samples (*vide infra*).

Since full breadths of the patterns cannot be uniformly excited in a single experiment (even with broadband DE or CP pulses), multiple experiments conducted at uniformly spaced transmitter frequencies were used to acquire each pattern in its entirety. Important factors in designing and executing these experiments include the influence of the overlapping satellite transition patterns on the mechanism of CP and the ability to maintain a ^{14}N spin-lock while ensuring adiabatic broadband polarization transfer – two considerations unique to integer spin nuclei. For all of the spectra acquired with BRAIN-CP, the sweep bandwidths of all of the WURST pulses and the transmitter positions were chosen such that only one of the two transitions for each crystallite orientation was within the range of the inversion sweep, and that transmitter frequencies near the centre of the Pake doublet were avoided. This scheme is simple to enact under the assumption that the MHz-broad ^{14}N powder patterns are largely influenced only by the quadrupolar interaction to first order, with negligible effects from the second-order quadrupolar interaction and chemical shift anisotropy. Using this approximation, a single transition for each crystallite orientation is observed by recording sub-spectra using pulses swept

towards the centre of the pattern (0 ppm), but without exceeding 0 ppm (crossing over to the negative ppm range). Since frequency-swept pulses do not yield complete population inversion near the edges of their sweep ranges, the polarization transfer at the centre of the powder pattern is reduced.

4.4.2 α-glycine

α-glycine, the most common polymorph of glycine, features a single crystallographically unique nitrogen site within an RNH_3^+ moiety.[40] It is an ideal starting point for comparison of UW SSNMR spectra acquired with DE and CP methods, since its $T_1(^1H)$ and $T_1(^{14}N)$ values are both small, allowing for short recycle delays (1 s) for each class of experiment. The ^{14}N SSNMR spectra acquired with DE and BCP methods are compared in **Figure 4.1A**. These patterns are ca. 1.8 MHz wide (C_Q = 1.19(2) MHz and η_Q = 0.52(2), in agreement with previous measurements),[7,25,41] and have been acquired with identical conditions in the WURST-CPMG portions of the respective sequences (i.e., the same parameters, including the number of scans, echoes, sub-spectra and spikelet spacings, see **Tables C1** and **C2**). It is important to note that twenty sub-spectra were collected to construct both the DE and BCP spectra, since the broadband CP excitation profile yielded by the BRAIN-CP sequence is comparable to that of the DE WURST echoes.

The BCP spectrum has a S/N ca. five times higher than that of the DE spectrum (**Table 4.1**), which means that under these same experimental conditions, it would take ca. twenty-five times longer to acquire a DE spectrum of comparable S/N. A quantitative appraisal of the BCP signal enhancement is made by comparing the S/N of five spikelets

from sub-spectra collected near the “horn” of the powder pattern (**Figure 4.1B**). While a dramatic enhancement, this is well under the maximum theoretical value for the signal enhancement of ca. 13.8 times (i.e., $\gamma(^{1}H)/\gamma(^{14}N)$) that should be possible in systems with better CP characteristics (e.g., polarization transfer rate is faster, coherence lifetimes are longer, etc.). The BCP spectrum is also richer in information than the DE spectrum. In particular, the outermost discontinuities, or the "feet" of the powder pattern, are clearly observed in the BCP spectrum, allowing for accurate spectral fitting of this region, which is not possible with the DE spectrum. The excitation bandwidth of BRAIN-CP is comparable to that of the WURST-CPMG experiment, and far superior to conventional CP (**Figure 4.1B**); in this case, frequency-stepped CP experiments would require the collection of ca. 3-5 times as many sub-spectra.

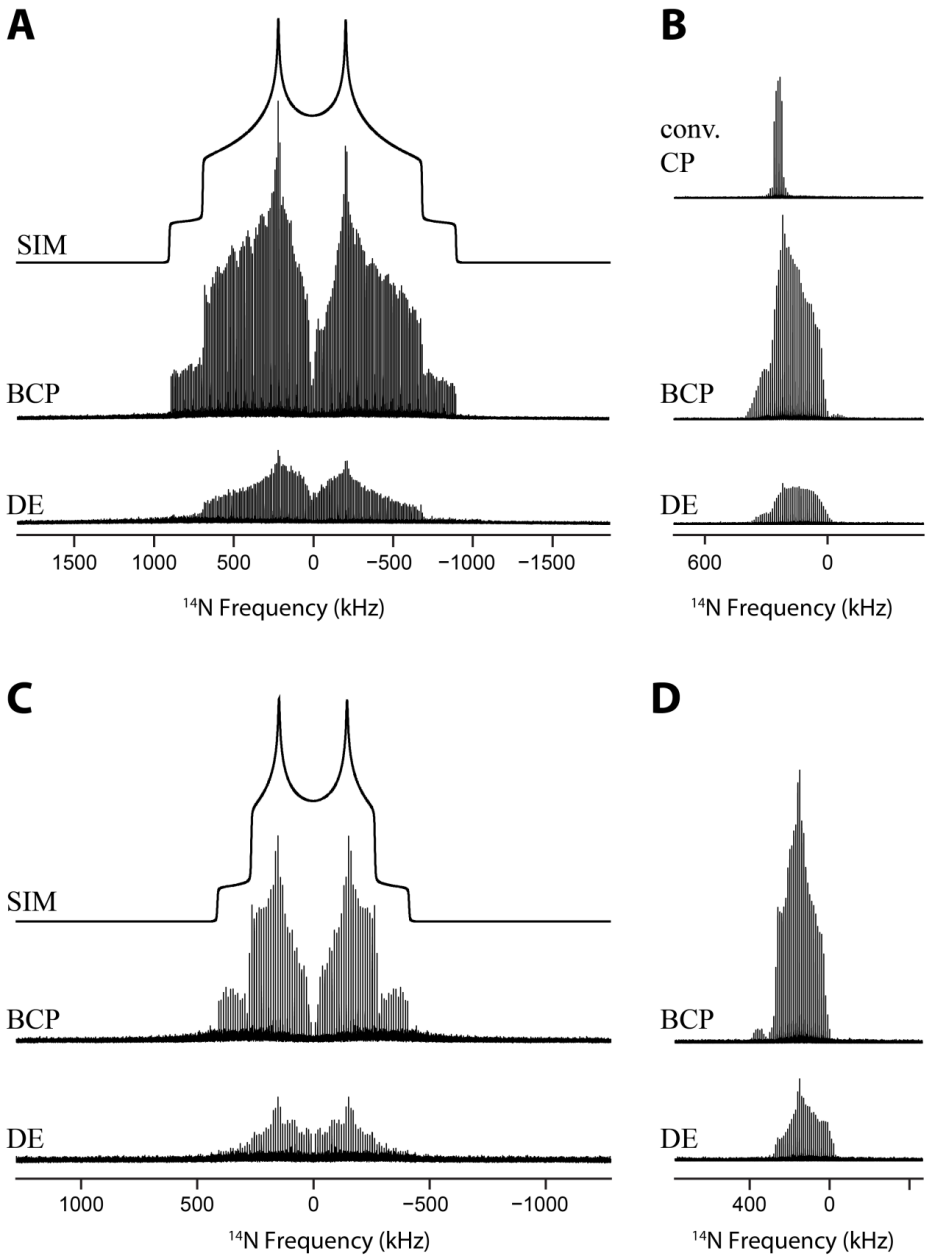

Figure 4.1: (A) Full ^{14}N UW SSNMR spectra of glycine acquired with WURST-CPMG (DE) and BRAIN-CP/WURST-CPMG (BCP) methods, presented together with an idealized analytical simulation (SIM). (B) Single ^{14}N SSNMR sub-spectra of glycine acquired using an equal number of scans and WURST-CPMG parameters at a transmitter ^{14}N Larmor frequency of 29.045 MHz using DE, BCP and conventional CP methods; note the narrower excitation bandwidth resulting from conventional CP when compared to the sub-spectrum acquired with BCP. (C) ^{14}N UW SSNMR spectra of trigonelline HCl acquired with DE and BCP methods. Only the high-frequency half of the pattern was acquired, with the total Pake doublet formed by "reflection" of this pattern about the isotropic shift. (D) Single ^{14}N SSNMR DE and BCP sub-spectra of trigonelline HCl acquired at a transmitter frequency of 29.045 MHz and identical WURST-CPMG parameters.

Table 4.1. Comparisons of S/N enhancements in single ^{14}N SSNMR sub-spectra acquired with BRAIN-CP/WURST-CPMG (BCP) and WURST-CPMG (DE) methods.

Compound	ν_{T_X} [1] (MHz)	Number of acquisitions	Recycle delay (s) [2]	Experimental time (min)	Ratio of S/N values (BCP:DE) [3]
Glycine	29.045	128	BCP: 5 DE: 5	BCP: 11 DE: 11	4.8
Trigonelline HCl	29.045	480	BCP: 15 DE: 45	BCP: 120 DE: 360	3.9
Isoxsuprine HCl	29.005	8640	BCP: 2.5 DE: 2.5	BCP: 360 DE: 360	6.3
Buflomedil HCl	29.405	1792	BCP: 5 DE: 10	BCP: 150 DE: 300	9.7

[1] ν_{T_X} denotes the transmitter frequency on the ^{14}N channel. The transmitter frequency was chosen such that it was proximate to the "horn" discontinuity of the ^{14}N powder pattern. [2] For BCP and DE experiments, recycle delays are estimated as $5\times T_1(^1\text{H})$ and $5\times T_1(^{14}\text{N})$, respectively. For a complete list of acquisition parameters, see **Table C2**. [3] The ratio of S/N values compares the average S/N obtained from BCP and DE experiments. The average S/N values from BCP and DE spectra are determined by measuring the S/N of five individual spikelets (phase corrected) in the proximity of the transmitter frequency.

4.4.3 Trigonelline HCl

Trigonelline HCl features an sp^2 nitrogen site in an aromatic heterocycle. The ^{14}N SSNMR spectra acquired with DE and BCP methods reveal spectra that are ca. 800 kHz wide (C_Q = 0.55(2) MHz, η_Q = 0.30(2), **Figure 4.1C**). Despite the narrowness of these patterns compared to those of glycine, the experimental times associated with their acquisition are much lengthier, due to the shorter $T_2(^{14}\text{N})$ values for trigonelline HCl, as well as the longer $T_1(^{14}\text{N})$ (in the case of DE experiments) and $T_1(^1\text{H})$ (in the case of BCP experiments) values. As discussed in the experimental section, only one half of the overall Pake doublet is acquired in both the DE and BCP experiments, with the total Pake doublet produced by "reflection" or "mirroring" (this is more or less a cosmetic effect,

due to the mirror symmetry of the pattern when the first-order quadrupolar interaction is dominant). The DE spectrum is comprised of four sub-spectra, each of which took two hours to acquire, for a total experimental time of eight hours. The BCP spectrum, which has significantly higher S/N, is also comprised of four sub-spectra, each of which took only 21 minutes to acquire. The BCP powder pattern clearly reveals the horn, shoulder and foot discontinuities, while the S/N of the DE spectrum is too low to allow extraction of the quadrupolar parameters because only one of the three characteristic discontinuities is observed. Comparison of single BCP and DE sub-spectra collected with the same number of scans (**Figure 4.1D**) reveals that the former has a ca. fourfold improvement S/N vs. the latter. The BCP experiment further benefits from the comparatively shorter recycle time that may be employed (15 s for BCP vs. 45 s for DE). If both of these factors are taken into account, the DE experiment would have to be run for ca. 25 hours to obtain comparable S/N to the CP spectrum (i.e., a sixteen-fold increase in the number of scans, each requiring three times longer to acquire).

4.4.4 Isoxsuprine HCl

Isoxsuprine HCl features an sp^3 nitrogen in an $R_2NH_2^+$ environment. The DE and BCP ^{14}N SSNMR spectra are approximately 1.5 MHz wide, with quadrupolar parameters of C_Q = 0.97(2) MHz and η_Q = 0.75(5) (**Figure 4.2A**). This is the only "high η_Q" pattern (i.e., η_Q is near 1, meaning that $|V_{22}| \approx |V_{33}|$) discussed in the current work, where the two "horns" are close to one another near the centre of the spectrum (the high η_Q is typical for this type of nitrogen environment). The DE spectrum is comprised of five sub-spectra acquired in 200 kHz steps, taking ca. 60 hours to acquire. By contrast, the total CP

spectrum required the acquisition of seven sub-spectra in 90 kHz steps, with a total experimental time of only 5 hours. The CPMG echoes in the FID of the DE experiment were closely spaced in order to maximize S/N, which leads to wider spacing of the spikelets in the frequency domain spectrum; this is in contrast to the BCP experiment, which yields a much higher resolution spectrum in a fraction of the time. In fact, the BCP spectrum was acquired ca. ten times faster than the DE spectrum, despite the smaller CPMG enhancement employed. For a quantitative comparison of S/N differences, the single sub-spectra acquired with the same number of scans (**Figure 4.2B**) and identical conditions in the WURST-CPMG portion of the pulse sequence reveal that the BCP method is much more efficient, yielding a spectrum with ca. six times higher S/N than the corresponding DE spectrum.

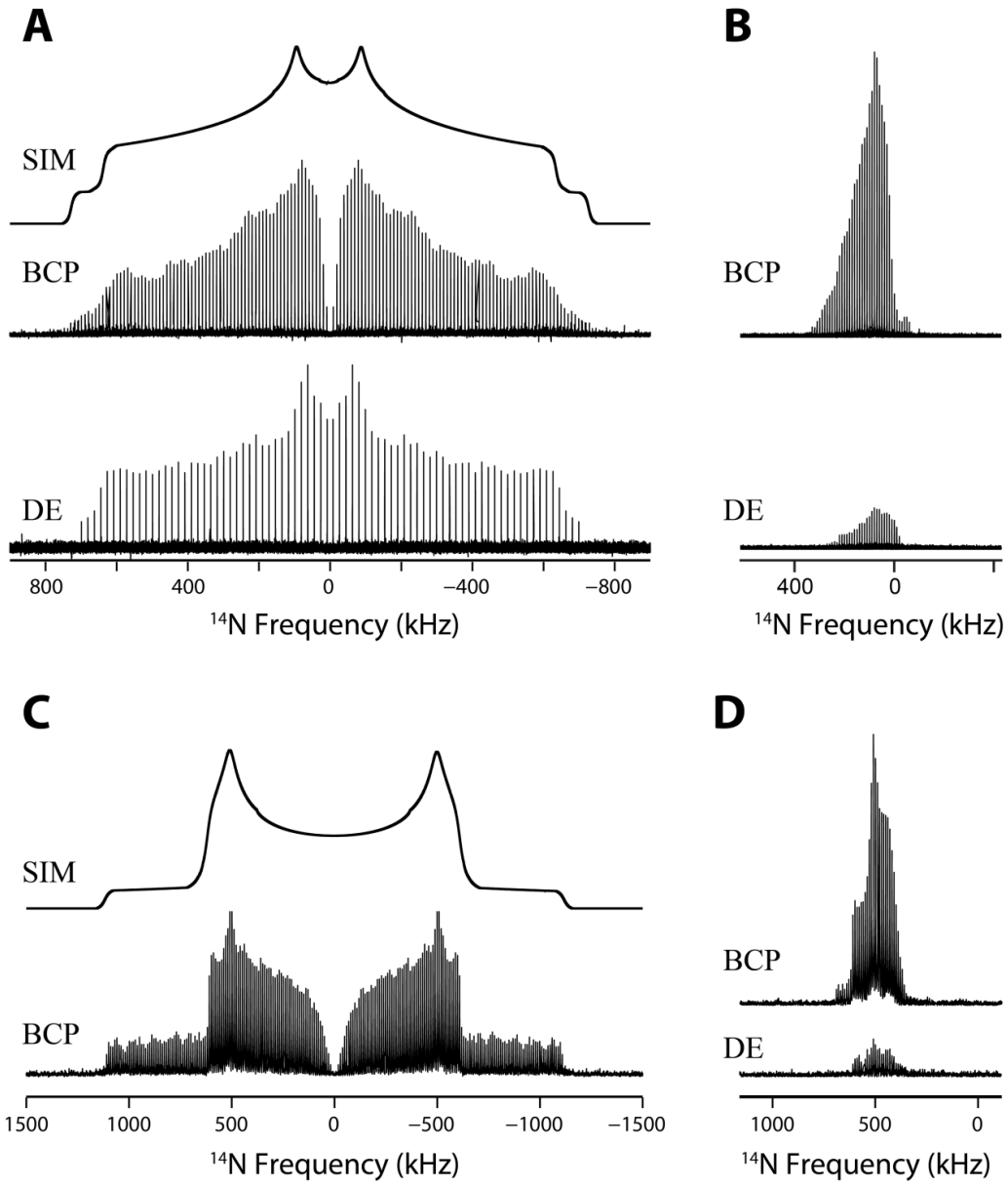

Figure 4.2: (A) ^{14}N UW SSNMR spectra of isoxsuprine HCl acquired with DE and BCP methods (high-frequency portion reflected), along with an analytical simulation. (B) Single ^{14}N SSNMR DE and BCP sub-spectra of isoxsuprine HCl acquired at a transmitter frequency of 29.005 MHz with the same number of scans and identical WURST-CPMG parameters. (C) ^{14}N UW SSNMR spectra of buflomedil HCl acquired with BCP (high-frequency portion reflected), along with an analytical simulation. (D) Single ^{14}N SSNMR DE and BCP sub-spectra of buflomedil HCl acquired with the same number of scans and identical WURST-CPMG parameters at a transmitter frequency of 29.405 MHz.

4.4.5 Buflomedil HCl

Buflomedil HCl features an sp^3 nitrogen environment where the N atom is part of a saturated five-membered ring. All attempts with DE ^{14}N SSNMR experiments, including those employing WURST-CPMG echo trains, failed to produce sub-spectra with sufficient S/N to construct a complete powder pattern in reasonable experimental times. However, a ^{14}N SSNMR spectrum of high quality was acquired with the BCP method (**Figure 4.2C**), revealing a pattern with a breadth of 2.2 MHz, and quadrupolar parameters of C_Q = 1.49(2) MHz and η_Q = 0.10(3). The high-frequency half of this extremely broad spectrum is constructed from 12 sub-spectra acquired in 90 kHz steps over a total experimental time of 12 hours, and the total pattern is generated by reflection. This spectrum was more difficult to acquire than the others discussed herein, due to the large breadth of the pattern as well as the reduced value of $T_2(^{14}N)$, which reduces the effectiveness of the CPMG enhancement; nonetheless, the positions of the outer discontinuities allow for the accurate extraction of quadrupolar parameters. The extremely low S/N of a single DE sub-spectrum (**Figure 4.2D**) reflects these difficulties; comparison of this single sub-spectrum to the BRAIN-CP sub-spectrum acquired at the same transmitter frequency reveals ca. ten times the S/N in the latter. The extreme breadth of the spectrum of buflomedil HCl shown in **Figure 4.2C** is clear evidence of the extraordinary sensitivity of the ^{14}N nucleus to its chemical environment, as well as the potential of the BRAIN-CP/WURST-CPMG method for the acquisition of ^{14}N SSNMR spectra that would otherwise be intractable.

4.5 Conclusions

We have demonstrated that it is possible to obtain high-quality ^{14}N UW SSNMR spectra of polycrystalline samples by combining the BRAIN-CP and WURST-CPMG pulse sequences to access the combined benefits of broadband cross polarization and broadband echo-train acquisition, respectively. A comparison of DE and BCP spectra clearly indicate that the latter are superior in terms of S/N, reduced experimental times and spectral appearance; the only exception may be in rare instances where the ^{1}H and ^{14}N relaxation conditions (in particular, a reduced $T_1(^{14}\text{N})$), support a faster DE experiment. The ability to use lower Hartmann-Hahn matching fields for BRAIN-CP than would be required for conventional CP is also appealing, as this reduces the probe duty cycle and limits the occurrences of arcing and/or probe damage. Finally, the experiments are facile to set up and execute, with parameters that are similar in many respects to conventional CP experiments (versions of these pulse sequences for Bruker and Varian spectrometers are available from the corresponding author).

This work only scratches the surface of what can be done with ^{1}H-^{14}N broadband CP NMR experiments. The four distinct nitrogen structural moieties discussed herein are common to many organic and biological systems; this suggests that these methods can be extended to the study of variety of nitrogen environments associated with a large range of quadrupolar coupling constants. For ^{14}N spectra with multiple patterns possessing similar quadrupolar parameters, it might be possible to use both variable-contact time experiments and "T_2 editing" of the CPMG echo trains to differentiate between these patterns; this is because ^{14}N nuclei in different structural environments have distinct CP efficiencies and dissimilar effective transverse relaxation times. In the case of RNH_3^+

and $R_2NH_2^+$ moieties, variable-temperature BRAIN-CP experiments may also be used to investigate dynamical processes (much like ^{2}H SSNMR), as well as for further signal enhancement and site differentiation (via alteration of effective T_2 values and/or CP efficiencies). Finally, we stress that the experiments discussed herein were all conducted at 9.4 T; the use of ultra-high fields (e.g., 18.8 T or greater) will further increase the efficiency of these experiments. Given all of these possibilities, we believe that ^{1}H-^{14}N BRAIN-CP/WURST-CPMG NMR experiments will find widespread use in probing the molecular-level structures of nitrogen-containing systems in many areas of chemistry and biochemistry, given the extreme sensitivity with which the ^{14}N NMR spectra report on nitrogen chemical environments.

4.6 Bibliography

(1) Whitehouse, B. A.; Ray, J. D.; Royer, D. J. *J. Magn. Reson.* **1969**, *1*, 311–326.

(2) Hilbers, C. W.; Maclean, C. *Mol. Phys.* **1969**, *16*, 275–284.

(3) Yannoni, C. S. *J. Chem. Phys.* **1970**, *52*, 2005–2010.

(4) Tycko, R.; Opella, S. J. *J. Chem. Phys.* **1987**, *86*, 1761.

(5) O'Dell, L. A.; Ratcliffe, C. I. *Chem. Phys. Lett.* **2011**, *514*, 168–173.

(6) Marinelli, L.; Wi, S.; Frydman, L. *J. Chem. Phys.* **1999**, *110*, 3100–3112.

(7) Giavani, T.; Bildsøe, H.; Skibsted, J.; Jakobsen, H. J. *J. Magn. Reson.* **2004**, *166*, 262–272.

(8) Jakobsen, H. J.; Hove, A. R.; Bildsøe, H.; Skibsted, J.; Brorson, M. *J. Magn. Reson.* **2007**, *185*, 159–163.

(9) Hill, E. A.; Yesinowski, J. P. *J. Chem. Phys.* **1997**, *106*, 8650.

(10) Hill, E. A.; Yesinowski, J. P. *J. Chem. Phys.* **1997**, *107*, 346.

(11) Cavadini, S. *Prog. Nucl. Magn. Reson. Spectrosc.* **2010**, *56*, 46–77.

(12) O'Dell, L. A. *Prog. Nucl. Magn. Reson. Spectrosc.* **2011**, *59*, 295–318.

(13) O'Dell, L. A.; Schurko, R. W. *Chem. Phys. Lett.* **2008**, *464*, 97–102.

(14) O'Dell, L. A.; Rossini, A. J.; Schurko, R. W. *Chem. Phys. Lett.* **2009**, *468*, 330–335.

(15) Massiot, D.; Farnan, I.; Gautier, N.; Trumeau, D.; Trokiner, A.; Coutures, J. P. *Solid State Nucl. Magn. Reson.* **1995**, *4*, 241–248.

(16) Medek, A.; Frydman, V.; Frydman, L. *J. Phys. Chem.* **1999**, *103*, 4830–4835.

(17) Shore, S. E.; Ansermet, J.-P.; Slichter, C. P.; Sinfelt, J. H. *Phys. Rev. Lett.* **1987**, *58*, 953–956.

(18) Larsen, F. H.; Jakobsen, H. J.; Ellis, P. D.; Nielsen, N. C. *J. Phys. Chem. A* **1997**, *101*, 8597–8606.

(19) Hung, I.; Gan, Z. *J. Magn. Reson.* **2010**, *204*, 256–265.

(20) Kupče, Ē.; Freeman, R. *J. Magn. Reson. Ser. A* **1995**, *115*, 273–276.

(21) Bhattacharyya, R.; Frydman, L. *J. Chem. Phys.* **2007**, *127*, 1–8.

(22) MacGregor, A. W.; O'Dell, L. A.; Schurko, R. W. *J. Magn. Reson.* **2011**, *208*, 103–113.

(23) Lucier, B. E. G.; Reidel, A. R.; Schurko, R. W. *Can. J. Chem.* **2011**, *89*, 919–937.

(24) O'Dell, L. A.; Schurko, R. W. *J. Am. Chem. Soc.* **2009**, *131*, 6658–6659.

(25) O'Dell, L. A.; Schurko, R. W. *Phys. Chem. Chem. Phys.* **2009**, *11*, 7069–7077.

(26) O'Dell, L. A.; Ratcliffe, C. I. *Chem. Commun.* **2010**, *46*, 6774–6776.

(27) O'Dell, L. A.; Schurko, R. W.; Harris, K. J.; Autschbach, J.; Ratcliffe, C. I. *J. Am. Chem. Soc.* **2011**, *133*, 527–546.

(28) Autschbach, J.; Zheng, S.; Schurko, R. W. *Concepts Magn. Reson. Part A* **2010**, *36A*, 84–126.

(29) Pines, A.; Gibby, M. G.; Waugh, J. S. *J. Chem. Phys.* **1973**, *59*, 569–590.

(30) Tycko, R.; Opella, S. J. *J. Am. Chem. Soc.* **1986**, *108*, 3531–3532.

(31) Tycko, R.; Stewart, P. L.; Opella, S. J. *J Am Chem Soc* **1986**, *108*, 5419–5425.

(32) Wolff, E. K.; Griffin, R. G.; Watson, C. *J. Chem. Phys.* **1977**, *66*, 5433.

(33) Bodenhausen, G.; Stark, R. E.; Ruben, D. J.; Griffin, R. G. *Chem. Phys. Lett.* **1979**, *67*, 424–427.

(34) Haberkorn. R. A.; Stark, R. E.; Van Willigen, H.; Griffin, R. G. *J. Am. Chem. Soc.* **1981**, *103*, 2534–2539.

(35) Pratum, T. K.; Klein, M. P. *J. Magn. Reson.* **1983**, *55*, 421–437.

(36) Pratum, T. K.; Klein, M. P. *J. Magn. Reson.* **1989**, *81*, 350–370.

(37) Harris, K. J.; Lupulescu, A.; Lucier, B. E. G.; Frydman, L.; Schurko, R. W. *J. Magn. Reson.* **2012**, *224*, 38–47.

(38) Tang, J. A.; Masuda, J. D.; Boyle, T. J.; Schurko, R. W. *ChemPhysChem* **2006**, *7*, 117–130.

(39) Eichele, K. WSolids1 — Solid State NMR Simulations, 2013.

(40) Power, L. F.; Turner, K. E.; Moore, F. H. *Acta Crystallogr. Sect. B Struct. Crystallogr. Cryst. Chem.* **1976**, *32*, 11–16.

(41) Edmonds, D. T.; Summers, C. P. *J. Magn. Reson.* **1973**, *12*, 134–142.

Chapter 5: Practical Considerations for the Acquisition of Ultra-Wideline ^{14}N NMR Spectra

5.1 Overview

Several considerations for the acquisition, processing and analysis of high quality ultra-wideline (UW) ^{14}N SSNMR powder patterns are discussed. The fundamental appearance of ^{14}N powder patterns that are dominated by the first-order quadrupolar interaction is explored, and it is shown that the ^{14}N quadrupolar parameters may be determined accurately using the frequencies of only two discontinuities. A framework for utilizing the WURST-CPMG pulse sequence to improve the efficiency of UW ^{14}N SSNMR acquisition is explored. This is achieved in two parts: (i) a systematic investigation of the design and parameterization of the WURST pulse is presented, and (ii) practical aspects for the use of CPMG refocusing for the acquisition of UW ^{14}N SSNMR powder patterns are discussed, with a focus on maximizing signal-to-noise and resolution, and minimizing spectral distortions. Finally, a strategy is presented that allows for the measurement of the ^{14}N quadrupolar parameters for any nitrogen moiety whose quadrupolar coupling constant falls within the range $0.8 \leq |C_Q| \leq 1.5$ MHz, by acquiring only two ^{14}N NMR sub-spectra at strategically located transmitter frequencies; these results are compared to spectra which are acquired using frequency-stepped methods. The methodologies and practical considerations outlined herein are not only useful for the rapid acquisition of UW ^{14}N NMR spectra, but may also be modified and applied for UW NMR of a plethora of quadrupolar and spin-1/2 nuclides.

5.2. Introduction

Nitrogen is an element that is important in all areas of chemistry, biology, and materials science, and has two NMR-active isotopes, ^{14}N and ^{15}N. ^{15}N NMR (I = ½) is more prevalent in the literature, despite its extremely low natural abundance (0.37%) and very poor sensitivity. This is largely due to the fact that, ^{14}N (I = 1), despite being 99.63% naturally abundant, is a quadrupolar nucleus. ^{14}N has a moderate quadrupole moment (eQ = 20.44 mbarn) and a very low gyromagnetic ratio ($\gamma(^{14}\text{N}) = 1.934 \times 10^7$ rad T^{-1} s^{-1}); however, it its integer spin generally results in very broad ^{14}N NMR powder patterns. For most nitrogen environments, ^{14}N SSNMR patterns are inhomogeneously broadened by the first-order quadrupolar interaction (FOQI). These patterns typically range from hundreds of kHz to several MHz in breadth, making their acquisition extremely challenging. However, despite these difficulties, there is much interest in acquiring ^{14}N SSNMR spectra, since the ^{14}N electric field gradient (EFG) tensor, which influences the FOQI, is very sensitive to even the most subtle differences and changes in the structural environments of nitrogen atoms. This in turn has allowed for the investigation of molecular dynamics, hydrogen-bonding, and polymorphism in various types of nitrogen-containing systems using ^{14}N solid-state NMR (SSNMR).[1–4]

In the presence of a strong magnetic field (Zeeman interaction), a spin-1 nucleus has three energy levels and two fundamental (single-quantum) transitions (**Scheme 5.1A**): $+1 \leftrightarrow 0$ and $0 \leftrightarrow -1$, which, in the absence of all other interactions, results in an NMR spectrum with a single resonance at the Larmor frequency, $\nu_0 = \gamma(^{14}\text{N})B_0/2\pi$. This is almost never the case, since the quadrupolar interaction (QI), the interaction between the ^{14}N nuclear quadrupole moment and the local EFGs, results in perturbations in the

Zeeman energy levels. The EFGs are described with second-rank tensors that are traceless and symmetric, and have three principal axis components, V_{11}, V_{22}, and V_{33}, which are defined according to the convention $|V_{11}| \leq |V_{22}| \leq |V_{33}|$. The EFG tensor parameters are often expressed using C_Q, the quadrupolar coupling constant (in MHz) and η_Q, the asymmetry parameter (dimensionless, $0 \leq \eta_Q \leq 1$):

$$C_Q = \frac{eQV_{33}}{h} \qquad [5.1]$$

$$\eta_Q = \frac{(V_{11} - V_{22})}{V_{33}} \qquad [5.2]$$

The FOQI perturbs the energies of the nuclear spin states (m) according to:[5,6]

$$E^{[1]}_{QI,m} = \frac{3hC_Q}{4I(2I-1)}[3m^2 - I(I+1)] \cdot \frac{1}{2}\left[(3\cos^2\theta - 1) + \frac{1}{2}\eta_Q \sin^2\theta \cos 2\phi\right] \qquad [5.3]$$

where θ and ϕ are the polar and azimuthal angles, respectively, which describe the orientation of $\mathbf{B}_0$ in the principal axis frame of the EFG tensor. In powdered, microcrystalline samples, ^{14}N NMR spectra having contributions from only the FOQI yield a pattern known as a *Pake doublet*, which is mirror-symmetric about the Larmor frequency or isotropic chemical shift (**Scheme 5.1B**).[3] The frequencies of all the crystallites in the powder pattern can be described by:

$$\nu_Q^{(1)} = \pm\frac{3}{8}C_Q\left(3\cos^2\theta - 1 + \eta_Q \sin^2\theta\cos 2\phi\right) \qquad [5.4]$$

Discontinuities in the pattern correspond to crystallite orientations for which V_{11}, V_{22}, or V_{33}, are parallel to B_0, which are defined as:

$$\nu_{11} = \nu_0 \pm \frac{3}{8}C_Q(1 - \eta_Q) \qquad [5.5a]$$

$$\nu_{22} = \nu_0 \pm \frac{3}{8} C_Q (1 + \eta_Q) \qquad [5.5b]$$

$$\nu_{33} = \nu_0 \pm \frac{3}{4} C_Q \qquad [5.5c]$$

The discontinuities at ν_{11}, ν_{22}, and ν_{33} are referred to as the "horns", "shoulders", and "feet" of the powder pattern, respectively. The effects of the second-order quadrupolar interaction (SOQI, **Scheme 5.1C**), nitrogen chemical shift anisotropy (CSA, **Scheme 5.1D**), and isotropic chemical shift, δ_{iso}, are not generally observed in patterns for which

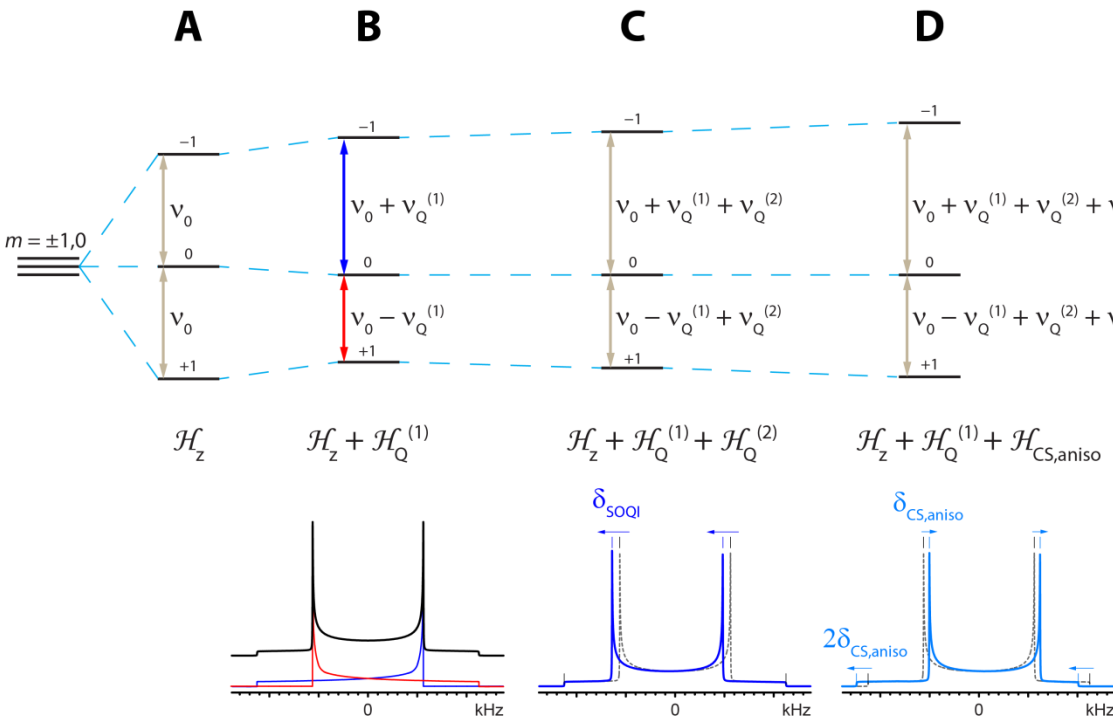

Scheme 5.1. Schematic spin-1 energy level diagram showing the perturbations to the ^{14}N spin states and the fundamental transitions (+1 ↔ 0 and 0 ↔ −1) under the influence of the (A) Zeeman, (B) first- and (C) second-order quadrupolar interactions, and (D) chemical shift anisotropy. In (B), the individual spectra associated with each transition are depicted: the red trace represents the +1 ↔ 0 transition while the blue trace is the 0 ↔ −1 transition. Note that the effects of the SOQI and CS interactions are greatly exaggerated compared to those of the Zeeman and FOQI.

C_Q is between 0.8 and 1.5 MHz. However, when the $C_Q(^{14}N)$ is small (e.g., $\lesssim$ 0.5 MHz), the δ_{iso} and CSA can make significant contributions, and when $C_Q(^{14}N)$ is large (e.g., $\gtrsim$ 2.00 MHz), the SOQI can make significant contributions. Therefore, these effects are neglected for the spectra discussed herein, which are dominated by the FOQI, due to $C_Q(^{14}N)$ values ranging from 1.0 to 1.5 MHz (see **Appendix D**, **Figure D1**).[7]

^{14}N powder patterns increase in breadth with increasing values of $C_Q(^{14}N)$, and correspondingly, their acquisition becomes progressively more difficult. According to eq. [5.5c], the breadth of a powder pattern influenced solely by the FOQI is equal to $1.5C_Q$. As an example, a common value of C_Q for an sp^3 hybridized nitrogen moiety (i.e., RNH_3^+) is 1 MHz;[8] therefore, the corresponding ^{14}N powder pattern has a breadth of 1.5 MHz. As a result, two complications arise in acquiring ultra-wideline (UW) ^{14}N NMR powder patterns: (i) they cannot be uniformly excited with a single, rectangular, high-power pulse, and (ii) they generally have extremely low signal-to-noise (S/N), because the signal intensity is spread across an wide frequency range.[9,10] Hence, a clear strategy is needed to enable the rapid acquisition of UW ^{14}N NMR patterns.

^{14}N NMR spectra have been previously acquired under conditions of magic-angle spinning (MAS), as proposed by Jakobsen and co-workers.[7] Their approach featured direct excitation pulses on the ^{14}N channel, and the use of specially designed NMR probes with extremely stable spinning speeds (less than ±1 Hz) and a precisely tuned magic angle (less than ±0.01°). These remarkable experiments allowed for the acquisition of ^{14}N NMR spectra comprising many spinning sidebands and spanning several MHz, from which it was possible to determine both the quadrupolar and anisotropic chemical shift parameters. However, in many cases, these experiments were

very long (e.g., in excess of 40 hours per experiment). Unfortunately, due to the hardware requirements and long experimental times, the popularity of these experiments has not grown.

A number of other methods have been explored for the acquisition of ^{14}N SSNMR spectra, including direct detection of ^{14}N NMR signals from single crystals,[11] anisotropically oriented samples,[12,13] and overtone ^{14}N NMR spectroscopy.[14–16] Indirect observation of ^{14}N in NMR spectra has also been widely reported, including via residual dipolar couplings observed in the NMR spectra of heteronuclear-dipolar coupled spin-½ nuclei (e.g., ^{13}C),[17–19] and in spectra obtained with indirect detection methods involving ^{1}H-^{14}N spin-spin correlations.[20–25] Indirect detection methods for acquiring ^{14}N NMR spectra have recently become prevalent in the literature; however, direct detection methods are not commonplace, due to the limits on the nature of the samples that can be studied and/or the need for sophisticated hardware and/or probes. For further details on direct and indirect detection of ^{14}N SSNMR spectra, the reader is referred to reviews by O'Dell and Cavadini.[3,4,26] We note that ^{14}N nuclear quadrupole resonance (NQR) has also been widely used to investigate many types of nitrogen systems,[8] but typically requires a dedicated NQR spectrometer.

Our research group has proposed a methodology that has been proven useful for the acquisition of UW SSNMR patterns,[9,10,27,28] including for the direct excitation (DE) and detection of ^{14}N NMR spectra under static (ν_{rot} = 0 Hz) conditions.[27–31] This methodology includes three main elements:

1. Pulses capable of sweeping over large frequency regions are utilized; in particular, we have found that WURST (wideband uniform-rate smooth-truncation)

pulses[32] are ideal for both excitation and refocusing, and are easy to calibrate and parameterize. The use of WURST pulses for the acquisition of NMR spectra of the central transitions (CT) of half-integer quadrupolar nuclides was first proposed by Bhattacharya and Frydman in 2007,[33] and extended to UW patterns of quadrupolar and spin-1/2 nuclides by our group.[28,29,31,34–38]

2. The WURST pulses are used in a Carr-Purcell-Meiboom-Gill (CPMG) type pulse sequence, which features an initial excitation pulse, followed by a train of intermittent refocusing pulses and acquisition periods (i.e., the WURST-CPMG sequence).[28] The resulting FID is a train of spin echoes, the number of which is dependent upon the transverse relaxation (T_2), or in cases where high-power ^{1}H decoupling is applied, the effective transverse relaxation (T_2^{eff}), which has its relaxative contributions from heteronuclear dipolar coupling partially or wholly removed. The FID may be processed by simple Fourier transformation, yielding a powder pattern consisting of spikelets whose outer manifold traces out the shape of the Pake doublet, or by co-addition of the spin echoes and subsequent Fourier transformation, which yields a conventional powder pattern.[39–41]

3. There are numerous cases where WURST pulses are unable to uniformly excite extremely broad UW ^{14}N SSNMR patterns, due to a combination of spectrometer and probe limitations; notably, the quality factor of the probe is a major factor in determining the maximum excitation and detection bandwidths. In such cases, it is possible to acquire the entire UW NMR spectrum by stepping the transmitter across the spectrum in even increments, collecting FIDs at each point, Fourier transforming these FIDs to produce sub-spectra, and then co-adding or skyline projecting them to form the total spectrum.

This is known as the variable-offset cumulative spectrum (VOCS) or frequency-stepped acquisition method.[42,43,27] Of course, the use of the WURST-CPMG pulse sequence in this context accelerates spectral acquisition and provides access to extremely broad patterns that could not otherwise be acquired.

^{14}N UW SSNMR patterns having breadths of 1 MHz or greater can be acquired with relative ease with this methodology, even at moderate magnetic field strengths (e.g., 9.4 T). Such experiments are almost always conducted with the application of high-power ^{1}H decoupling, due to the aforementioned influence of heteronuclear dipolar coupling on $T_2^{\text{eff}}(^{14}\text{N})$. We have also been investigating the application of broadband ^{1}H-^{14}N cross polarization (CP) with the BRAIN-CP pulse sequence,[44] as well as the effects of changing temperature on $T_2^{\text{eff}}(^{14}\text{N})$, CP efficiency and overall spectral quality.[45] Other groups have been exploring the use of ^{14}N overtone SSNMR and indirect detection of ^{14}N SSNMR spectra – clearly, there is much interest in developing reliable and convenient means of expeditiously acquiring such spectra.[4,15,16,22–24,26,46]

Since the first use of WURST-CPMG for DE ^{14}N SSNMR experiments in 2009 by our research group,[30,31] the experimental parameters have remained largely unchanged, since this sequence appeared to be quite insensitive to parameter settings and missets. However, in our ongoing investigations of organic and biological nitrogen-containing molecules, it has become apparent that in order to obtain the best quality ^{14}N NMR spectra in a reasonable timeframe, the following must be systematically investigated: (i) the WURST-CPMG pulse sequence, alteration of its parameters, and the resulting effects on ^{14}N SSNMR spectra, and (ii) the nature of ^{14}N powder patterns, including their origins, discontinuity locations, and overall spectral breadths.

In this work, we demonstrate that the ^{14}N quadrupolar parameters, C_Q and η_Q, can be accurately determined from UW ^{14}N SSNMR powder patterns that are dominated by the FOQI by only having to consider the locations of two discontinuities (most often the horn and shoulder). Practical considerations for spectral processing and parameterizing ^{14}N NMR experiments employing CPMG refocusing are considered, with a focus on maximizing the S/N, retaining the best possible spectral resolution, and minimizing spectral distortions. We also demonstrate the effects of WURST pulse parameters on the overall quality of the ^{14}N spectra; in particular, a detailed investigation of their dwell times and linear sweep rates is presented. Lastly, we show for ^{14}N NMR patterns arising from C_Q values ranging from 0.8 to 1.5 MHz, that it is possible to determine the quadrupolar parameters from a powder pattern comprised of only two sub-spectra acquired at strategically placed transmitter frequencies (N.B., the C_Q values of most pseudo-tetrahedral nitrogen moieties in organic molecules, i.e., RNH_3^+, $RR'NH_2^+$, and $RR'R''NH^+$, fall in this range). Although this work focuses on improving the efficiency of UW ^{14}N SSNMR, many elements of pulse sequence design and spectral acquisition strategies discussed herein are applicable to larger ranges of C_Q values, including those of other nuclides, and may be of particular interest to spectroscopists who are just beginning to investigate ultra-wideline NMR methods.

5.3. Experimental

5.3.1 Chemicals

Samples of α-glycine, glycine HCl, glycylglycine, and L-tyrosine were purchased from Sigma Aldrich and used without further purification. 4-hydroxy-L-proline was purchased from Sigma Aldrich and recrystallized from $D_2O(l)$ (in order to increase the $T_2^{eff}(^{14}N)$ value). Samples were powdered and packed into shortened glass NMR tubes (outer diameter, o.d. = 5 mm).

5.3.2 NMR Spectroscopy

^{14}N SSNMR experiments were carried out on a Varian InfinityPlus spectrometer and a Bruker Avance IIIHD spectrometer (following an upgrade of the Varian system), both equipped with an Oxford wide-bore 9.4 T magnet operating at Larmor frequencies of $\nu_0(^{14}N)$ = 28.9 MHz and $\nu_0(^{1}H)$ = 399.9 MHz. A Varian/Chemagnetics 5.0 mm double-resonance static (non-spinning) HX probe and a low-gamma tuning accessory were used for all ^{14}N experiments. A sample of $NH_4Cl(s)$ was used to calibrate the rf power on the ^{14}N channel, as well as to reference the ^{14}N chemical shifts (δ_{iso} = 0 ppm); however, the ^{14}N chemical shifts are not reported due to the large uncertainties associated with their measurement.

Direct excitation ^{14}N SSNMR experiments were conducted with the WURST-CPMG pulse sequence.[28] WURST-80[32] pulses with sweep ranges between 250 and 6000 kHz and pulse lengths between 18 and 200 μs were used throughout the study. In all cases, high-power ^{1}H decoupling was applied, with typical decoupling fields of ca. 40

kHz. For a complete list of experimental parameters we refer the readers to the tables in **Appendix D**.

Due to the large breadths of the ^{14}N powder patterns, all spectra herein were acquired using the variable-offset cumulative spectrum (VOCS) or frequency stepped method.[27,42,43] The transmitter frequency was stepped in even increments across the pattern, with frequency increments equal to an integer multiple of the *spikelet* spacings arising from the CPMG portion of the pulse sequence.[27] Unless otherwise stated in the text, individual echoes of the FIDs were co-added, apodized using Gaussian broadening, zero-filled at least one time and Fourier transformed. The FOQI dominates ^{14}N powder patterns with C_Q values of ca. 0.7 – 2.0 MHz; hence, the Pake doublet has mirror symmetry about the ^{14}N Larmor frequency (the isotropic chemical shift range of nitrogen spans such a small fraction of the Pake doublet, that it cannot be reliably measured). As a result, only half of the pattern has to be acquired. The total Pake doublet is produced by "mirroring" of one half of the powder pattern, as discussed elsewhere (though this is largely for aesthetic purposes).[3] Analytical simulations of ^{14}N powder patterns were performed using the WSOLIDS1 software package.[47] The effects of varying the parameters of the WURST pulses were modelled using the SIMPSON software package[48] using a personal computer (see **Figure D2** for further details).

In cases where C_Q and η_Q were determined by using the frequencies of only two discontinuities, the upper bounds for the associated propagated uncertainties were determined from the breadth of the corresponding discontinuity; these are typically 10 kHz for the horn (ν_{11}) and 10 to 20 kHz for the shoulder (ν_{22}).

5.4. Results and Discussion

5.4.1. Positions of the discontinuities in ^{14}N NMR powder patterns

Powder patterns of integer spin nuclides like ^{2}H and ^{6}Li are normally easy to acquire in comparison to those of ^{14}N, since the breadths of the former are comparatively smaller. However, due to their smaller breadths, the effects of the CSA can alter the positions of key discontinuities (i.e., they are not symmetric about the Larmor frequency), making simulations more challenging.[49–52] By comparison, since ^{14}N powder patterns are dominated by the FOQI, the positions of the discontinuities on either side of the Larmor frequency are approximately the same (detection of slight differences is limited by the relatively low resolution of ^{14}N NMR patterns, *vide infra*). Therefore, whereas acquisition of the entire pattern might be necessary for ^{2}H and ^{6}Li, it is not for ^{14}N; the acquisition of only half of the ^{14}N pattern represents a substantial time savings. We and others have "mirrored" the pattern about the apparent chemical shift/Larmor frequency, if only to give the pattern the aesthetic appearance of a traditional Pake doublet (in theory, it is only necessary to display either the low- or high-frequency halves of these patterns). This is demonstrated for the ^{14}N SSNMR pattern of α-glycine (**Figure 5.1**), which shows that the discontinuities on either side of the pattern can be utilized to obtain the quadrupolar parameters.

A further consequence of the dominance of the FOQI on ^{14}N powder patterns, and the fact that EFG tensors are traceless, is that the positions of the discontinuities are directly related to the EFG tensor components. Equations [5.5a-c] can be rearranged to show that:

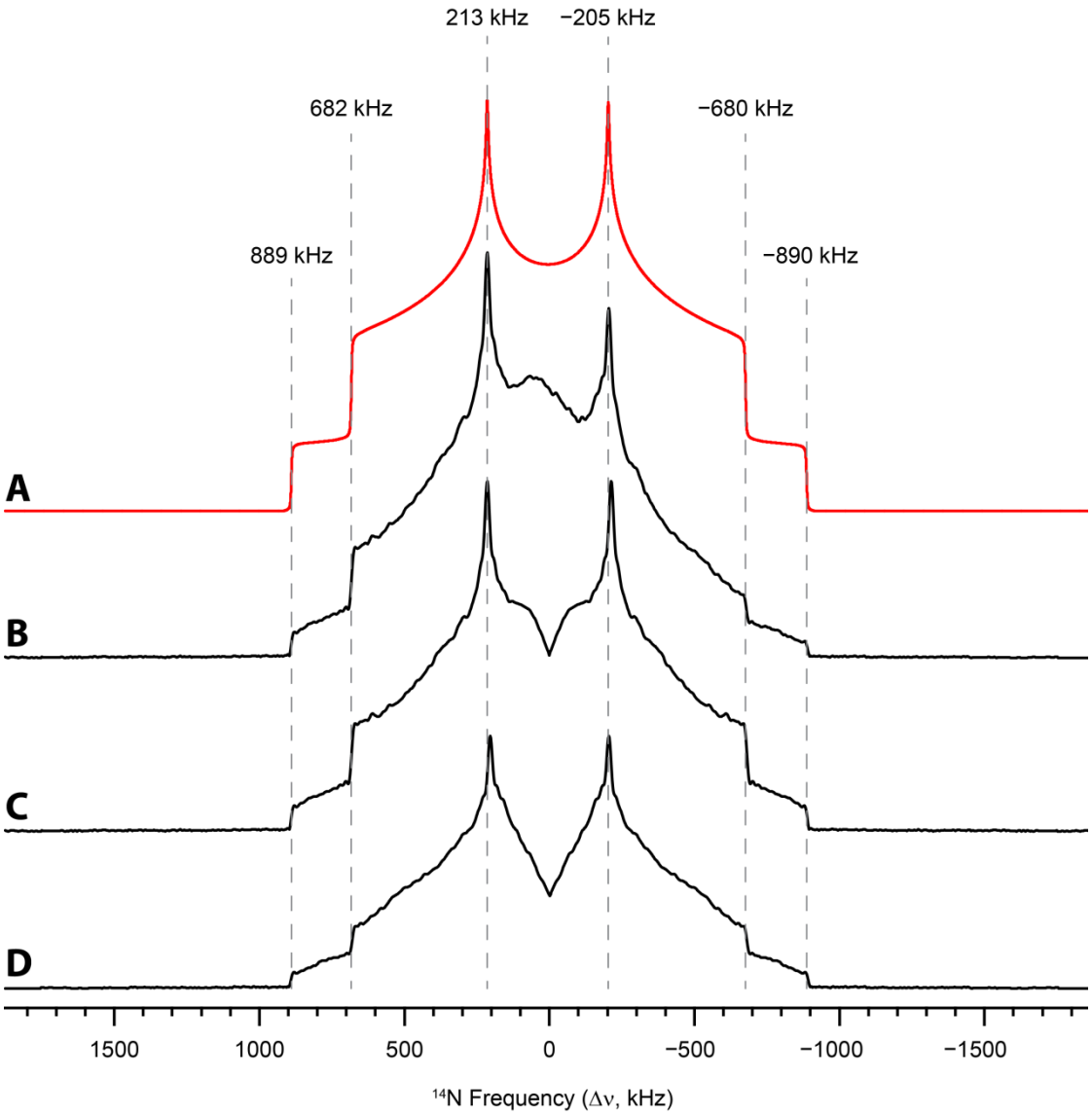

Figure 5.1. (A) Idealized ^{14}N powder pattern with C_Q = 1.19(1) MHz and η_Q = 0.53(1). (B) Experimental ^{14}N powder pattern of α-glycine acquired using 13 sub-spectra without mirroring. The frequencies of the discontinuities are marked by the vertical dashed lines. (C) ^{14}N powder pattern of α-glycine produced by "mirroring" the high-frequency half (7 sub-spectra) of the spectrum in **B**. (D) ^{14}N powder pattern of α-glycine made by "mirroring" the low-frequency half (6 sub-spectra) of the spectrum in **B**. The spectra in **C** and **D** are both fit using C_Q = 1.19(2) MHz and η_Q = 0.53(2). The upper uncertainties in the frequencies of the discontinuities were determined from their corresponding breadths: these are typically 10 kHz for the horn and 10 to 20 kHz for the shoulder.

$$\nu_{11} + \nu_{22} = -\nu_{33} \quad [5.6a]$$

$$\eta_Q = \frac{(\nu_{11} - \nu_{22})}{\nu_{33}} \quad [5.6b]$$

Hence, to first order, the frequencies of the discontinuities are not independent from one another. This means that if the frequencies of two discontinuities are known, the frequency of the third discontinuity can be determined, and therefore, C_Q and η_Q are measured from the positions of only two discontinuities.

As an example, a theoretical ^{14}N powder pattern simulated with C_Q = 1.00 MHz and η_Q = 0.20 is considered (**Figure 5.2A**). If only the frequencies of the horn and shoulder discontinuities (ν_{11} = +300 kHz and ν_{22} = +450 kHz, respectively, where the plus sign indicates the high-frequency direction from the Larmor frequency) are known (e.g., because the foot discontinuity is obscured by noise), the frequency of the foot is calculated to be ν_{33} = −750 kHz. Equations [5.5c] and [5.6b] are rearranged and solved to yield C_Q = 1.00 MHz and η_Q = 0.2. (N.B., the magnitude, but not the sign, of C_Q is determined, since the FOQI perturbs both +1 and −1 energy levels in an equal but opposite sense). The exact same result is obtained from discontinuities to low frequency of the Larmor frequency, i.e., ν_{11} = −300 kHz and ν_{22} = −450 kHz.

This is extended to experimental ^{14}N SSNMR powder patterns shown in **Figs. 5.2B** and **5.2C**. The high-frequency half of the ^{14}N powder pattern of L-tyrosine (**Figure 5.2B**) has high S/N and all of the discontinuities are clearly visible. The analytical simulation of the ^{14}N powder pattern yields C_Q = 1.02(1) MHz and η_Q = 0.41(1) (red trace). The frequencies of the horn and shoulder discontinuities are measured from the spectrum as ν_{11} = 227 kHz and ν_{22} = 533 kHz, respectively, yielding a value of ν_{33} = −760

kHz for the foot discontinuity. From these measurements, the quadrupolar parameters are determined to be C_Q = 1.01(2) MHz and η_Q = 0.40(2), which match extremely well with those obtained from the analytical simulation. The same approach can be applied to the low-frequency half of the ^{14}N powder pattern of α-glycine (**Figure 5.2C**): with ν_{11} = −205 kHz and ν_{22} = −686 kHz, it is determined that C_Q = 1.19(2) MHz and η_Q = 0.54(4), in good agreement with the analytical simulation (C_Q = 1.19(1) MHz and η_Q = 0.53(1)).

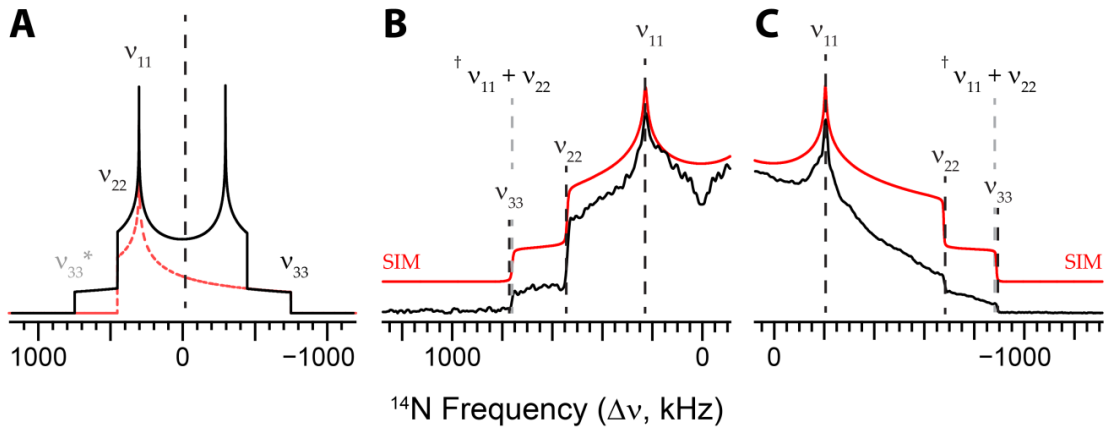

Figure 5.2. (A) Analytical simulation of a ^{14}N powder pattern with C_Q = 1.00 MHz and η_Q = 0.20. The frequencies of the "horn" and "shoulder" discontinuities are marked on the spectrum; ν_{11} = 300 kHz and ν_{22} = 450 kHz, respectively. ν_{33} is calculated using eq. [5.6a], from which C_Q and η_Q can then be deduced. * Indicates the ν_{33} discontinuity arising from the 0 ⟷ −1 transition. (B) High-frequency half of a ^{14}N SSNMR powder pattern of L-tyrosine (black) with an analytical simulation using C_Q = 1.02(1) MHz and η_Q = 0.41(1) (red). The frequencies of all three discontinuities can be extracted from the spectrum, resulting in C_Q = 1.01(1) MHz and η_Q = 0.40(2). $^{\dagger}\nu_{33} \approx \nu_{11} + \nu_{22}$; see text for explanation. (C) Low-frequency half of a ^{14}N SSNMR powder pattern of α-glycine (black) with an analytical simulation using C_Q = 1.19(1) MHz and η_Q = 0.54(1) (red). The frequencies of all three discontinuities can be extracted from the spectrum, resulting in C_Q = 1.19(2) MHz and η_Q = 0.54(4).

Close inspection of **Figure 5.2B** and **5.2C** reveals that the frequencies of the foot discontinuities determined from the sums above are slightly different than the ones

measured directly from the spectra (for L-tyrosine ν_{33} = 763 kHz while $\nu_{11} + \nu_{22}$ = 760 kHz, and for α-glycine ν_{33} = −896 kHz while $\nu_{11} + \nu_{22}$ = −891 kHz). These small differences arise from uncertainties in the measurements of the positions of the horn and shoulder discontinuities, which are on the order of ±10 and ±20 kHz, respectively for both L-tyrosine and α-glycine. We note that the differences of ca. 3 to 5 kHz reported above represent less than 1% of the overall breadths of the powder patterns, and hence, have no significant impact on the measurement of C_Q and η_Q from UW ^{14}N NMR spectra.

The ability to accurately determine the ^{14}N quadrupolar parameters using either the low- or high-frequency half of the powder pattern (α-glycine and L-tyrosine, respectively) is a consequence of the mirror-symmetric nature of the ^{14}N UW NMR powder patterns which are dominated by the FOQI (*vide supra*). For illustrative purposes, the spectra that were presented have all of the three discontinuities clearly defined; however, this method can safely be applied to powder patterns in which one of three discontinuities is absent or obscured. In addition, this is also advantageous when one region of the ^{14}N Pake doublet is not amenable to spectral acquisition, e.g., in cases of interference or probe tuning difficulties, which are often encountered on probes specialized for low-γ NMR studies (*vide infra*).

5.4.2. Resolution and Signal-to-Noise in ^{14}N NMR powder patterns

A key factor that affects the acquisition time of ^{14}N powder patterns collected with the use of CPMG refocusing is the *effective* T_2, or $T_2^{\text{eff}}(^{14}\text{N})$. If ^{1}H decoupling is applied during acquisition periods, the effects of the ^{14}N-^{1}H dipolar coupling mechanism on the T_2 relaxation are either partially or wholly removed, resulting in an effective T_2

value which is generally longer than the actual T_2 value. Longer values of $T_2^{eff}(^{14}N)$ permit the collection of more echoes, which in turn increase the S/N in the resulting spectrum. The total acquisition time needed to collect a train of CPMG echoes is dependent primarily on the $T_2^{eff}(^{14}N)$, as well as on parameters such as the dwell time (spectral width) and spin-echo timings utilized in the CPMG experiment (*vide infra*).

For clarity in the subsequent discussion, we use the following terms and symbols to describe the CPMG echo train (see **Figure 5.3**): (i) The time interval between the centres of two consecutive refocusing pulses in a CPMG echo train is equivalent to the time interval between the tops of two subsequent spin echoes; this is denoted as the *spin echo time*, τ_{echo}. The top of the spin echo (i.e., maximum signal intensity) occurs at exactly $\frac{1}{2}\tau_{echo}$ from the centre of the first π pulse. (ii) The *acquisition window*, τ_{window}, is the time period during which the receiver is turned on and the transverse magnetization is detected. The centre of this window corresponds to the echo top, and the duration of this window is less than τ_{echo}, to permit time for blanking of amplifiers and receivers. The *acquisition time*, τ_{acq}, is the total time taken to collect a train of CPMG echoes in a single scan (i.e., the time to acquire a single FID). The acquisition time is determined by the *number* (N) of repeated spin echo times, τ_{echo}.

If the CPMG echo trains are directly Fourier transformed, the result is a spectrum comprised of *spikelets*, whose outer manifold traces the outline of the powder pattern. The spectral resolution of a powder pattern processed in this manner is dependent upon the spacing between the spikelets, which are inversely proportional to τ_{echo}. Another processing option is to shift the echoes and co-add them (we will refer to this as *echo co-addition*, to distinguish it from co-addition of frequency-domain spectra), followed by

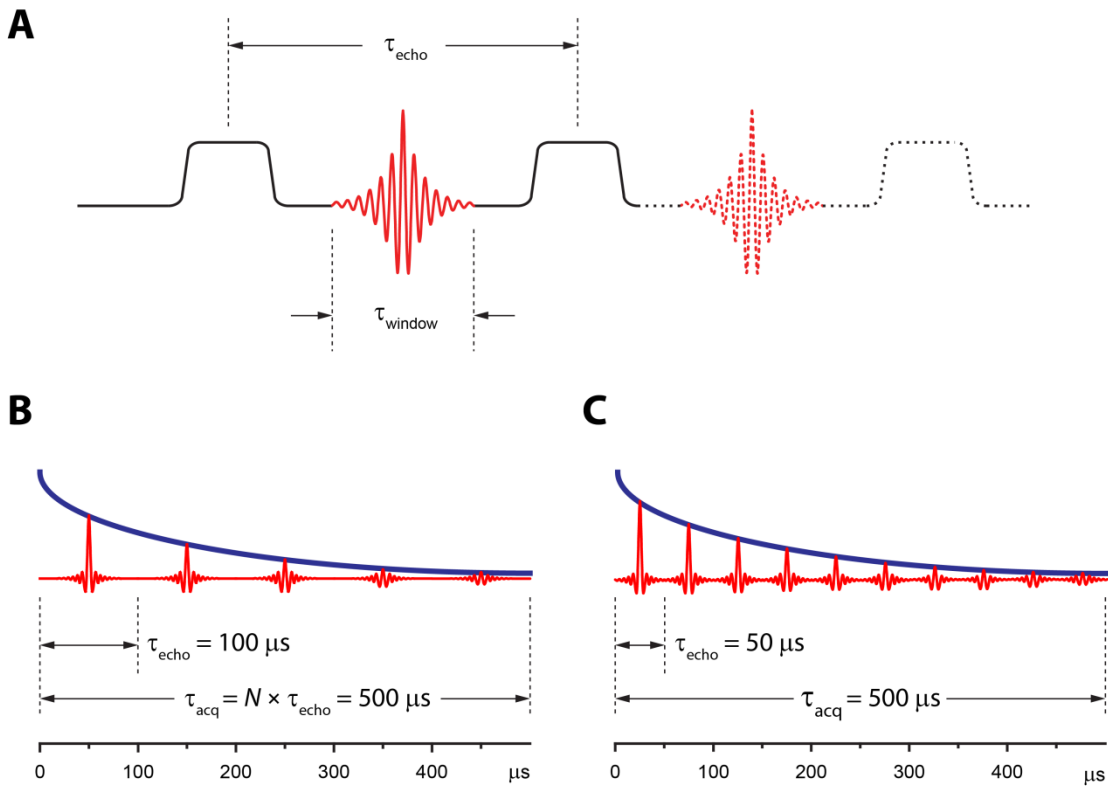

Figure 5.3. (A) Schematic representation of spin echo acquisition during CPMG refocusing. τ_{echo} represents the time between the centres of two refocusing pulses (or equivalently, the time between the tops of two subsequent spin echoes). τ_{window} is the time period during which the receiver is on and recording signal and is centered at $\frac{1}{2}\tau_{echo}$. In order to collect a CPMG echo train, τ_{echo} is repeated N times. Two schematic FIDs showing an acquisition time, τ_{acq}, of 500 μs; in (B) τ_{echo} = 100 μs and N = 5, while in (C) τ_{echo} = 50 μs and N = 10.

subsequent Fourier transformation, which results in a standard powder pattern. In this case, the resolution of the pattern is limited by the dwell time, as in conventional NMR experiments.[39–41]

The effects of the spikelet separation and spin echo time on the overall quality of ^{14}N powder patterns are investigated with a series of spectra of α-glycine (**Figure 5.4**). The spectra in the left column have been processed by Fourier transforming the FIDs with the full echo trains, while those in the right column were processed by echo co-addition. All acquisition parameters are the same (see **Table D1**), except for τ_{echo}, τ_{window},

and *N*. The echo train parameters are (from top to bottom): τ_{window} = 200, 100, 50, and 25 μs (all with identical dwell times), and *N* = 50, 100, 200, and 400, respectively.

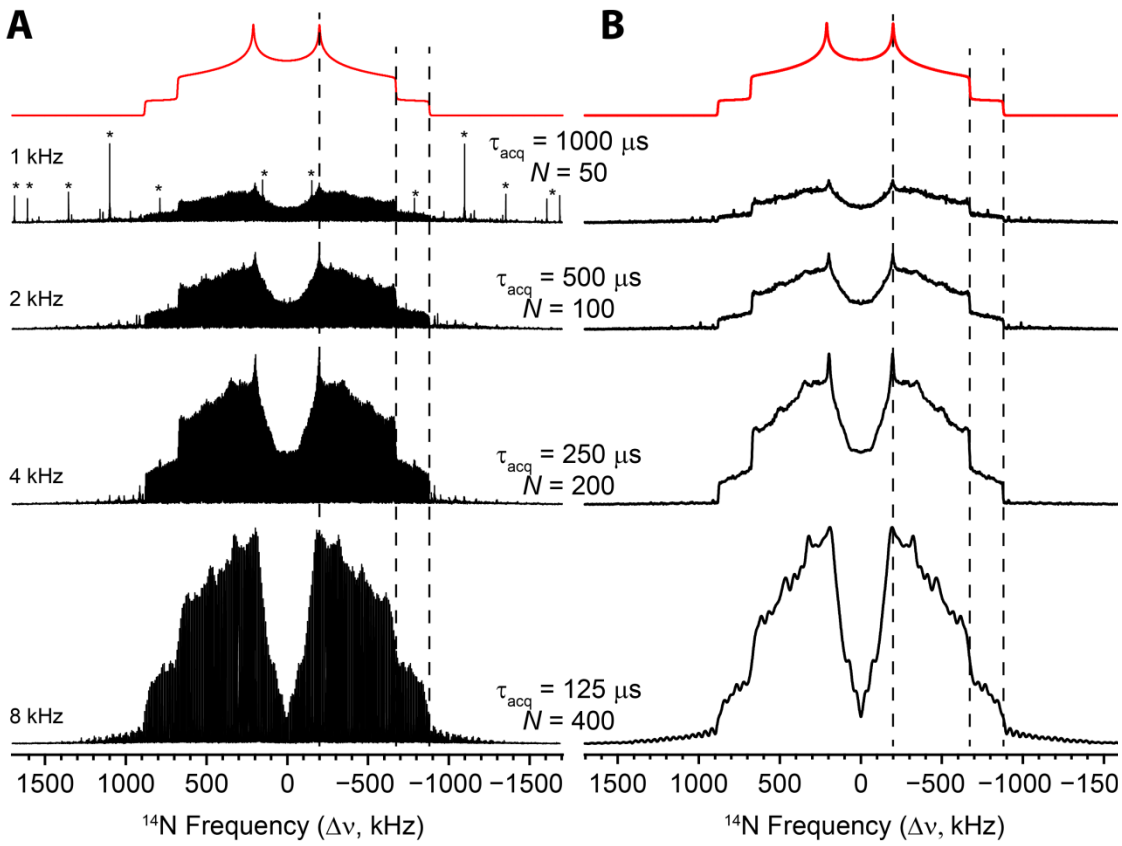

Figure 5.4. ^{14}N SSNMR powder patterns of α-glycine processed in A) spikelet and B) echo-coaddition modes. From top to bottom, the spectra were acquired with the following WURST parameters: τ_{acq} = 1000, 500, 250, and 125 μs and *N* = 50, 100, 200, and 400, respectively, which result in spectra that have spikelet separations of 1, 2, 4, and 8 kHz, respectively. * rf interference from the NMR hardware.

The ^{14}N spikelet patterns resulting from direct Fourier transform of the entire echo train have 1, 2, 4, and 8 kHz spikelet separations, respectively. The S/N approximately doubles with each doubling of *N*; the corresponding spectra produced from echo co-addition show the same trend. Interestingly, the S/N ratios of the spectra with τ_{acq} = 125 μs are only ca. 1.2 times higher than that of the spectra acquired with τ_{acq} = 250 μs, which

deviates from the observed trend for the other three spectra. This is because the spin echoes are truncated, since the time that an observable spin echo exists exceeds the time of the acquisition window. Truncated echoes result not only in reduced S/N, but also in potential distortions at key points in the powder pattern, as is the case with the powder pattern acquired with τ_{acq} = 25 μs.[39] Therefore, one must consider two major factors when setting up CPMG experiments: (i) the total duration of the CPMG train, which depends on $T_2^{eff}(^{14}N)$, and (ii) the durations of τ_{window} and τ_{echo}, ,which are set according to the decay rate of the observable spin echo, T_2*. In solid-state NMR spectra, this apparent T_2* decay is largely influenced by the wide breadths of the powder patterns, and not magnetic field inhomogeneities, as in the case of most solution NMR experiments; therefore, the τ_{window} and τ_{echo} can be chosen based on rough estimates of either the breadth of the powder pattern or the T_2*. In α-glycine, the observable spin-echoes were found to be approximately 50 μs in length. For the powder pattern with spikelet spacings of 8 kHz, in order to set τ_{acq} = 125 μs, τ_{window} has to be set to 25 μs; this results in significant truncation of the observable spin echoes (**Figure 5.5**), which in turn results in decreased S/N and potential distortions in the final Fourier transformed spectrum.[39]

The ^{14}N quadrupolar parameters determined from simulations of all four spikelet spectra are similar (**Table 5.1**); however, their uncertainties increase with increased spikelet separation. The quadrupolar parameters determined from the spectra processed by co-adding the spin echoes are essentially identical (provided that the individual spin echoes are not truncated), and have lower associated uncertainties. Accordingly, it is highly recommended to co-add the spin echoes prior to Fourier transformation, since the

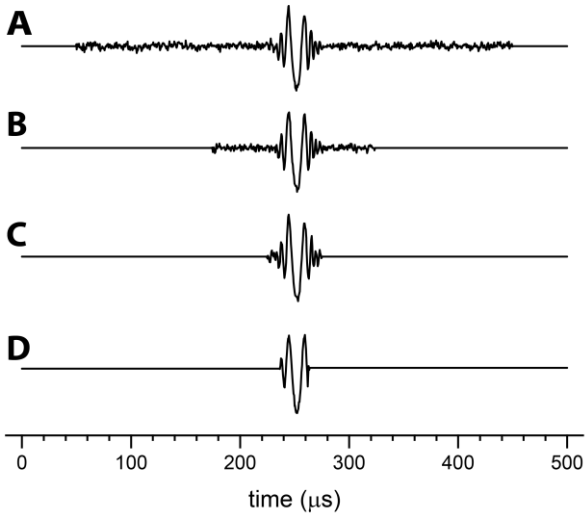

Figure 5.5. Individual acquisition windows extracted from corresponding ^{14}N FIDs of α-glycine. τ_{acq} = 500 μs in all cases, τ_{window} = (A) 400, (B) 200, (C) 75, and (D) 25 μs. The truncation of the observable spin-echoes becomes apparent as τ_{window} decreases.

spectral resolution is limited by the dwell time rather than by the separation of the spikelets (as in the case of directly Fourier transforming the echo train).

The tradeoff between high S/N and high resolution in NMR spectra acquired with CPMG methods is important to consider when parameterizing such experiments. For initial experiments, it is key to acquire the maximum number of echoes, while ensuring that the individual spin echoes are not truncated. Spectra with higher S/N but lower resolution may be acquired quickly in order to get a rough idea of the locations of the discontinuities, followed by higher-resolution experiments aimed at extracting the locations of the discontinuities with greater accuracy. This strategy is applicable to the acquisition of ^{14}N NMR patterns, as well as to UW NMR spectra of other nuclides that are acquired with the use of CPMG refocusing.

Table 5.1. ^{14}N quadrupolar parameters of α-glycine measured from spectra in **Figure 5.3**.

	Spikelet spectra [a]		Echo co-addition spectra [b]	
τ_{echo} (μs)	$\lvert C_Q\rvert$/MHz [c]	η_Q [d]	$\lvert C_Q\rvert$/MHz	η_Q
200	1.190(5) [e]	0.525(5)	1.190(5)	0.525(5)
100	1.19(1)	0.52(1)	1.190(5)	0.525(5)
50	1.19(2)	0.52(2)	1.190(5)	0.525(5)
25	1.21(4)	0.53(4)	1.190(10)	0.52(2)

[a] Spectra are processed by direct Fourier transformation of the CPMG echo train. [b] Spectra are processed with echo co-addition. [c] $C_Q = eQV_{33}/h$. Note, that the sign of C_Q cannot be determined from ^{14}N SSNMR spectra. [d] $\eta_Q = (V_{11} - V_{22})/V_{33}$. [e] Uncertainty is reported to the last decimal place.

5.4.3. Improving excitation bandwidths with WURST pulse modifications

WURST pulses, originally introduced by Kupče and Freeman in 1995 for the purposes of broadband inversion and decoupling,[32] achieve their frequency sweep by a quadratic phase modulation described by the formula:[53]

$$\phi(t) = \pm 2\pi \left\{ \left(\nu_{off} + \frac{\Delta}{2} \right) t - \left(\frac{\Delta}{2\tau_p} \right) t^2 \right\} \qquad [5.7]$$

where $\phi(t)$ is the phase of the pulse (in radians) at time t, Δ is the total sweep range of the pulse (in Hz), τ_p is the pulse width (in s), and ν_{off} is the offset frequency from the transmitter frequency, ν_{T_X} (herein, the ν_{off} is set to zero, meaning that the centre of the frequency sweep range occurs at ν_{T_X}). The "effective" (or "apparent") frequency of the pulse is then:[53]

$$\nu_{eff}(t) = \frac{d\phi}{dt}\frac{1}{2\pi} = \pm\left(\frac{\Delta}{2} - \frac{\Delta}{\tau_p}t\right) \quad [5.8]$$

From eq. [5.8], it is clear that Δ and τ_p play key roles in determining how WURST pulses behave. Note that the direction of the frequency sweep is from low to high frequency when eq. [5.8] is negative, and from high- to low-frequency when positive.

In producing a WURST pulse with digital phase modulation, a discrete number of increments must be chosen such to accurately represent the phase profile. Therefore, the number of points (*np*) making up the pulse (and corresponding phase modulation) is one factor that controls how accurately the phase profile is represented. The other is the *dwell time* of the WURST pulse ($dwp = \tau_p/np$, reported in ns). The effect of *np* and *dwp* on the appearance of a WURST phase profile is demonstrated in **Figure 5.6A, 5.6B** and **5.6C**, with τ_p = 50 μs and Δ = 2000 kHz and 50, 100, and 200 points, respectively (this corresponds to *dwp* values of 1000, 500, and 250 ns, respectively). It is clear that the phase profiles with shorter dwell times produce "smoother" phase sweeps. However, the choice of *dwp* depends on two important considerations: (i) *dwp* determines the maximum possible sweep range (Δ_{max}) of the WURST pulse according to $\Delta_{max} = 1/dwp$,[53] and (ii) *dwp* has to satisfy the Nyquist criterion, which generally states that in order to accurately represent the digital signal, the sampling frequency has to be at least twice as high as the highest frequency in the digital signal.[54]

As it pertains to WURST pulses, the Nyquist criterion can be viewed as the maximum dwell time that allows for the proper execution of the WURST pulse (we refer to this as the dwp_{max}). For instance, for Δ = 1000 kHz, the WURST pulse is sweeping a region of ±500 kHz around the transmitter frequency. The *dwp* must be 1000 ns or less, since values even slightly higher than this result in a phase profile that does not correctly

represent the virtual frequency sweep at the limits of ±500 kHz (i.e., the sweep width is reduced), and much longer dwell times can corrupt the intended sweep altogether (*vide infra*).

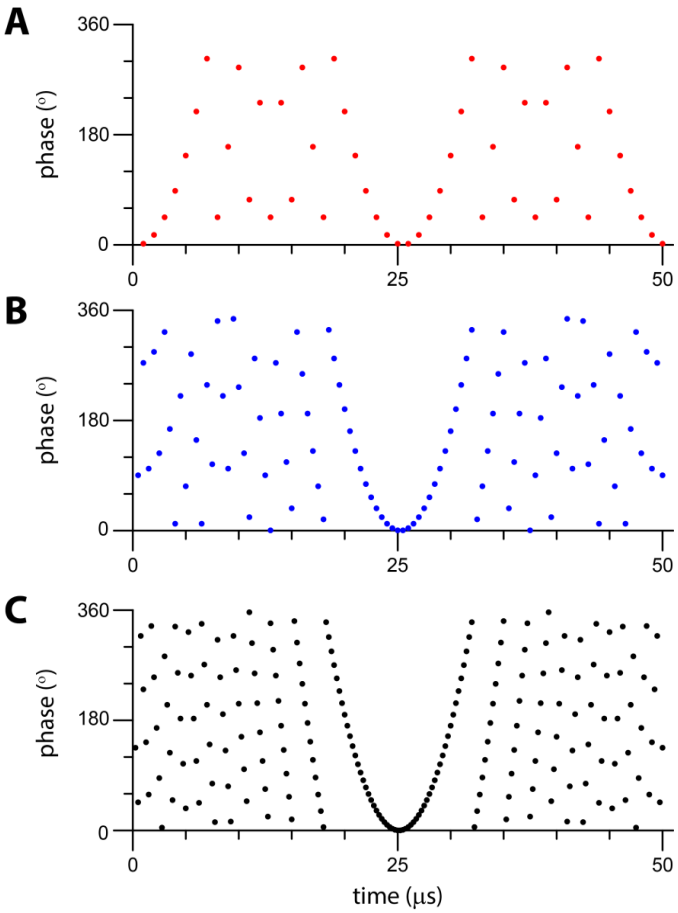

Figure 5.6. Phase profiles of 50 μs WURST pulses with Δ = 200 kHz made up of (A) 50, (B) 100, and (C) 200 points, resulting in dwell times (*dwp*) of 200 ns, 100 ns, and 50 ns, respectively.

In order to demonstrate the effect of the *dwp* value on ^{14}N NMR powder patterns, and how the dwp_{max} changes depending on the choice of Δ, we have acquired a series of ^{14}N sub-spectra of glycine HCl utilizing the WURST-CPMG pulse sequence (**Figure 5.7,** the transmitter frequency is set to −250 kHz from the ^{14}N Larmor frequency, i.e., ν_{T_X} =

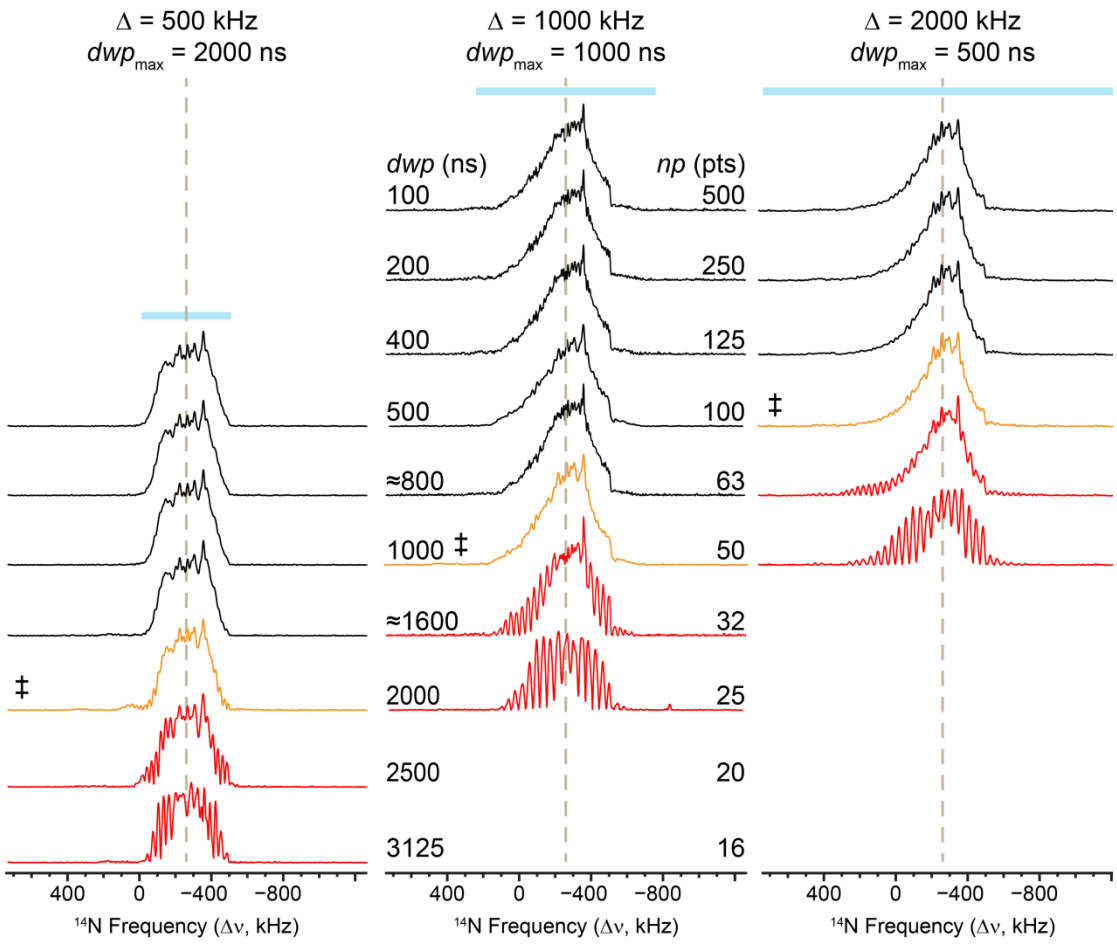

Figure 5.7. ^{14}N SSNMR sub-spectra of glycine HCl acquired at $\Delta\nu_{T_X}$ = −250 kHz (marked by the vertical dashed line) demonstrating the effect of the *dwp* on the spectral quality. Each column represents a different Δ (listed at the top and represented by the blue pale box) and corresponding Nyquist dwell time (dwp_{max}). In their respective columns, sub-spectra acquired with $dwp < dwp_{max}$ (black) look essentially identical, appear free of distortions, and are invariant to the *dwp* value. Sub-spectra acquired with $dwp = dwp_{max}$ (orange, marked by ‡) show signs of distortions near the outer edges of the sweep range. Sub-spectra acquired with $dwp > dwp_{max}$ (red) are severely distorted.

28.599 MHz at 9.4 T, marked by the vertical dashed line. Herein, the offset of the transmitter frequency from the Larmor frequency is symbolized by $\Delta\nu_{T_X} = \nu_{T_X} - \nu_0$. There are three columns, each representing different Δ values (from left to right: 500, 1000, and 2000 kHz, represented by the pale boxes). All pulses are τ_p = 50 μs in length, and from top to bottom in each column, the *np* and *dwp* decrease and increase, respectively. The

sub-spectra corresponding to the condition $dwp = dwp_{max}$ are marked by double daggers (‡) in their respective columns (these are referred to as the *Nyquist spectra* for short). In each column, when $dwp < dwp_{max}$ (sub-spectra displayed above the Nyquist spectrum), the sub-spectra are essentially identical and distortion free, since the phase profile results in a correctly executed frequency sweep. By contrast, if $dwp > dwp_{max}$ (sub-spectra displayed below the Nyquist spectrum), there are severe distortions arising from errant frequency sweeps, which result from the undersampled phase profile. It is noted that minor distortions are observed in the Nyquist spectra.

From these data, we can conclude that decreasing the *dwp* allows for uniform excitation of the desired spectral range and the avoidance of distortions in the spectrum due to undersampling of the WURST pulse. There is no benefit to using *dwp* values that are larger than the Nyquist limit. The only issues we have encountered with using small *dwp* and large *np* values are spectrometer memory allocation errors. Based on numerous tests and experiments on other samples, we recommend using a *dwp* between 100 – 400 ns to avoid spectrometer memory allocation issues while still having potential to execute very broad WURST sweep ranges ranging from 10.0 to 2.5 MHz.

Another important factor in obtaining uniform excitation is the *linear sweep rate* (R) of the pulse ($R = \Delta/\tau_p$, reported in kHz/μs herein). The value of R must be selected in order to ensure that the maximum amount of spin polarization that is excited during the sweep remains locked along the effective field, $\mathbf{B}_{eff}$. The phase profiles for three 50 μs WURST pulses are shown in **Figs. 5.8A-C**, with Δ = 500, 1000, and 2000 kHz, respectively. R is the second derivative of the phase profile; hence, the steepest slope corresponds to the largest Δ (**Figure 5.8D**).

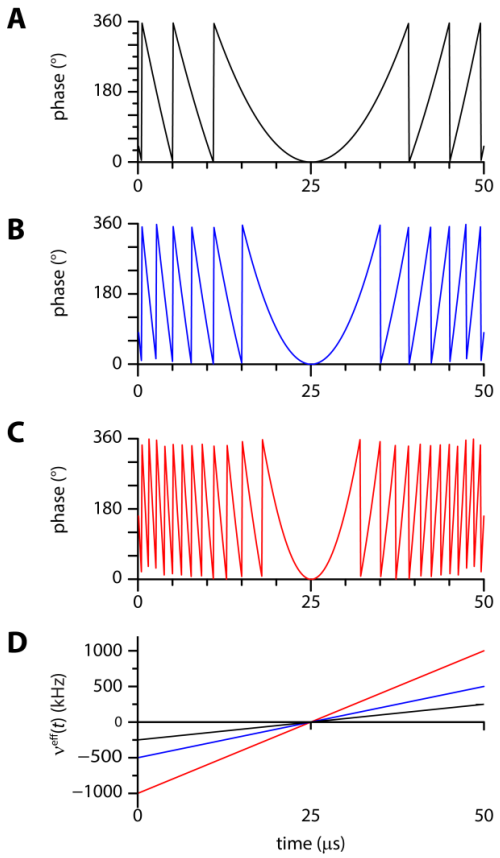

Figure 5.8. Phase profiles of 50 μs WURST pulses with *dwp* = 100 ns and Δ = (A) 500, (B) 1000, and (C) 2000 kHz, resulting in linear sweep rates (*R*) of 10 kHz/μs, 20 kHz/μs, and 40 kHz/μs, respectively. (D) The first derivative (effective transmitter frequency, $\nu^{eff}(t)$, *vs*. time) of the phase profiles in A, B, and C.

Some criteria for choosing *R* have been suggested by Frydman *et al*.[33] and O'Dell *et al*.[28] In both cases, the suggested value of *R* for use with WURST pulses is related to their rf amplitudes by the formula:

$$\nu_{rf} = \frac{A\sqrt{R}}{I + \frac{1}{2}} \qquad [5.9]$$

where ν_{rf} is the rf frequency of the pulse (in Hz), *R* is the linear sweep rate of the pulse (Hz/s or s^{-2}), and *A* is an empirically determined parameter (unitless), found to range from 0.12 to 0.49.[28,33]

In our ^{14}N NMR experiments, the typical value of ν_{rf} is 28.8 kHz (corresponding to a $\pi/2 = 9$ μs pulse); hence, this means that *R* can range from as slow as 7.8 kHz/μs to as fast as 129.6 kHz/μs. If 50 μs pulses are used, the Δ of the pulse can range from 390 to 6480 kHz. These Δ and *R* values result in dramatically different pulses; hence, an investigation into how to make the best choices for these values for the acquisition of UW ^{14}N SSNMR powder patterns was undertaken.

The value of *R* is chosen by changing either Δ or τ_p while keeping the other constant. **Figure 5.9A** illustrates the effect of *R* on the overall quality of the ^{14}N sub-spectra when Δ is varied between 250 and 6000 kHz (top to bottom) while keeping τ_p constant ($\tau_p = 50$ μs). In **Figure 5.9B**, Δ is kept constant (Δ = 750 kHz) and τ_p is varied from 150 to 18 μs (top to bottom). All of the WURST waveforms have *dwp* = 100 ns and $\Delta\nu_{T_x} = -250$ kHz. On the left side of each sub-spectrum, the Δ or τ_p and related *R* values are listed. On the right side, two more numbers are listed: the total breadth of the resulting sub-spectrum (*B*, in kHz) and a ratio of *B*/Δ (expressed in %).

Careful examination of these sub-spectra reveal that when *R* = 10 kHz/μs (i.e., the blue sub-spectra, marked with ‡), their breadths are nearly 100% of Δ and they are free of distortions. This *R* value corresponds to an *A* = 0.42, which is within the range of suggested *A* values.[28] We have conducted SIMPSON simulations to investigate whether the excitation bandwidths produced by our WURST pulses are limited by the excitation or detection bandwidths of our probe (**Figure D2**). The simulations match well with the experimental patterns, indicating that the probe characteristics (i.e., the *Q*-factor) are not relevant in this case. For nuclides with higher Larmor frequencies, where broader sweeps are possible, this may become a factor.

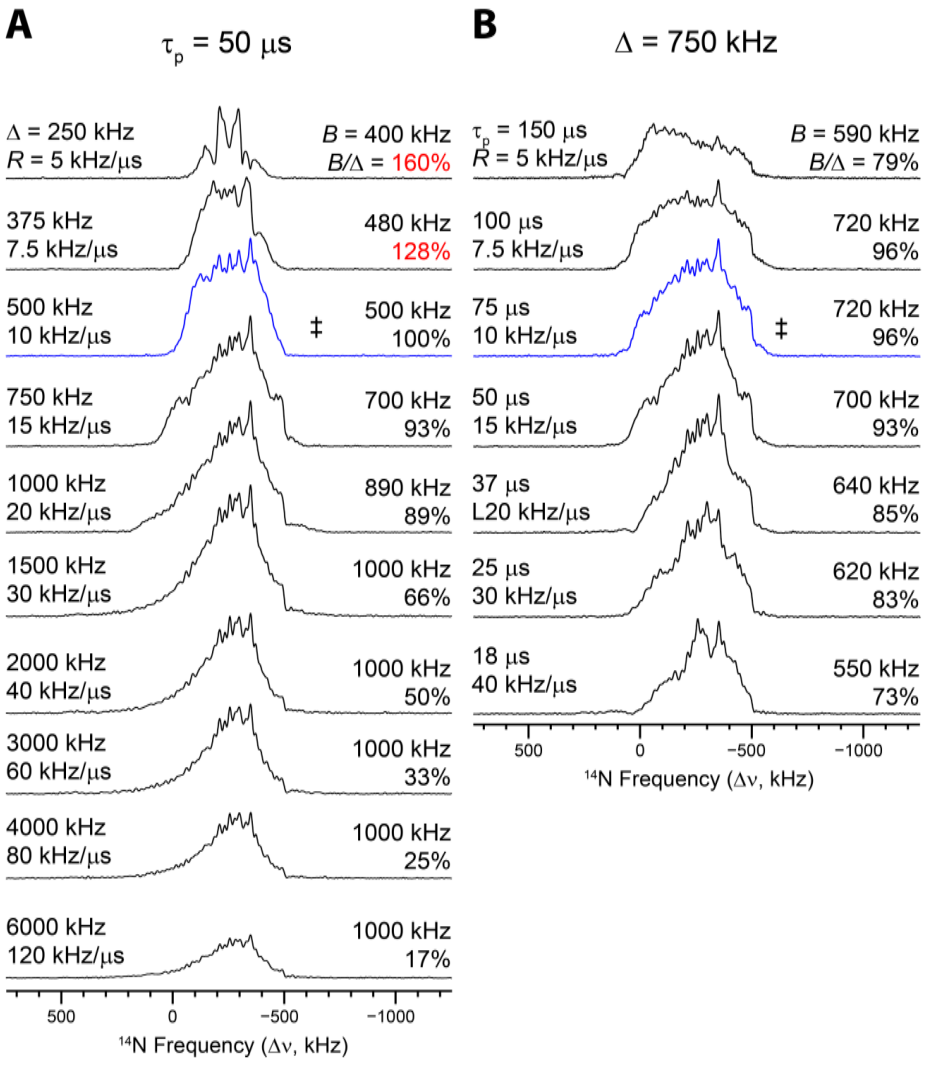

Figure 5.9. ^{14}N SSNMR sub-spectra of glycine HCl acquired at $\Delta\nu_{T_x}$ = −250 kHz demonstrating the effect of the *linear sweep rate* (*R*) of the WURST pulse on the spectral quality. In (A) the pulse length is kept constant (τ_p = 50 μs) while Δ is increased from 250 (top) to 6000 kHz (bottom). In (B), the sweep range, Δ, is kept constant (Δ = 750 kHz) while τ_p is shortened from 150 (top) to 18 μs (bottom). In both cases (A and B), R increases from top to bottom. The τ_p or Δ and corresponding *R* are listed on the left side of each sub-spectrum. The excitation bandwidth, *B*, of each sub-spectrum is listed on the right side (both as kHz and as a percentage, *B*/Δ). The sub-spectra are represented without scaling of their intensities. The sub-spectra highlighted in blue (marked with ‡) represent the optimal cases of broad excitation bandwidth and minimal distortions.

There are many combinations of τ_p and Δ that result in the same value of *R* (e.g., τ_p = 50 μs and Δ = 500 kHz, τ_p = 125 μs and Δ = 1250 kHz, etc.); therefore, it is important to find the optimal combination of τ_p and Δ that will provide both high S/N and uniform excitation. ^{14}N sub-spectra of glycine HCl and α-glycine (**Figure 5.10**) have been acquired with various combinations of τ_p and Δ that all correspond to an *R* value of 10 kHz/μs. For both samples, the blue sub-spectra (marked with a ‡) are optimal in terms of S/N, excitation breadth, and uniformity (a frequency range of ca. 900 kHz is excited), and also have the best efficiency in terms of excitation breadth, as expressed by the ratio B/Δ. These were obtained with τ_p and Δ values of 100 μs and 1000 kHz, respectively. Longer values of τ_p permit for excitation of broader regions; however, as τ_p is increased, there is increased stress on the probe. During such experiments, one must be mindful of the duty cycle and work within the limitations of the hardware (mainly the probe). In cases where a longer τ_p is advantageous for broader sweeps, the number of echoes that are collected can be slightly reduced to reduce the duty cycle; this is useful in cases where the gain in excitation breadth outweighs the small reduction in S/N (**Figure D3**).

These pulse widths, sweep ranges, and concomitant sweep rates and *A* values, were used to acquire the remainder of the ^{14}N spectra that are discussed herein. Of course, further work is necessary to examine the effects of variation of these parameters on the spectra of extremely broad ^{14}N patterns arising from larger quadrupolar interactions.

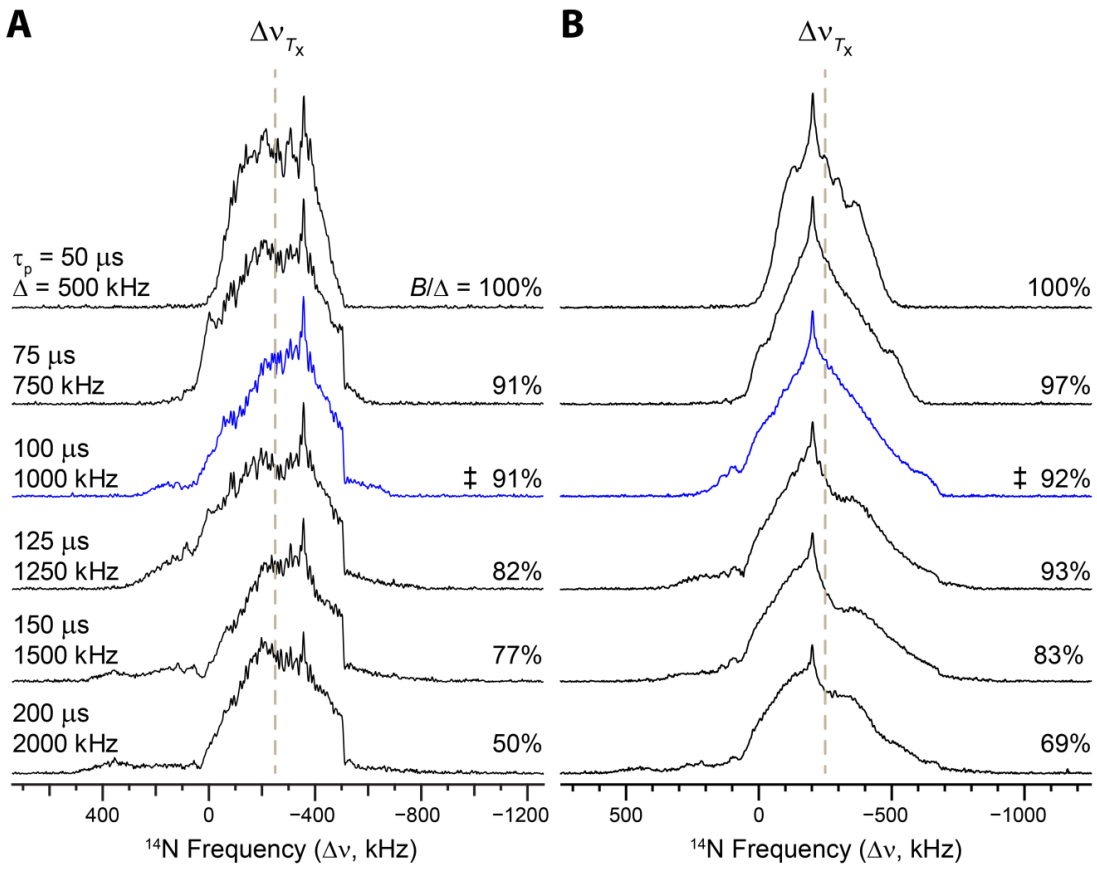

Figure 5.10. ^{14}N SSNMR sub-spectra acquired at $\Delta\nu_{T_x}$ = −250 kHz (marked by the vertical dashed line) using WURST pulses with R = 10 kHz/μs. Sub-spectra in column (A) are of glycine HCl while those in column (B) are of α-glycine. The τ_p and corresponding Δ are listed for each row. B/Δ is listed for each sub-spectrum. The sub-spectra highlighted in blue (marked with a ‡) represent the best combination of S/N and excitation bandwidth while minimizing spectral distortions.

5.4.4. Minimizing the number of sub-spectra for a frequency-stepped acquisition

For UW NMR experiments on most quadrupolar nuclides, it is crucial that the entire powder pattern be acquired, so that all of the discontinuities can be identified, and the relevant NMR interaction tensor parameters can be extracted. As discussed in section 3.1, this is not the case for ^{14}N powder patterns with breadths between ca. 0.7 and 3.0 MHz, since these patterns are dominated by the FOQI and are mirror symmetric to first order. This raises the intriguing possibility of minimizing the number of sub-spectra that

have to be acquired in order to obtain an accurate measurement of all of the positions of the discontinuities in the ^{14}N NMR spectra. Hence, in this section, a strategy is presented for determining the C_Q and η_Q values for ^{14}N sites with $0.8 \leq |C_Q| \leq 1.5$ MHz by collecting only two sub-spectra. Again, this range is of particular interest, since most pseudo-tetrahedral nitrogens (i.e., RNH_3^+, $RR'NH_2^+$, and $RR'R''NH^+$) have C_Q values within these limits. It is noted that in this case, the choice of two sub-spectra is determined by the pattern breadths as well as the *Q*-factor of our 5 mm HX probe. The methodology proposed below can be altered to suit different probe configurations.

Analytical simulations of ^{14}N powder patterns with C_Q = 0.80, 1.25, and 1.50 MHz are shown in **Figs. 5.11A-C**, respectively. For each value of C_Q, four spectra with different values of η_Q were simulated (0, 0.33, 0.66, and 1). From each spectrum, the frequencies of the horn (ν_{11}) and shoulder (ν_{22}) discontinuities were determined (N.B., we focus on the horn and shoulder discontinuities since they are much more intense than the foot discontinuities). The frequencies are measured with respect to the ^{14}N Larmor frequency (i.e., $\Delta\nu_{T_X}$ = 0 kHz) for the purpose of this discussion. Considering only the high frequency halves of the powder pattern, ν_{11} values range from 0 kHz to +568 kHz and ν_{22} values range from +300 kHz to +1120 kHz, for all combinations of C_Q and η_Q (N.B., for the low-frequency halves, all of the discontinuities have the same frequencies (but opposite signs) as those of the corresponding discontinuities in the high-frequency halves). The frequency ranges in which the discontinuities ν_{11} and ν_{22} occur span 568 kHz and 820 kHz, respectively; therefore, with the use of optimized WURST pulses that are positioned approximately at the centre of each range, it is possible to observe the horn

and shoulder discontinuities (the sweep ranges of the WURST pulses are represented in the figure by the blue and pink pale boxes, respectively).

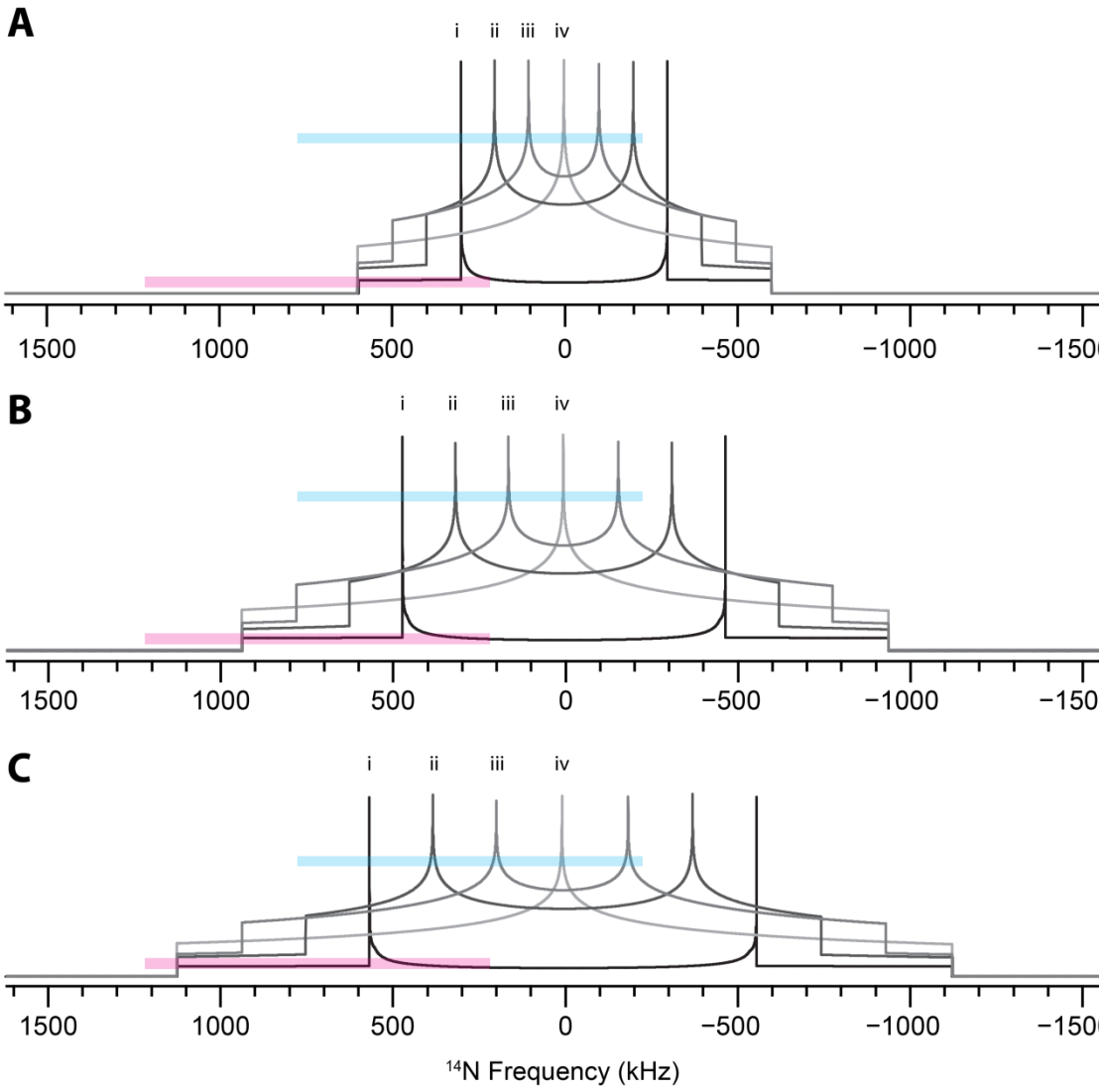

Figure 5.11. Analytical simulations of ^{14}N powder patterns with (A) C_Q = 0.80 MHz, (B) C_Q = 1.25 MHz, and (C) C_Q = 1.5 MHz. The positions of the horn discontinuities in the high-frequency halves of the powders patterns are marked with i, ii, iii, and iv for η_Q = 0, 0.33, 0.66, and 1, respectively. Pale blue box represents a WURST pulse with a 1000 kHz sweep range, centered at $\Delta\nu_{T_x}$ = +283 kHz. Pale pink box represents a WURST pulse with a 1000 kHz sweep range, centered at $\Delta\nu_{T_x}$ = +714 kHz.

The centre frequency of the ν_{11} range is +284 kHz; therefore, applying a WURST pulse near $\Delta\nu_{T_x}$ = +284 kHz permits a frequency sweep that guarantees the excitation of the horn discontinuity, regardless of the magnitude of η_Q. The centre of the ν_{22} frequency range is at approximately +714 kHz; so similarly, applying a WURST pulse near this position excites the shoulder discontinuity, regardless of the magnitude of η_Q. The frequency of the foot discontinuity falls within the sweep range of the WURST pulse meant to excite the ν_{22} discontinuity (pink pale box); however, in some cases, the detection of the edge of the foot discontinuity may be complicated due to the low S/N in this region.

This approach is demonstrated for a series of compounds in **Figure 5.12**. In each case, the WURST pulse has a sweep range (illustrated by the pale box in the figure) wide enough to ensure that it sweeps over all of the possible frequencies of the horn and shoulder discontinuities in their respective sub-spectra (the results are shown in **Table 5.2**). Sub-spectra were acquired at $\Delta\nu_{T_x}$ = ±275 kHz and ±715 kHz, depending upon the hardware configuration (a recent hardware change has temporarily limited our ability to tune to frequencies much higher than $\nu_0(^{14}N)$).

In the two sub-spectra of α-glycine (**Figs. 5.12A** and **5.12B**), all three discontinuities are clearly resolved, and the quadrupolar parameters were determined to be C_Q = 1.19(2) MHz and η_Q = 0.53(3). These values match closely to those measured from the full spectra and reported previously in the literature.[7,8,31,45,55] Using the same strategy for glycylglycine (but with $\Delta\nu_{T_x}$ = −275 kHz and −715 kHz for the two sub-spectra), only the frequencies of the horn and shoulder discontinuities can be measured (**Figs. 5.12C** and **5.12D**). In low-η_Q patterns, the foot discontinuities often have low S/N,

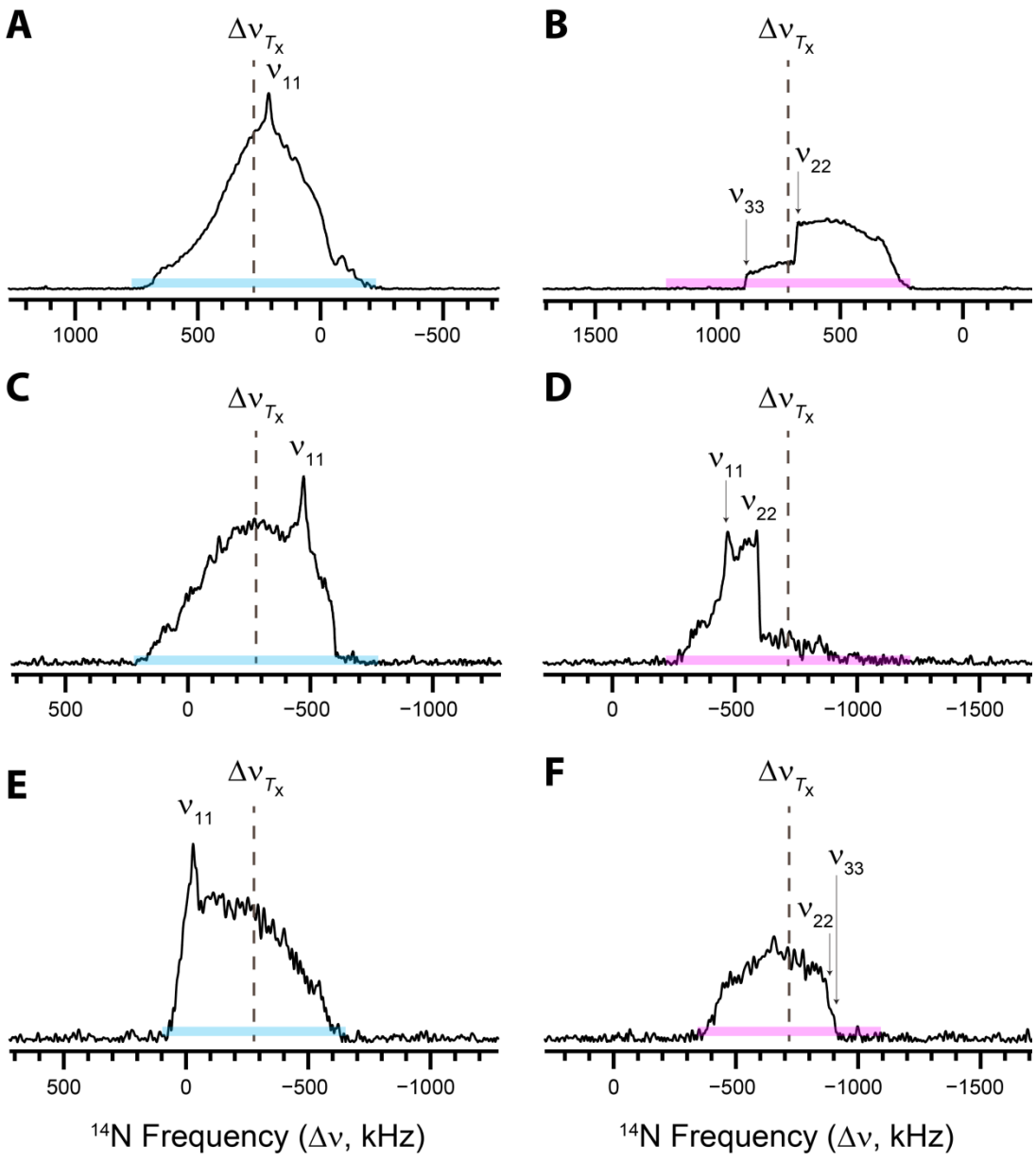

Figure 5.12. ^{14}N sub-spectra acquired at $\Delta\nu_{T_x}$ = ±275 kHz and $\Delta\nu_{T_x}$ = ±715 kHz for (A) and (B) α-glycine, (C) and (D) glycylglycine, and (E) and (F) 4-hydroxy-L-proline-d_2, respectively. $\Delta\nu_{T_x}$ is marked by the vertical dashed line. The pale boxes indicate the sweep ranges of the WURST pulses. Locations of ν_{11} and ν_{22} are marked directly on the sub-spectra. Where observable, ν_{33} is also indicated.

and cannot clearly be identified. From the horn and shoulder, the ^{14}N quadrupolar parameters were determined to be C_Q = 1.42(2) MHz and η_Q = 0.12(2), also in agreement with previous results.[56] It is of interest to note, that because the pseudo-tetrahedral nitrogen moiety of glycylglycine has an η_Q that is nearly zero, the horn and shoulder discontinuities nearly overlap and are both observed in the same sub-spectrum. The sub-spectra of 4-hydroxy-*L*-proline-d_2 (**Figs. 5.12E** and **5.12F**) show all three discontinuities, yielding C_Q = 1.21(2) MHz and η_Q = 0.94(3), which are also in good agreement with values from a previous ^{14}N NQR study.[8]

This strategy is effective for determining C_Q and η_Q from ^{14}N SSNMR powder patterns having $0.8 \leq |C_Q| \leq 1.5$ MHz and any value of η_Q. In all cases herein, a minimum of two discontinuities were observed, from which the quadrupolar parameters were extracted. It is important to note that ^{14}N powder patterns can sometimes display

Table 5.2. Frequencies of the horn, shoulder, and foot discontinuities, with associated ^{14}N quadrupolar parameters.

Sample	$\Delta\nu_{T_x}$ (kHz)	Frequency of discontinuities (kHz)[a] ν_{11}	ν_{22}	ν_{33}	Calculated using $\nu_{11} + \nu_{22}$ [b] $\lvert C_Q\rvert$ (MHz)	η_Q	WSolids Simulation $\lvert C_Q\rvert$ (MHz)	η_Q
α-glycine	+275	211(10)	--	--	1.19(2)	0.53(3)	1.19(2)	0.52(2)
	+715	--	681(20)	890(20)				
glycyl glycine	−275	−469(10)	--	--	1.42(1)	0.12(1)	1.44(2)	0.12(2)
	−715	--	−597(20)	--				
4-hydroxy-*L*-proline-d_2	−275	−29(20)	--	--	1.21(2)	0.94(3)	1.20(2)	0.92(2)
	−715	--	−875(20)	−907(20)				

[a] Uncertainty in frequency of discontinuity is based on the breadth of the discontinuity. The frequencies of the discontinuities are listed in the same rows as the transmitter frequencies used to obtain them. [b] $|C_Q|$ and η_Q were calculated from eqs. [5.5c] and [5.6b], respectively.

the effects of dynamical motions,[1] which may be misinterpreted or missed entirely if only two sub-spectra are collected; however, this is only a problem if these motions introduce an asymmetry into the ^{14}N patterns. This strategy should also be suitable for dealing with ^{14}N spectra arising from two or more overlapping ^{14}N patterns (provided that both are within the aforementioned range of C_Q values); simulation of overlapping patterns is aided by the observation of all of the discontinuities from each pattern.

5.5. Conclusions

In this work, we have demonstrated several methods that may be used to acquire UW ^{14}N SSNMR powder patterns that are uniformly excited and have high S/N ratios.

First, if ^{14}N patterns are dominated by the FOQI, the positions of the horn, shoulder and foot discontinuities on each side of the pattern are equidistant from the ^{14}N Larmor frequency (consideration of nitrogen chemical shifts can generally be neglected due to the small chemical shift range of organic pseudo-tetrahedral nitrogen moieties, *ca*. 30 ppm, i.e., ca. 900 Hz at 9.4 T and ca. 2000 Hz at 21.1 T). This means that only half of the pattern needs to be acquired. Furthermore, since the ^{14}N EFG tensor is traceless, accurate measurement of the positions of only two discontinuities is sufficient for determining C_Q and η_Q.

Second, when using WURST-CPMG and related pulse sequences, we have demonstrated that care must be taken to (i) not truncate the spin echoes in each acquisition window (for this class of ^{14}N experiments we recommend acquisition windows of 50 μs or longer), (ii) acquire as many echoes as possible by ensuring their spacings are as close as possible, and (iii) temper the total acquisition period by

considering the total duty cycle on the probe, especially since high-power ^{1}H decoupling is almost always applied over the entire duration of the pulse sequence. It is highly recommended to co-add the spin echoes prior to Fourier transform, since the spectral resolution is limited by the dwell time in this case, and not the separation of the spikelets (as in the case of directly Fourier transforming the echo train).

Third, we have carefully investigated the relationships between key parameters which define the WURST pulses: the number of points (*np*), the pulse width (τ_p), and the sweep range (Δ). The first key parameter for producing a WURST pulse which yields maximum S/N and uniform excitation is the dwell time of the pulse ($dwp = np/\tau_p$). If *dwp* is set to be shorter than the Nyquist dwell time (dwp_{max}), the resulting spectra are generally free of distortions; however, if $dwp \geq dwp_{max}$, the resulting spectra exhibit distortions arising from undersampling (i.e., the WURST pulse does not have the appropriate values of *dwp* and *np* to properly sweep over the specified Δ). The second key parameter is the linear sweep rate (*R*) of the WURST pulse; for the ^{14}N SSNMR experiments focused on patterns with breadths of 1 MHz or greater, we found that $R = 10$ kHz/μs yielded high S/N and minimal distortions. Attention must be paid to the values of τ_p and Δ that are chosen to define *R* (for these ^{14}N spectra, a combination $\tau_p = 100$ μs and $\Delta = 1000$ kHz was observed to yield the best results for α-glycine).

Finally, a strategy was developed that incorporates the three points above, which allows the determination of the ^{14}N quadrupolar parameters for nitrogen moieties having $0.8 \leq |C_Q| \leq 1.5$ MHz by acquiring only two sub-spectra (at $\Delta\nu_{T_x} = \pm 275$ kHz and at $\Delta\nu_{T_x} = \pm 715$ kHz, respectively). This strategy can been modified accordingly for patterns arising

from even larger C_Q values, or for cases where the probe/hardware combination results in expanded or reduced excitation and/or detection bandwidths.

We believe that the discussion presented herein is not only beneficial to those who are interested in utilizing ^{14}N SSNMR for the characterization of a wide variety of nitrogen-containing materials, but also for applying WURST pulses for the acquisition of ultra-wideline NMR spectra of many nuclides across the periodic table. For instance, these same methods may be of interest to NMR spectroscopists who are interested in acquiring natural abundance ^{10}B (I = 3) NMR spectra, which exhibit similarly broad and symmetric patterns, but with an increased number of satellite transitions.[29,57] This could find use in the study of both crystalline and amorphous materials, including many type of borosilicate glasses. Further systematic studies, involving both experimental trials and theoretical simulations, are currently underway in our research group.

5.6 Bibliography

(1) O'Dell, L. A.; Schurko, R. W.; Harris, K. J.; Autschbach, J.; Ratcliffe, C. I. *J. Am. Chem. Soc.* **2011**, *133*, 527.

(2) Mirzaei, M.; Elmi, F.; Hadipour, N. L. *J. Phys. Chem. B* **2006**, *110*, 10991.

(3) O'Dell, L. A. *Prog. Nucl. Magn. Reson. Spectrosc.* **2011**, *59*, 295.

(4) O'Dell, L. A. *Annu. Reports NMR Spectrosc.* **2015**, *86*, 211.

(5) Abragam, A. In *The Principles of Nuclear Magnetic Resonance*; Claredon Press: Oxford, 1983; p. Chapter VII.

(6) *Introduction to Solid-State NMR Spectroscopy*; Duer, M. J., Ed.; Wiley-Blackwell, 2004.

(7) Giavani, T.; Bildsøe, H.; Skibsted, J.; Jakobsen, H. J. *J. Magn. Reson.* **2004**, *166*, 262.

(8) Edmonds, D. T. *Phys. Rep.* **1977**, *29*, 233.

(9) Schurko, R. W. *Acc. Chem. Res.* **2013**, *46*, 1985.

(10) Schurko, R. W. Acquisition of Wideline Solid-State NMR Spectra of Quadrupolar Nuclei. *Encyclopedia of Magnetic Resonance*, 2012.

(11) Whitehouse, B. A.; Ray, J. D.; Royer, D. J. *J. Magn. Reson.* **1969**, *1*, 311.

(12) Hilbers, C. W.; Maclean, C. *Mol. Phys.* **1969**, *16*, 275.

(13) Yannoni, C. S. *J. Chem. Phys.* **1970**, *52*, 2005.

(14) Tycko, R.; Opella, S. J. *J. Chem. Phys.* **1987**, *86*, 1761.

(15) O'Dell, L. A.; Brinkmann, A. *J. Chem. Phys.* **2013**, *138*, 064201.

(16) O'Dell, L. A.; He, R.; Pandohee, J. *CrystEngComm* **2013**, *15*, 8657.

(17) Harris, R. K.; Jonsen, P.; Packer, K. J. *Magn. Reson. Chem.* **1985**, *23*, 565.

(18) Harris, R. K.; Olivieri, A. C. *Prog. Nucl. Magn. Reson. Spectrosc.* **1992**, *24*, 435.

(19) Cavadini, S.; Lupulescu, A.; Antonijevic, S.; Bodenhausen, G. *J. Am. Chem. Soc.* **2006**, *128*, 7706.

(20) Cavadini, S.; Abraham, A.; Ulzega, S.; Bodenhausen, G. *J. Am. Chem. Soc.* **2008**, *130*, 10850.

(21) Cavadini, S.; Vitzthum, V.; Ulzega, S.; Abraham, A.; Bodenhausen, G. *J. Magn. Reson.* **2010**, *202*, 57.

(22) Tatton, A. S.; Pham, T. N.; Vogt, F. G.; Iuga, D.; Edwards, A. J.; Brown, S. P. *Mol. Pharm.* **2013**, *10*, 999.

(23) Shen, M.; Trébosc, J.; Lafon, O.; Pourpoint, F.; Hu, B.; Chen, Q.; Amoureux, J.-P. *J. Magn. Reson.* **2014**, *245*, 38.

(24) Pandey, M. K.; Nishiyama, Y. *Solid State Nucl. Magn. Reson.* **2015**, *70*, 15.

(25) Reddy, G. N. M.; Marsh, A.; Davis, J. T.; Masiero, S.; Brown, S. P. *Cryst. Growth Des.* **2015**, *15*, 5945.

(26) Cavadini, S. *Prog. Nucl. Magn. Reson. Spectrosc.* **2010**, *56*, 46.

(27) Tang, J. A.; Masuda, J. D.; Boyle, T. J.; Schurko, R. W. *ChemPhysChem* **2006**, *7*, 117.

(28) O'Dell, L. A.; Schurko, R. W. *Chem. Phys. Lett.* **2008**, *464*, 97.

(29) O'Dell, L. A.; Rossini, A. J.; Schurko, R. W. *Chem. Phys. Lett.* **2009**, *468*, 330.

(30) O'Dell, L. A.; Schurko, R. W. *J. Am. Chem. Soc.* **2009**, *131*, 6658.

(31) O'Dell, L. A.; Schurko, R. W. *Phys. Chem. Chem. Phys.* **2009**, *11*, 7069.

(32) Kupče, Ē.; Freeman, R. *J. Magn. Reson. Ser. A* **1995**, *115*, 273.

(33) Bhattacharyya, R.; Frydman, L. *J. Chem. Phys.* **2007**, *127*, 1.

(34) Tang, J. A.; O'Dell, L. A.; Aguiar, P. M.; Lucier, B. E. G.; Sakellariou, D.; Schurko, R. W. *Chem. Phys. Lett.* **2008**, *466*, 227.

(35) Lucier, B. E. G.; Johnston, K. E.; Xu, W.; Hanson, J. C.; Senanayake, S. D.; Yao, S.; Bourassa, M. W.; Srebro, M.; Autschbach, J.; Schurko, R. W. *J. Am. Chem. Soc.* **2014**, *136*, 1333.

(36) Rossini, A. J.; Macgregor, A. W.; Smith, A. S.; Schatte, G.; Schurko, R. W.; Briand, G. G. *Dalton Trans.* **2013**, *42*, 9533.

(37) Lucier, B. E. G.; Reidel, A. R.; Schurko, R. W. *Can. J. Chem.* **2011**, *89*, 919.

(38) MacGregor, A. W.; O'Dell, L. A.; Schurko, R. W. *J. Magn. Reson.* **2011**, *208*, 103.

(39) Lefort, R.; Wiench, J. W.; Pruski, M.; Amoureux, J.-P. *J. Chem. Phys.* **2002**, *116*, 2493.

(40) Dey, K. K.; Ash, J. T.; Trease, N. M.; Grandinetti, P. J. *J. Chem. Phys.* **2010**, *133*, 054501.

(41) Hung, I.; Gan, Z. *J. Magn. Reson.* **2010**, *204*, 256.

(42) Massiot, D.; Farnan, I.; Gautier, N.; Trumeau, D.; Trokiner, A.; Coutures, J. P. *Solid State Nucl. Magn. Reson.* **1995**, *4*, 241.

(43) Medek, A.; Frydman, V.; Frydman, L. *J. Phys. Chem.* **1999**, *103*, 4830.

(44) Harris, K. J.; Lupulescu, A.; Lucier, B. E. G.; Frydman, L.; Schurko, R. W. *J. Magn. Reson.* **2012**, *224*, 38.

(45) Veinberg, S. L.; Friedl, Z. W.; Harris, K. J.; O'Dell, L. A.; Schurko, R. W. *CrystEngComm* **2015**, 17.

(46) Cavadini, S.; Abraham, A.; Bodenhausen, G. *J. Magn. Reson.* **2008**, *190*, 160.

(47) Eichele, K. WSolids1 — Solid State NMR Simulations, 2013.

(48) Bak, M.; Rasmussen, J. T.; Nielsen, N. C. *J. Magn. Reson.* **2000**, *147*, 296.

(49) Penner, G. H. *Chem. Phys.* **1996**, *261*, 665.

(50) Boddenberg, B.; Grosse, R. *Zeitschrift fur Naturforsch. - Sect. A J. Phys. Sci.* **1986**, *41a*, 1361.

(51) Boddenberg, B.; Große, R. *Zeitschrift fur Naturforsch. - Sect. A J. Phys. Sci.* **1988**,

43a, 497.

(52) Schimiczek, B.; Greth, R.; Boddenberg, B. *Mol. Phys.* **1994**, *82*, 369.

(53) O'Dell, L. A. *Solid State Nucl. Magn. Reson.* **2013**, *55-56*, 28.

(54) Fukushima, E.; Roeder, S. B. W. *Experimental Pulse NMR - A Nuts and Bolts Approach*; Addison-Wesley Publishing Company, Inc.: Reading, Massachusetts, 1981.

(55) Harris, K. J.; Veinberg, S. L.; Mireault, C. R.; Lupulescu, A.; Frydman, L.; Schurko, R. W. *Chem. Eur. J.* **2013**, *19*, 16469.

(56) Veinberg, S. L.; Friedl, Z. W.; Lindquist, A. W.; Kispal, B. M.; Harris, K. J.; O'Dell, L. A.; Schurko, R. W. *Chem. Eur. J.* **2016**, *submitted*.

(57) Holland, D.; Feller, S. A.; Kemp, T. F.; Smith, M. E.; Howes, A. P.; Winslow, D.; Kodama, M. *Eur. J. Glas. Sci. Technol. Part B* **2007**, *48*, 1.

Chapter 6 – Natural Abundance ^{14}N and ^{15}N Solid-State NMR of Pharmaceuticals and their Polymorphs

6.1 Overview

^{14}N ultra-wideline (UW), ^{1}H{^{15}N} indirectly-detected HETCOR (idHETCOR) and ^{15}N dynamic nuclear polarization (DNP) solid-state NMR (SSNMR) experiments, in combination with plane-wave density functional theory (DFT) calculations of ^{14}N EFG tensors, were utilized to characterize a series of nitrogen-containing active pharmaceutical ingredients (APIs), including HCl salts of scopolamine, alprenolol, isoprenaline, acebutolol, dibucaine, nicardipine, and ranitidine. A case study applying these methods for the differentiation of polymorphs of bupivacaine HCl is also presented. All experiments were conducted upon samples with naturally-abundant nitrogen isotopes. For most of the APIs, it was possible to acquire frequency-stepped UW ^{14}N SSNMR spectra of stationary samples, which display powder patterns corresponding to pseudo-tetrahedral (*i.e.*, RR′R″NH^{+} and RR′NH$_2^{+}$) or other (*i.e.*, RNH$_2$ and RNO$_2$) nitrogen environments. Directly-excited ^{14}N NMR spectra were acquired using the WURST-CPMG pulse sequence, which incorporates WURST (wideband, uniform rate, and smooth truncation) pulses and a CPMG (Carr-Purcell Meiboom-Gill) refocusing protocol. In certain cases, spectra were acquired using ^{1}H $\rightarrow$ ^{14}N broadband cross-polarization, via the BRAIN-CP (broadband adiabatic inversion - cross polarization) pulse sequence. These spectra provided ^{14}N electric field gradient (EFG) tensor parameters and orientations that are particularly sensitive to variations in local structure and intermolecular hydrogen-bonding interactions. The ^{1}H{^{15}N} idHETCOR spectra, acquired under conditions of fast magic-angle spinning (MAS), used CP transfers to

provide ^{1}H-^{15}N chemical shift correlations for all nitrogen environments, except for two sites in acebutolol and nicardipine. One of these two sites ($RR'NH_2^+$ in acebutolol) was successfully detected using the DNP-enhanced $^{15}N\{^{1}H\}$ CP/MAS measurement, and one (RNO_2 in nicardipine) remained elusive due to the absence of nearby protons. This exploratory study suggests that this combination of techniques has great potential for the characterization of solid APIs and numerous other organic, biological and inorganic systems.

6.2. Introduction

Most active pharmaceutical ingredients (APIs) are manufactured, shipped, stored and ingested as solids (ca. 80%).[1] Characterization of APIs is essential, providing important information on their molecular-level structures and corresponding relationships to their biological activity,[2] solubility,[3,4] stability[5,6] and bioavailability.[5–7] In addition, approximately 80% of all solid APIs exhibit polymorphism or pseudopolymorphism (i.e., formation of hydrates and solvates). The identification and differentiation of polymorphic forms is of the utmost importance to the pharmaceutical industry as each polymorph may possess a unique set of physiochemical properties, which also has implications in patenting rights.[8–11]

APIs and their associated polymorphs are most commonly characterized using techniques such as single-crystal or powder X-ray diffraction (scXRD, pXRD), as well as ^{1}H and ^{13}C solution- and solid-state NMR (SSNMR). Several multinuclear SSNMR studies of APIs featuring other nuclides such as ^{2}H, ^{11}B, ^{15}N, ^{17}O, ^{19}F, ^{23}Na, ^{27}Al, ^{31}P, and ^{77}Se have also been reported in recent years.[12–35] Furthermore, it has been recently

demonstrated that ^{35}Cl SSNMR can provide important structural information about the chlorine sites in different polymorphic forms in APIs, including the nature of the hydrogen bonding environments and impurity phases, in reduced experimental times compared to conventional pXRD and ^{13}C SSNMR experiments.[21,29,36–38] For further reading on the use of SSNMR to characterize pharmaceutical compounds, we refer readers to recent reviews by Vogt and Monti *et al*.[39–41]

Given the ubiquity of nitrogen in functional groups such as amines, amides and heterocyclic nitrogen atoms, and the importance of intermolecular hydrogen-bonding interactions of nitrogen in solid APIs, the naturally occurring NMR-active nitrogen nuclei, ^{14}N and ^{15}N, could provide exclusive insights into their structures. Both nuclides yield NMR responses that are exceptionally sensitive to their local environments, and yet are among the most challenging isotopes for spectroscopic investigation by NMR (*vide infra*). Numerous studies employing ^{14}N and ^{15}N SSNMR, as well as quantum chemical computations, have recently been attempted for a variety of different compounds, including organic and biological samples,[42–51] amino acids,[52–59] and pharmaceuticals.[24,60–66] ^{14}N nuclear quadrupole resonance (NQR) spectroscopy has also recently been applied, with some success, to a variety of APIs for purposes of quantification and polymorph differentiation.[67–72]

The vast majority of SSNMR studies involving nitrogen have focussed upon the spin-1/2 ^{15}N nuclide, predominantly due to its relatively narrow spectral lines. However, owing to the inherently low natural abundance and low gyromagnetic ratio (γ) of ^{15}N, samples are typically isotopically enriched, which can be both costly and difficult to achieve. By contrast, there are far fewer ^{14}N (spin = 1) SSNMR studies,[73] due to an even

lower value of γ, and more importantly, its large nuclear quadrupole moment (eQ = 20.44 mbarn). The quadrupolar nature of ^{14}N nuclei is particularly challenging for SSNMR experimentation, as the first-order quadrupolar interaction can cause extreme broadening of ^{14}N SSNMR powder patterns, yielding the so-called Pake doublets which can span several MHz. This broadening occurs in cases where an aspherical ground-state electronic environment causes a sizeable electric field gradient (EFG) at the ^{14}N nucleus; in fact, this is the case for most systems, with the exception of ^{14}N nuclei in environments of very high spherical/Platonic symmetry, e.g., NH_4^+ ions.[45,74]

A variety of techniques have been explored for the acquisition of ^{14}N SSNMR spectra, including the direct observation of ^{14}N NMR signals from single crystals,[75] ^{14}N magic-angle spinning (MAS) NMR using specialized probes with precisely tuned rotor angles,[53,76] overtone ^{14}N MAS NMR,[77–80] ^{14}N NMR enhanced by dynamic nuclear polarization (DNP)[81] and various indirect detection techniques.[82–86] However, many of these techniques have not been widely adopted thus far owing to technical difficulties, costly hardware and/or issues relating to the nature of the nitrogen sites in samples under investigation. O'Dell and Cavadini recently provided thorough reviews of ^{14}N SSNMR experiments involving direct and indirect detection, respectively.[73,87]

Recently, O'Dell, Schurko and co-workers[55–57] demonstrated that comprehensive SSNMR structural studies of nitrogen-containing systems can be carried out using direct excitation of ^{14}N nuclei by means of the frequency-stepped WURST-CPMG protocol, which proved essential for the rapid acquisition of ^{14}N ultra-wideline (UW) SSNMR spectra.[55,88–91] This protocol is comprised of three major components: (i) utilizing WURST (wideband, uniform rate, and smooth truncation) pulses[92] for uniform, direct

excitation of broad powder patterns,[93] (ii) using CPMG (Carr-Purcell Meiboom-Gill) echo trains for enhancing the signal-to-noise ratio (S/N),[94] and (iii) stepping the transmitter in even increments across the breadth of the powder pattern (the 'frequency-stepped' method) to acquire sub-spectra at each frequency and subsequently generate the variable offset cumulative spectrum (VOCS).[95,96] Successful utilization of the frequency-stepped WURST-CPMG sequence has been demonstrated for various spin-1/2[97,98] and quadrupolar nuclei (integer and half-integer spins).[59,91,99–105]

We recently demonstrated that the excitation of UW SSNMR spectra can be achieved using cross-polarization (CP) instead of direct excitation. The BRAIN-CP (broadband adiabatic inversion CP) pulse sequence is utilized to enable polarization transfer over a wide frequency range (an order of magnitude larger than conventional CP experiments).[106] A major advantage of this sequence is the ability to perform efficient CP at low radio frequency (rf) power levels, making the sequence particularly attractive for NMR experiments involving low-γ nuclei with broad powder patterns, like ^{14}N. Several test cases of ^{14}N{^{1}H} BRAIN-CP-WCPMG NMR experiments have been presented for APIs, amino acids, and transition metal compounds.[59,63,99]

In recent years there have also been significant advancements in the techniques utilized for the acquisition of ^{15}N SSNMR spectra. The availability of very fast MAS and the resulting boost in ^{1}H resolution offered opportunities for the indirect detection of ^{15}N nuclei (as well as the spectra of other dilute or low-γ nuclides).[51,107,108] The technique, known as indirectly-detected heteronuclear correlation (idHETCOR) spectroscopy, has been successfully utilized in synthetic polymers and biopolymers,[108] organic-inorganic hybrid materials,[109] isotopically enriched proteins,[110] peptides,[51,111] and functionalized

mesoporous silicas.[112,113] Ishii and Tycko initially proposed a pulse sequence in which polarization transfers between ^{1}H and ^{15}N are achieved via adiabatic CP[114] using a tangentially shaped pulse in the ^{15}N channel.[107] A variation of this sequence was also recently proposed by Mao and Pruski, in which heteronuclear correlations are mediated through-bond.[115] The indirect detection approach offers a sensitivity advantage exceeding one order of magnitude in comparison to conventional ^{1}H-^{15}N HETCOR experiments,[51] thereby enabling routine acquisition of such spectra on *naturally abundant* samples without the need for costly ^{15}N isotopic labelling.

Another technique that is available for NMR studies of insensitive nuclei is the aforementioned DNP,[116,117] which due to recent developments of gyrotron technology,[118] low-temperature MAS probes[119] and suitable biradical polarizing agents,[120,121] has offered enhancements of nuclear polarization exceeding two orders of magnitude in biological systems and various classes of materials.[122–125] Current state-of-the-art DNP experiments in solids utilize the so-called cross effect, which relies on polarization exchange between three coupled spins, comprising two unpaired electrons, typically located in a single biradical molecule, and a nucleus. Measurements involving the detection of low-γ nuclei, such as ^{15}N, often involve an indirect route via protons, where the electron to ^{1}H transfer via DNP is followed by ^{1}H to ^{15}N transfer via CP. Several DNP CP/MAS studies of ^{15}N nuclei located on the surface and in the bulk of materials were recently reported.[126–128]

Herein, we present a combined ^{14}N and ^{15}N SSNMR study of a series of naturally-abundant nitrogen-containing APIs and their associated polymorphic forms. It is demonstrated that investigating APIs using nitrogen NMR will allow for accurate

fingerprinting, differentiation and discovery of polymorphs via measurement of their unique chemical shift and quadrupolar NMR parameters, and will also assist in the identification of impurity phases. We apply the WURST-CPMG and BRAIN-CP/WCPMG pulse sequences for the fast acquisition of UW ^{14}N SSNMR spectra at moderate (9.4 T) and high magnetic field strengths (21.1 T). We also show that the ^{1}H{^{15}N} idHETCOR technique is ideal for the measurement of the chemical shifts and through-space connectivities between ^{1}H and ^{15}N in APIs. Finally, we employ DNP-enhanced ^{15}N{^{1}H} CP/MAS measurements to detect the most elusive ^{15}N sites. Experimentally obtained ^{14}N EFG tensor parameters and ^{15}N chemical shifts are also compared to those derived from DFT calculations, and correlations between these parameters, tensor orientations and molecular-level structures are discussed. Commentary is provided on the potential application of these ^{14}N and ^{15}N SSNMR techniques for screening of bulk APIs and their dosage forms.

6.3. Experimental and Computational Details

6.3.1 Sample Preparation

Schematic representations of the molecules, along with their abbreviations, are given in **Scheme 6.1**. Samples were purchased from Sigma-Aldrich and were used without further purification, except for instances outlined below. The polymorphic form of bupivacaine HCl, termed bupivacaine II HCl (**Bupi II**), was synthesized by heating bupivacaine HCl (**Bupi**) at 170 °C for 3 hours.[36,129] To increase the ^{14}N transverse relaxation time constants (T_2) for the **Bupi** samples (**I** and **II**), **Bupi** was partially deuterated by heating a saturated solution in 99.9% D_2O (Aldrich) at 80 °C for 1 hour.

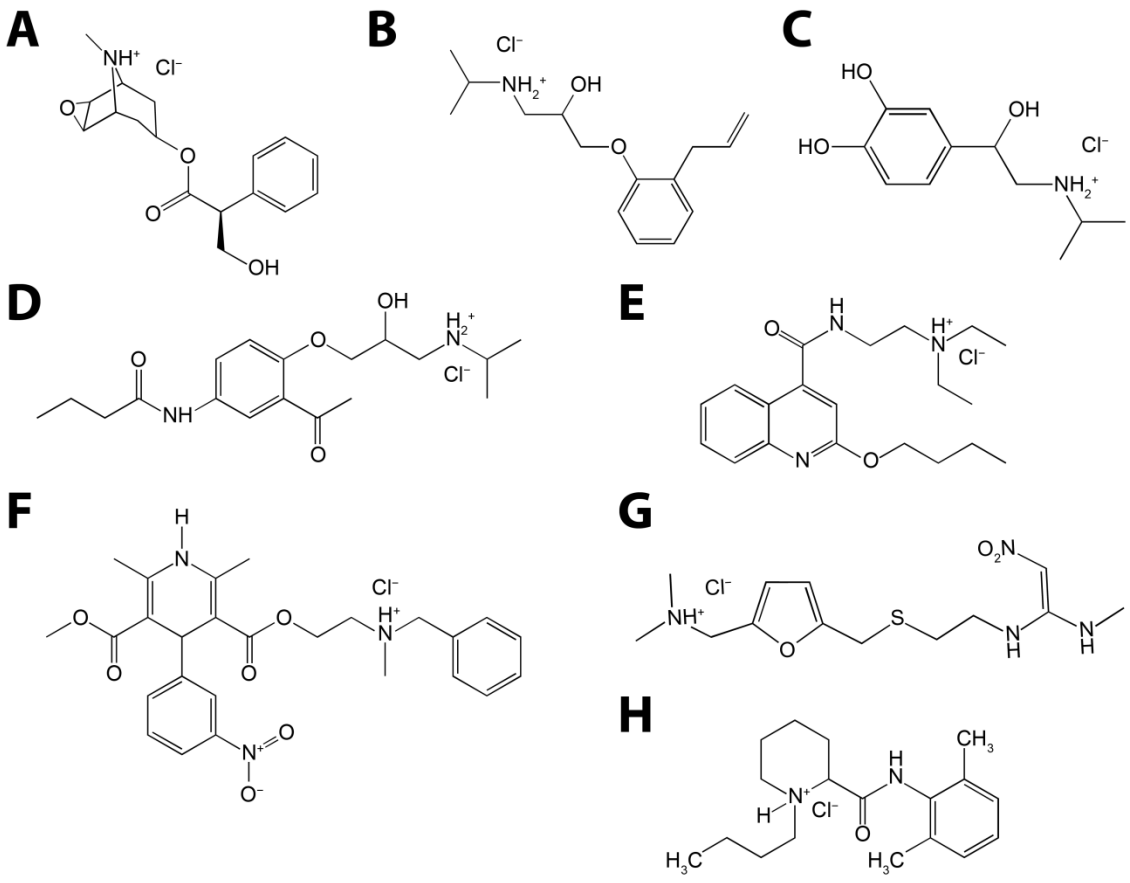

Scheme 6.1. Schematic representations of HCl salts of APIs studied by ^{14}N and ^{15}N SSNMR: (A) Scopolamine (**Scop**), (B) Alprenolol (**Alpr**), (C) Isoprenaline (**Isop**), (D) Acebutolol (**Aceb**), (E) Dibucaine (**Dibu**), (F) Nicardipine (**Nica**), (G) Ranitidine (**Rani**), and (H) Bupivacaine (**Bupi**).

The D_2O was removed by slow evaporation and the samples were dried in a desiccator. Partially deuterated **Bupi II** was then synthesized following the same procedure as mentioned above.

6.3.2 X-ray Diffraction

To confirm the phase purity of each sample, powder X-ray diffraction (pXRD) experiments were carried out on a Bruker AXS HI-STAR system using a General Area

Detector Diffractions system and Cu-K_α (λ = 1.540598 Å) radiation. The experimentally obtained pXRD patterns were compared with theoretical pXRD patterns simulated using either the PowderCell software package[130] or CrystalDiffract[131] based on previously reported crystal structure data.[36,129,132–138] The pXRD diffraction patterns are provided in **Appendix E**, **Figures E1-E3**.

6.3.3 ^{14}N SSNMR

Moderate-field static ^{14}N SSNMR experiments (i.e., performed on stationary samples) were conducted at 9.4 T on a wide-bore Oxford magnet equipped with a Varian Infinity Plus console, using a Larmor frequency of 28.88 MHz for ^{14}N. Experiments were completed with a Varian/Chemagnetics double-resonance static HX probe fitted with a 5-mm coil and a low-γ tuning accessory. High-field static ^{14}N NMR experiments were completed at the National Ultrahigh-Field NMR facility for Solids in Ottawa, on a Bruker 900 Avance II spectrometer equipped with a standard-bore 21.1 T magnet, operated at a Larmor frequency of 65.03 MHz for ^{14}N. Experiments were completed using a home-built 7-mm static HX probe. The powdered samples were packed into shortened 5-mm and 7-mm glass NMR tubes. A sample of NH_4Cl (s) was used to calibrate the rf power on the ^{14}N channel. Due to the enormous breadths of the ^{14}N powder patterns, chemical shifts are not reported, as they have very large uncertainties.

As expected, the ^{14}N NMR powder patterns were too broad to be uniformly excited with a single high-power rectangular pulse of constant amplitude and phase; hence, they were acquired and processed using several UW techniques. For experiments involving direct excitation of the ^{14}N nuclei, the WURST-CPMG pulse sequence[88,89] was

applied, using an eight-step phase cycle and WURST-80 pulses[92] of equal amplitude and length for excitation and refocusing. $^{1}H \rightarrow {}^{14}N$ CP NMR experiments were conducted using the BRAIN-CP-WCPMG pulse sequence.[106] In all cases, high-power proton decoupling was applied, with the decoupling RF fields between 30 and 82 kHz. Due to the limited excitation bandwidths associated with the WURST pulses, all spectra were acquired using the previously mentioned VOCS method,[95,96] with frequency increments equal to an integer multiple of the spikelet spacings arising from the CPMG portion of the pulse sequence.[139] The experimental times ranged from as long as 40 hours to as short as 8.4 hours, with a mean of approximately 16 hours. Further experimental details are given in the Supporting Information (**Appendix E**, **Tables E1 – E3**).

Processing of all ^{14}N SSNMR spectra was performed using the NUTS program from Acorn Software. Individual FIDs were Fourier transformed to produce sub-spectra, which were skyline-projected or co-added to produce the final spectrum. For all cases, except **Bupi** and **Bupi II,** only one half of the overall Pake doublet was acquired in both the direct excitation and CP experiments. Under the assumption of a dominant first-order quadrupolar interaction, the total Pake doublet is centrosymmetric, and can be produced by 'reflection' or 'mirroring' of the high-frequency portion of the pattern about the center of the spectrum.[56] The positions of the three discontinuities in each half of the Pake doublet (i.e., the 'foot', 'shoulder,' and 'horn') depend directly on the values of C_Q and η_Q. These values do not depend on the exact positions or intensities of the individual spikelets, though the precision of their measurement is limited by the spikelet spacing. Alternatively, the echo train can be co-added and Fourier transformed to produce a

continuous powder pattern, as shown in **Figure E4**. Analytical simulations of ^{14}N powder patterns were performed using the WSolids software package.[140]

6.3.4 ^{15}N SSNMR

The 2D $^{1}H\{^{15}N\}$ idHETCOR experiments were performed at 14.1 T on a Varian NMR System spectrometer, equipped with a 1.6-mm triple-resonance FastMAS™ probe and operated at 599.6 MHz for ^{1}H and 60.8 MHz for ^{15}N. All experiments were carried out under fast MAS at a rate of ν_{rot} = 40 kHz using the idHETCOR pulse sequence shown in **Figure E5** and described in detail in earlier studies.[51] In short, the experiment commenced with $^{1}H \rightarrow {}^{15}N$ CP transfer, followed by a t_1 period during which ^{15}N magnetization evolved in the presence of heteronuclear ^{1}H decoupling (SPINAL-64[141]). Any residual ^{1}H magnetization remaining after the evolution period was eliminated using rotor resonance recoupling by a pair of long pulses with orthogonal phases,[108,142] whose RF amplitudes satisfied the HORROR condition $\nu_{RF}(^{1}H) = \nu_{rot}/2$. The ^{1}H magnetization was detected following the final $^{15}N \rightarrow {}^{1}H$ CP transfer, this time under heteronuclear ^{15}N SPINAL-64 decoupling. All spectra were acquired at ambient temperature and were processed using the GSim software package.[143] The ^{15}N nitrogen chemical shifts were referenced to nitromethane at 0 ppm.[144]

The DNP-enhanced $^{15}N\{^{1}H\}$ CP/MAS spectra of **Aceb** and **Nica** were obtained on a Bruker BioSpin DNP NMR spectrometer equipped with a 3.2-mm low-temperature MAS probe and a 263 GHz gyrotron, and operated at 400.3 MHz for ^{1}H and 40.6 MHz for ^{15}N. The samples were impregnated with a 16 mM 1,1,2,2-tetrachloroethane solution of TEKPol,[121] packed in a sapphire MAS rotor and spun at a MAS rate of 10 kHz and

temperature of ~100 K. For comprehensive lists of acquisition parameters used in ^{1}H{^{15}N}idHETCOR and DNP-enhanced ^{15}N{^{1}H} CP/MAS experiments we refer the reader to the Supporting Information (**Tables E4** and **E5**, respectively).

6.3.5. Nomenclature

There are numerous pulse sequences applied in this work; for clarity, the following abbreviations are used herein: (1) ^{14}N UW spectra acquired with WURST-CPMG are denoted as 'direct-excitation' or 'DE'; (2) the ^{14}N UW spectra obtained *via* BRAIN-CP/WURST-CPMG are denoted as '^{14}N{^{1}H} BCP' or simply 'BCP'; (3) the indirectly detected heteronuclear correlation spectra are denoted as '^{1}H{^{15}N} idHETCOR' or 'idHETCOR'; and (4) the spectra enhanced by dynamic nuclear polarization are referred to as 'DNP ^{15}N{^{1}H} CP/MAS' or 'DNP CP/MAS'.

6.3.6. First-Principles Calculations

Calculations of NMR interaction tensors were completed using the CASTEP[145] DFT code in the Materials Studio 5.0 software suite. CASTEP is a plane-wave pseudopotential method that utilizes the gauge-including projector augmented wave (GIPAW) formalism.[146] The generalized gradient approximation (GGA) and revised Perdew, Burke and Ernzerhof (rPBE) functionals were used, with the core-valence interactions being described by on-the-fly pseudopotentials. Integrals over the Brillouin zone were performed using a Monkhorst-Pack grid with a k-point spacing of 0.08 Å^{-1}. Wavefunctions were expanded in plane waves, with kinetic energy less than a cut-off energy, typically 500 or 610 eV. Calculations output both the absolute shielding tensor,

σ and the electric field gradient (EFG) tensor, **V**, in the crystal frame. Crystal structures were obtained from the Cambridge Structural Database (CSD) and geometry optimization of the structure was performed (also within CASTEP in the Materials Studio software) prior to calculation of the NMR parameters. During geometry optimization of each structure only the proton positions were allowed to vary. Calculations were performed using the Shared Hierarchical Academic Research Computing Network (SHARCNET). Typical times for calculations ranged from 1 to 92 hours for geometry optimization and 8 to 110 hours for NMR calculations using 8, 16, 32, or 64 cores and 1, 2, or 4 GB of memory per core.

6.4. Results and Discussion

Below, the ^{14}N and ^{15}N SSNMR data are presented for each API, and discussed in terms of spectral features and the quadrupolar or chemical shift parameters extracted from each spectrum. Following this, the experimentally measured and theoretically calculated ^{14}N quadrupolar parameters are correlated to the local structural environments of the nitrogen-containing moieties.

6.4.1 Nitrogen NMR of APIs

Before the NMR data for each API are discussed, we identify several common features for all ^{14}N SSNMR spectra. Using DE and BCP, it was possible to acquire ^{14}N SSNMR spectra of some of these sites (see **Figures 6.1-6.3** and **6.5-6.7**) in reasonable time frames with high S/N and high resolution at 9.4 T and 21.1 T. Broad ^{14}N SSNMR powder patterns are observed at both fields, dominated by the quadrupolar interaction to

first order, with negligible effects from the second-order quadrupolar interaction and chemical shift anisotropy (**Figure E6**). It has been demonstrated by O'Dell *et al*. that nitrogen sites with pseudo-tetrahedral geometries possess much smaller values of C_Q (0.8 – 1.5 MHz) in comparison to those with pyramidal or planar geometries (2.8 – 4.0 MHz).[55–57] Given the extreme breadth of powder patterns associated with pyramidal or planar nitrogen sites, it is generally only feasible to probe pseudo-tetrahedral sites via DE ^{14}N SSNMR for the systems discussed herein, even though in some cases the signal arising from certain planar sites can be discerned in the baseline. We also note that considerable variation in CP efficiency is observed across the range of samples discussed below. Research is underway in our laboratory to access these much broader patterns via modified ^{14}N UW SSNMR experiments, including the effects of motion, relaxation mechanisms, and the various contributions to CP; further discussion of these topics is beyond the scope of the current work.

6.4.1.1 Scopolamine HCl

Scopolamine HCl (**Scop**) is used in the treatment of postoperative nausea and vomiting. Its crystal structure has a single nitrogen site with pseudo-tetrahedral geometry created by three nitrogen-carbon single bonds (**Scheme 6.1A**).[132] The ^{14}N DE spectrum (**Figure 6.1A**) was simulated with a single nitrogen environment, characterized by C_Q = 1.29 MHz and η_Q = 0.29 (**Table 6.1**). These quadrupolar parameters are accurately determined from the positions of the previously mentioned discontinuities of the Pake doublet (the shoulder and horn); despite the fact that the third discontinuity at the edge (the foot) is not clearly resolved (see **Figures E7** and **E8** for additional information). In

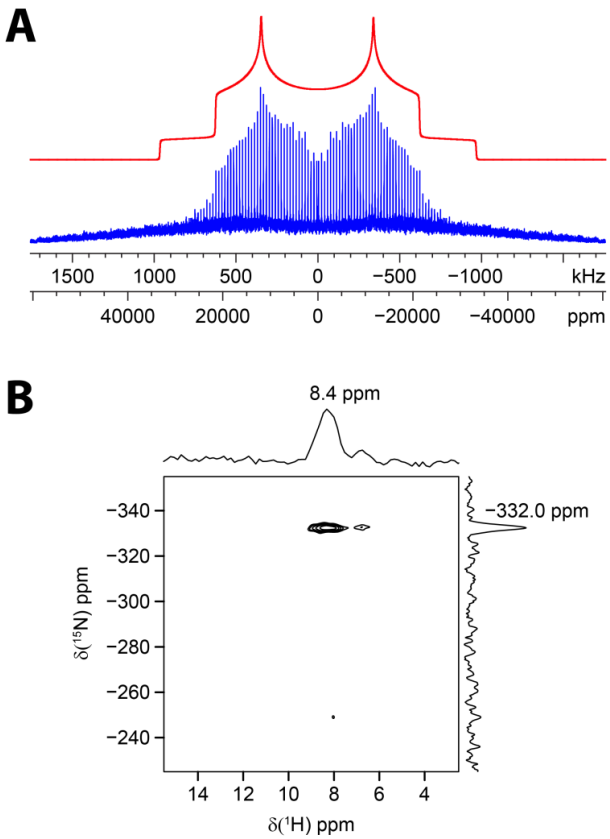

Figure 6.1. (A) Static ^{14}N SSNMR spectrum (9.4 T using DE) and (B) ^{1}H{^{15}N} idHETCOR spectrum (14.1 T) of **Scop**. We refer the reader to the Supporting Information, SI, for detailed lists of the acquisition parameters.

many cases, S/N in the outer foot region is low, because there are fewer crystallites giving rise to observable signal. There is also the possibility that lower signal results from T_2-dependent signal enhancement by CPMG refocusing, which differentiates spectral regions with distinct *effective* T_2's, $T_2^{\text{eff}}(^{14}\text{N})$ (N.B.: the $T_2^{\text{eff}}(^{14}\text{N})$ is distinct from $T_2(^{14}\text{N})$ in that the contributions from heteronuclear dipolar coupling are wholly or partially removed by high-power ^{1}H decoupling for the former). In some cases, it was possible to enhance these spectral regions utilizing broadband CP methods;[55–57,106] however, the ^{14}N{^{1}H} BCP experiment on **Scop** yielded very low S/N across the entire

pattern; possible reasons for this include a short $T_{1\rho}$ for ^{14}N and/or ^{1}H, or slow buildup of spin polarization for ^{14}N.

Table 6.1. Experimental[a] and calculated[b] (using NMR CASTEP) ^{14}N EFG tensor and nitrogen chemical shift parameters.

API	Site	Expt. C_Q (MHz)[c]	Calc. C_Q (MHz)	Expt. η_Q[d]	Calc. η_Q	Expt. δ_{iso} (ppm)	Calc. σ_{iso} (ppm)
Scop[e]	RR′R″NH$^+$	1.29(5)	−1.36	0.29(3)	0.37	−332(1)	169.04
Alpr[f]	RR′NH$_2^+$	1.13(3)	1.53	0.82(3)	0.63	−346(2)	154.45
Isop[f]	RR′NH$_2^+$	1.01(2)	1.08	0.91(3)	0.85	−345(1)	168.36
Aceb[f]	RR′NH$_2^+$	1.04(3)	−1.10	0.90(2)	0.86	−329(1)[h]	156.40
	RR′NH	-	−3.39	-	0.40	−250(1)	85.30
Dibu	RR′R″NH$^+$	-	−1.51	-	0.17	−326(2)	165.27
	RR′NH	-	−3.48	-	0.33	−264(1)	97.17
	RR′N	-	−3.99	-	0.07	−135(3)[g]	−32.67
Nica[f]	RR′R″NH$^+$	1.43(3)	−1.31	0.14(2)	0.24	−348(2)	170.32
	RR′NH	-	−2.97	-	0.33	−265(5)	74.99
	RNO$_2$	-	−1.10	-	0.20	-	−144.25
Rani[f]	RR′R″NH$^+$	1.62(10)	−1.50	0.22(5)	0.17	−340(2)	176.40
	RR′NH	3.25(10)	−3.82	0.50(5)	0.38	−281(2)	143.70
	RR′NH	3.25(10)	−3.68	0.58(5)	0.53	−292(2)	133.25
	RNO$_2$	1.15(5)	1.32	0.49(5)	0.37	−22(2)	−113.27
Bupi[e]	RR′R″NH$^+$	1.00(3)	−1.16	0.30(3)	0.29	−342(1)	162.27
	RR′NH	-	−3.20	-	0.40	−269(1)	89.77
Bupi II[e]	RR′R″NH$^+$	1.25 (4)	−1.54	0.19(4)	0.18	−345(2)	162.94
	RR′NH	-	−3.38	-	0.44	−267(2)	85.30

[a] The uncertainty in the last digit(s) of each value is denoted in brackets. [b] EFG and chemical shift parameters were calculated after optimization of the proton positions. [c] $C_Q = eQV_{33}/h$. [d] $\eta_Q = (V_{11} - V_{22})/V_{33}$. [e] Spectra acquired using DE. [f] Spectra acquired using BCP. [g] Site observed using a longer contact time (**Figure E9**). [h] Site observed using DNP-enhanced ^{15}N{^{1}H} CP/MAS.

The $^{1}H\{^{15}N\}$ idHETCOR spectrum of **Scop** is shown in **Figure 6.1B** and displays a nitrogen resonance at $\delta_{iso} = -332$ ppm (**Table 6.1**) corresponding to a single nitrogen site, which is again in agreement with the crystal structure. This spectrum also reveals that the proton directly bound to nitrogen resonates at 8.4(5) ppm (throughout this work the uncertainties in the last decimal place of the proton chemical shifts are given in parentheses). Such correlations are extremely useful for structural characterization as they provide vital structural information regarding protons that are either directly bound or proximate in space to nitrogen.

6.4.1.2 Alprenolol HCl and Isoprenaline HCl

Alprenolol HCl (**Alpr**) is a non-cardioselective beta blocker, reported to have intrinsic sympathomimetic activity and some membrane-stabilizing properties. Isoprenaline HCl (**Isop**) is used in the treatment of slow heart rates and is structurally similar to adrenaline. **Alpr** and **Isop** each possess a single pseudo-tetrahedral $RR'NH_2^+$ nitrogen environment (**Scheme 6.1B** and **6.1C**).[133,134] The $^{14}N\{^{1}H\}$ BCP spectrum of **Alpr** shown in **Figure 6.2A** has a much higher S/N than the DE spectrum (not shown), and was simulated with a single nitrogen environment: $C_Q = 1.13$ MHz and $\eta_Q = 0.82$. Again, the well-defined positions of the central horns and the overall pattern breadth allow for the accurate measurement of the quadrupolar parameters, despite the fact that other singularities are difficult to distinguish (see **Figure E9**). Despite the structural similarity of **Isop** to **Alpr**, the acquisition of its ^{14}N NMR spectrum was considerably more challenging. It was not possible to observe any signal using DE methods; however, a $^{14}N\{^{1}H\}$ BCP spectrum was acquired (**Figure 6.2B**). The S/N in this spectrum is very

poor, largely due to the short $T_2^{eff}(^{14}N)$. We also note that a fair amount of background noise and interference is observed. Nonetheless, because of the clearly visible discontinuities, it was possible to simulate the spectrum, yielding quadrupolar parametrs of C_Q = 1.01 MHz and η_Q = 0.91. Variable-temperature DE and BCP experiments were also attempted in an effort to increase $T_2^{eff}(^{14}N)$ and thereby lengthen the CPMG echo trains;[59] however, they were unsuccessful.

The $^1H\{^{15}N\}$ idHETCOR spectra for **Alpr** and **Isop**, shown in **Figures 6.2C** and **6.2D**, respectively, both display single resonances in agreement with the reported crystal structures.[132,134] The spectrum of **Alpr** features a single peak at δ_{iso} = −346 ppm, which is strongly correlated with its directly bound protons (~4.9(5) ppm) and weakly correlated with the nearby CH_3 groups (1.0(5) ppm). The idHETCOR spectrum of **Isop** displays a nitrogen resonance at δ_{iso} = −345 ppm, which is also correlated with directly bound hydrogens (6.3(5) ppm) and the nearby CH_3 groups (0.5(5) ppm). The broad peak centered around 3-4 ppm, observed for both **Alpr** and **Isop**, corresponds to the nearby CH_2 groups.

Despite the structural similarities between **Alpr** and **Isop**, it is interesting to note that they show markedly different NMR responses in two respects: First, the pronounced differences in $T_2^{eff}(^{14}N)$ make the acquisition of ^{14}N NMR spectra trivial for the former, and challenging for the latter. Second, notwithstanding their similar nitrogen chemical shifts, the dipolar correlations observed in the $^1H\{^{15}N\}$ idHETCOR spectra are distinct from one another, revealing different spatial proximities between nitrogen and hydrogen.

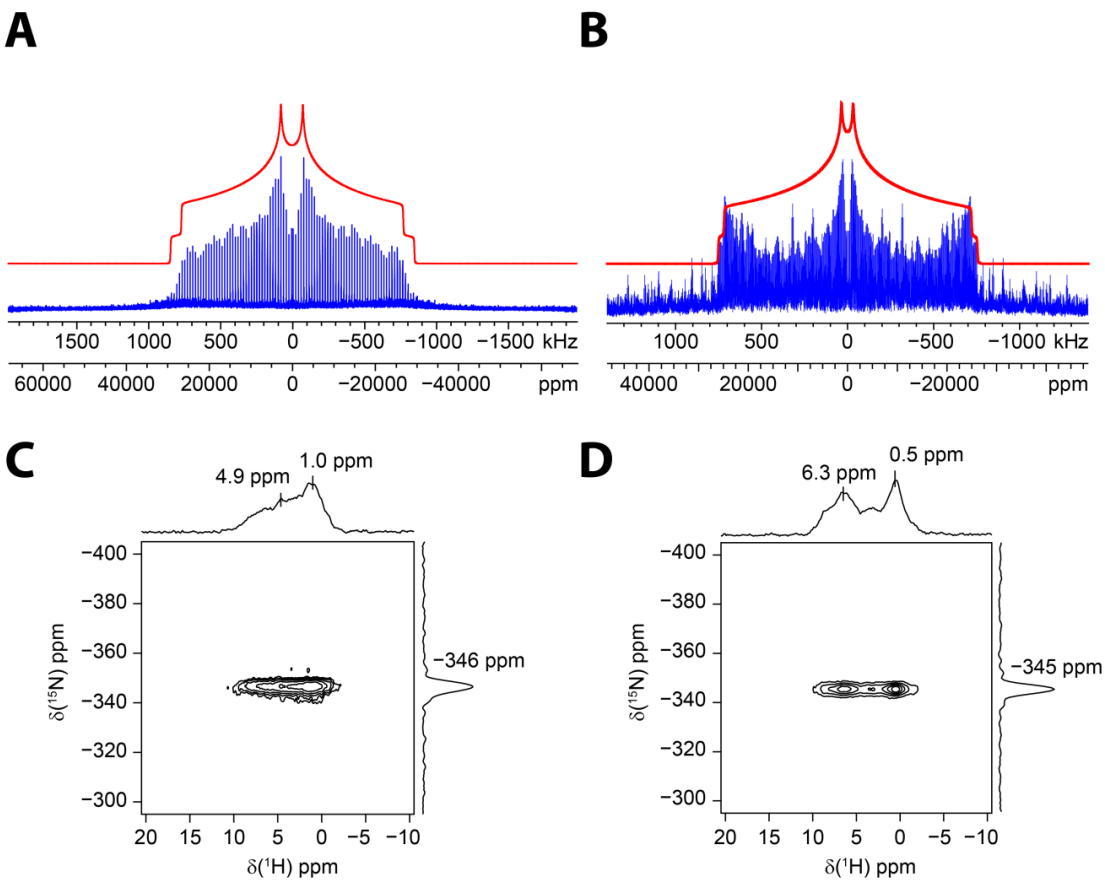

Figure 6.2. Static ^{14}N SSNMR spectra (9.4 T using BCP) of (A) **Alpr** and (B) **Isop**. ^{1}H{^{15}N} idHETCOR (14.1 T) spectra of (C) **Alpr** and (D) **Isop**.

6.4.1.3 Acebutolol HCl

Acebutolol HCl (**Aceb**) is a beta blocker typically used to treat high blood pressure and irregular heartbeats. It has two distinct nitrogen environments, one having pseudo-tetrahedral geometry ($RR'NH_2^+$) with two nitrogen-carbon single bonds and the other having planar geometry (**Scheme 6.1D**).[135] The UW ^{14}N powder pattern of **Aceb** is shown in **Figure 6.3A** and is indicative of the single pseudo-tetrahedral nitrogen environment. Simulation of the ^{14}N powder pattern yields C_Q = 1.04 MHz and η_Q = 0.90. In this instance, all three discontinuities are clearly resolved. As stated earlier, it is not

possible to observe the full ^{14}N powder pattern corresponding to the planar nitrogen using the experimental conditions described in the Supporting Information. However, some signal intensity corresponding to these sites is visible on the outer edge of the powder pattern (marked with asterisks).

The $^{1}H\{^{15}N\}$ idHETCOR spectrum of **Aceb** (**Figure 6.3B**) displays a single cross-peak, in this case corresponding to nitrogen resonance at δ_{iso} = −250 ppm and proton resonance at 8.7(5) ppm, which is assigned to the RR′NH planar site. Efforts to observe the $RR'NH_2^+$ environment by increasing the spectral window and varying the contact time during CP were unsuccessful, which is surprising given that resonances of similar $RR'NH_2^+$ environments in both **Alpr** and **Isop** were clearly observed under similar conditions (*vide supra*). To verify the presence of both ^{15}N resonances, we resorted to DNP $^{15}N\{^{1}H\}$ CP/MAS measurement, which yielded two resonances at −250 ppm and −329 ppm (**Figure 6.3C**).

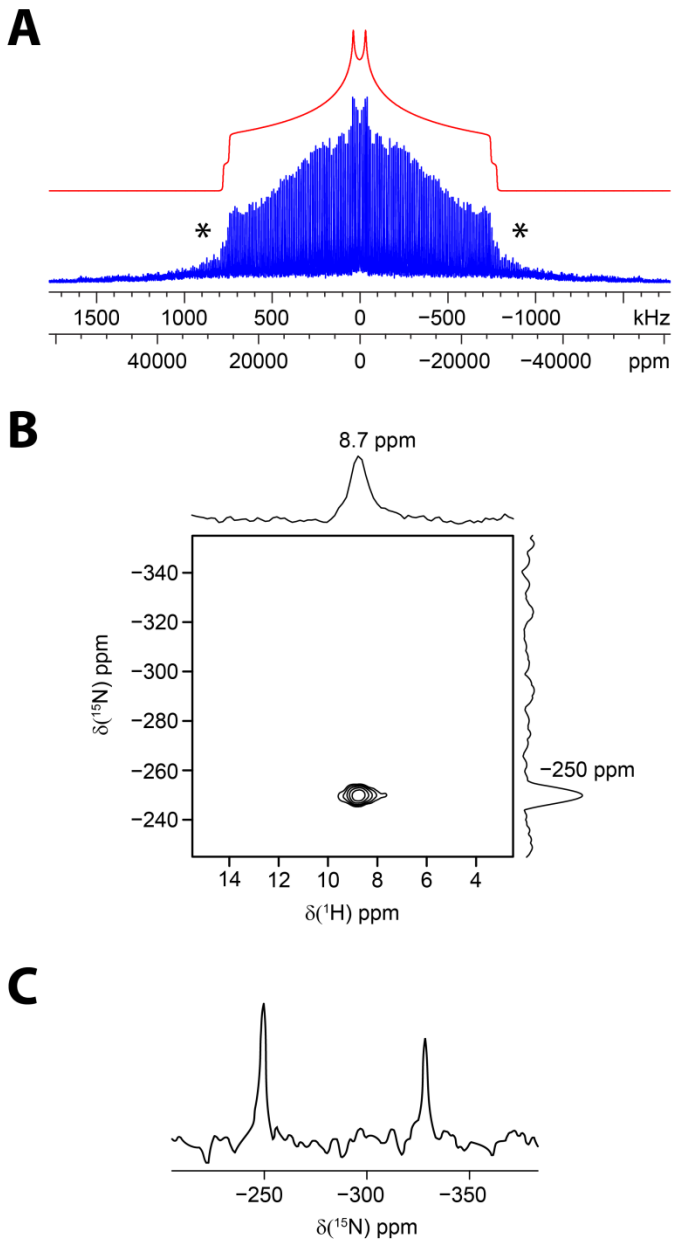

Figure 6.3. (A) Static ^{14}N SSNMR spectrum (9.4 T using BCP), (B) ^{1}H{^{15}N} idHETCOR spectrum (14.1 T), and (C) DNP-enhanced ^{15}N{^{1}H} CP/MAS spectrum (263 GHz gyrotron, 9.4 T magnet) of **Aceb**. In (A) signal corresponding to the RR′NH moiety is denoted by *.

6.4.1.4 Dibucaine HCl

Dibucaine HCl (**Dibu**) is a topical local anesthetic used to relieve pain and itching from burns, bites and stings. It has three distinct nitrogen sites in the unit cell; one having pseudo-tetrahedral geometry with three nitrogen-carbon single bonds ($RR'R''NH^+$), the second with planar geometry ($RR'NH$) and the third in an aromatic moiety (**Scheme 6.1E**).[136] Unfortunately, it was not possible to detect any of these sites using room- and variable-temperature DE and BCP experiments. We hypothesize that strong heteronuclear ^1H-^{14}N dipolar interactions are reducing the $T_2^{eff}(^{14}N)$, thereby preventing the acquisition of a sufficient CPMG echo train; however, our attempts to reduce the dipolar interactions by high-power ^1H decoupling or partial deuteration were unsuccessful. A superficial comparison of the crystal structures of **Dibu** and other compounds for which ^{14}N SSNMR spectra are easily acquired does not reveal any obvious structural differences which can be correlated to this phenomenon.

All three nitrogen environments in **Dibu** are observed by the $^1H\{^{15}N\}$ idHETCOR method, with additional correlation information to multiple proton sites. Two distinct nitrogen resonances are observed in the $^1H\{^{15}N\}$ idHETCOR spectrum of **Dibu** (**Figure 6.4**) at $\delta_{iso} = -264$ ppm and $\delta_{iso} = -326$ ppm, which are correlated to their directly bound protons at 8.0(5) ppm and 10.7(5) ppm, and assigned to the planar and pseudo-tetrahedral nitrogen environments, respectively. The planar site is also weakly correlated to the proton in the neighbouring aromatic ring (8.6(5) ppm). Using the CP contact time of 3 ms (**Table E4**), it was not possible to observe the nitrogen in the aromatic group, as is does not have a directly bound proton. However, by increasing the CP contact time to 10 ms, we were able to observe this resonance at $\delta_{iso} = -135$ ppm (**Figure E10**), albeit at the

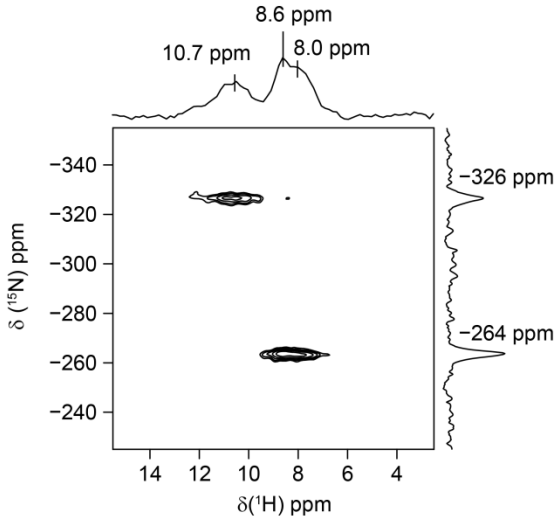

Figure 6.4. $^{1}H\{^{15}N\}$ idHETCOR spectrum (14.1 T) of **Dibu**.

expense of the S/N of the two other sites, which may be reduced due to fast $T_{1\rho}$ (^{1}H or ^{14}N) relaxation.

6.4.1.5 Nicardipine HCl

Nicardipine HCl (**Nica**) belongs to a class of calcium channel blockers and is used to treat high blood pressure and angina. There are three distinct nitrogen environments in **Nica**: one with pseudo-tetrahedral geometry ($RR'R''NH^{+}$), one with planar geometry ($RR'NH$), and one in a nitro group (RNO_2) of planar geometry (**Scheme 6.1F**).[137] The ^{14}N BCP powder pattern of **Nica** is shown in **Figure 6.5A** and is indicative of a single nitrogen environment, corresponding to the $RR'R''NH^{+}$ nitrogen site. Simulation of the ^{14}N powder pattern yielded C_Q = 1.43 MHz and η_Q = 0.14. Signal arising from the RNO_2 group is not observed in the ^{14}N BCP spectrum (even though the calculated C_Q is −1.10

MHz); this is likely due to the absence of directly bound or proximate protons (the nearest proton is *ca*. 2.66 Å away from the nitrogen).

The idHETCOR spectrum in **Figure 6.5B** displays two distinct ^{15}N resonances at −265 ppm and −348 ppm, which are assigned to the planar (RR′NH) and pseudo-tetrahedral nitrogen environments, respectively. The resonance at δ_{iso} = −265 ppm displays a strong correlation at 9.2(5) ppm corresponding to the proton directly bound to the planar nitrogen (RR′NH), and a much weaker correlation at 3.4(5) ppm attributed to protons in the CH_3 group adjacent to the NH group (**Scheme 6.1F**). The pseudo-tetrahedral nitrogen resonating at δ_{iso} = −348 ppm exhibits detectable interactions with several proton sites. The correlation at 3.4(5) ppm belongs to the protons in the adjacent CH_3 group, the broad low-intensity peak in the range between 5 and 7 ppm corresponds to the nearby CH_2 groups, and the peak at 7.9(5) ppm is due to the aromatic hydrogen atoms. The weaker correlation observed at 11.4(5) ppm is assigned to the hydrogen atoms directly bonded to the pseudo-tetrahedral nitrogen. Its low intensity is most likely due to fast $T_{1\rho}$ relaxation processes, which may have attenuated this resonance during two CP transfers, each lasting 3 ms.

It is noted that the RNO_2 group in **Nica** is not observed in the idHETCOR spectrum, even at a longer CP contact time of 10 ms. As in the case of **Aceb**, we carried out a DNP CP/MAS measurement of this sample (**Figure 6.5C**), which also failed to produce any new resonances in addition to those at −265 ppm and −348 ppm. The ^{1}H → ^{15}N CP process is clearly not efficient enough to yield any discernible signal from the RNO_2 moiety, at both 100 and 298 K.

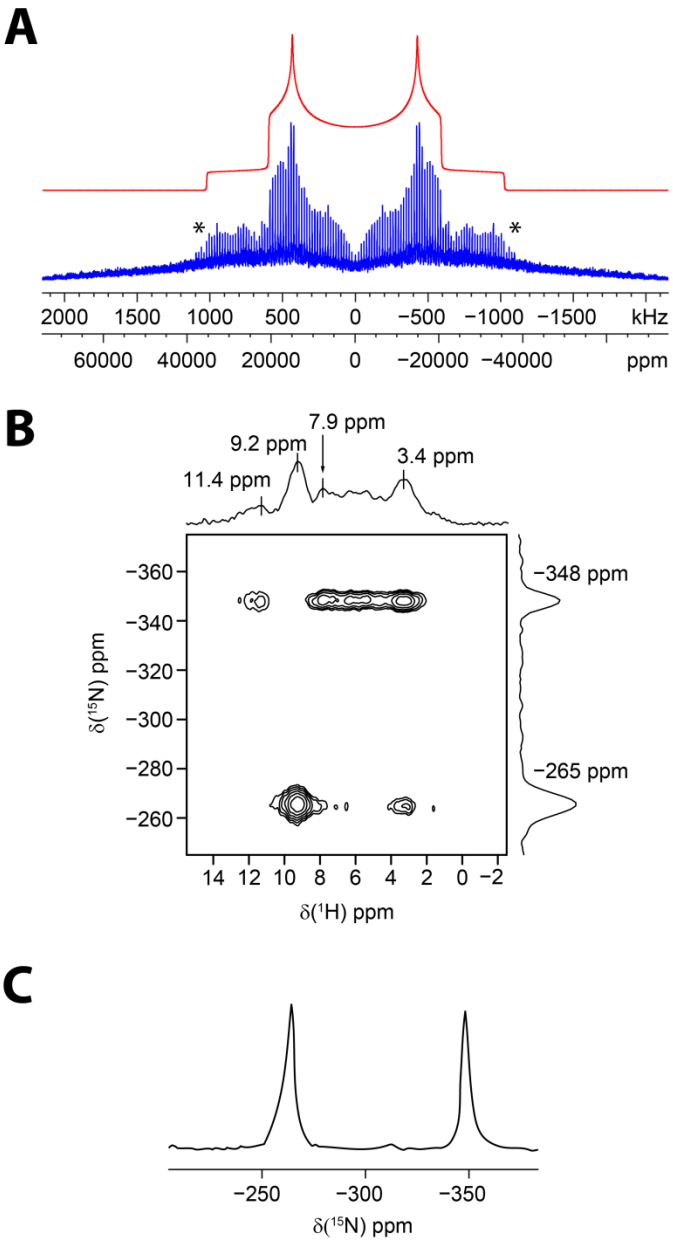

Figure 6.5. (A) Static ^{14}N SSNMR spectrum (9.4 T using BCP), (B) ^{1}H{^{15}N} idHETCOR spectrum (14.1 T), and (C) DNP-enhanced ^{15}N{^{1}H} CP/MAS spectrum (263 GHz gyrotron, 9.4 T magnet) of **Nica**. In (A) signal corresponding to one of the other nitrogen sites is observed, as denoted by *.

6.4.1.6 Ranitidine HCl

Ranitidine HCl (**Rani**) is a histamine H_2-receptor antagonist that inhibits stomach acid production and is commonly used in the treatment of peptic ulcer disease. **Rani** has four distinct nitrogen environments in the unit cell: one with pseudo-tetrahedral geometry ($RR'R''NH^+$), two with planar geometries ($RR'NH$) and one in a nitro group (RNO_2) (**Scheme 6.1G**).[138] The ^{14}N BCP spectrum of **Rani** is shown in **Figure 6.6A**. Remarkably, powder patterns corresponding to all four sites are present, and simulated with values of C_Q = 1.15, 1.62, 3.25 and 3.25 MHz and η_Q = 0.49, 0.22, 0.50 and 0.58, respectively (see **Figures E11** and **E12** for detailed information regarding this simulation). ^{14}N EFG tensors obtained from DFT calculations greatly aided in the fitting process.

The $^1H\{^{15}N\}$ idHETCOR spectrum of **Rani** (**Figure 6.6B**) also has four distinct resonances, associated with $RR'R''NH^+$ (δ_{iso} = −340 ppm), $RR'NH$ (δ_{iso} = −292 and −281 ppm), and RNO_2 (δ_{iso} = −22 ppm) nitrogen environments.[138] These assignments are corroborated by the observed correlations with the directly bound hydrogen atoms at 11.4(5) ppm ($RR'R''NH^+$) and 9.4(5) ppm (both $RR'NH$ sites). The resonance at δ_{iso} = −281 ppm is assigned to the planar $RR'NH$ nitrogen environment near the end of the alkyl chain (labelled site 1 in **Figure E13**). The resonance at δ_{iso} = −292 ppm belongs to the second planar nitrogen (labelled site 2 in **Figure E13**) because it also exhibits a weak correlation with the adjacent CH_2 group (7.4(5) ppm). The resonance at δ_{iso} = −22 ppm corresponds to the nitro group that does not possess any directly bound protons, and is correlated to a proton in the adjacent ethylene group.

The characterization of **Rani** benefits significantly from the tandem ^{14}N and ^{15}N NMR techniques. Typically, only the pseudo-tetrahedral nitrogen sites are observed in ^{14}N SSNMR spectra at moderate magnetic fields (i.e., 9.4 T); however, in this case, the BCP experiment makes it possible to see contributions from all of the crystallographically distinct ^{14}N nuclei. In addition, in the $^{1}H\{^{15}N\}$ idHETCOR spectra, all four of the nitrogen environments are observed, providing important heteronuclear correlation information that aids in structural assignment.

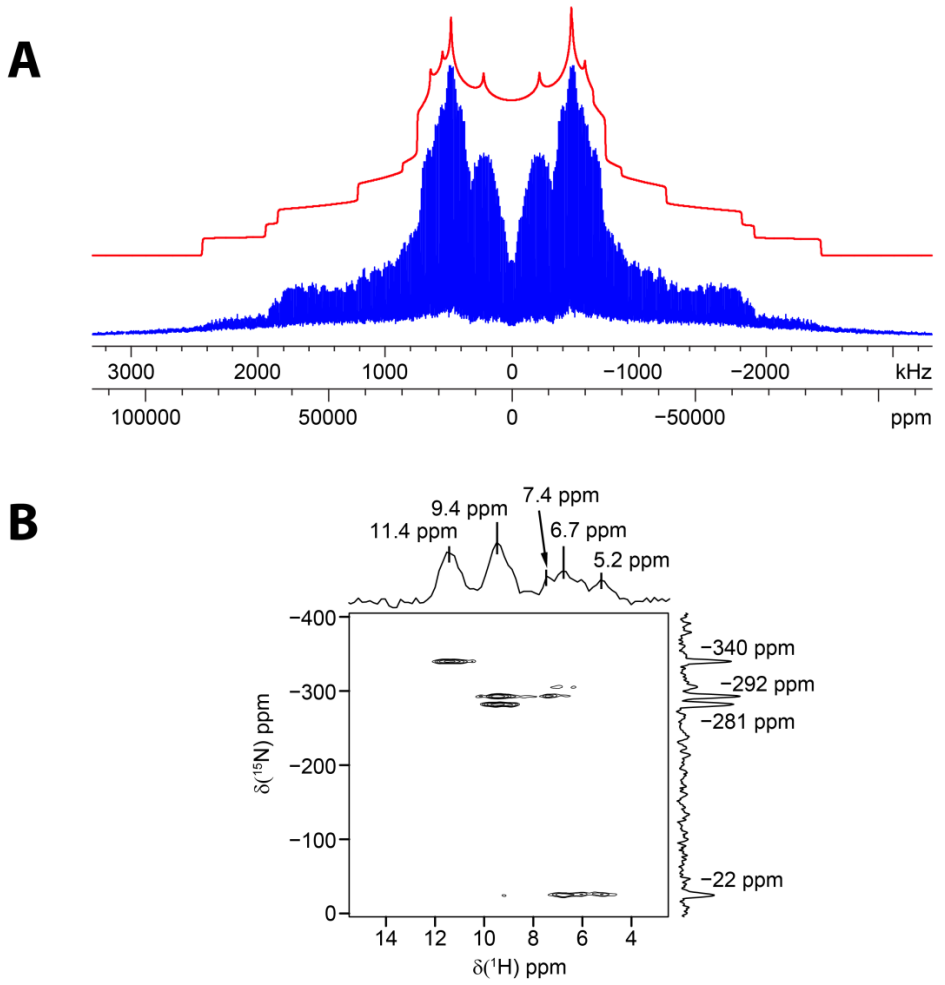

Figure 6.6. (A) Static ^{14}N SSNMR spectrum (9.4 T using BCP) and (B) $^{1}H\{^{15}N\}$ idHETCOR spectrum (14.1 T) of **Rani**.

6.4.1.7. Bupivacaine HCl and its Polymorphs

Bupivacaine HCl is a local anesthetic and is one of many APIs that exhibit polymorphism. There are several known polymorphs of bupivacaine HCl; in this study we are focusing upon the main form, bupivacaine HCl (**Bupi**), which is the bulk form obtained from Sigma-Aldrich (and also found in dosage forms),[36] and the polymorph known as bupivacaine II HCl (**Bupi II**).[129] **Bupi** and **Bupi II** each have two nitrogen environments: one with planar geometry, and the other with pseudo-tetrahedral geometry formed by one N-H bond and three nitrogen-carbon single bonds (**Scheme 6.1H**).[36,129] The planar sites are expected to have large values of C_Q, as confirmed by DFT calculations (*vide infra*), and are not observed.

^{14}N UW NMR spectra of **Bupi** and **Bupi II** were acquired at 9.4 T (**Figures E14** and **E15**, respectively) and 21.1 T (**Figure 6.7**). The spectral discontinuities at the horn, shoulder, and foot positions are very well defined at 21.1 T, enabling differentiation between the two polymorphs. Each of the ^{14}N powder patterns was simulated with a single nitrogen site corresponding to the pseudo-tetrahedral environment, yielding C_Q = 1.00 MHz, η_Q = 0.30 and C_Q = 1.25 MHz, η_Q = 0.19, for **Bupi** and **Bupi II**, respectively. It is noted that there is underlying signal intensity corresponding to the second nitrogen site in both ^{14}N SSNMR spectra as well as in the 9.4 T spectra of **Bupi** (**Figure E14**). In these cases, the favourable relaxation characteristics (i.e., short $T_1(^{14}\text{N})$ and long $T_2^{\text{eff}}(^{14}\text{N})$) of the planar nitrogen site seem to allow for its detection, even at moderate magnetic fields; however, we did not obtain the entire ^{14}N UW spectrum for this site – this will be the subject of future investigations.

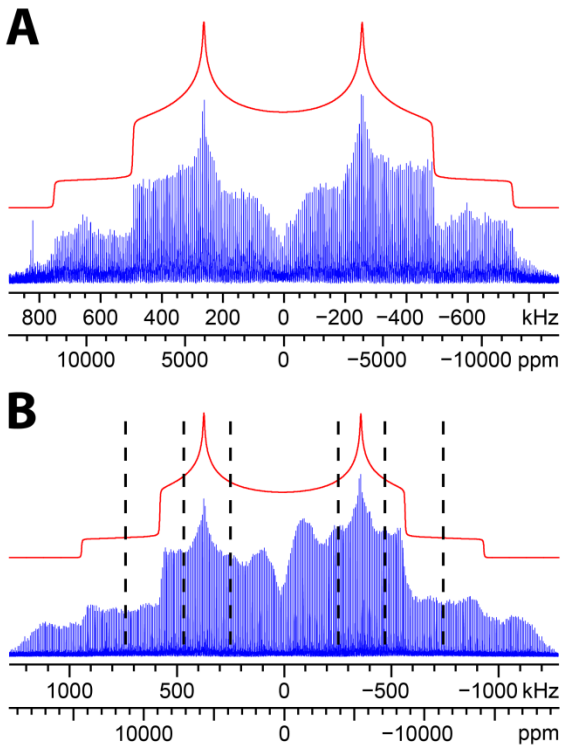

Figure 6.7. Static ^{14}N SSNMR spectra (21.1 T using DE) acquired for (A) **Bupi** and (B) **Bupi II**. The total powder pattern was acquired for each, i.e., no "mirroring" was performed. Dashed lines corresponding to the discontinuities of **Bupi** are also shown in (B) for comparison.

Each of the ^{1}H{^{15}N} idHETCOR spectra of **Bupi** and **Bupi II** (**Figures 6.8A** and **6.8B**) feature two distinct nitrogen resonances: δ_{iso} = −342 ppm and δ_{iso} = −269 ppm for **Bupi** and δ_{iso} = −345 ppm and δ_{iso} = −267 ppm for **Bupi II,** which are assigned to the pseudo-tetrahedral and planar sites, in each case. All of these resonances show strong correlations with their directly bound hydrogen atoms: at 10.0(5) and 10.7(5) ppm for the pseudo-tetrahedral sites, and at 10.8(5) ppm and 12.1(5) ppm for the planar sites in **Bupi** and **Bupi II**, respectively. Several weaker correlations are also observed in both polymorphs, between the nitrogen sites and their adjacent aliphatic protons.

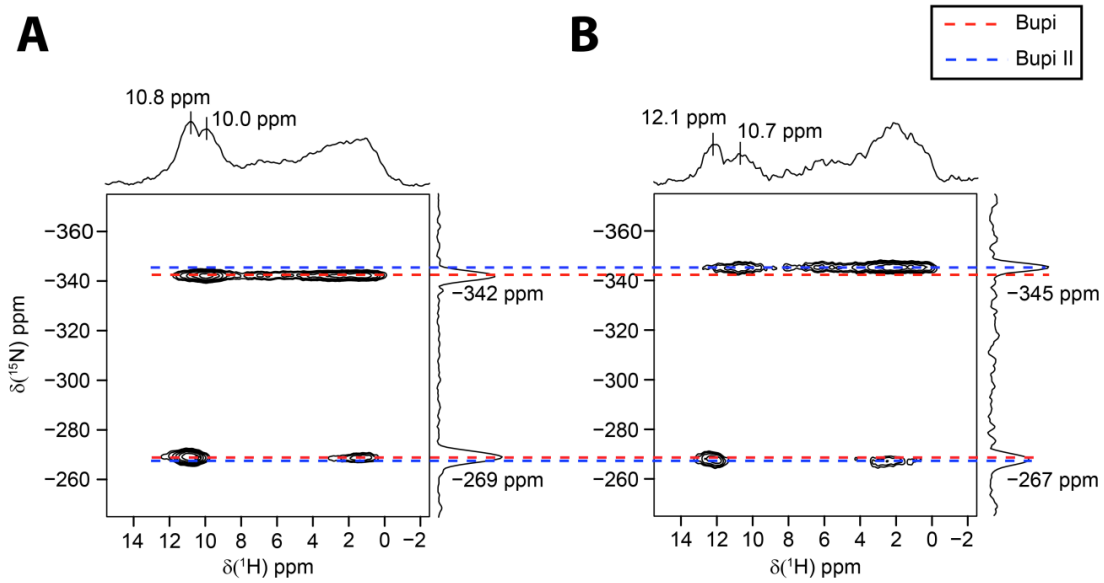

Figure 6.8. $^{1}H\{^{15}N\}$ idHETCOR spectra (14.1 T) of (A) **Bupi** and (B) **Bupi II**.

6.4.1.8. Summary of ^{14}N and ^{15}N SSNMR data

For most samples, ^{14}N SSNMR spectra are dominated by powder patterns corresponding to pseudo-tetrahedral nitrogen environments, due to their reduced values of C_Q and correspondingly narrower powder patterns. There are some exceptions, where either the relaxation and/or the CP conditions enable the rapid acquisition of broader patterns (e.g., **Rani**) or prevent acquisition altogether (e.g., **Dibu**). Nonetheless, the exclusive observation of the nitrogen patterns corresponding to pseudo-tetrahedral sites is extremely useful for the differentiation of polymorphs (see *Section 6.4.1.7*), because the ^{14}N EFG tensors are very sensitive to different hydrogen bonding configurations (much more so than nitrogen chemical shifts in many instances). The ^{14}N SSNMR spectra yield η_Q values that are closer to zero or one for $RR'R''NH^+$ or $RR'NH_2^+$ environments, respectively. A particularly valuable aspect of having experimentally determined ^{14}N EFG tensors is the ease with which they can be modeled via quantum chemical

computations; the relationships between local symmetries and EFG tensor parameters and orientations are discussed in *Section 6.4.2*.

The majority of nitrogen sites in these APIs were observed using $^{1}H\{^{15}N\}$ idHETCOR spectroscopy. Two sites did not polarize well under CP (note that the idHETCOR pulse sequence uses two CP processes), $RR'NH_2^+$ in **Aceb** and RNO_2 in **Nica**; however, the former was identified using the DNP-enhanced $^{15}N\{^{1}H\}$ CP/MAS method. The $^{1}H\{^{15}N\}$ idHETCOR spectra provide more structural insights about the APIs than are typically obtained in conventional ^{15}N solution NMR spectra, i.e., it is not simply a matter of observing the different nitrogen environments, but rather, collecting much richer structural information on intermolecular interactions, hydrogen bonding, and conformational differences. These 2D spectra also have potential for polymorph fingerprinting and differentiation. Indeed, distinct ^{1}H and ^{15}N chemical shifts are observed in **Bupi** and **Bupi II**, highlighting the subtle structural differences between the two polymorphs.

6.4.2. Plane-wave DFT Calculations of NMR Interaction Tensors

Plane-wave DFT calculations of ^{14}N EFG tensor parameters and nitrogen nuclear magnetic shielding (NMS) parameters were conducted on models derived from known crystal structures for each API.[36,129,132–138] DFT calculations were completed using the CASTEP software package[145] (see Experimental Section for details). Molecular systems involved in strong intermolecular hydrogen-bonding interactions typically require structural optimization prior to calculation of the NMR parameters. In particular, it is almost always necessary to optimize the hydrogen atom positions in the absence of

neutron diffraction data. In addition, it is noted that several of the pharmaceuticals discussed herein have extremely large unit cells containing a large number of atoms, which can be problematic for plane-wave calculations.

6.4.2.1 Experiment vs. Theory

The calculated ^{14}N EFG tensor parameters and isotropic NMS values obtained after optimization of the hydrogen atom positions in each structure are listed in **Table 6.1**. Given the limited number of systems, the variety of nitrogen environments, and the great variability in unit cell sizes, quality of crystal structures and temperatures of XRD experiments, overarching statements regarding the accuracy of the calculations cannot be made. There is reasonably close agreement between the experimental and theoretical values of C_Q and η_Q; in particular, the asymmetry parameters are extremely useful for differentiating distinct bonding environments in the pseudo-tetrahedral nitrogens (*vide infra*). In order to draw correlations between experimental and theoretical chemical shifts, a more detailed study involving comparison of chemical shift and NMS tensors must be made. This is beyond the scope of the current study; nonetheless, the preliminary set of nitrogen NMS calculations are presented in this work. The remainder of this section focuses only upon the ^{14}N EFG tensors. A complete summary of all EFG and NMS tensor parameters is given in **Table E6**.

6.4.2.2 ^{14}N EFG Tensor Orientations and the Sign of C_Q

By examining the ^{14}N EFG tensor orientations obtained from DFT calculations, it is possible to make correlations between the experimentally measured tensor parameters

and known molecular structures and local symmetries. This aids in understanding the origins of the ^{14}N quadrupolar interactions and their relation to molecular structure, and provides an attractive means of making structural predictions for systems with hitherto unknown structures. The signs of the components of the EFG tensor also show variation with differences in bonding and structure, and are intimately related to the tensor orientations. Since $C_Q = eQV_{33}/h$, C_Q and V_{33} have the same signs for ^{14}N, since the value of eQ is positive. Furthermore, since the EFG tensor is traceless (i.e., $V_{11} + V_{22} + V_{33} = 0$), the signs of V_{11} and V_{22} are always opposite to that of V_{33}. It is important to note that the sign of C_Q cannot be determined directly from a ^{14}N NMR spectrum, but can be determined from *J*- and dipolar spin pairs subjects to a variety of single- and double-resonance experiments.

The ^{14}N EFG tensor in **Scop** has V_{33} oriented near the direction of the N-H bond ($\angle(V_{33}\text{-N-H}) = 10.19°$), which is typical for $RR'R''NH^+$ pseudo-tetrahedral nitrogen environments (**Figure 6.9A**).[56] The orientations of V_{11} and V_{22} can vary for such environments, and the value of η_Q indicates that these components are similar in magnitude. For the $RR'NH_2^+$ nitrogen environments in **Alpr** and **Isop**, the high values of η_Q indicate that the magnitudes of V_{22} and V_{33} are similar (but opposite in sign), and that V_{11} is the distinct component of the EFG tensor. V_{33} is oriented in a direction approximately perpendicular to the H-N-H plane in each case ($\angle(V_{33}\text{-N-H}_A) = 93.00°$ and $\angle(V_{33}\text{-N-H}_A) = 97.81°$, respectively) and V_{11} is oriented between the two hydrogen atoms in the same plane, approximately bisecting the H-N-H angle (**Figures 6.9B** and **6.9C**).[56] The calculated values of C_Q for these $RR'R''NH^+$ and $RR'NH_2^+$ environments are negative and positive, respectively, which means that negative EFGs are observed in the

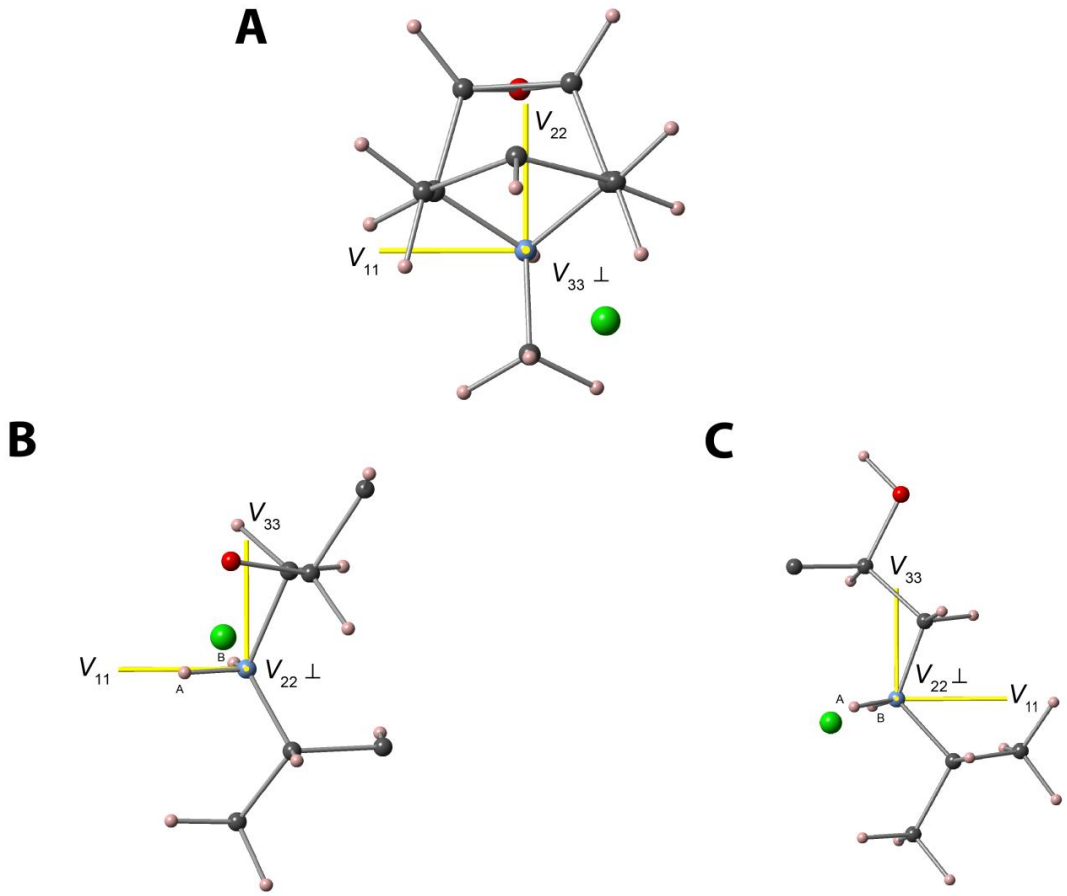

Figure 6.9. Theoretical ^{14}N EFG tensor orientations in the molecular frames of (A) **Scop**, (B) **Alpr**, and (C) **Isop**. Tensor orientations are taken from ^{14}N EFG calculations completed using NMR CASTEP after geometry optimization of the proton positions. Molecular fragments shown for clarity (see **Appendix E** for full structures).

direction/plane of covalent N-H bonds, and positive EFGs are observed perpendicular to these bonds.

For the $RR'NH_2^+$ nitrogen environment in **Aceb**, V_{22} is oriented perpendicular to the H-N-H plane ($\angle(V_{33}\text{-N-H}_A) = 98.91°$, **Figures 6.10A** and **6.10B**), rather than V_{33} (as in the cases of **Alpr** and **Isop**). In addition, the sign of the C_Q is opposite to those of **Alpr** and **Isop**. However, the signs of the EFGs in **Aceb** are the same as those in **Alpr** and **Isop**: positive and negative in directions perpendicular and parallel to the H-N-H

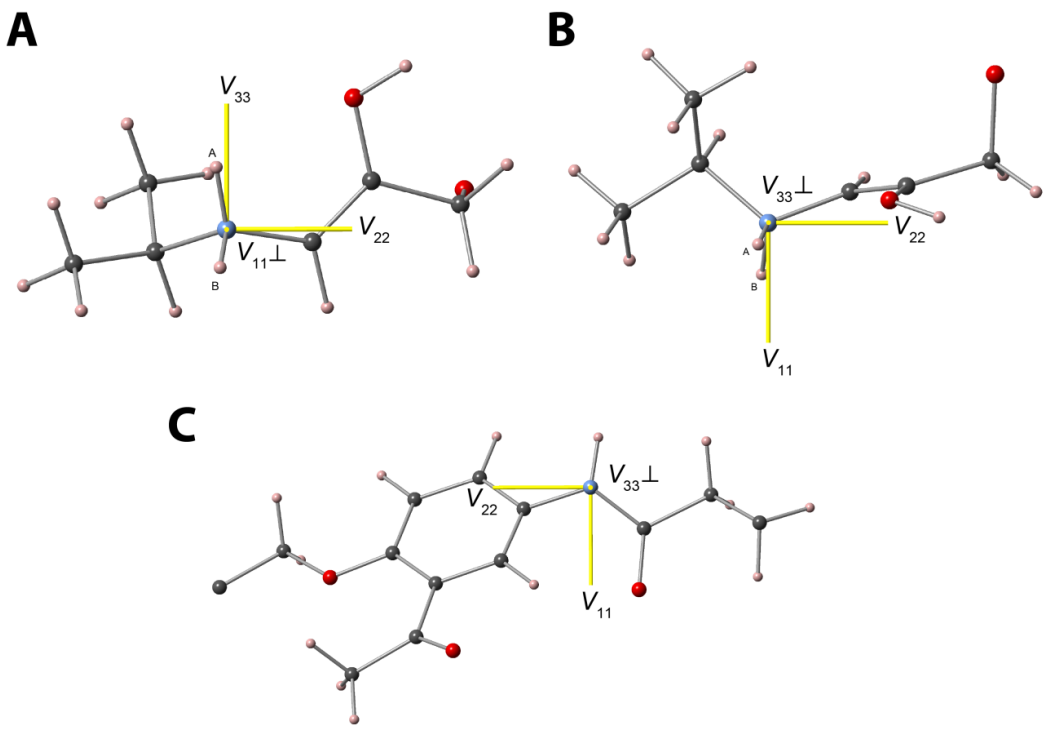

Figure 6.10. Theoretical ^{14}N EFG tensor orientations in the molecular frames of (A,B) the pseudo-tetrahedral nitrogen and (C) the planar nitrogen in **Aceb**. In (A) the molecular frame is viewed down the V_{11} component of the tensor and in (B) the molecule is viewed down V_{33}. Molecular fragments shown for clarity (see **Appendix E** for full structure).

plane, respectively. Since V_{22} and V_{33} are similar in magnitude (but opposite in sign), the change in sign of C_Q is not as dramatic a difference in tensor orientation as one would think; rather, the absolute magnitudes of the negative EFGs are greater than those of the positive EFGs in **Aceb**; the reverse is true for **Alpr** and **Isop**.

The three-coordinate, planar RR′NH nitrogen moiety in **Aceb** is structurally and electronically distinct from the aforementioned pseudo-tetrahedral sites (R and R′ correspond to the aromatic and carbonyl moieties, **Figure 6.10C**). V_{33} is directed approximately perpendicular to the C_{Ar}-N-C_{CO} plane ($\angle(V_{33}\text{-N-}C_{Ar})$ = 82.52°), while V_{11} is slightly below this plane and near the N-H bond ($\angle(V_{11}\text{-N-H})$ = 13.96°). Here, V_{33} is

the distinct tensor component, indicating a large negative EFG along the direction of the nitrogen p_z orbital, in agreement with previous observations.[56,147,148]

There are three distinct nitrogen-containing moieties in **Nica**, and as such, three unique ^{14}N EFG tensors. Despite the fact that only the ^{14}N pattern for the pseudo-tetrahedral RR′R″NH$^+$ moiety is observed, the tensor orientations are still of interest, and can be compared to those of **Rani** (*vide infra*). The RR′R″NH$^+$ and planar RR′NH moieties have tensor orientations and EFG signs akin to those described above (**Figures 6.11A** and **6.11B**): the former has V_{33} (negative EFG) oriented near the N-H bond ($\angle(V_{33}$-N-H) = 3.67°), and the latter has V_{33} (negative EFG) perpendicular to the C-N-C plane and V_{11} close to the N-H bond. The planar RNO_2 group has V_{11} oriented approximately perpendicular to the O-N-O plane, and V_{33} near the direction of the C-N bond ($\angle(V_{33}$-N-C) = 1.14°, **Figure 6.11C**).

Rani has four distinct nitrogen-containing moieties that all give rise to unique ^{14}N EFG tensors. The ^{14}N EFG tensor of the RR′R″NH$^+$ moiety has a similar orientation to that described above for **Nica** and **Scop**; V_{33} is oriented nearly along the N-H bond ($\angle(V_{33}$-N-H) = 1.18°, **Figure 6.12A**). The RR′NH moieties have tensor orientations and EFG signs that are also consistent with those described above: V_{33} is oriented nearly perpendicular to the C-N-C plane and V_{11} approximately bisects the C-N-C angle (**Figure 6.12B**). The RNO_2 moiety has an EFG tensor orientation with V_{11} oriented perpendicular to the O-N-O plane ($\angle(V_{11}$-N-O) = 88.04°) and V_{22} oriented nearly coincident with the C-N bond ($\angle(V_{22}$-N-C) = 7.57°) (unlike V_{33} in **Nica**).

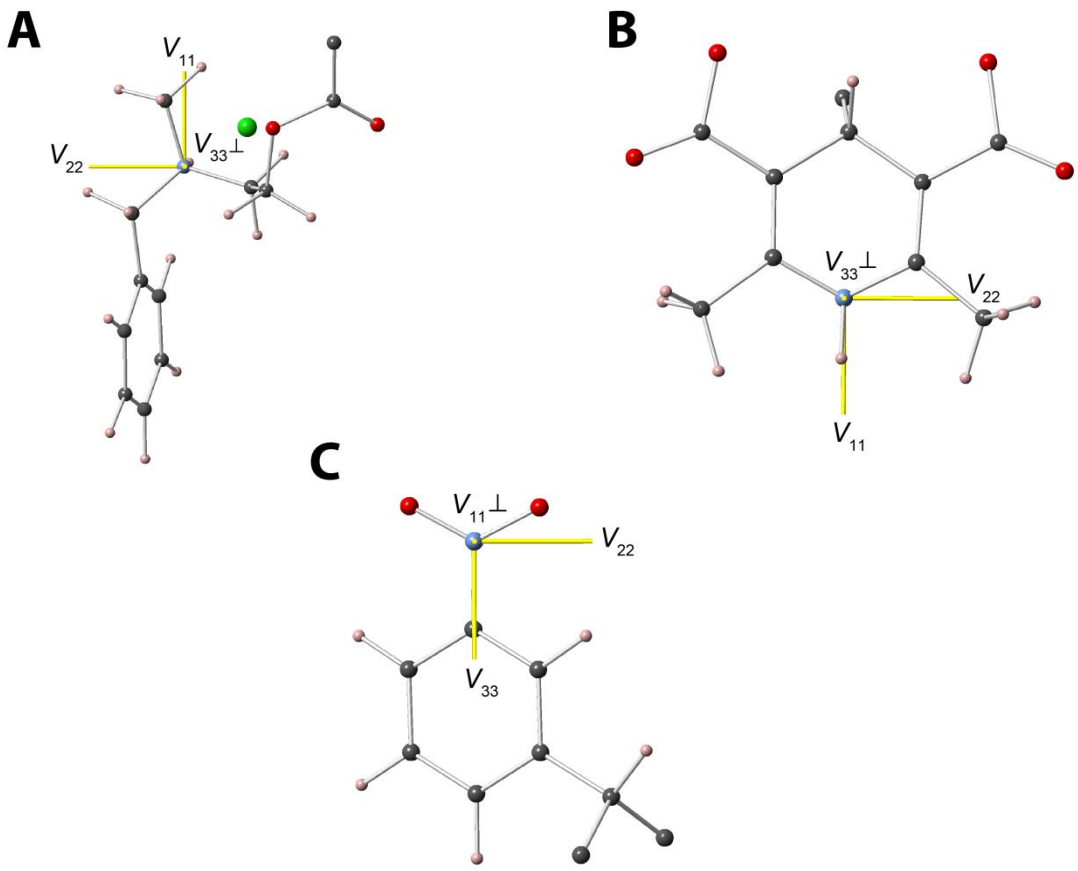

Figure 6.11. Theoretical ^{14}N EFG tensor orientations in the molecular frames of **Nica**. In (A) the pseudo-tetrahedral RR′R″NH^{+} site, (B) the planar RR′NH nitrogen, and (C) the RNO_2 group. Molecular fragments shown for clarity (see **Appendix E** for full structure).

To date, the ^{14}N EFG tensors of RNO_2 groups have only been investigated by a handful of researchers, including by Cox *et al*. (nitromethane using microwave spectroscopy),[149,150] Subbarao *et al*. (a series of aromatic nitro compounds with ^{14}N NQR and Townes-Dailey theory)[151] and Harris *et al*. (nitrobenzene via ^{13}C-^{14}N residual dipolar couplings measured in ^{13}C CP/MAS NMR spectra).[152] The current work on **Nica** and **Rani** represents a modern instance of the application electronic structure calculations on periodic solids to examine this class of ^{14}N EFG tensors. Interestingly, previous work has shown great variation in the ^{14}N EFG tensor orientations and the signs of C_Q, which may

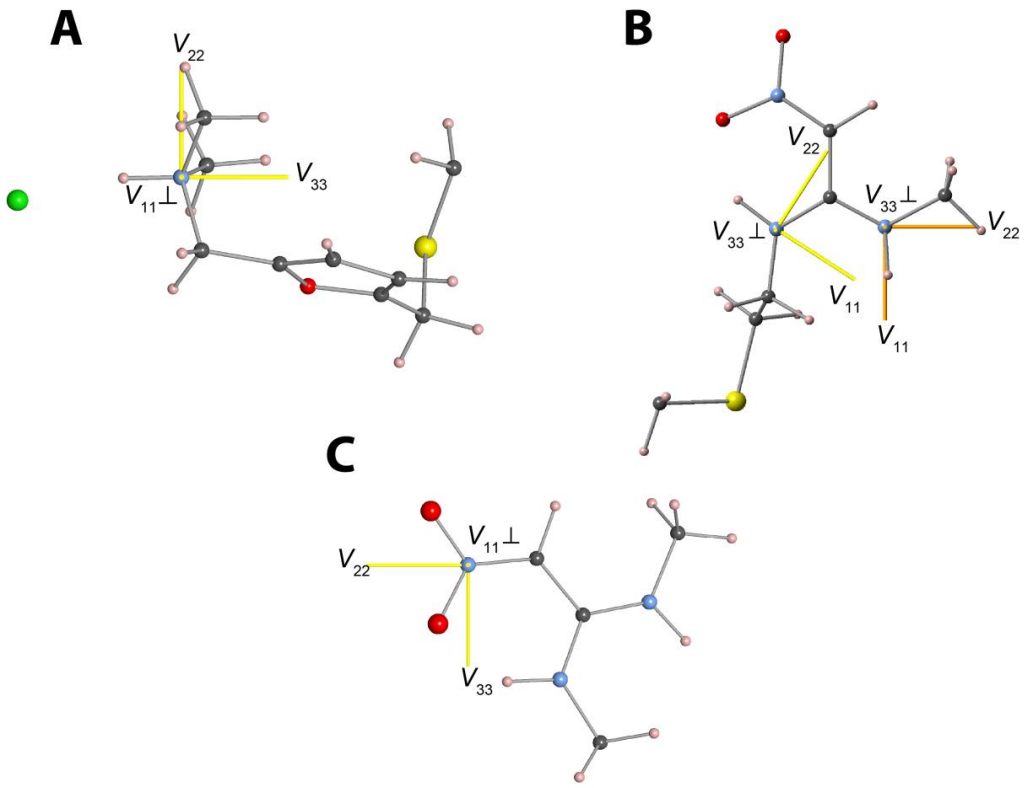

Figure 6.12. Theoretical ^{14}N EFG tensor orientations in the molecular frame of **Rani**. In (A) the pseudo-tetrahedral RR′R″NH$^+$ site, (B) the two planar RR′NH nitrogen groups, and (C) the RNO_2 group. Molecular fragments are shown for clarity (see **Appendix E** for full structure).

result from not only differences in local molecular structures, but also because of intermolecular hydrogen bonding in solids.[151] Clearly, more work is necessary to examine the variations of these tensors with structure, especially in condensed phases; for now, we have summarized the full set of results in a simple diagram (**Figure E19**).

Finally, the ^{14}N EFG tensors for **Bupi** and **Bupi II** are shown in **Figure 6.13**. The tensor orientations for the pseudo-tetrahedral RR′R″NH$^+$ moieties (**Figures 6.13A** and **6.13C**) are consistent with those of other RR′R″NH$^+$ groups, with V_{33} (negative EFG) being oriented nearly along the N-H bond ($\angle(V_{33}$-H-N) = 8.35° for **Bupi** and $\angle(V_{33}$-H-N) = 17.40° for **Bupi II**). For the planar RR′NH groups (**Figures 6.13B** and **6.13D**), tensor

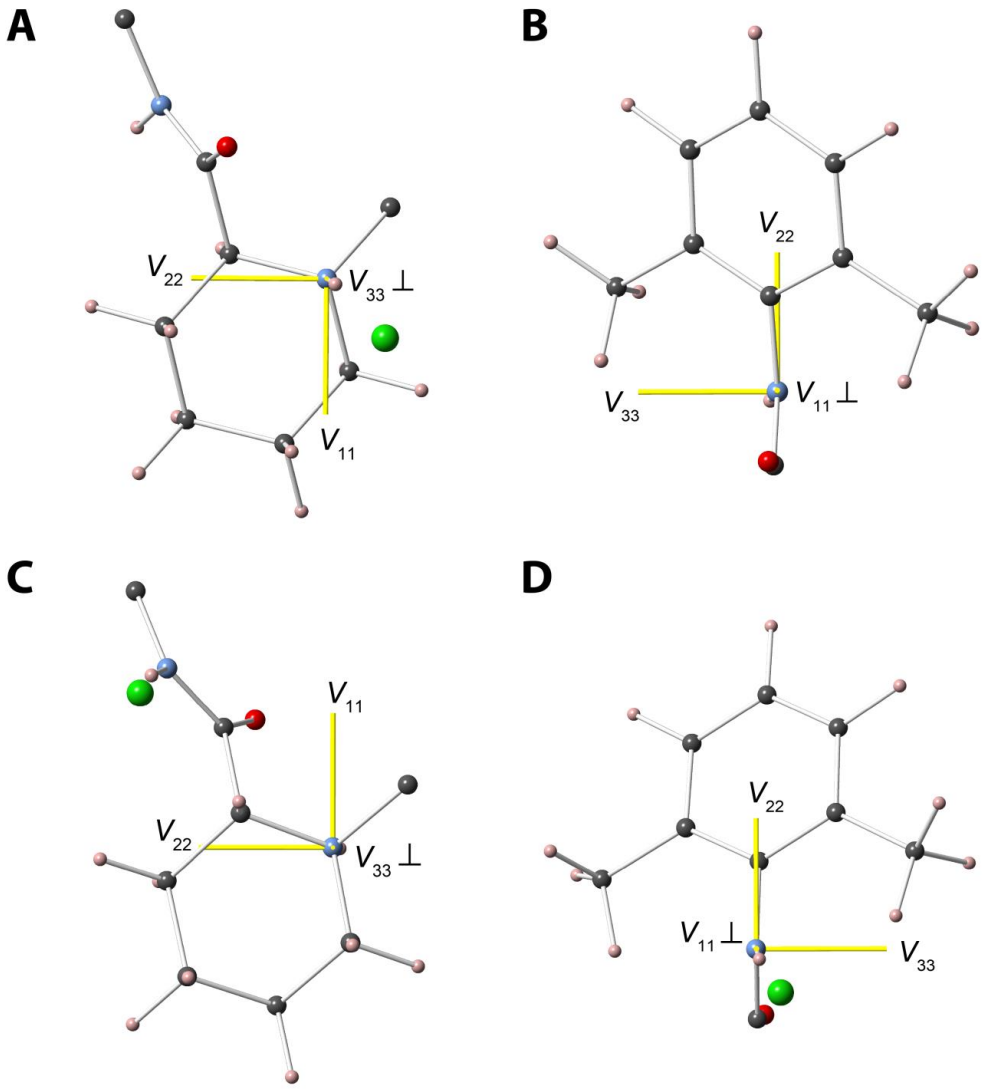

Figure 6.13. Theoretical ^{14}N EFG tensor orientations in the molecular frames of **Bupi** (A and B) and **Bupi II** (C and D). The ^{14}N EFG tensors of the pseudo-tetrahedral RR′R″NH^{+} sites are depicted in (A) and (C), while the planar RR′NH nitrogen groups are depicted in (B) and (D). Molecular fragments shown for clarity (see **Appendix E** for full structures).

orientations feature V_{33} (negative) oriented nearly perpendicular to the C-N-C plane ($\angle(V_{33}\text{-N-C}_{Ar})$ = 86.25° for **Bupi** and $\angle(V_{33}\text{-N-C}_{Ar})$ = 111.58° for **Bupi II**) and V_{11} is close to the direction of the N-H bond ($\angle(V_{11}\text{-H-N})$ = 8.64° for **Bupi** and $\angle(V_{11}\text{-H-N})$ = 9.05° for **Bupi II**).

6.4.2.3 Summary of ^{14}N EFG tensor orientations

For pseudo-tetrahedral RR′R″NH$^+$ nitrogen environments, V_{33} is found to be near the direction of the N-H bond, the η_Q is low (i.e., < 0.30), and the sign of C_Q is negative. For pseudo-tetrahedral RR′NH$_2^+$ nitrogen moieties, the η_Q is close to one, and the sign of C_Q is positive if V_{33} is oriented nearly perpendicular to the H-N-H plane (e.g., **Alpr** and **Isop**), and negative if V_{22} is oriented perpendicular to the H-N-H plane rather than V_{33} (e.g., **Aceb**), resulting in a negative value of C_Q. For planar RR′NH nitrogen sites, C_Q is negative, with V_{11} oriented close to the N-H bond and V_{33} approximately perpendicular to the C-N-C plane. Finally, for planar RNO$_2$ nitrogen sites, V_{11} is oriented perpendicular to the O-N-O plane. There is some variation in the orientations of V_{22} and V_{33}, which may result from intermolecular interactions; however, the signs of the EFGs along and perpendicular to the C-NO$_2$ bond are always negative and positive, respectively.

6.5. Conclusions

We have demonstrated that the combined use of ^{14}N and ^{15}N SSNMR methods, including DE, BCP, ^{1}H{^{15}N} idHETCOR and DNP, in conjunction with plane-wave DFT calculations of ^{14}N EFG tensors, can provide sets of NMR parameters needed for comprehensive structural characterization of nitrogen-containing APIs. It was found that our UW ^{14}N methods favor the observation of signals arising from pseudo-tetrahedral nitrogen moieties, due to their smaller values of C_Q (*ca*. 1 – 1.5 MHz) and correspondingly narrower patterns in comparison to those of ^{14}N nuclei in planar nitrogen environments. These patterns enable accurate determinations of C_Q and η_Q, which are found to be extremely sensitive to even the most subtle structural differences, including

distinct hydrogen bonding configurations. The $^{1}H\{^{15}N\}$ idHETCOR method proved instrumental in providing important chemical shift and spatial correlation information in natural abundance samples. In most cases, well-resolved peaks and correlations corresponding to multiple nitrogen environments of different geometries were observed, even for sites with no directly bound hydrogen atoms. By using ^{14}N and ^{15}N SSNMR in tandem, it is possible to accurately distinguish between different polymorphic forms of APIs, as demonstrated for bupivacaine HCl. Plane-wave DFT calculations provide additional important information on the relationships between the ^{14}N EFG tensors, the signs of the EFGs, and the molecular structures of the APIs.

This work represents a first exploratory effort in using tandem ^{14}N and ^{15}N SSNMR methods for studying APIs. First, further work must be done on enhancing the performance of the ^{14}N and ^{15}N NMR experiments. For the former, the development of new protocols for broadband cross polarization, efficient ^{1}H decoupling, and uniform excitation with broadband pulses are all crucial. Investigation of the use of ^{14}N static NMR experiments under DNP conditions would also be of great interest, perhaps for accessing some of the extremely broad patterns arising from planar nitrogen sites (e.g., RR′NH). In addition, ^{14}N NMR experiments that are targeted at enhancing selection regions of the powder patterns (as opposed to the full patterns) may also have great utility in this regard. For the latter, the use of advanced ultra-fast MAS probes (i.e.., rotation speeds of 100+ kHz)[153–155] may further refine the idHETCOR experiments in terms of resolution in the ^{1}H dimension, and the use of enhanced ^{1}H decoupling schemes may allow for the use of larger rotor sizes for increased S/N. Projects focused on addressing these issues are currently underway in our laboratories. Second, efforts must be made to

ameliorate agreement between experimental and theoretical NMR tensor parameters. Full geometry optimizations, better density functionals, the use of superior basis sets, and the inclusion of dispersion effects,[156] may all be of value. Given such improvements, it is possible that $^{14/15}$N NMR data sets obtained with our methods may be useful in the emerging area of NMR crystallography,[157] where structural predictions can be made with computational methods including *ab initio* random structural searching (AIRSS) algorithm[158–161] and other algorithms.[162–164]

Finally, we hope that this work encourages others to consider applying the methodologies for ^{14}N and ^{15}N SSNMR presented herein, for not only study of APIs (i.e., polymorph differentiation, impurity detection, and discovery of new structures in both bulk and dosage forms), but also to a wide assortment of organic, biological, inorganic and organometallic nitrogen-containing systems.

6.6 Bibliography

(1) Geppi, M.; Mollica, G.; Borsacchi, S.; Veracini, C. A. *Appl. Spectrosc. Rev.* **2008**, *43*, 202–302.

(2) Giron, D. *J. Therm. Anal. Calorim.* **2003**, *73*, 441–457.

(3) Byrn, S. R.; Pfeiffer, R. R.; Stephenson, G. A.; Grant, D. J. W.; Gleason, W. B. *Chem. Mater.* **1994**, *6*, 1148–1158.

(4) Giron, D. *J. Therm. Anal. Calorim.* **2001**, *64*, 37–60.

(5) Giron, D. *Am. Pharm. Rev.* **2005**, *8*, 32.

(6) Giron, D. *Am. Pharm. Rev.* **2005**, *8*, 72.

(7) Giron, D. In *Lipophilicity Symposium*; Zurich, 2006; p. 307.

(8) Brittain, H. G. *Polymorphism in Pharmaceutical Solids*; Marcel Dekker: New

York, 1999; Vol. 95.

(9) Haleblian, J. K.; McCrone, W. *J. Pharm. Sci.* **1969**, *58*, 911–929.

(10) Karpinski, P. H. *Chem. Eng. Technol.* **2006**, *29*, 233–238.

(11) Llinàs, A.; Box, K. J.; Burley, J. C.; Glen, R. C.; Goodman, J. M. *J. Appl. Crystallogr.* **2007**, *40*, 379–381.

(12) Chupin, V.; de Kroon, A. I. P. M.; de Kruijff, B. *J. Am. Chem. Soc.* **2004**, *126*, 13816–13821.

(13) Griffin, J. M.; Martin, D. R.; Brown, S. P. *Angew. Chemie - Int. Ed.* **2007**, *46*, 8036–8038.

(14) Li, Z. J.; Abramov, Y.; Bordner, J.; Leonard, J.; Medek, A.; Trask, A. V. *J. Am. Chem. Soc.* **2006**, *128*, 8199–8210.

(15) Smith, E. D. L.; Hammond, R. B.; Jones, M. J.; Roberts, K. J.; Mitchell, J. B. O.; Price, S. L.; Harris, R. K.; Apperley, D. C.; Cherryman, J. C.; Docherty, R. *J. Phys. Chem. B* **2001**, *105*, 5818–5826.

(16) Vogt, F. G.; Brum, J.; Katrincic, L. M.; Flach, A.; Socha, J. M.; Goodman, R. M.; Haltiwanger, R. C. *Cryst. Growth Des.* **2006**, *6*, 2333–2354.

(17) Wawer, I.; Pisklak, D. M.; Chilmonczyk, Z. *J. Pharm. Biomed. Anal.* **2005**, *38*, 865–870.

(18) Wenslow, R. M. *Drug Dev. Ind. Pharm.* **2002**, *28*, 555–561.

(19) Vogt, F. G.; Yin, H.; Forcino, R. G.; Wu, L. *Mol. Pharm.* **2013**, *10*, 3433–3446.

(20) Rossini, A. J.; Widdifield, C. M.; Zagdoun, A.; Lelli, M.; Schwarzwälder, M.; Copéret, C.; Lesage, A.; Emsley, L. *J. Am. Chem. Soc.* **2014**, *136*, 2324–2334.

(21) Vogt, F. G.; Williams, G. R.; Strohmeier, M.; Johnson, M. N.; Copley, R. C. B. *J. Phys. Chem. B* **2014**, *118*, 10266–10284.

(22) Dicaire, N. M.; Perras, F. A.; Bryce, D. L. *Can. J. Chem.* **2014**, *92*, 9–15.

(23) Kong, X.; Shan, M.; Terskikh, V. V; Hung, I.; Gan, Z.; Wu, G. *J. Phys. Chem. B* **2013**, *117*, 9643–9654.

(24) Przybylski, P.; Pyta, K.; Klich, K.; Schilf, W.; Kamieñskib, B. *Magn. Reson. Chem.* **2014**, *52*, 10–21.

(25) Paradowska, K.; Wawer, I. *J. Pharm. Biomed. Anal.* **2014**, *93*, 27–42.

(26) Vogt, F. G.; Dell'Orco, P. C.; Diederich, A. M.; Su, Q.; Wood, J. L.; Zuber, G. E.; Katrincic, L. M.; Mueller, R. L.; Busby, D. J.; DeBrosse, C. W. *J. Pharm. Biomed. Anal.* **2006**, *40*, 1080–1088.

(27) Brittain, H. G.; Morris, K. R.; Bugay, D. E.; Thakur, A. B.; Serajuddin, a. T. M. *J. Pharm. Biomed. Anal.* **1993**, *11*, 1063–1069.

(28) Burgess, K. M. N.; Perras, F. A.; Lebrun, A.; Messner-Henning, E.; Korobkov, I.; Bryce, D. L. *J. Pharm. Sci.* **2012**, *101*, 2930–2940.

(29) Vogt, F. G.; Williams, G. R.; Copley, R. C. B. *J. Pharm. Sci.* **2013**, *102*, 3705–3716.

(30) Hem, S. L.; Johnston, C. T. *Production and Characterization of Aluminum-Containing Adjuvants*; Wen, E. P.; Ellis, R.; Pujar, N. S., Eds.; 1st ed.; John Wiley & Sons, Inc.: Hoboken, NJ, USA, 2015.

(31) Kiang, Y.-H.; Nagapudi, K.; Wu, T.; Peterson, M. L.; Jona, J.; Staples, R. J.; Stephens, P. W. *J. Pharm. Sci.* **2015**, *104*, 2161–2168.

(32) Kong, X.; Terskikh, V. V.; Toubaei, A.; Wu, G. *Can. J. Chem.* **2015**, *93*, 1–9.

(33) Liu, J.; Nagapudi, K.; Kiang, Y.-H.; Martinez, E.; Jona, J. *Drug Dev. Ind. Pharm.* **2009**, *35*, 969–975.

(34) Skotnicki, M.; Apperley, D. C.; Aguilar, J. A.; Milanowski, B.; Pyda, M.; Hodgkinson, P. *Mol. Pharm.* **2016**, *13*, 211–222.

(35) Vogt, F. G.; Roberts-Skilton, K.; Kennedy-Gabb, S. A. *Pharm. Res.* **2013**, *30*, 2315–2331.

(36) Hamaed, H.; Pawlowski, J. M.; Cooper, B. F. T.; Fu, R.; Eichhorn, S. H.; Schurko, R. W. *J. Am. Chem. Soc.* **2008**, *130*, 11056–11065.

(37) Hildebrand, M. P.; Hamaed, H.; Namespetra, A. M.; Donohue, J. M.; Fu, R.; Hung, I.; Gan, Z.; Schurko, R. W. *CrystEngComm* **2014**, *16*, 7334–7356.

(38) Pandey, M. K.; Kato, H.; Ishii, Y.; Nishiyama, Y.; Pandy, M. K.; Kato, H.; Ishii, Y.; Nishiyama, Y. *Phys. Chem. Chem. Phys.* **2016**, *18*, 6209–6216.

(39) Vogt, F. G. *Solid-State NMR in Drug Discovery and Development*; 2013.

(40) Monti, G. A.; Chattah, A. K.; Linck, Y. G. *Solid-State Nuclear Magnetic Resonance in Pharmaceutical Compounds*; 1st ed.; Elsevier Ltd., 2014; Vol. 83.

(41) Vogt, F. G. *eMagRes* **2015**, *4*, 255–268.

(42) Bradley, D. C.; Hodge, S. R.; Runnacles, J. D.; Hughes, M.; Mason, J.; Richards, R. L. *J. Chem. Soc. Dalt. Trans.* **1992**, 1663.

(43) Harbison, G. S.; Kye, Y.-S.; Penner, G. H.; Grandin, H. M.; Monette, M. *J. Phys. Chem. B* **2002**, *106*, 10285–10291.

(44) Rudakov, T. N.; Mikhaltsevitch, V. T.; Hayes, P. A.; Chisholm, W. P. *Chem. Phys. Lett.* **2004**, *387*, 405–409.

(45) Jakobsen, H. J.; Hove, A. R.; Hazell, R. G.; Bildsøe, H.; Skibsted, J. *Magn. Reson. Chem.* **2006**, *44*, 348–356.

(46) Lee, D. K.; Santos, J. S.; Ramamoorthy, A. *Chem. Phys. Lett.* **1999**, *309*, 209–214.

(47) Portieri, A.; Harris, R. K.; Fletton, R. A.; Lancaster, R. W.; Threlfall, T. L. *Magn. Reson. Chem.* **2004**, *42*, 313–320.

(48) Fujiwara, T.; Todokoro, Y.; Yanagishita, H.; Tawarayama, M. *J. Biomol. NMR* **2004**, *28*, 311–325.

(49) Amoureux, J.-P.; Trébosc, J.; Hu, B.; Halpern-Manners, N.; Antonijevic, S. *J. Magn. Reson.* **2008**, *194*, 317–320.

(50) Antonijevic, S.; Halpern-Manners, N. *Solid State Nucl. Magn. Reson.* **2008**, *33*, 82–87.

(51) Althaus, S. M.; Mao, K.; Stringer, J. A.; Kobayashi, T.; Pruski, M. *Solid State Nucl. Magn. Reson.* **2014**, *57-58*, 17–21.

(52) Ashikawa, M.; Shoji, A.; Ozaki, T.; Ando, I. *Macromolecules* **1999**, *32*, 2288–2292.

(53) Giavani, T.; Bildsøe, H.; Skibsted, J.; Jakobsen, H. J. *J. Magn. Reson.* **2004**, *166*,

262–272.

(54) Elmi, F.; Hadipour, N. L. *J. Phys. Chem. A* **2005**, *109*, 1729–1733.

(55) O'Dell, L. A.; Schurko, R. W. *Phys. Chem. Chem. Phys.* **2009**, *11*, 7069–7077.

(56) O'Dell, L. A.; Schurko, R. W.; Harris, K. J.; Autschbach, J.; Ratcliffe, C. I. *J. Am. Chem. Soc.* **2011**, *133*, 527–546.

(57) O'Dell, L. A.; Ratcliffe, C. I.; Kong, X.; Wu, G. *J. Phys. Chem. A* **2012**, *116*, 1008–1014.

(58) Elmi, M. M.; Kaykhaei, A. A.; Elmi, F. *Magn. Reson. Chem.* **2012**, *50*, 314–319.

(59) Veinberg, S. L.; Friedl, Z. W.; Harris, K. J.; O'Dell, L. A.; Schurko, R. W. *CrystEngComm* **2015**, 17–19.

(60) Tatton, A. S.; Pham, T. N.; Vogt, F. G.; Iuga, D.; Edwards, A. J.; Brown, S. P. *CrystEngComm* **2012**, *14*, 2654.

(61) Tatton, A. S.; Pham, T. N.; Vogt, F. G.; Iuga, D.; Edwards, A. J.; Brown, S. P. *Mol. Pharm.* **2013**, *10*, 999–1007.

(62) Rossini, A. J.; Emsley, L.; O'Dell, L. A. *Phys. Chem. Chem. Phys.* **2014**, *16*, 12890–12899.

(63) Harris, K. J.; Veinberg, S. L.; Mireault, C. R.; Lupulescu, A.; Frydman, L.; Schurko, R. W. *Chem. Eur. J.* **2013**, *19*, 16469–16475.

(64) Chattah, A. K.; Zhang, R.; Mroue, K. H.; Pfund, L. Y.; Longhi, M. R.; Ramamoorthy, A.; Garnero, C. *Mol. Pharm.* **2015**, *12*, 731–741.

(65) Smith, J. R.; Xu, W.; Raftery, D. *J. Phys. Chem. B* **2006**, *110*, 7766–7776.

(66) Song, Y.; Yang, X.; Chen, X.; Nie, H.; Byrn, S.; Lubach, J. W. *Mol. Pharm.* **2015**, *12*, 857–866.

(67) Balchin, E.; Malcolme-Lawes, D. J.; Poplett, I. J. F.; Rowe, M. D.; Smith, J. A. S.; Pearce, G. E. S.; Wren, S. A. C. *Anal. Chem.* **2005**, *77*, 3925–3930.

(68) Barras, J.; Murnane, D.; Althoefer, K.; Assi, S.; Rowe, M. D.; Poplett, I. J. F.; Kyriakidou, G.; Smith, J. A. S. *Anal. Chem.* **2013**, *85*, 2746–2753.

(69) Lavrič, Z.; Pirnat, J.; Lužnik, J.; Seliger, J.; Žagar, V.; Trontelj, Z.; Srčič, S. *J. Pharm. Sci.* **2010**, *99*, 4857–4865.

(70) Shinohara, J.; Kobayashi, K.; Sato-Akaba, H.; Itozaki, H. *Solid State Nucl. Magn. Reson.* **2011**, *40*, 121–125.

(71) Gregorovič, A.; Apih, T. *J. Magn. Reson.* **2013**, *233*, 96–102.

(72) Latosińska, J. N.; Latosińska, M.; Seliger, J.; Žagar, V.; Kazimierczuk, Z. *J. Phys. Chem. B* **2014**, *118*, 10837–10853.

(73) O'Dell, L. A. *Prog. Nucl. Magn. Reson. Spectrosc.* **2011**, *59*, 295–318.

(74) Hove, A. R.; Bildsøe, H.; Skibsted, J.; Brorson, M.; Jakobsen, H. J. *Inorg. Chem.* **2006**, *45*, 10873–10881.

(75) Whitehouse, B. A.; Ray, J. D.; Royer, D. J. *J. Magn. Reson.* **1969**, *1*, 311–326.

(76) Jakobsen, H. J.; Hove, A. R.; Bildsøe, H.; Skibsted, J.; Brorson, M. *J. Magn. Reson.* **2007**, *185*, 159–163.

(77) Tycko, R.; Opella, S. J. *J. Chem. Phys.* **1987**, *86*, 1761–1774.

(78) O'Dell, L. A.; Ratcliffe, C. I. *Chem. Phys. Lett.* **2011**, *514*, 168–173.

(79) O'Dell, L. A.; Brinkmann, A. *J. Chem. Phys.* **2013**, *138*, 064201–064210.

(80) Nishiyama, Y.; Malon, M.; Gan, Z.; Endo, Y.; Nemoto, T. *J. Magn. Reson.* **2013**, *230*, 160–164.

(81) Vitzthum, V.; Caporini, M. A.; Bodenhausen, G. *J. Magn. Reson.* **2010**, *205*, 177–179.

(82) Cavadini, S.; Antonijevic, S.; Lupulescu, A.; Bodenhausen, G. *J. Magn. Reson.* **2006**, *182*, 168–172.

(83) Cavadini, S.; Antonijevic, S.; Lupulescu, A.; Bodenhausen, G. *ChemPhysChem* **2007**, *8*, 1363–1374.

(84) Cavadini, S.; Vitzthum, V.; Ulzega, S.; Abraham, A.; Bodenhausen, G. *J. Magn. Reson.* **2010**, *202*, 57–63.

(85) Ulzega, S. *Chimia (Aarau).* **2010**, *64*, 157–160.

(86) Gan, Z.; Amoureux, J.-P.; Trébosc, J. *Chem. Phys. Lett.* **2007**, *435*, 163–169.

(87) Cavadini, S. *Prog. Nucl. Magn. Reson. Spectrosc.* **2010**, *56*, 46–77.

(88) O'Dell, L. A.; Schurko, R. W. *Chem. Phys. Lett.* **2008**, *464*, 97–102.

(89) O'Dell, L. A.; Rossini, A. J.; Schurko, R. W. *Chem. Phys. Lett.* **2009**, *468*, 330–335.

(90) O'Dell, L. A.; Schurko, R. W. *J. Am. Chem. Soc.* **2009**, *131*, 6658–6659.

(91) O'Dell, L. A.; Ratcliffe, C. I. *Chem. Commun.* **2010**, *46*, 6774–6776.

(92) Kupče, Ē.; Freeman, R. *J. Magn. Reson. Ser. A* **1995**, *115*, 273–276.

(93) Bhattacharyya, R.; Frydman, L. *J. Chem. Phys.* **2007**, *127*, 1–8.

(94) Shore, S. E.; Ansermet, J.-P.; Slichter, C. P.; Sinfelt, J. H. *Phys. Rev. Lett.* **1987**, *58*, 953–956.

(95) Massiot, D.; Farnan, I.; Gautier, N.; Trumeau, D.; Trokiner, A.; Coutures, J. P. *Solid State Nucl. Magn. Reson.* **1995**, *4*, 241–248.

(96) Medek, A.; Frydman, V.; Frydman, L. *J. Phys. Chem. A* **1999**, *103*, 4830–4835.

(97) MacGregor, A. W.; O'Dell, L. A.; Schurko, R. W. *J. Magn. Reson.* **2011**, *208*, 103–113.

(98) Lucier, B. E. G.; Reidel, A. R.; Schurko, R. W. *Can. J. Chem.* **2011**, *89*, 919–937.

(99) Lucier, B. E. G.; Johnston, K. E.; Xu, W.; Hanson, J. C.; Senanayake, S. D.; Yao, S.; Bourassa, M. W.; Srebro, M.; Autschbach, J.; Schurko, R. W. *J. Am. Chem. Soc.* **2014**, *136*, 1333–1351.

(100) Xu, J.; Lucier, B. E. G.; Lin, Z.; Sutrisno, A.; Terskikh, V. V; Huang, Y. *J. Phys. Chem. C* **2014**, *118*, 27353–27365.

(101) Johnston, K. E.; O'Keefe, C. A.; Gauvin, R. M.; Trébosc, J.; Delevoye, L.; Amoureux, J.-P.; Popoff, N.; Taoufik, M.; Oudatchin, K.; Schurko, R. W. *Chem. Eur. J.* **2013**, *19*, 12396–12414.

(102) O'Keefe, C. A.; Johnston, K. E.; Sutter, K.; Autschbach, J.; Gauvin, R. M.; Trebosc, J.; Delevoye, L.; Popoff, N.; Taoufik, M.; Udachin, K. A.; Schurko, R.

W. *Inorg. Chem.* **2014**, *53*, 9581–9597.

(103) Viger-Gravel, J.; Korobkov, I.; Bryce, D. L. *Cryst. Growth Des.* **2011**, *11*, 4984–4995.

(104) Faucher, A.; Terskikh, V. V; Wasylishen, R. E. *Solid State Nucl. Magn. Reson.* **2014**, *61-62*, 54–61.

(105) Yu, H.; Tan, X.; Bernard, G. M.; Terskikh, V. V; Chen, J.; Wasylishen, R. E. *J. Phys. Chem. A* **2015**, *119*, 8279–8293.

(106) Harris, K. J.; Lupulescu, A.; Lucier, B. E. G.; Frydman, L.; Schurko, R. W. *J. Magn. Reson.* **2012**, *224*, 38–47.

(107) Ishii, Y.; Tycko, R. *J. Magn. Reson.* **2000**, *142*, 199–204.

(108) Ishii, Y.; Yesinowski, J. P.; Tycko, R. *J. Am. Chem. Soc.* **2001**, *123*, 2921–2922.

(109) Mao, K.; Wiench, J. W.; Lin, V. S.-Y.; Pruski, M. *J. Magn. Reson.* **2009**, *196*, 92–95.

(110) Paulson, E. K.; Morcombe, C. R.; Gaponenko, V.; Dancheck, B.; Byrd, R. A.; Zilm, K. W. *J. Am. Chem. Soc.* **2003**, *125*, 15831–15836.

(111) Pawlak, T.; Paluch, P.; Trzeciak-Karlikowska, K.; Jeziorna, A.; Potrzebowski, M. J. *CrystEngComm* **2013**, *15*, 8680–8692.

(112) Wiench, J. W.; Bronnimann, C. E.; Lin, V. S.-Y.; Pruski, M. *J. Am. Chem. Soc.* **2007**, *129*, 12076–12077.

(113) Kobayashi, T.; Mao, K.; Wang, S. G.; Lin, V. S.-Y.; Pruski, M. *Solid State Nucl. Magn. Reson.* **2011**, *39*, 65–71.

(114) Hediger, S.; Meier, B. H.; Ernst, R. R. *Chem. Phys. Lett.* **1995**, *240*, 449–456.

(115) Mao, K.; Pruski, M. *J. Magn. Reson.* **2009**, *201*, 165–174.

(116) Overhauser, A. W. *Phys. Rev.* **1953**, *92*, 411–415.

(117) Carver, T. R.; Slichter, C. P. *Phys. Rev.* **1953**, *92*, 212–213.

(118) Joye, C. D.; Griffin, R. G.; Hornstein, M. K.; Hu, K.; Kreischer, K. E.; Rosay, M.; Shapiro, M. A.; Sirigiri, J. R.; Temkin, R. J.; Woskov, P. P. *IEEE Trans. Plasma*

Sci. **2006**, *34*, 518–523.

(119) Barnes, A. B.; Mak-jurkauskas, M. L.; Matsuki, Y.; Bajaj, V. S.; Wel, P. C. A. Van Der; Derocher, R.; Bryant, J.; Sirigiri, J. R.; Temkin, R. J.; Lugtenburg, J.; Herzfeld, J.; Griffin, R. G. *J. Magn. Reson.* **2009**, *198*, 261–270.

(120) Song, C.; Hu, K.; Joo, C.; Swager, T. M.; Griffin, R. G. *J. Am. Chem. Soc.* **2006**, *128*, 11385–11390.

(121) Zagdoun, A.; Casano, G.; Ouari, O.; Der, M. S.; Rossini, A. J.; Aussenac, F.; Yulikov, M.; Jeschke, G.; Cope, C.; Lesage, A.; Tordo, P.; Emsley, L. *J. Am. Chem. Soc.* **2013**, *135*, 12790–12797.

(122) Maly, T.; Debelouchina, G. T.; Bajaj, V. S.; Hu, K.; Joo, C.; Jurkauskas, M. L. M.; Sirigiri, J. R.; Wel, P. C. A. Van Der; Herzfeld, J.; Temkin, R. J.; Griffin, R. G. *J. Chem. Phys.* **2008**, *128*, 052211–052219.

(123) Lesage, A.; Lelli, M.; Gajan, D.; Caporini, M. A.; Vitzthum, V.; Mie, P.; Alauzun, J.; Roussey, A.; Mehdi, A.; Bodenhausen, G. *J. Am. Chem. Soc.* **2010**, *132*, 15459–15461.

(124) Takahashi, H.; Lee, D.; Dubois, L.; Bardet, M.; Hediger, S. *Angew. Chemie Int. Ed.* **2012**, *51*, 11766–11769.

(125) Perras, F. A.; Kobayashi, T.; Pruski, M. *J. Am. Chem. Soc.* **2015**, *137*, 8336–8339.

(126) Zagdoun, A.; Casano, G.; Ouari, O.; Lapadula, G.; Rossini, A. J.; Lelli, M.; Baffert, M.; Gajan, D.; Veyre, L.; Maas, W. E.; Rosay, M.; Weber, R. T.; Thieuleux, C.; Coperet, C.; Lesage, A.; Tordo, P.; Emsley, L. *J. Am. Chem. Soc.* **2012**, *134*, 2284–2291.

(127) Guo, Z.; Kobayashi, T.; Wang, L.; Goh, W.; Xiao, C.; Caporini, M. A.; Rosay, M.; Johnson, D. D.; Pruski, M.; Huang, W. *Chem. Eur. J.* **2014**, 16308–16313.

(128) Kobayashi, T.; Gupta, S.; Caporini, M. A.; Pecharsky, V. K.; Pruski, M. *J. Phys. Chem. C* **2014**, *118*, 19548–19555.

(129) Csöregh, I. *Acta Crystallogr. Sect. C Cryst. Struct. Commun.* **1992**, *48*, 1794–1798.

(130) Nolze, G.; Kraus, W. *Powder Diffr.* **1998**, *13*, 256–259.

(131) CrystalDiffract, **2015**.

(132) Glaser, R.; Shiftan, D.; Drouin, M. *Can. J. Chem.* **2000**, *78*, 212–223.

(133) Barrans, Y.; Cotrait, M.; Dangoumau, J. *Acta Crystallogr. Sect. B Struct. Crystallogr. Cryst. Chem.* **1973**, *29*, 1264–1272.

(134) Kingsford-Adaboh, R.; Hayashi, E.; Haisa, M.; Kashida, S. *Bull. Chem. Soc. Jpn.* **1993**, *66*, 2883–2888.

(135) Carpy, A.; Gadret, M.; Hickel, D.; Leger, J. M. *Acta. Cryst. B.* **1979**, *35*, 185–188.

(136) Hayward, B. S.; Donohue, J. *J. Cryst. Mol. Struct.* **1977**, *7*, 275–294.

(137) Moreno-Calvo, E.; Muntó, M.; Wurst, K.; Ventosa, N.; Masciocchi, N.; Veciana, J. *Mol. Pharm.* **2011**, *8*, 395–404.

(138) Ishida, T.; In, Y.; Inoue, M. *Acta Crystallogr. Sect. C Cryst. Struct. Commun.* **1990**, *46*, 1893–1896.

(139) Tang, J. A.; Masuda, J. D.; Boyle, T. J.; Schurko, R. W. *ChemPhysChem* **2006**, *7*, 117–130.

(140) Eichele, K. WSolids1 — Solid State NMR Simulations, 2013.

(141) Fung, B. M.; Khitrin, A. K.; Ermolaev, K. *J. Magn. Reson.* **2000**, *142*, 97–101.

(142) Oas, T. G.; Griffin, R. G.; Levitt, M. H. *J. Chem. Phys.* **1988**, *89*, 692–695.

(143) Zorin, V. E. GSim - visualisation and processing tool for NMR experiments and simulations, 2013.

(144) Harris, R. K.; Becker, E. D.; De Menezes, S. M. C.; Granger, P.; Hoffman, R. E.; Zilm, K. W. *Pure Appl. Chem.* **2008**, *80*, 59–84.

(145) Clark, S. J.; Segall, M. D.; Pickard, C. J.; Hasnip, P. J.; Probert, M. I. J.; Refson, K.; Payne, M. C. *Zeitschrift für Krist.* **2005**, *220*, 567–570.

(146) Pickard, C. J.; Mauri, F. *Phys. Rev. B* **2001**, *63*, 245101–245113.

(147) Amini, S. K.; Shaghaghi, H.; Bain, A. D.; Chabok, A.; Tafazzoli, M. *Solid State Nucl. Magn. Reson.* **2010**, *37*, 13–20.

(148) Hexem, J. G.; Frey, M. H.; Opella, S. J. *J. Am. Ceram. Soc.* **1981**, *103*, 224–226.

(149) Cox, A. P.; Waring, S.; Motgenstern, K. *Nature* **1971**, *229*, 22–23.

(150) Cox, A. P.; Waring, S. *J. Chem. Soc. Faraday Trans. 2* **1972**, *6*, 1060–1071.

(151) Subbarao, S. N.; Bray, P. J. *J. Chem. Phys.* **1977**, *67*, 3947–3955.

(152) Harris, R. K.; Jonsen, P.; Packer, K. J. *Magn. Reson. Chem.* **1985**, *23*, 565–577.

(153) Kobayashi, T.; Mao, K.; Paluch, P.; Nowak-Krõl, A.; Sniechowska, J.; Nishiyama, Y.; Gryko, D. T.; Potrzebowski, M. J.; Pruski, M. *Angew. Chemie - Int. Ed.* **2013**, *52*, 14108–14111.

(154) Qi, Y.; Malon, M.; Martineau, C.; Taulelle, F.; Nishiyama, Y. *J. Magn. Reson.* **2014**, *239*, 75–80.

(155) Nishiyama, Y.; Kobayashi, T.; Malon, M.; Singappuli-Arachchige, D.; Slowing, I. I.; Pruski, M. *Solid State Nucl. Magn. Reson.* **2015**, *66*, 56–61.

(156) McNellis, E. R.; Meyer, J.; Reuter, K. *Phys. Rev. B - Condens. Matter Mater. Phys.* **2009**, *80*, 1–10.

(157) *NMR Crystallography*; Harris, R. K.; Wasylishen, R. E.; Duer, M. J., Eds.; John Wiley & Sons, Ltd.: Chichester, U.K., 2009.

(158) Baias, M.; Widdifield, C. M.; Dumez, J.-N.; Thompson, H. P. G.; Cooper, T. G.; Salager, E.; Bassil, S.; Stein, R. S.; Lesage, A.; Day, G. M.; Emsley, L. *Phys. Chem. Chem. Phys.* **2013**, *15*, 8069–8080.

(159) Malone, B. D.; Cohen, M. L. *Phys. Rev. B - Condens. Matter Mater. Phys.* **2012**, *85*, 1–5.

(160) Morris, A. J.; Grey, C. P.; Needs, R. J.; Pickard, C. J. *Phys. Rev. B* **2011**, *84*, 224106.

(161) Pickard, C. J.; Needs, R. J. *J. Phys. Condens. Matter* **2011**, *23*, 053201.

(162) Dračínský, M.; Hodgkinson, P. *CrystEngComm* **2013**, *15*, 8705–8712.

(163) Rossi, G.; Ferrando, R. *J. Phys. Condens. Matter* **2009**, *21*, 084208.

(164) Schön, J. C.; Doll, K.; Jansen, M. *Phys. Status Solidi Basic Res.* **2010**, *247*, 23–39.

Chapter 7: Conclusions and Future Outlook

7.1 Conclusions

The research presented in this thesis demonstrates the effectiveness of nitrogen SSNMR for the study of a variety of organic, biochemical, and pharmaceutical materials. The outcomes of this thesis include: (i) Developing a set of practical methods for the acquisition of high quality ^{14}N SSNMR spectra, such that the experiments are easy to conduct, and the pulse sequence parameterizations are well understood. (ii) Establishing a protocol for spectral acquisition related to the number of sub-spectra that are acquired, and how they are processed and analyzed to yield information on the ^{14}N quadrupolar parameters. (iii) Applying ^{14}N SSNMR experiments to the characterization of a variety of organic solids, including amino acids and active pharmaceutical ingredients. (iv) Comparing ^{14}N EFG tensors derived from experiment and quantum chemical calculations, and examining their relationships to molecular structure, symmetry, intermolecular bonding and dynamics.

It was demonstrated that acquisition of ^{14}N SSNMR powder patterns can be facile, even at moderate magnetic fields (i.e., 9.4 T), and that the ^{14}N quadrupolar parameters can be extracted with ease, due to the overwhelming dominance of the FOQI in the range $0.8 \leq C_Q \leq 1.5$ MHz. This range of is of particular concern, because most pseudo-tetrahedral nitrogen moieties have C_Q values that fall within these limits. The WURST-CPMG and BRAIN-CP pulse sequences, when properly parameterized, are essential for acquiring spectra which have high S/N, good resolution, and minimal distortions.

The consideration of ^{14}N SSNMR patterns in terms of their breadths, positions of discontinuities, and symmetries, enabled us to propose a number of time saving measures for spectral acquisition, while still allowing for extractions of quadrupolar parameters from analytical simulations. It was shown that: (i) only half of the pattern needs to be acquired, due to the dominance of the FOQI – the other half of the pattern can be mirrored; (ii) the quadrupolar parameters can be obtained from the positions of only two discontinuities, due to the nature of the EFG tensor; and (iii) for the range of C_Q values above, it is only necessary to acquire two sub-spectra representing key frequency regions over which the discontinuities appear, which removes the need to use frequency-stepped acquisitions to acquire every sub-spectrum comprising each half pattern.

^{14}N SSNMR spectra have now been acquired for almost every naturally occurring amino acid, related amino acid derivatives, and a number of pharmaceutical compounds. Simple structural correlations between the value of η_Q and the local hydrogen-bonding environments of RNH_3^+, $RR'NH_2^+$, and $RR'R''NH^+$ groups were realized, which could have value in aiding structural predictions from crystallographic and computational studies. The DFT plane-wave calculations of ^{14}N EFG tensor parameters with the use of CASTEP and NMR CASTEP are of great importance, since they help establish the relationships between the quadrupolar parameters and local structure. The tandem approach of ^{14}N and ^{15}N SSNMR to studying APIs shows promise for future structural prediction and discovery (*vide infra*).

Finally, in relation to the studies on amino acids and APIs, ^{14}N SSNMR has been shown to be a sensitive probe of intermolecular interactions. The ^{14}N EFG tensor is very sensitive to even the slightest distortions of the geometry surrounding the nitrogen atom,

making it well-suited to investigate hydrogen bonding in molecular solids. In this regard, ^{14}N SSNMR can be utilized as a complementary technique to X-ray diffraction for the differentiation of polymorphs, which may be of great value for characterization and differentiation of active pharmaceutical ingredients and their polymorphs, and possibly for the detection of impurities. The influence of dynamic motions on the ^{14}N NMR spectra acquired with CPMG methods has also been demonstrated, and has potential value for not only enhancing S/N in ^{14}N SSNMR spectra, but also probing the nature and rates of molecular motion over a wide temperature range.

Throughout this dissertation, ultra-wideline ^{14}N SSNMR has shown great promise for molecular structure characterization and polymorph differentiation. The relative ease with which ^{14}N UW SSNMR powder patterns may be acquired and the rich structural information that they provide demonstrate its practicality and value. It is our hope that direct detection ^{14}N SSNMR gains popularity amongst NMR spectroscopists, and that its future applications to the study of a vast array of systems relevant in chemistry, biology and materials science prove invaluable.

7.2 Future Outlook

The findings presented in this dissertation suggest that we are only scratching the surface in terms of what can be done with UW ^{14}N SSNMR. Below, extensions of this work to several new avenues are proposed.

7.2.1 Continued Improvements of Experimental Methods

NMR experiments tend to rely on two key factors: hardware (i.e., the spectrometer, probes, amplifiers, consoles, tuning accessories, etc.) and methodologies (e.g., pulse sequences, acquisition techniques, etc.). Simple and effective strategies for increasing the excitation and detection bandwidths of NMR probes[1] should be explored in greater detail, as they may prove beneficial for increasing the rates of acquisitions of ^{14}N powder patterns by allowing the collection of fewer sub-spectra than conventional NMR probes. Investigation into alternative amplitude- and phase-modulated (AM and PM) pulses for improved broadband excitation (e.g., *hyperbolic secant*[2–4] and *tanh/tan*[5–7] pulses) and comparison of their performance against standard WURST pulses may help improve the WURST-CPMG and BRAIN-CP pulse sequences. Broadband pulses designed with optimal control theory (OCT)[8–12] may also prove beneficial for the acquisition of UW SSNMR powder patterns. It may also be advantageous to explore alternative schemes for broadband cross polarization and improved decoupling. For instance, the application of WURST pulses with distinct digital PMs on both the H and X channels may be useful in increasing the efficiency of BCP. In addition, there are numerous sequences that have been developed for heteronuclear decoupling under MAS conditions, but very little attention has been paid, by contrast, to static experiments.[13]

7.2.2 Developing Strategies for the Acquisition of Broader Powder Patterns

The techniques applied herein for the acquisition of ^{14}N SSNMR powder patterns arising from C_Q values ranging from 0.8 to 1.5 MHz, are applicable, with minor

modifications, to ^{14}N powder patterns that arise from larger values of C_Q (i.e., > 1.5 MHz). A strategy for acquiring these broad patterns should be developed as follows:

1. In the event that structural data is available (either of the system itself, or of a structural analogue), ^{14}N quadrupolar parameters can be determined from plane-wave DFT calculations. If structures are not available, the quadrupolar parameters can be estimated from literature values of comparable structures.

2. Analytical simulations of the powder patterns based on these theoretical or literature ^{14}N quadrupolar parameters are carried out.

3. Based on the simulations, transmitter frequencies are chosen to target specific areas of the powder pattern; specifically, the regions where the key discontinuities are located.

4. Experiments are conducted at selected transmitter frequencies using the WURST-CPMG and BRAIN-CP methods outlined herein. It is not necessary to acquire the full pattern in cases where the sample is pure; rather, only the spectral regions where the discontinuities are observable need to be scanned. If impurities are present, it may be necessary to scan other select frequency regions.

5. Overlapping patterns can be differentiated by varying the magnitude of the ^{1}H decoupling field, which can aid in altering the values of $T_2^{\text{eff}}(^{14}\text{N})$ for magnetically distinct ^{14}N nuclei. Furthermore, a variety of spectral editing techniques can be applied, including experimental options like variable-contact time (BRAIN-CP) and variable-temperature experiments, and processing options like echo train editing and relaxation-assisted separation (*vide infra*).[14,15] The first exploratory steps in spectral editing are currently underway in our research group.

A demonstration of the proposed methodology is shown in **Figure 7.1**, where only select regions of the broader ^{14}N site arising from the indole nitrogen of L-tryptophan were collected. The quadrupolar parameters (to first order) are in agreement with those obtained from NMR CASTEP calculations.

The acquisition of broader ^{14}N powder patterns (i.e., having C_Q > 1.5 MHz) was demonstrated by O'Dell *et al*. using WURST-CPMG and ultra-high magnetic fields (i.e., 21.1 T).[16] The combination of BRAIN-CP/WURST-CPMG and ultra-high magnetic fields should therefore allow for the routine study of ^{14}N nuclei in less symmetric

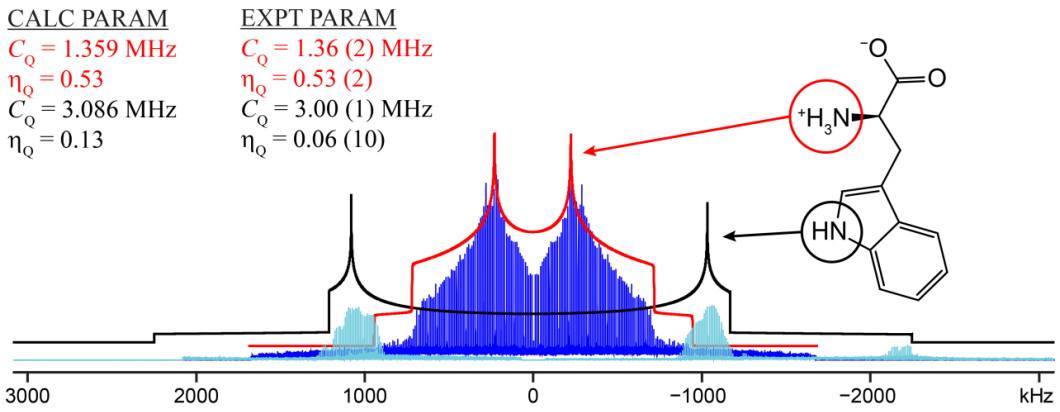

Figure 7.1. NMR CASTEP-guided acquisition of ^{14}N powder pattern of the indole nitrogen of L-tryptophan (light blue sub-spectrum, black trace is analytical simulation).

environments that are found in systems like MOFs, ZIFs, polymers, proteins, etc. The imidazole nitrogen environment is of particular interest: its ^{14}N C_Q value is approximately 1.6 MHz,[16–19] and traces of the underlying signal from the imidazole ring has been observed in our ^{14}N SSNMR powder patterns of L-histidine. Preliminary investigations to establish the optimal experimental parameters for the selective detection of ^{14}N signal from the imidazole ring are currently underway in our laboratory.

7.2.3 Dynamic Nuclear Polarization

The dynamic nuclear polarization (DNP) NMR experiment has recently become a technique of great interest, due to the development of high-frequency gyrotrons, the astounding S/N gains in DNP NMR spectra, and the vast array of new systems (including surfaces) that can be studied with the technique.[20–32] In the DNP experiment, the sample is doped with a radical, followed by polarization of the electron spin populations with the use of microwave radiation. This polarization is then transferred to dipolar-coupled protons, typically at low temperatures ranging from 1 to 100 K (this is dependent on the type of DNP spectrometer, radical choice, and DNP mechanism). The enormous spin polarization build up at the protons is then transferred via CP processes to dilute nuclei (the most common examples are ^{13}C and ^{15}N). An investigation into the feasibility of acquiring ^{14}N UW SSNMR spectra under DNP conditions should be undertaken; however, a number of concerns would have to be addressed, including ^{1}H-^{14}N CP efficiencies at low temperatures, the efficacy of CPMG-type sequences (relatively little is known about the variations in T_2 values in organic and biochemical systems at temperatures under 100 K), and the effects of DNP microwave irradiation on static samples (sample rotation promotes uniform irradiation and increases the signal enhancements from DNP).

7.2.4 ^{14}N Relaxation Processes and Molecular Dynamics

The influences of dynamic processes on ^{14}N SSNMR powder patterns acquired with CPMG echo trains have been touched upon only briefly in this dissertation; this is undoubtedly an area that needs further study. At this time, we are uncertain of the exact

nature of the mechanisms which influence $T_2^{eff}(^{14}N)$ – they are likely a combination of secular and non-secular contributions from heteronuclear dipolar coupling. A systematic study should be undertaken of several model compounds that can be easily selectively deuterated at key positions, and subjected to a series of ^{14}N NMR experiments with controlled temperature variation and ^{1}H decoupling fields. The groundwork laid out herein suggests several good model systems for these purposes. Further investigation into these processes may yield invaluable information regarding the motion of the RNH_3^+ moieties (rates and activation energies), their influence on structure, the relevant relaxation mechanisms, and potentially, consistent means by which CPMG experiments can yield maximum signal enhancement.

The variation in the $T_2^{eff}(^{14}N)$ with temperature and decoupling field strength proved beneficial for the differentiation of polymorphs, as the different hydrogen-bonding networks in the polymorphs clearly have an effect on the ^{14}N relaxation characteristics. Frydman and coworkers proposed a method for differentiating signals arising from magnetically inequivalent sites according to their T_1 relaxation characteristics; they have termed this method *relaxation-assisted separation* (RAS).[14] The frequencies of the powder pattern (of quadrupolar or spin-1/2 nuclei) is displayed in the direct dimension, while the relaxation rates (in this case T_1^{-1}) are displayed in the indirect dimension. The acquisition of a T_1 dataset can be very lengthy for an UW NMR spectrum; as such, RAS processing of such datasets is limited to samples with much narrower spectra. Our research group has recently explored the use of RAS processing of T_2 CPMG datasets.[33] The proposed T_2^{eff} RAS method, which utilizes non-negative least squares and non-negative Tikhonov fitting routines, has been demonstrated to be

effective at differentiating ^{35}Cl powder patterns arising from mixtures of APIs,[15] and has been theoretically demonstrated to be applicable to ^{14}N UW SSNMR,[34] provided that the T_2^{eff} time constants are significantly different for the two species (*ca.* 2−10× difference). Preliminary ^{14}N SSNMR investigations show some promise for using T_2^{eff}(^{14}N) datasets, variable decoupling fields, and RAS processing to resolve overlapping patterns.

7.2.5. Application to Structure Refinement and NMR Crystallography

Nitrogen SSNMR also shows promise for use in the emerging field of NMR crystallography,[35] where molecular structure predictions and refinements are accomplished with the use of computational techniques such as ab initio random structural searching (AIRSS)[36–39] and other algorithms that account for molecular dynamics,[40] as well as, energy landscapes and energy minimization.[41,42] Crystal structure prediction (CSP) methods involve a series of calculations on a large number of structures, followed by the filtering of the lowest energy candidates, and then refinement of structure choice by comparison of experimental NMR data with theoretically obtained NMR parameters. CSP methods have been shown to work best with ^{1}H chemical shifts, which can be reliably calculated using plane-wave DFT methods.[36,43,44] However, the accurate measurement of ^{1}H chemical shifts from SSNMR spectra of molecules of increased complexity can be challenging, and structural solutions for highly flexible molecules are still evasive at the current time. Carbon and nitrogen chemical shifts have also been utilized in CSP studies, with a limited degree of success.[45–47]

Given that ^{14}N EFG tensors can be calculated very reliably, and show greater variation in their tensor parameters with structural differences than corresponding

nitrogen CS tensors, it is quite possible that ^{14}N quadrupolar data could greatly aid in CSP and structural refinement processes. In addition, CSP methods may be further aided if ^{1}H-^{15}N dipolar correlations are available from corresponding $^{15}N\{^{1}H\}$ idHETCOR spectra, along with ^{1}H and ^{15}N shift data. This may prove especially useful for structural characterization of molecules which cannot easily form single crystals suitable for X-ray investigations, [48] or for micro- and nanocrystals of simple organic molecules contained within complex matrices (e.g., crystalline APIs in the excipients of pills and tablets).

All of the methodologies and applications proposed above have the potential to truly revolutionize ^{14}N SSNMR and make it widely applicable in all areas of chemistry, biology, and materials science.

7.3 Bibliography

(1) Basse, K.; Jain, S. K.; Bakharev, O. N.; Nielsen, N. C. *J. Magn. Reson.* **2014**, *244*, 85–89.

(2) Siegel, R.; Nakashima, T. T.; Wasylishen, R. E. *Concepts Magn. Reson. Part A* **2005**, *26A*, 47–61.

(3) Dey, K. K.; Prasad, S.; Ash, J. T.; Deschamps, M.; Grandinetti, P. J. *J. Magn. Reson.* **2007**, *185*, 326–330.

(4) Burgess, K. M. N.; Perras, F. A.; Moudrakovski, I. L.; Xu, Y.; Bryce, D. L. *Can. J. Chem.* **2015**, *807*, 1–9.

(5) Riedel, K.; Herbst, C.; Leppert, J.; Ohlenschläger, O.; Görlach, M.; Ramachandran, R. *J. Biomol. NMR* **2006**, *35*, 275–283.

(6) Pell, A. J.; Clément, R. J.; Grey, C. P.; Emsley, L.; Pintacuda, G. *J. Chem. Phys.* **2013**, *138*, 114201.

(7) Pell, A. J.; Pintacuda, G. *Prog. Nucl. Magn. Reson. Spectrosc.* **2015**, *84-85*, 33–72.

(8) Kehlet, C. T.; Sivertsen, A. C.; Bjerring, M.; Reiss, T. O.; Khaneja, N.; Glaser, S. J.; Nielsen, N. C. *J. Am. Chem. Soc.* **2004**, *126*, 10202–10203.

(9) Vosegaard, T.; Kehlet, C. T.; Khaneja, N.; Glaser, S. J.; Nielsen, N. C. *J. Am. Chem. Soc.* **2005**, *127*, 13768–13769.

(10) O'Dell, L. A.; Harris, K. J.; Schurko, R. W. *J. Magn. Reson.* **2010**, *203*, 156–166.

(11) MacGregor, A. W.; O'Dell, L. A.; Schurko, R. W. *J. Magn. Reson.* **2011**, *208*, 103–113.

(12) O'Dell, L. A.; Ratcliffe, C. I. *J. Phys. Chem. A* **2011**, *115*, 747–752.

(13) Hodgkinson, P. *Prog. Nucl. Magn. Reson. Spectrosc.* **2005**, *46*, 197–222.

(14) Lupulescu, A.; Kotecha, M.; Frydman, L. *J. Am. Chem. Soc.* **2003**, *125*, 3376–3383.

(15) Sandre, A. R. *The Application of ^{35}Cl SSNMR to Pharmaceuticals: Detection of Polymorphs and Impurity Phases*, Undergraduate Thesis, Windsor, 2014.

(16) O'Dell, L. A.; Schurko, R. W.; Harris, K. J.; Autschbach, J.; Ratcliffe, C. I. *J. Am. Chem. Soc.* **2011**, *133*, 527–546.

(17) Edmonds, D. T. *Phys. Rep.* **1977**, *29*, 233–290.

(18) O'Dell, L. A.; Ratcliffe, C. I. *Chem. Commun.* **2010**, *46*, 6774–6776.

(19) O'Dell, L. A. *Prog. Nucl. Magn. Reson. Spectrosc.* **2011**, *59*, 295–318.

(20) Maly, T.; Debelouchina, G. T.; Bajaj, V. S.; Hu, K.; Joo, C.; Jurkauskas, M. L. M.; Sirigiri, J. R.; Wel, P. C. A. Van Der; Herzfeld, J.; Temkin, R. J.; Griffin, R. G. *J. Chem. Phys.* **2008**, *128*, 052211–052219.

(21) Barnes, A. B.; De Paëpe, G.; Van Der Wel, P. C. A.; Hu, K. N.; Joo, C. G.; Bajaj, V. S.; Mak-Jurkauskas, M. L.; Sirigiri, J. R.; Herzfeld, J.; Temkin, R. J.; Griffin, R. G. *Appl. Magn. Reson.* **2008**, *34*, 237–263.

(22) Lesage, A.; Lelli, M.; Gajan, D.; Caporini, M. A.; Vitzthum, V.; Mie, P.; Alauzun, J.; Roussey, A.; Mehdi, A.; Bodenhausen, G. *J. Am. Chem. Soc.* **2010**, *132*, 15459–15461.

(23) Zagdoun, A.; Casano, G.; Ouari, O.; Lapadula, G.; Rossini, A. J.; Lelli, M.; Baffert, M.; Gajan, D.; Veyre, L.; Maas, W. E.; Rosay, M.; Weber, R. T.; Thieuleux, C.; Coperet, C.; Lesage, A.; Tordo, P.; Emsley, L. *J. Am. Chem. Soc.* **2012**, *134*, 2284–2291.

(24) Kobayashi, T.; Lafon, O.; Thankamony, A. S. L.; Slowing II; Kandel, K.; Carnevale, D.; Vitzthum, V.; Vezin, H.; Amoureux, J.-P.; Bodenhausen, G.;

Pruski, M. *Phys. Chem. Chem. Phys.* **2013**, *15*, 5553–5562.

(25) Perras, F. A.; Kobayashi, T.; Pruski, M. *J. Am. Chem. Soc.* **2015**, *137*, 8336–8339.

(26) Kobayashi, T.; Perras, F. A.; Slowing, I. I.; Sadow, A. D.; Pruski, M. *ACS Catal.* **2015**, *5*, 7055–7062.

(27) Rossini, A. J.; Zagdoun, A.; Lelli, M.; Lesage, A.; Copéret, C.; Emsley, L. *Acc. Chem. Res.* **2013**, *46*, 1942–1951.

(28) Rossini, A. J.; Zagdoun, A.; Lelli, M.; Canivet, J.; Aguado, S.; Ouari, O.; Tordo, P.; Rosay, M.; Maas, W. E.; Copéret, C.; Farrusseng, D.; Emsley, L.; Lesage, A. *Angew. Chemie - Int. Ed.* **2012**, *51*, 123–127.

(29) Vitzthum, V.; Mieville, P.; Carnevale, D.; Caporini, M. A.; Gajan, D.; Coperet, C.; Lelli, M.; Zagdoun, A.; Rossini, A. J.; Lesage, A.; Emsley, L.; Bodenhausen, G. *Chem. Commun.* **2012**, *48*, 1988–1990.

(30) Rossini, A. J.; Zagdoun, A.; Hegner, F.; Schwarzwälder, M.; Gajan, D.; Copéret, C.; Lesage, A.; Emsley, L. *J. Am. Chem. Soc.* **2012**, *134*, 16899–16908.

(31) van der Wel, P. C. A.; Hu, K.-N.; Lewandowski, J.; Griffin, R. G. *J. Am. Chem. Soc.* **2006**, *128*, 10840–10846.

(32) Bajaj, V. S.; Mak-Jurkauskas, M. L.; Belenky, M.; Herzfeld, J.; Griffin, R. G. *Proc. Natl. Acad. Sci.* **2009**, *106*, 9244–9249.

(33) Jaroszewicz, M. J. *Frequency-Swept Pulses in Ultra-Wideline NMR*, M.Sc. Thesis, Windsor, 2015.

(34) Kispal, B. M. *T_2^{eff} Relaxation Assisted Separation of Overlapping Ultra-Wideline Powder Patterns: Practical Considerations and Applications to ^{14}N SSNMR*, Undergraduate Thesis, Windsor, 2015.

(35) *NMR Crystallography*; Harris, R. K.; Wasylishen, R. E.; Duer, M. J., Eds.; John Wiley & Sons, Ltd.: Chichester, U.K., 2009.

(36) Baias, M.; Widdifield, C. M.; Dumez, J.-N.; Thompson, H. P. G.; Cooper, T. G.; Salager, E.; Bassil, S.; Stein, R. S.; Lesage, A.; Day, G. M.; Emsley, L. *Phys. Chem. Chem. Phys.* **2013**, *15*, 8069–8080.

(37) Malone, B. D.; Cohen, M. L. *Phys. Rev. B - Condens. Matter Mater. Phys.* **2012**, *85*, 1–5.

(38) Morris, A. J.; Grey, C. P.; Needs, R. J.; Pickard, C. J. *Phys. Rev. B* **2011**, *84*.

(39) Pickard, C. J.; Needs, R. J. *J. Phys. Condens. Matter* **2011**, *23*, 053201.

(40) Dračínský, M.; Hodgkinson, P. *CrystEngComm* **2013**, *15*, 8705.

(41) Rossi, G.; Ferrando, R. *J. Phys. Condens. Matter* **2009**, *21*, 084208.

(42) Schön, J. C.; Doll, K.; Jansen, M. *Phys. Status Solidi Basic Res.* **2010**, *247*, 23–39.

(43) Salager, E.; Day, G. M.; Stein, R. S.; Pickard, C. J.; Elena, B.; Emsley, L. *J. Am. Chem. Soc.* **2010**, *132*, 2564–2566.

(44) Baias, M.; Dumez, J.-N.; Svensson, P. H.; Schantz, S.; Day, G. M.; Emsley, L. *J. Am. Chem. Soc.* **2013**, *135*, 17501–17507.

(45) Mali, G.; Trebosc, J.; Martineau, C.; Mazaj, M. *J. Phys. Chem. C* **2015**, *119*, 7831–7841.

(46) Kalakewich, K.; Iuliucci, R.; Mueller, K. T.; Eloranta, H.; Harper, J. K. *J. Chem. Phys.* **2015**, *143*, 194702.

(47) Märker, K.; Pingret, M.; Mouesca, J. M.; Gasparutto, D.; Hediger, S.; De Paëpe, G. *J. Am. Chem. Soc.* **2015**, *137*, 13796–13799.

(48) Görbitz, C. H.; Törnroos, K. W.; Day, G. M. *Acta Crystallogr. Sect. B Struct. Sci.* **2012**, *68*, 549–557.

Appendix A: Supplementary Tables and Figures for Chapter 2

Table A1. Experimental parameters for ^{14}N WURST-CPMG NMR experiments acquired at 9.4 T

	ala	arg HCl	asn	cys	gln	ile-d_3	lys	met	ser	thr	trp	tyr	val /val-d_3	gly-gly	lys HCl	glu-β	hyp-d_2	A/B-his
# scans	3600	1024	3600	3600	2048	2000	3600	7200	2048	2048	7200	7200	14336	1600	4096	2048	1432	1800
# sub-spectra	5	5	6	7	7	5	5	5	7	5	6	5	5	7	6	4	4	6
Transmitter step (kHz)	150	150	150	150	150	150	~150	150	150	150	150	~150	~150	150	~150	150	150	~150
Recycle delay (s)	1	5	1	1	1	4	1	0.5	1	1	0.5	0.5	0.25	1	0.25	1	10	0.5
time (hours)	5.2	7.2	6.3	7.3	4.2	11.3	5	5.2	4.7	3	6.4	5.2	5.2	3.2	1.7	2.4	15.9	1.5
WURST sweep range (kHz)	3000	2000	2000	3000	3000	3000	750	3000	3000	3000	3000	750	1000/ 750	2000	750	2000	3000	1000
# echoes	200	200	200	200	200	200	50	100	200	200	150	100	100	200	100	200	200	75
Echo length (μs)	100	100	100	100	100	100	100	100	100	100	100	100	100	100	100	100	100	100
WURST pulse length (μs)	50	50	50	50	50	50	75	50	50	50	50	75	50/75	50	50	50	50	100
^{1}H decoupling rf (kHz)	40	40	40	40	40	40	50	40	40	40	40	58	25/50	40	40	40	40	50
^{14}N rf (kHz)	28	28	28	28	28	28	28	28	28	28	28	28	28	28	28	28	28	28
SW (kHz)	2000	2000	2000	2000	2000	2000	2000	2000	2000	2000	2000	2000	2000	2000	2000	2000	2000	2000

Table A2. Experimental parameters for ^{14}N WURST-CPMG NMR experiments acquired at 21.1 T

	ser	tyr	thr	hyp-d_2	gln
Number of scans per sub-spectrum	1200	1200	1200	5600	1024
Number of sub-spectra	4	4	4	2	2
Transmitter frequency step (kHz)	300	300	300	400	300
^{14}N Recycle delay (s)	1	1.5	1.5	1	1
Experimental time (hours)	1.3	2	2	3.1	0.6
WURST sweep range (kHz)	1000	1000	1000	1000	1000
# of echoes	64	128	64	100	100
Echo length (μs)	270	70	270	70	70
WURST pulse length (μs)	50	50	50	50	50
^{1}H decoupling power (kHz)	40	40	40	40	40
WURST pulse power (kHz)	28	28	28	28	28
SW (kHz)	1000	1000	1000	1000	1000

Table A3. Experimental parameters for ^{14}N WURST-CPMG Variable Temperature NMR experiments of individual sub-spectra

	val	val-d_3	asp	phe	tyr
Number of scans per sub-spectrum	7168	14336	1024	2048	2400
Number of sub-spectra	7	5	6	7	5
Transmitter frequency step (kHz)	~150	~150	150	150	150
^{14}N Recycle delay (s)	0.25	0.25	0.5	1	0.5
Experimental time (hours)	3.5	5.2	0.9	4.2	1.7
WURST sweep range (kHz)	750	750	2000	2000	750
# of echoes	100	100	100	200	100
Echo length (μs)	100	100	100	100	100
WURST pulse length (μs)	75	75	50	50	75
^{1}H decoupling power (kHz)	50	50	40	40	58
WURST pulse power (kHz)	28	28	28	28	28
SW (kHz)	2000	2000	2000	2000	2000
Temperature (°C)	130	100	108	171	171

Table A4. Experimental parameters for ^{14}N BRAIN-CP/WURST-CPMG NMR experiments for complete powder pattern acquisition

	tyr
Number of transients per sub-spectrum	256
Number of sub-spectra	7
Transmitter frequency step (kHz)	~90
^{1}H Recycle delay (s)	1
Experimental time (hours)	0.5
^{1}H excitation ($\pi/2$) pulse (μs)	5
^{1}H excitation ($\pi/2$) pulse rf (kHz)	50
^{1}H Spin-lock rf power (kHz)	40
^{14}N Spin-lock rf power (kHz)	23
Contact time (ms)	12.5
CP sweep range (kHz)	750
WURST refocusing pulse length (μs)	75
WURST refocusing pulse power (kHz)	28
WURST refocusing sweep range (kHz)	750
Number of Meiboom-Gill Loops	100
CPMG echo length (per echo, μs)	100
^{1}H decoupling power (kHz)	58
SW (kHz)	2000
Temperature (°C)	171

Table A5. Summary of C_Q and η_Q values calculated by NMR CASTEP.

Amino Acid	Moiety	NMR CASTEP result C_Q (MHz)	η_Q
Ala	CNH_3^+	1.204	0.26
Arg	CNH_2	−4.371	0.18
	$C{=}NH_2^+$	−3.400	0.47
	$C{=}NH_2^+$	−3.347	0.42
	CNC′	−4.189	0.33
ArgHCl	CNH_3^+	1.248	0.06
	C=NH2+	−2.975	0.37
	C=NH2+	−3.445	0.08
	CNC′	−4.289	0.21
Asn	CNH_3^+	1.316	0.48
	CNH_2	−2.708	0.32
Asp	CNH_3^+	1.338	0.16
Cys	CNH_3^+	1.289	0.50
Glu-β	CNH_3^+	1.127	0.15
Gln	CNH_3^+	1.132	0.51
	CNH_2	−3.092	0.21
Glygly	CNH_3^+	1.453	0.10
	CNC′	−3.261	0.37
A-His	CNH_3^+	1.252	0.12
	CNHC′	−1.510	0.88
	CNC′	−3.483	0.08
B-His	CNH_3^+	1.279	0.13
	CNHC′	−1.492	0.84
	CNC′	−3.330	0.18
Hyp-d_2	$CC'NH_2^+$	−1.281	0.92
Ile-d_3	CNH_3^+	1.218	0.45
	CNH_3^+	1.255	0.17
LysHCl	CNH_3^+	1.212	0.33
	CNH_3^+	1.151	0.10
Met	CNH_3^+	1.246	0.52
	CNH_3^+	1.220	0.13
Phe	CNH_3^+	1.540	0.64
Ser	CNH_3^+	1.174	0.11
Thr	CNH_3^+	1.130	0.39
Trp	CNH_3^+	1.359	0.53
	CNHC′	−3.086	0.13
Tyr	CNH_3^+	1.054	0.46
Val-d_3	CNH_3^+	1.198	0.46
	CNH_3^+	1.247	0.17

Table A6. Bond distances of structures used for NMR CASTEP calculations.

Amino acid	Space grp	N-H_1	N-H_2	N-H_3	H_1···O	H_2···O	H_3···O	∢V_{33}-N-C	NMR CASTEP C_Q (MHz)	η_Q
ArgHCl	$P2_1$	1.052	1.045	1.048	2.138 (Cl)	1.860	1.744	2.074	1.248	0.06
Asp	$P2_1$	1.052	1.047	1.051	1.753	1.802	1.758	2.601	1.338	0.16
Glygly	$P2_{1/c}$	1.045	1.051	1.051	1.828	1.805	1.704	1.357	1.453	0.10
Ser	$P2_12_12_1$	1.044	1.049	1.048	1.810	1.826	1.862	2.736	1.174	0.11
Glu-β	$P2_12_12_1$	1.038	1.037	1.027	1.845	1.868	1.895	1.966	1.127	0.15
Ala	$P2_12_12_1$	1.028	1.047	1.030	1.858	1.779	1.825	3.003	1.204	0.26
A-his	$P2_12_12_1$	1.031	1.036	1.018	1.786	1.841	-	2.327	1.252	0.12
B-his	$P2_1$	1.051	1.048	1.051	1.745	1.814	1.869 (N)	2.835	1.279	0.13
Ile (low η_Q)	$P2_1$	1.054	1.052	1.046	1.708	1.818	1.930	1.994	1.255	0.17
Lys HCl (low η_Q)	$P2_{1/c}$	1.054	1.046	1.050	2.121 (Cl)	1.863	2.152 (Cl)	1.831	1.151	0.10
Met (low η_Q)	$P2_1$	1.046	1.049	1.049	1.836	1.731	1.821	2.374	1.220	0.13
Val (low η_Q)	$P2_1$	1.052	1.051	1.052	1.846	1.840	1.723	2.964	1.247	0.17
Asn	$P2_1$	1.058	1.052	1.044	1.702	1.760	1.883	6.983	1.316	0.48
Cys	$P2_12_12_1$	1.051	1.036	1.068	1.763	2.045	1.694	11.03	1.289	0.50
Gln	$P2_12_12_1$	1.058	1.049	1.038	1.737	1.842	1.926	10.215	1.132	0.51
Phe	$P2$	1.047	1.049	1.079	1.826	1.827	1.581	7.291	1.540	0.64
Thr	$P2_12_12_1$	1.033	1.037	1.024	1.791	1.900	2.201 (OH)	6.311	1.130	0.39
Trp	$P2_{1/c}$	1.045	1.049	1.070	1.796	1.773	1.640	5.568	1.359	0.53
Tyr	$P2_12_12_1$	1.052	1.037	1.060	1.836	2.090	1.770	6.614	1.054	0.46
Ile (int η_Q)	$P2_1$	1.040	1.048	1.064	1.933	1.819	1.715	5.137	1.218	0.45
LysHCl (int η_Q)	$P2_{1/c}$	1.046	1.052	1.041	1.808	1.756	2.395 (Cl)	3.013	1.212	0.33
Met (int η_Q)	$P2_1$	1.036	1.044	1.066	1.929	1.811	1.668	6.516	1.246	0.52
Val (int η_Q)	$P2_1$	1.039	1.049	1.065	2.003	1.824	1.707	5.136	1.198	0.46

Table A7. Atomic parameters for **met**, **ile**, **val**, and **leu** following H-atom optimization.

Geometry parameters (H-optimized)								
	met		ile		val		leu	
	low η_Q	int η_Q	low η_Q	int η_Q	low η_Q	int η_Q	low η_Q	int η_Q
C-N (Å)	1.465	1.483	1.500	1.497	1.497	1.495	1.497	1.503
N-H_1 (Å)	1.049	1.036	1.054	1.040	1.052	1.039	1.047	1.039
N-H_2 (Å)	1.049	1.044	1.052	1.048	1.051	1.049	1.048	1.043
N-H_3 (Å)	1.046	1.066	1.046	1.064	1.052	1.065	1.041	1.060
C-N-H_1 (°)	110.757	108.895	110.103	107.975	110.895	109.196	110.079	109.375
C-N-H_2 (°)	113.146	111.713	113.208	113.587	112.521	112.773	113.241	111.218
C-N-H_3 (°)	109.674	109.250	110.125	110.717	110.531	109.228	110.191	110.544
$H_1 \cdots O_1$ (Å)	1.731	1.929	1.708	1.933	1.723	2.003	1.722	1.844
$H_2 \cdots O_2$ (Å)	1.821	1.811	1.818	1.819	1.840	1.824	1.806	1.853
$H_3 \cdots O_3$ (Å)	1.836	1.668	1.930	1.715	1.846	1.707	2.086	1.731
$N \cdots O_1$ (Å)	2.778	2.835	2.760	2.839	2.770	2.865	2.764	2.811
$N \cdots O_2$ (Å)	2.854	2.849	2.851	2.859	2.869	2.869	2.843	2.886
$N \cdots O_3$ (Å)	2.862	2.733	2.948	2.778	2.889	2.771	3.071	2.789

List A1. CSDS id and Citations for crystal structures used for CASTEP geometry optimization and NMR CASTEP ^{14}N EFG tensor calculations.

Amino acid	CSDS id	Citation
No H-position optimization		
Ala	LALNIN12	Mogens S. Lehmann, Thomas F. Koetzle, and Walter C. Hamilton, "Precision Neutron Diffraction Structure Determination of Protein and Nucleic Acid Components. I. Crystal and Molecular Structure of the Amino Acid L-Alanine," *Journal of the American Chemical Society* 94, no. 8 (April 1972): 2657–60, doi:10.1021/ja00763a016.
Cys	LCYSTN12	B. Khawas, "X-Ray Study of L-Arginine HCl, L-Cysteine, DL-Lysine and DL-Phenylalanine," *Acta Crystallographica Section B Structural Crystallography and Crystal Chemistry* 27, no. 8 (1971): 1517–20, doi:10.1107/S056774087100431X.
Glu-β	LGLUAC11	Mogens S. Lehmann, Thomas F. Koetzle, and Walter C. Hamilton, "Precision Neutron Diffraction Structure Determination of Protein and Nucleic Acid Components. VIII: The Crystal and Molecular Structure of the B-Form of the Amino Acid L-Glutamic Acid," *Journal of Crystal and Molecular Structure* 2, no. 5–6 (1972): 225–33, doi:10.1007/BF01246639.
Glygly	GLYGLY14	Stephen A Moggach et al., "Effect of Pressure on the Crystal Structure of Alpha-Glycylglycine to 4.7 GPa; Application of Hirshfeld Surfaces to Analyse Contacts on Increasing Pressure.," *Acta Crystallographica. Section B, Structural Science* 62, no. Pt 2 (2006): 310–20, doi:10.1107/S0108768105042072.
A-His	LHISTD13	Mogens S. Lehmann, Thomas F. Koetzle, and Walter C. Hamilton, "PRECISION NEUTRON DIFFRACTION STRUCTURE DETERMINATION OF PROTEIN AND NUCLEIC ACID COMPONENTS. IV. THE CRYSTAL AND MOLECULAR STRUCTURE OF THE AMINO ACID L-HISTIDINE," *Internation Journal of Protein Research* 4 (1972): 229–39.
Thr	LTHREO02	M Ramanadham, S K Sikka, and R Chidambaram, "Structure Determination of L-Threonine by Neutron Diffraction," *Pramana* 1, no. 6 (1973): 247–59.
Hpro	HOPROL12	Thomas F. Koetzle, Mogens S. Lehmann, and Walter C. Hamilton, "4-Hydroxy-L-Proline," *Acta Crystallographica Section B Structural Crystallography and Crystal Chemistry* 29 (1973): 231.
Gln	GLUTAM01	Thomas F. Koetzle et al., "Precision Neutron Diffraction Structure Determination of Protein and Nucleic Acid Components. XIII. Molecular and Crystal Structure of the Amino Acid L-Glutamine," *Acta Crystallographica* B29, no. 17 (1973): 2571–75.
argHCl	LARGIN	S. K. Mazumdar et al., "The Crystal Structure of L-Arginine Hydrochloride," *Zeitschrift Fur Kristallographie* 130 (1969): 328–39.
Asn	VIKKEG	Kazuhiko Yamada et al., "L-Asparagine," *Acta Crystallographica Section E Structure Reports Online* 63, no. 9 (September 15, 2007): o3802–3, doi:10.1107/S1600536807039505.
Asp	LASPRT03	El Eulmi Bendeif and Christian Jelsch, "The Experimental Library

		Multipolar Atom Model Refinement of L-Aspartic Acid," *Acta Crystallographica Section C: Crystal Structure Communications* 63, no. 6 (2007): 361–64, doi:10.1107/S0108270107021671.
B-His	LHISTD04	M T Averbuchpouchot, "Crystal-Structure of L-Histidinium Phosphite and a Structure Reinvestigation of the Monoclinic Form of L-Histidine," *Zeitschrift Fur Kristallographie* 207, no. 1 (1993): 111–20, doi:10.1524/zkri.1993.207.Part-1.111.
Ile	LISLEU02	C. H. Görbitz and B. Dalhus, "L-Isoleucine, Redetermination at 120K," *Acta Crystallographica Section C Crystal Structure Communications* 52, no. 6 (1996): 1464–66, doi:10.1107/S0108270195016386.
LysHCl	DLLYSC11	Ralf Flaig et al., "Intra- and Intermolecular Topological Properties of Amino Acids: A Comparative Study of Experimental and Theoretical Results," *Journal of the American Chemical Society* 124, no. 10 (2002): 3407–17, doi:10.1021/ja011492y.
Met	LMETON10	K. Torii and Y. Iitaka, "Crystal Structures and Molecular Conformations of L-Methionine and L-Norleucine," *Acta Crystallographica Section B Structural Crystallography and Crystal Chemistry* 29 (1973): 2799–2807, doi:10.1107/S0567740873007569.
Phe	QQQAUJ04	P. Andrew Williams et al., "Expanding the Solid-State Landscape of L -Phenylalanine: Discovery of Polymorphism and New Hydrate Phases, with Rationalization of Hydration/dehydration Processes," *Journal of Physical Chemistry C* 117, no. 23 (2013): 12136–45, doi:10.1021/jp401547f.
Ser	LSERIN01	Thomas J Kistenmacher, George A Rand, and Richard E Marsh, "Refinementsd of the Crystal Structures of DL-Serine and Anhydrous L-Serine," *Acta Cryst. B* 30 (1974): 2573–78.
Trp	QQQBTP02	Carl Henrik Görbitz, Karl Wilhelm Törnroos, and Graeme M. Day, "Single-Crystal Investigation of L-Tryptophan with Z′ = 16," *Acta Crystallographica Section B: Structural Science* 68, no. 5 (2012): 549–57, doi:10.1107/S0108768112033484.
Tyr	LTYROS10	Arvid Mostad, Hans Martin Nissen, and Christian Rømming, "Crystal Structure of L-Tyrosine," *Acta Chemica Scandinavica* 26, no. 10 (1972): 3819–33, doi:10.3891/acta.chem.scand.26-3819.
Val	LVALIN01	B. Dalhus and C. H. Gorbitz, "Crystal-Structures of Hydrophobic Amino-Acids. 1. Redetermination of L-Methionine and L-Valine at 120K," *Acta Chemica Scandinavica* 50, no. 6 (1996): 544–48.
Leu	LEUCIN01	M. Coll et al., "Structure of L-Leucine: A Redetermination," *Acta Crystallographica* C42 (1986): 599–601.

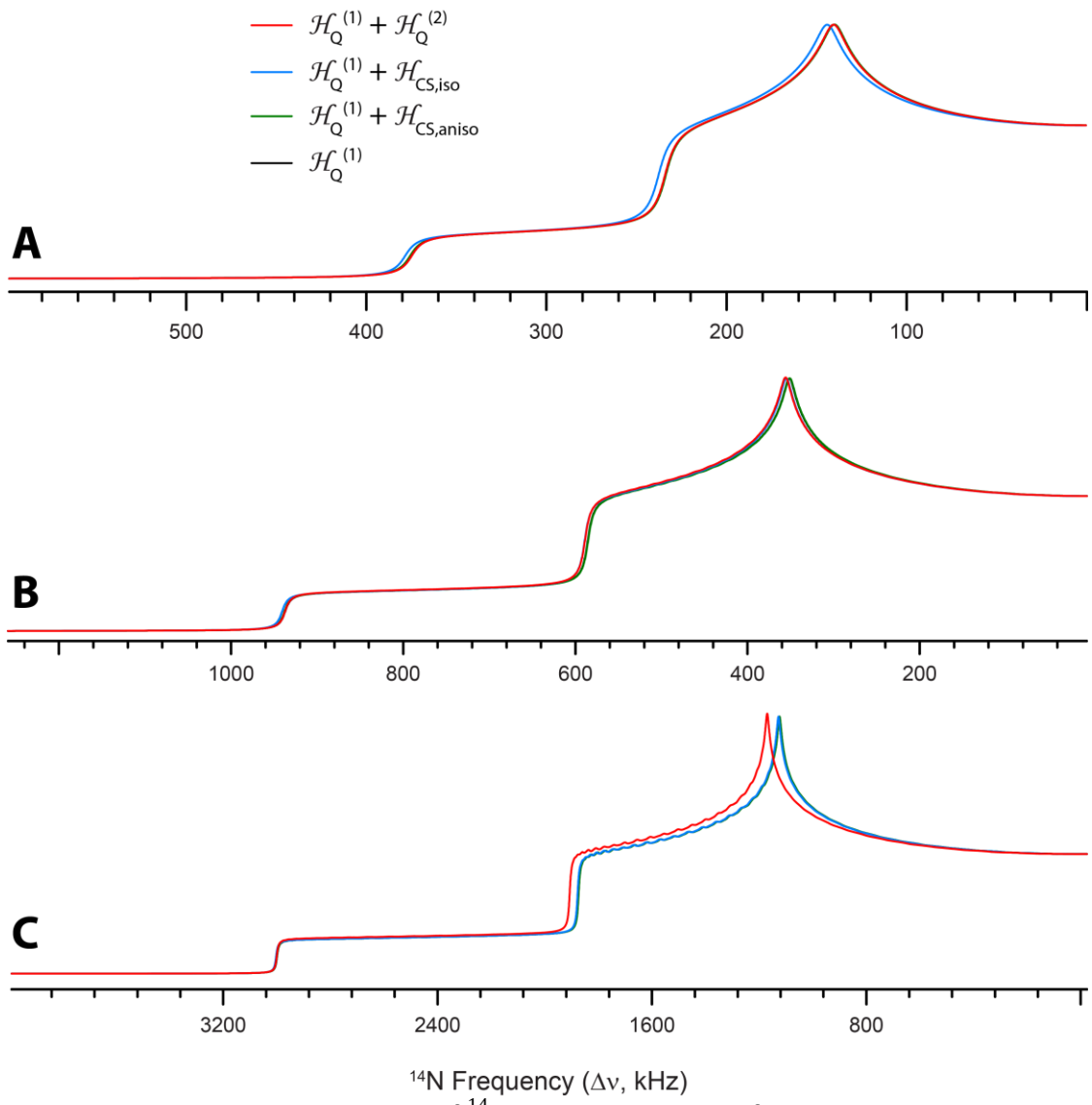

Figure A1. Analytical simulations of ^{14}N powder patterns influenced by the FOQI (black traces) and additionally CSA (green traces), diso (light blue traces), and the SOQI (red traces) for ^{14}N EFG parameters: (A) C_Q = 0.50 MHz and η_Q = 0.25, (B) C_Q = 1.25 MHz and η_Q = 0.25, and (C) C_Q = 4.0 MHz and η_Q = 0.25. The CS tensor is assumed to be coincident with the EFG tensor, with a span of 30 ppm, a skew of 0, and δ_{iso} = 130 ppm. The contributions of CSA (anisotropic) are negligible for all C_Q values with the exception of δ_{iso} for $C_Q \leq 0.5$ MHz; δ_{iso} = 3.6 kHz. In (B) the FOQI dominates and the effects of CSA and SOQI are negligible (δ_{iso} contribution = 3.6 kHz, SOQI contribution = 4.5 kHz). In (C) the SOQI makes significant contribution to the first-order pattern (SOQI contribution = 46 kHz) and the patterns have lost their perfect mirror symmetry. The case in (b) is representative of the pseudo-tetrahedral nitrogen moieties (i.e., RNH_3^+, $RR'NH_2^+$, $RR'R''NH^+$).

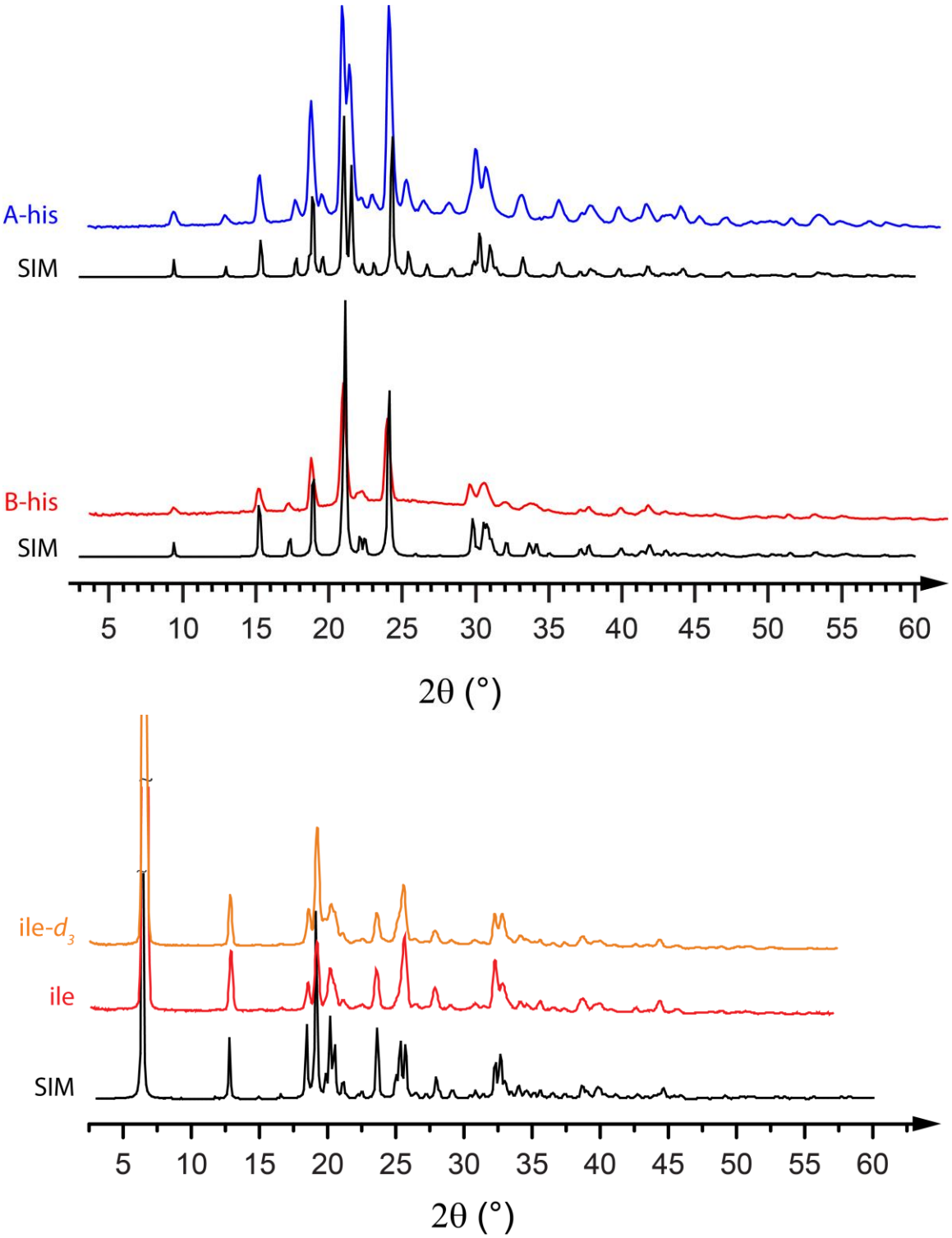

Figure A2. Experimental and theoretical X-ray diffraction patterns of deuterated (***d*₃** and ***d*₂**) and non-deuterated **val**, **hyp**, and **ile**.

Figure A3. Experimental and theoretical X-ray diffraction patterns of **A-his** and **B-his**.

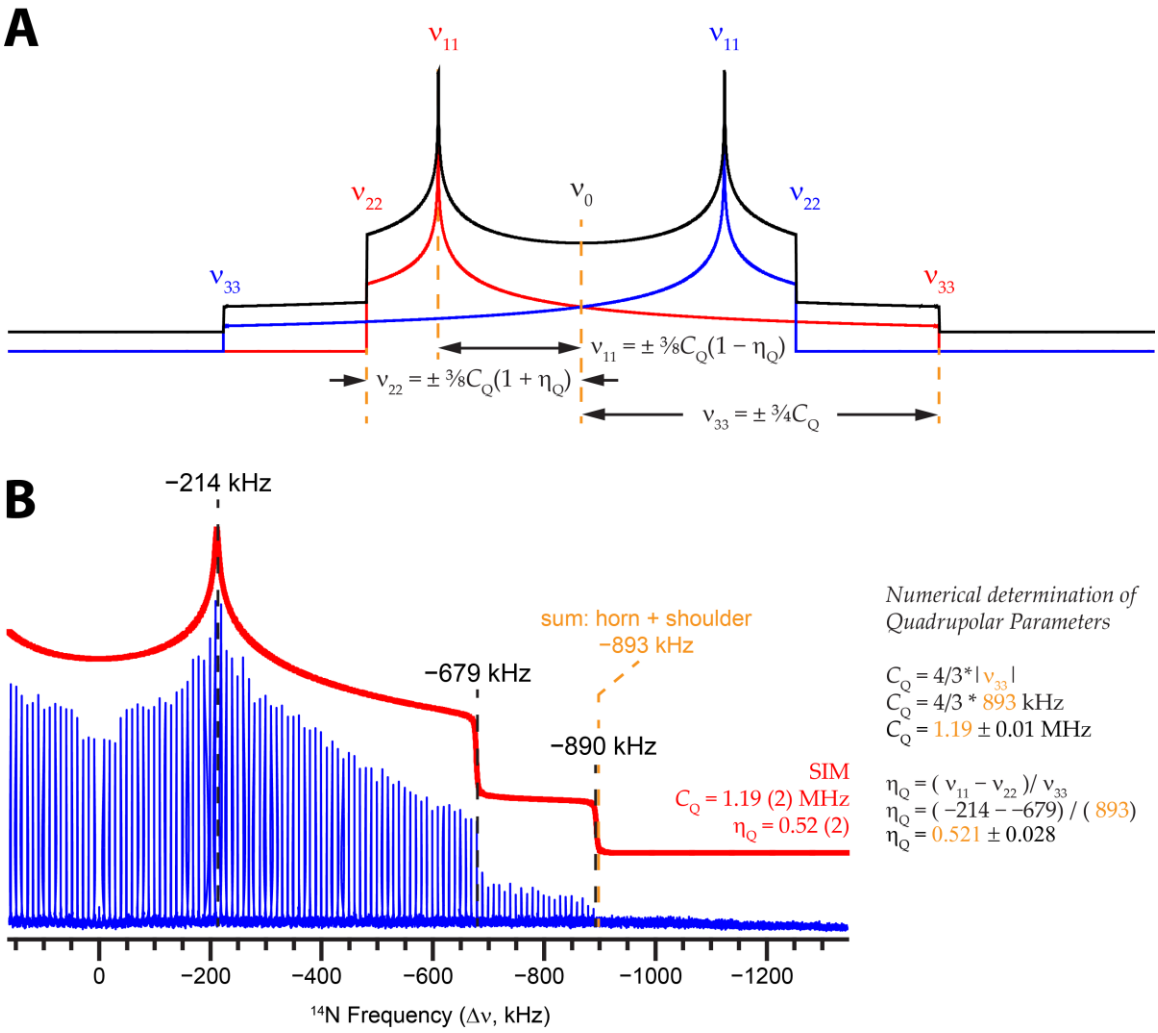

Figure A4. (A) Analytical simulation of an idealized ^{14}N powder pattern dominated by the first-order quadrupolar interaction. Owing to the traceless nature of the EFG tensor and the frequencies of the discontinuities being proportional to the principal components of the EFG tensor, the same relation holds for the frequencies of the discontinuities. Thus, since $V_{11} + V_{22} = -V_{33}$, $\nu_{11} + \nu_{22} = -\nu_{33}$ must also be true. Since the frequencies of all three discontinuities are closely related, knowing the frequency of any two of the discontinuities allows accurate determination of the quadrupolar parameters. (B) ^{14}N SSNMR powder pattern of α-glycine demonstrating the relationship in (A). Values in orange are calculated from the frequencies of the horn and shoulder discontinuities, while values in red are determined from fitting of the entire powder pattern.

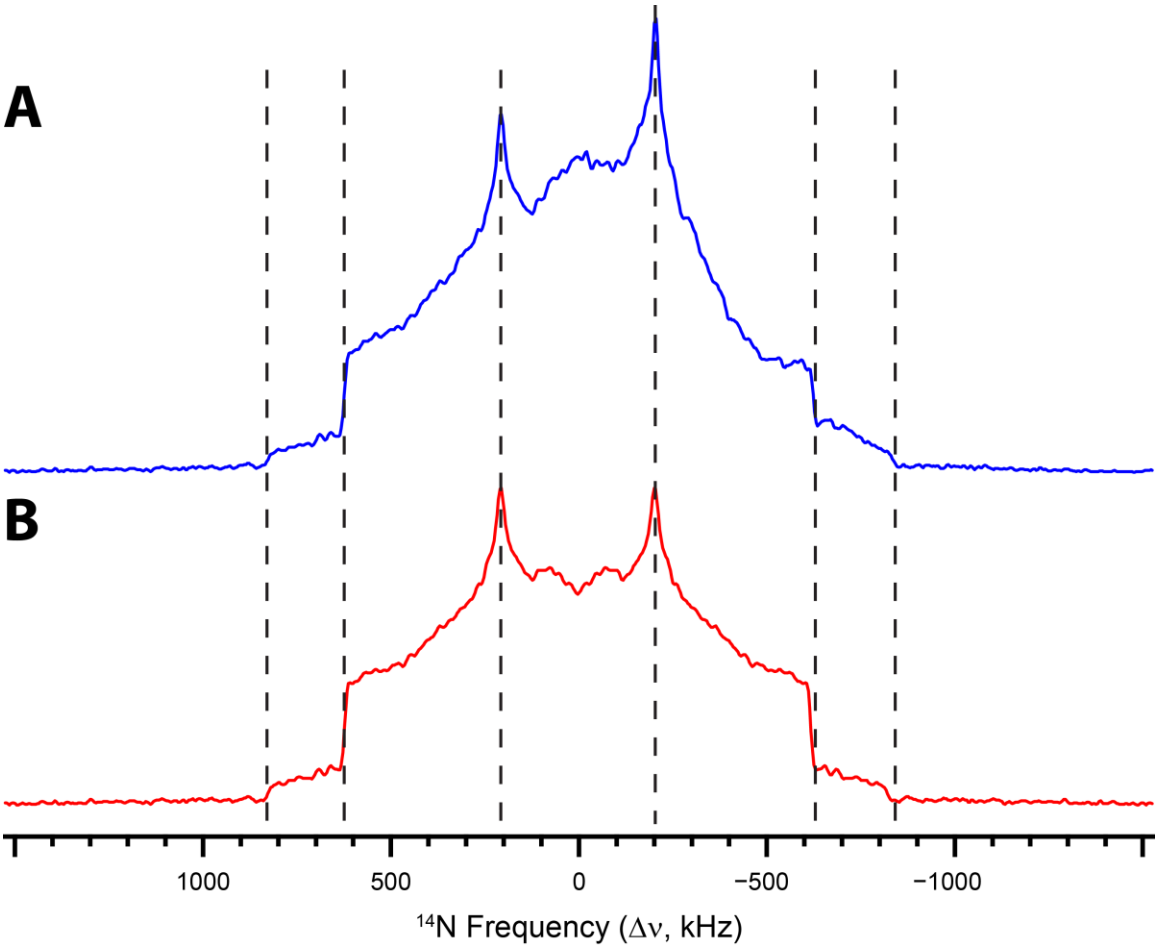

Figure A5. ^{14}N SSNMR powder patterns of **gln** acquired by (A) collecting the entire ^{14}N powder pattern (thirteen sub-spectra) and (B) collecting the high-frequency side of the powder pattern (six sub-spectra) and building the low-frequency side by reflection. The vertical dashed lines show that the frequencies of the discontinuities are the same in both cases, so it is possible to reduce the experimental time by acquiring only half of the powder pattern and building the other by reflection.

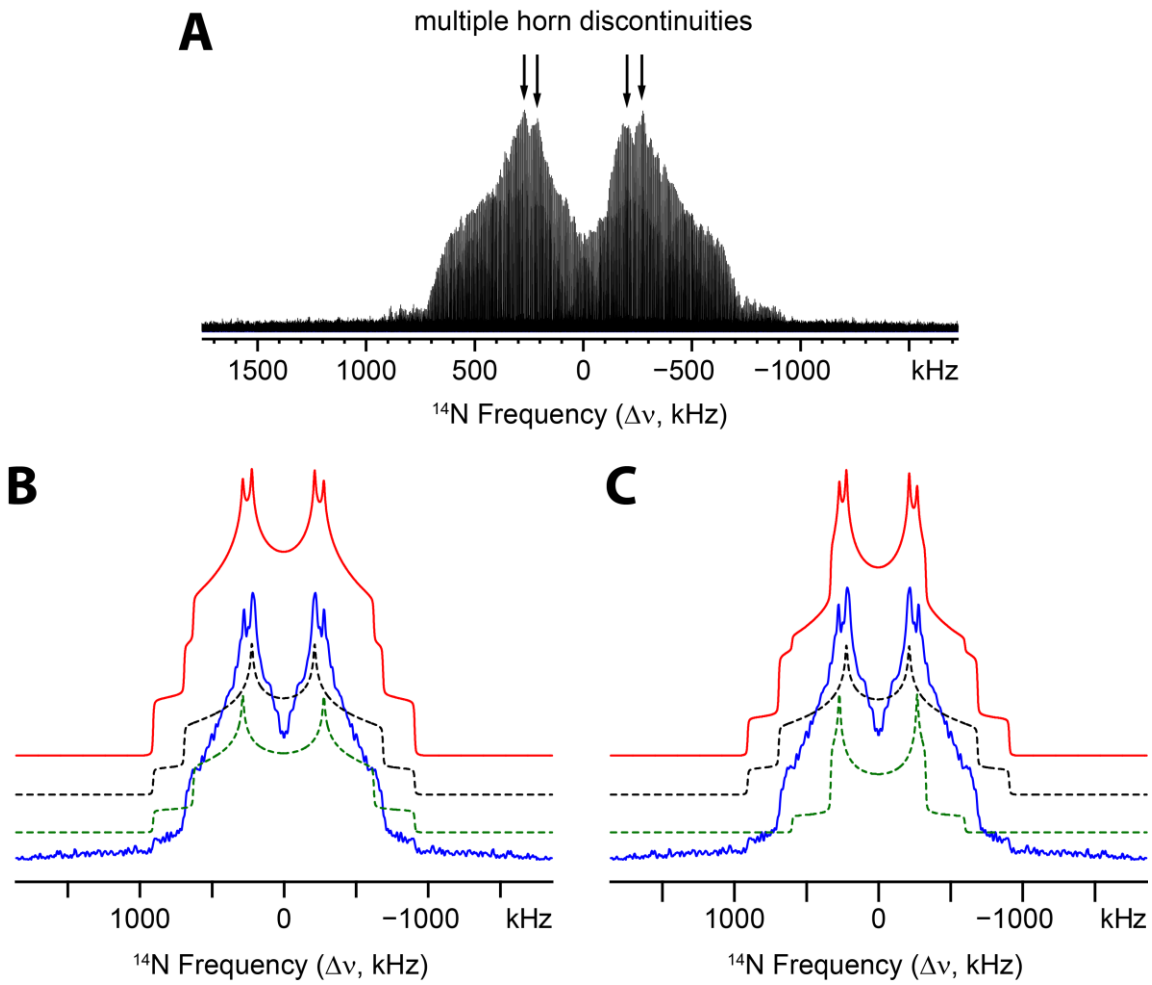

Figure A6. (A) ^{14}N SSNMR powder pattern of **trp** acquired with WCPMG at 21.1 T. The powder pattern has multiple horn discontinuities, which is generally indicative of two magnetically distinct nitrogen environments. Unfortunately, due to the lack of definition of the shoulder and foot discontinuities, an accurate determination of the C_Q and η_Q values for both sites is not possible. Proposed two-site simulations of **trp**: (B) site 1 (green dashed trace): C_Q = 1.2(1) MHz and η_Q = 0.35(10) and site 2 (black dashed trace): C_Q = 1.21(2) MHz and η_Q = 0.52(2) and (C) site 1: C_Q = 0.8(3) MHz and η_Q = 0.1(2) and site 2: C_Q = 1.21(2) MHz and η_Q = 0.52(2).

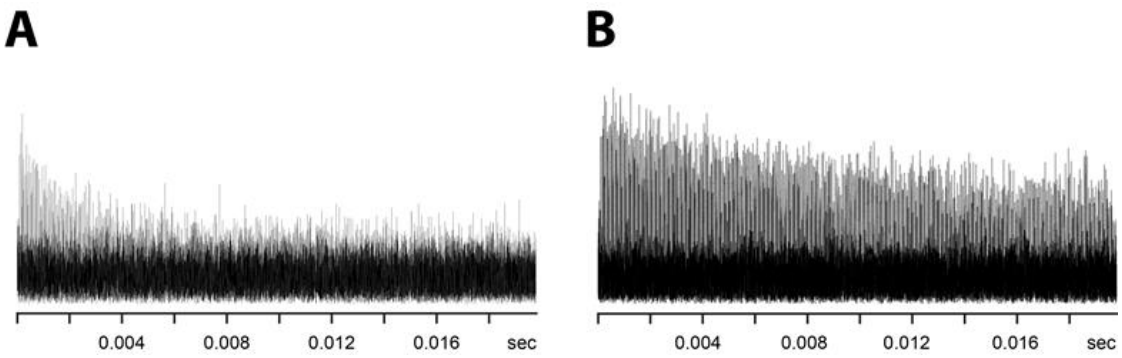

Figure A7. (A) ^{14}N SSNMR FID of **hyp** as received. (B) ^{14}N SSNMR FID of **hyp-*d*$_2$** (recrystallized from D_2O (*l*)). The longer CPMG echo train in B) provides a spectrum of significantly higher S/N.

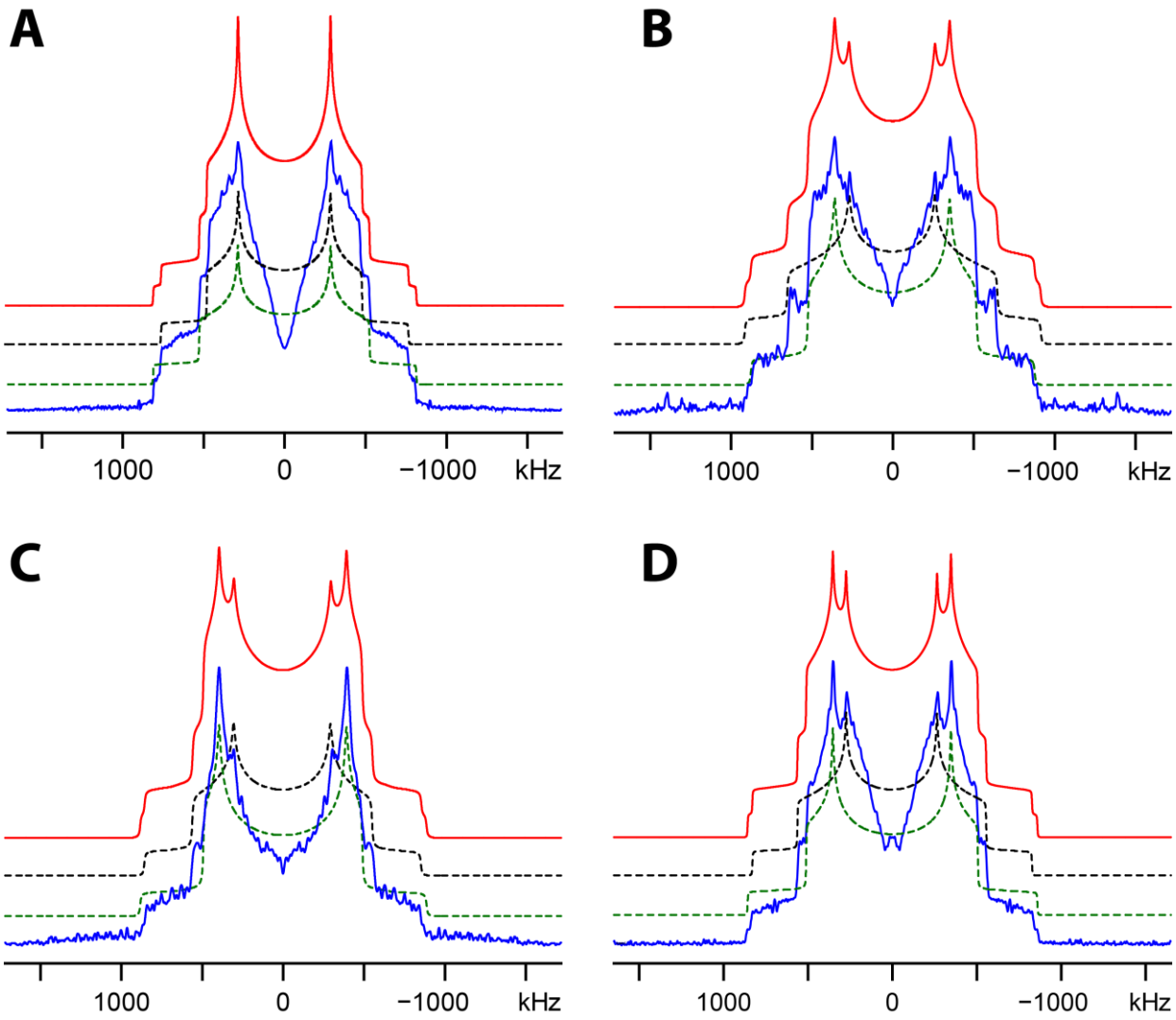

Figure A8. ^{14}N SSNMR powder patterns, associated two-site simulation (red trace), and two site deconvolutions for (A) **lysHCl** (site 1 (green dashed trace): C_Q = 1.09(2) MHz and η_Q = 0.30(2). site 2 (black dashed trace): C_Q = 1.02(2) MHz and η_Q = 0.26(2)), (B) **met** (site 1: C_Q = 1.22(2) MHz and η_Q = 0.42(2). site 2: C_Q = 1.17(2) MHz and η_Q = 0.19(2)), (C) **ile-*d*$_3$** (site 1: C_Q = 1.14(2) MHz and η_Q = 0.30(2). site 2: C_Q = 1.18(2) MHz and η_Q = 0.11(2)), and(D) **val** acquired at T_{max} = 150 °C (site 1: C_Q = 1.11(2) MHz and η_Q = 0.35(2). site 2: C_Q = 1.15(2) MHz and η_Q = 0.19(2)).

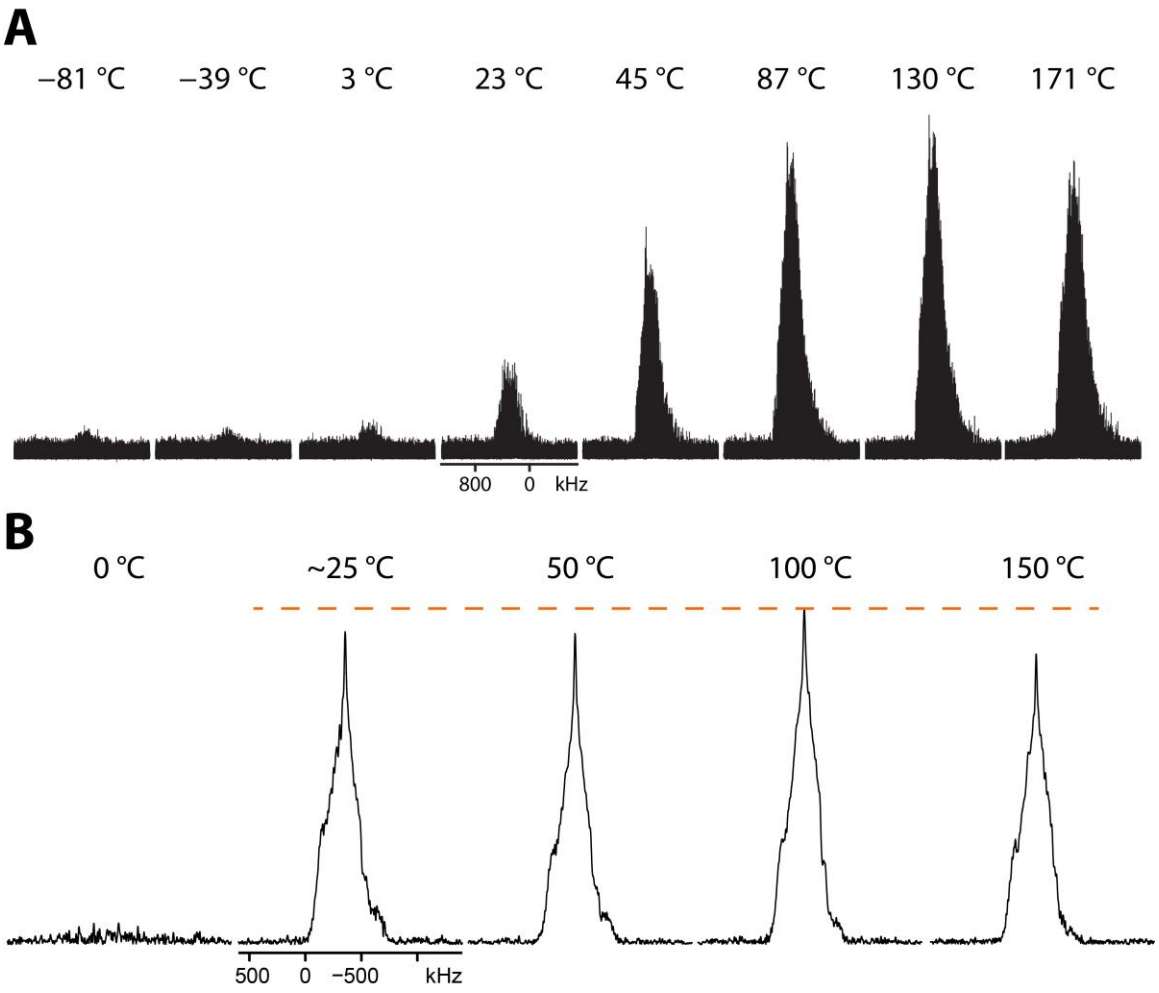

Figure A9. (A) Temperature dependence of ^{14}N SSNMR signal intensity in the temperature range of −81 to +171 °C for **val**. (B) Temperature dependence of ^{14}N SSNMR signal intensity in the temperature range of 0 to +150 °C for **val-*d*$_3$**.

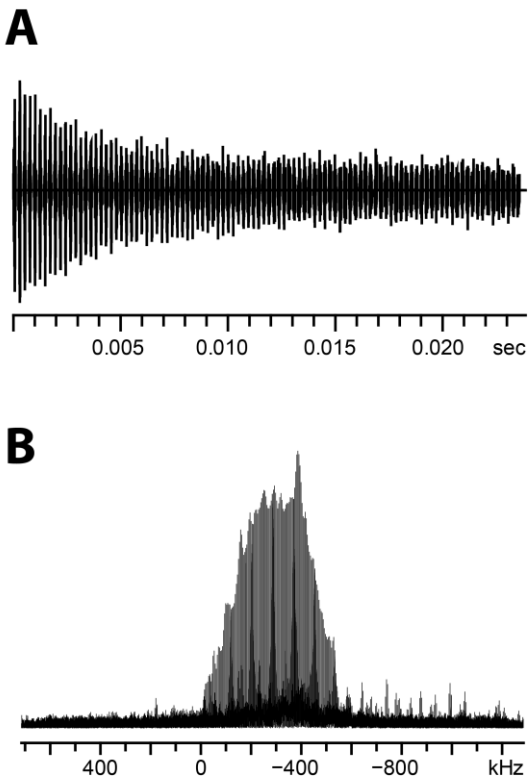

Figure A10. (A) ^{14}N SSNMR FID of **asp** acquired at room temperature and (B) the corresponding FT ^{14}N SSNMR sub-spectrum. The S/N of the sub-spectrum is relatively poor given the experimental time (*ca*. 2 hours).

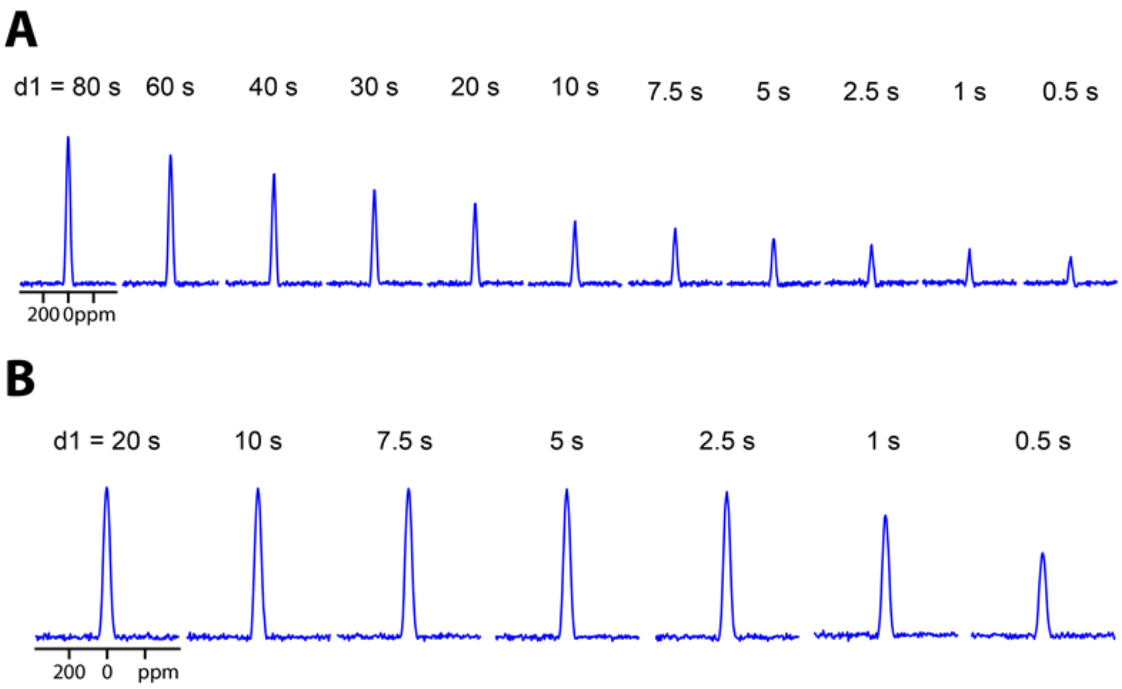

Figure A11. ^{1}H pulse delay arrays of **tyr** at (A) T_{RT} and (B) T_{max} = 171 °C. At T_{RT}, the ^{1}H pulse delay is >60 s ($T_1(^{1}H)$ > 12 s) while at T_{max}, the ^{1}H pulse day is 2.5 s ($T_1(^{1}H)$ ≈ 0.5 s).

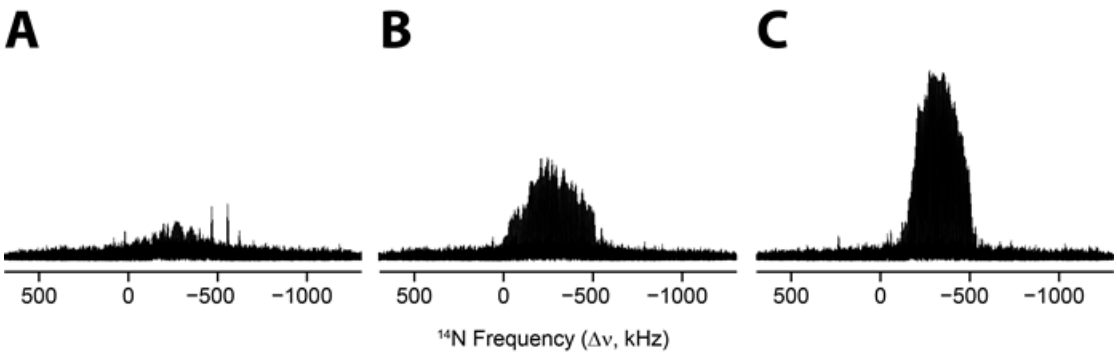

Figure A12. Individual ^{14}N SSNMR sub-spectra of **tyr** acquired with (A) WCPMG at T_{RT}, (B) WCPMG at T_{max} = 171 °C, and (C) BRAIN-CP/WCPMG at T_{max} = 171 °C. All spectra were acquired with the same number of scans and CPMG refocusing parameters (e.g., # of echoes, echo length, etc.). The S/N enhancement from acquiring the WCPMG spectrum at T_{max} versus at T_{RT} is roughly 2.5 times. The S/N enhancement from acquiring the BRAIN-CP/WCPMG spectrum at T_{max} versus acquiring the WCPMG spectrum at T_{RT} is roughly 5 times.

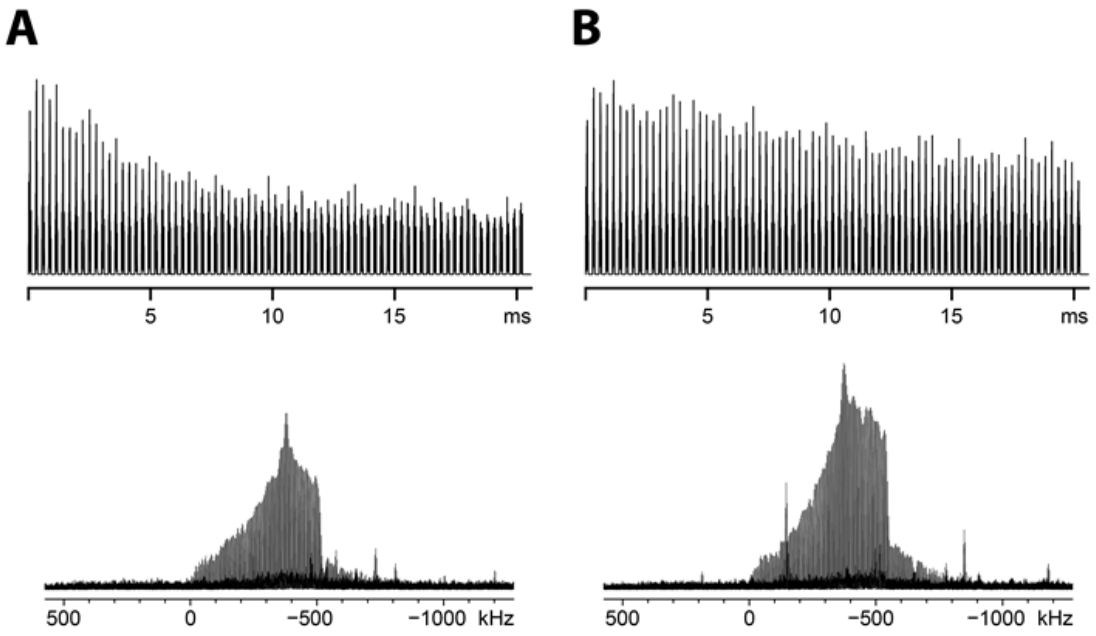

Figure A13. ^{14}N SSNMR FIDs acquired at the horn discontinuity of (A) **A-his** and (B) **B-his**. The $T_2^{eff}(^{14}N)$ values were determined to be 7 ± 3 and 24 ± 4 ms, respectively. The corresponding FT sub-spectra are below the FIDs.

Appendix B: Supplementary Tables and Figures for Chapter 3

Table B1. Experimental parameters for ^{14}N WURST-CPMG NMR experiments

	α-glycine	β-glycine	γ-glycine*	glycine HCl
Number of transients per sub-spectrum	256	7200	512	256
Number of sub-spectra	8	7	8	8
Transmitter frequency step (kHz)	150	150	150	150
^{14}N Recycle delay (s)	1	0.5	1	1
Experimental time (minutes)	35.5	455.4	71.1	35.5
WURST sweep range (kHz)	2000	3000	2000	2000
Number of Meiboom-Gill Loops	200	200	200	200
Acquisition points per echo	200	200	200	200
Spikelet Separation (kHz)	10	10	10	10
WURST pulse length (μs)	50	50	50	50
^{1}H decoupling power (kHz)	40	40	40	40
WURST pulse power (kHz)	28	28	28	28
Spectral window width (kHz)	2000	2000	2000	2000

* Identical experimental parameters used for acquisition of γ-glycine-ND_3^+.

Table B2. Experimental parameters for ^{14}N WURST-CPMG Variable Temperature NMR experiments of individual sub-spectra

	α-glycine	γ-glycine	glycine HCl
Transmitter Frequency (MHz)	29.175	29.175	29.325
Number of transients per sub-spectrum	512	512	128
Experimental time (minutes)	8.9	8.9	2.2
WURST sweep range (kHz)	2000	2000	2000
Recycle delay (s)	1	1	1
Number of Meiboom-Gill Loops	200	200	200
Acquisition points per echo	200	200	200
Spikelet Separation (kHz)	10	10	10
WURST pulse length (μs)	50	50	50
^{1}H decoupling power (kHz)	40	40	40
WURST pulse power (kHz)	28	28	28
Spectral window width (kHz)	2000	2000	2000
Temperature Range (°C)	−65 to 181	−43 to 136	−88 to 92

Table B3. Experimental parameters for ^{14}N WURST-QCPMG Variable Temperature NMR experiments for complete powder pattern acquisition

	α-glycine	γ-glycine
Number of transients per sub-spectrum	256	512
Number of sub-spectra	8	8
Transmitter frequency step (kHz)	150	150
^{14}N Recycle delay (s)	1	1
Experimental time (minutes)	35.5	71.1
WURST sweep range (kHz)	2000	2000
Number of Meiboom-Gill Loops	200	200
Acquisition points per echo	200	200
Spikelet Separation (kHz)	10	10
WURST pulse length (μs)	50	50
^{1}H decoupling power (kHz)	40	40
WURST pulse power (kHz)	28	28
Spectral window width (kHz)	2000	2000
Temperature (°C)	−43	92

Table B4. Experimental parameters for comparison of ^{14}N BRAIN-CP/WURST-CPMG NMR experiment versus ^{14}N WURST-CPMG NMR experiment using a sub-spectrum of glycine HCl

	BRAIN-CP/ WURST-CPMG	WURST-CPMG
Transmitter Frequency (MHz)	29.225	29.225
Number of transients per sub-spectrum	256	256
^{14}N Recycle delay (s)	–	2.5
^{1}H Recycle delay (s)	2.5	–
Experimental time (minutes)	10.8	10.8
Spectrum width (kHz)	2000	2000
Dwell time (μs)	0.5	0.5
^{1}H excitation ($\pi/2$) pulse (μs)	4.0	–
^{1}H excitation ($\pi/2$) pulse rf (kHz)	62.5	–
^{1}H Spin-lock rf power (kHz)	45	–
Contact time (ms)	10	–
CP sweep range (kHz)	400	–
WURST refocusing pulse length (μs)	50	50
WURST refocusing pulse power (kHz)	28	28
WURST refocusing sweep range (kHz)	450	460
Number of Meiboom-Gill Loops	200	200
Acquisition points per echo	200	200
CPMG echo length (per echo, μs)	100	100
Spikelet Separation (kHz)	10	10
^{1}H decoupling power (kHz)	45	45
Spectral window width (kHz)	2600	2600

Table B5. Experimental parameters for ^{14}N BRAIN-CP/WURST-CPMG NMR experiments for complete powder pattern acquisition

	glycine HCl
Number of transients per sub-spectrum	64
Number of sub-spectra	11
Transmitter frequency step (kHz)	90
^{1}H Recycle delay (s)	1
Experimental time (minutes)	11.8
Spectrum width (kHz)	2000
Dwell time (μs)	0.5
^{1}H excitation ($\pi/2$) pulse (μs)	4.0
^{1}H excitation ($\pi/2$) pulse rf (kHz)	62.5
^{1}H Spin-lock rf power (kHz)	45
Contact time (ms)	10
CP sweep range (kHz)	400
WURST refocusing pulse length (μs)	50
WURST refocusing pulse power (kHz)	28
WURST refocusing sweep range (kHz)	450
Number of Meiboom-Gill Loops	200
Acquisition points per echo	200
CPMG echo length (per echo, μs)	100
Spikelet Separation (kHz)	10
^{1}H decoupling power (kHz)	45
Spectral window width (kHz)	2600

Table B6. Atomic parameters for the four compounds under investigated. Atomic distances and angles were measured using the structures from the respective references, without optimization of the crystal structures.

Geometry parameters (no H-optimization)				
	α-glycine [51]	β-glycine [4]	γ-glycine [52]	glycine HCl [53]
C-N (Å)	1.475 (1)	1.475 (3)	1.488 (1)	1.461 (6)
$N\text{-}H_1$ (Å)	1.053 (1)	0.901 (18)	1.055 (1)	1.013 (3)
$N\text{-}H_2$ (Å)	1.036 (1)	0.884 (20)	1.054 (1)	1.037 (1)
$N\text{-}H_3$ (Å)	1.025 (1)	0.895 (25)	1.046 (1)	1.038 (1)
H_1---O (Å)	1.725 (1)	1.864 (19)	1.755 (1)	2.222 (9)
H_2---O (Å)	1.827 (1)	1.967 (30)	1.809 (1)	–
H_3---O (Å)	2.118 (1)	2.302 (24)	1.929 (1)	–
H_2---Cl (Å)	–	–	–	2.123 (2)
H_3---Cl (Å)	–	–	–	2.160 (2)
$C\text{-}N\text{-}H_1$ (°)	112.08 (1)	111.72 (125)	111.96 (1)	111.34 (1)
$C\text{-}N\text{-}H_2$ (°)	112.00 (1)	113.28 (141)	107.96 (1)	109.62 (1)
$C\text{-}N\text{-}H_3$ (°)	110.22 (1)	109.95 (147)	110.94 (1)	112.45 (1)

Table B7. Atomic parameters for the four compounds under investigated. Atomic distances and angles were measured using the structures from the respective references after geometry optimization of the proton positions.

Geometry parameters (H-optimization)				
	α-glycine [51]	β-glycine [4]	γ-glycine [52]	glycine HCl [53]
C-N (Å)	1.475	1.475	1.488	1.461
$N\text{-}H_1$ (Å)	1.065	1.067	1.060	1.038
$N\text{-}H_2$ (Å)	1.052	1.036	1.052	1.052
$N\text{-}H_3$ (Å)	1.038	1.053	1.042	1.052
H_1---O (Å)	1.712	1.697	1.750	2.206
H_2---O (Å)	1.812	2.201	1.806	–
H_3---O (Å)	2.112	1.802	1.933	–
H_2---Cl (Å)	–	–	–	2.106
H_3---Cl (Å)	–	–	–	2.143
$C\text{-}N\text{-}H_1$ (°)	112.693	111.07	112.226	111.580
$C\text{-}N\text{-}H_2$ (°)	112.115	110.586	107.293	109.305
$C\text{-}N\text{-}H_3$ (°)	110.465	111.662	110.941	112.983

Table B8. Calculated EFG tensor values

	Plane-wave DFT			Plane-wave DFT (optimized)		
	V_{11} (a.u.)	V_{22} (a.u.)	V_{33} (a.u.)	V_{11} (a.u.)	V_{22} (a.u.)	V_{33} (a.u.)
α-glycine	−0.0573	−0.1980	0.2553	−0.0491	−0.261	0.2552
β-glycine	−0.1280	−0.2114	0.3394	−0.0629	−0.2104	0.2733
γ-glycine	−0.0765	−0.1890	0.2655	−0.0771	−0.1858	0.2629
glycine HCl	−0.1039	−0.1448	0.2488	−0.0919	−0.1453	0.2372

Table B9. Statistically calculated CP enhancement for glycine HCl based on five spikelets.

Spikelet frequency (MHz)	DE S/N (au)	BCP S/N (au)	CP enhancement (BCP S/N ÷ DE S/N)
29.193995	46.9	299.7	6.39
29.213999	44.1	293.2	6.65
29.233987	56.5	379.3	6.71
29.253992	47.0	318.0	6.76
29.2739966	35.7	242.8	6.80
		average:	6.66 $\pm$ 0.16

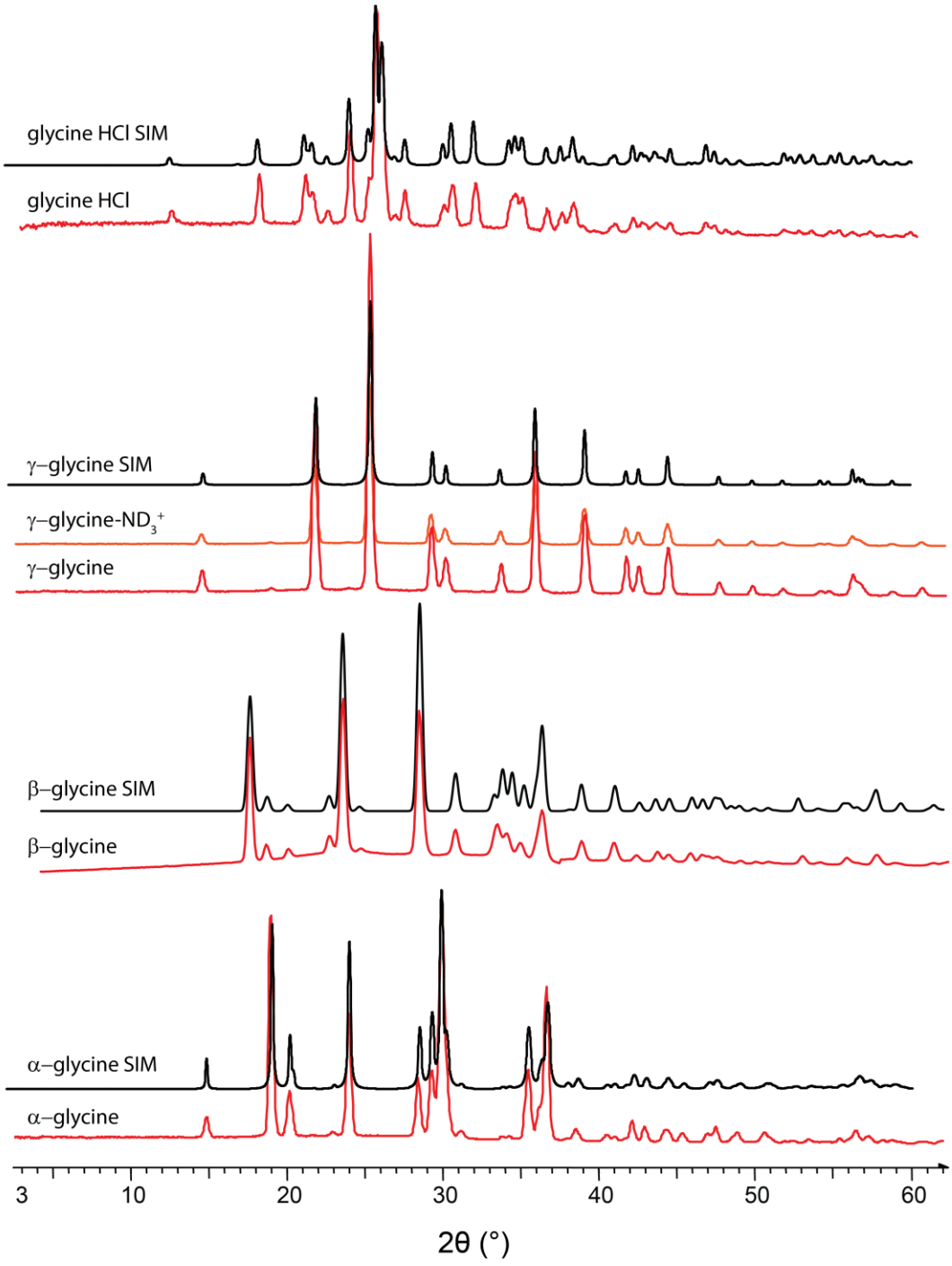

Figure B1. Powder X-ray Diffraction (pXRD) patterns for the three polymorphic forms of glycine and its HCl salt (red) along with simulated patterns (black).

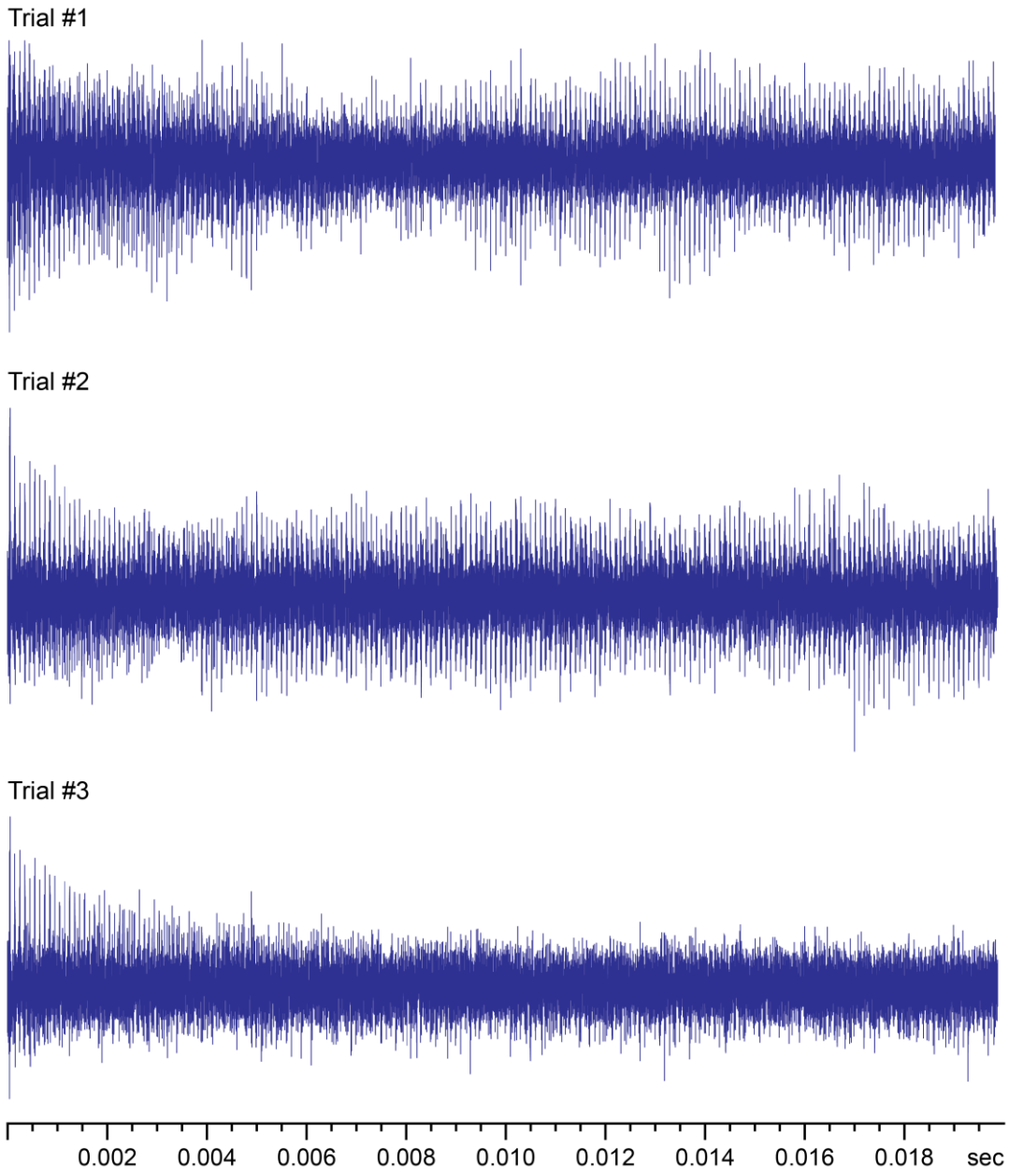

Figure B2. Severe acoustic ringing is observed in three individual ^{14}N FIDs of γ-glycine after 256 scans. All three trials were conducted with identical acquisiting parameters. The ringing is seen throughout the FIDs, is semi-coherent in nature, and is random in every scan. To minimize the contribution of the ringing to the FID, many acquisitions are required.

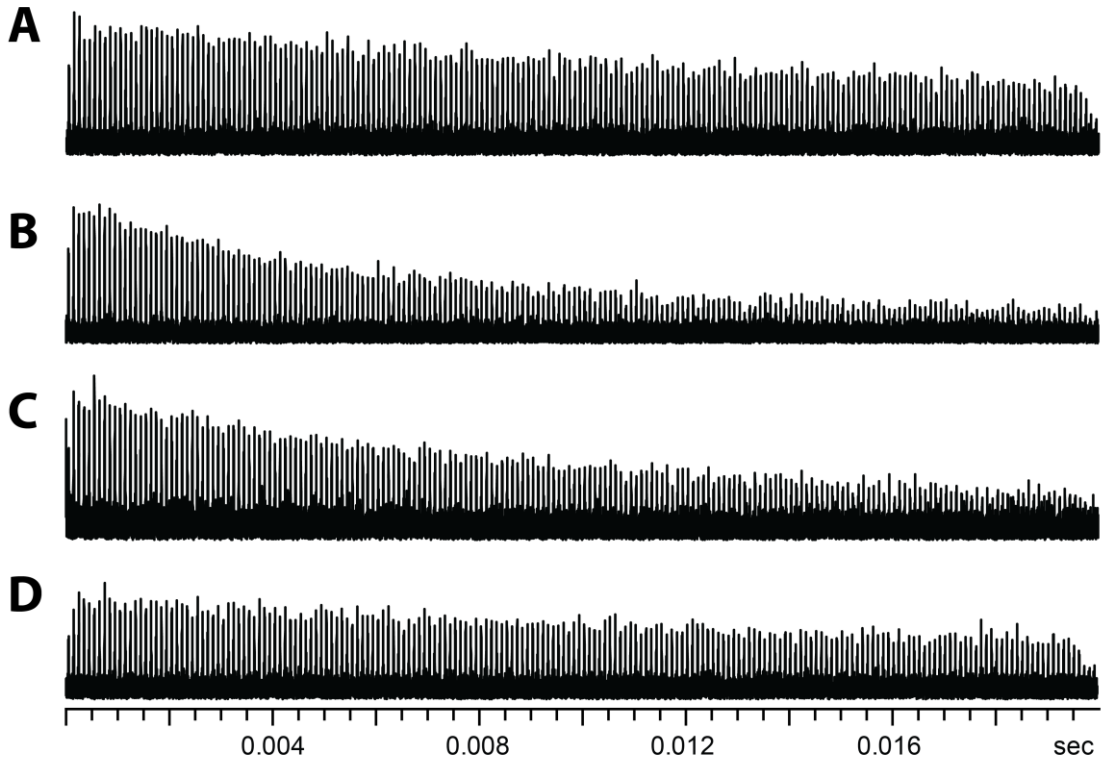

Figure B3. ^{14}N FIDs for (A) α-glycine, (B) β-glycine, (C) γ-glycine, and (D) glycine HCl after 256, 7200, 512, and 256 acquisitions, respectively. By fitting the FIDs with a first-order exponential decay function, the $T_2^{eff}(^{14}N)$ values for α-glycine, β-glycine, γ-glycine, and glycine HCl were determined to be 54 ± 14 ms,12 ± 1 ms, 25 ± 4 ms, and 40 ± 10 ms, respectively

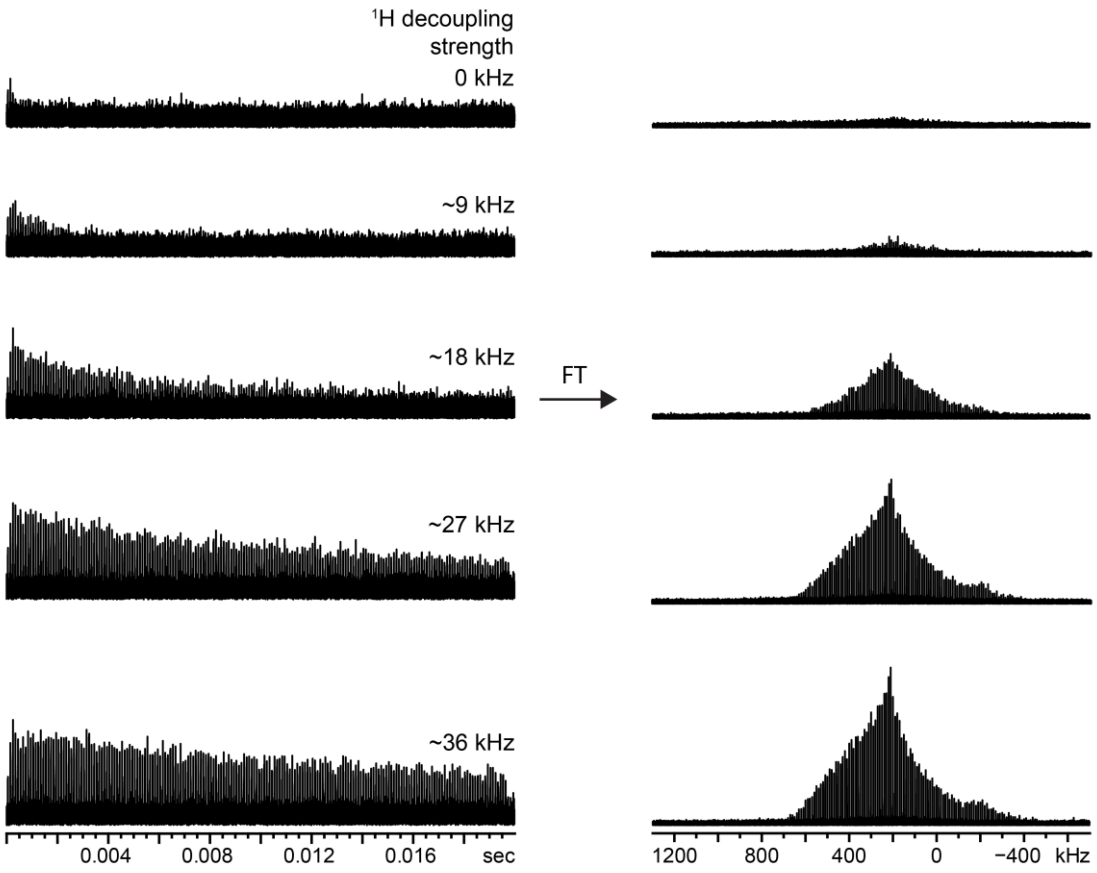

Figure B4. ^{14}N FIDs and corresponding FT NMR sub-spectra of α-glycine acquired at 29.175 MHz with varying1H decoupling rf field strengths. The number of spin echoes that form in the CPMG echo train, and their intensity,increases with increasing ^{1}H decoupling strength, resulting in FT NMR spectra with higher S/N.

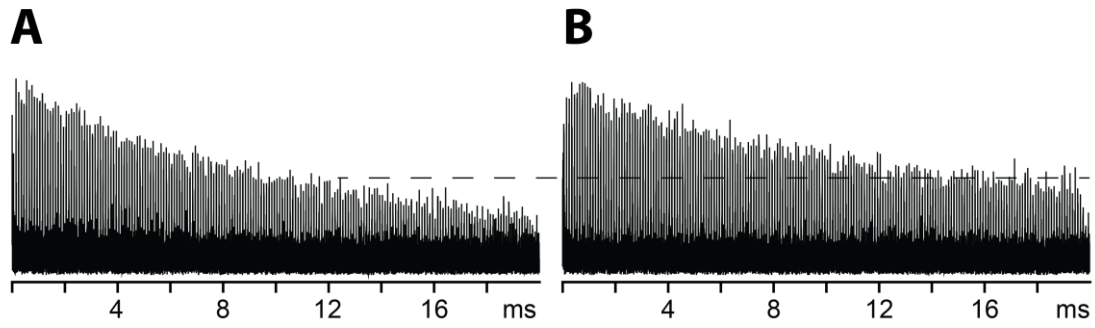

Figure B5. ^{14}N FIDs of γ-glycine acquired at sample temperatures of (a) 20 °C and (b) 92 °C. As evidenced by the horizontal dashed line, the intensity of the CPMG echo-train persists further in the time domain for the 92 °C FID. As a result, the corresponding Fourier-Transformed sub-spectrum at 92 °C has higher S/N than its 20 °C counterpart.

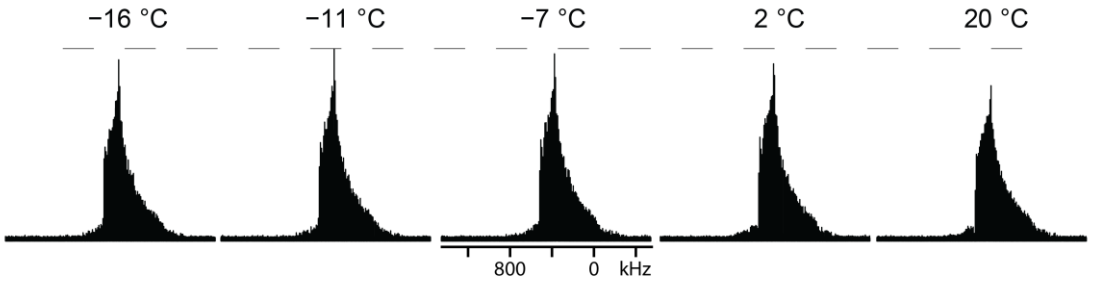

Figure B6. ^{14}N variable-temperature SSNMR of glycine HCl in the temperature range of −16 to 20 °C. The horizontal dashed line indicates the intensity of the ^{14}N sub-spectrum that has the highest S/N (T_{max} = −11 °C).

Appendix C: Supplementary Tables and Figures for Chapter 4

Table C1. Experimental parameters employed for full BCP and DE powder patterns; parameters are the same for both methods unless indicated.

	α-glycine	trigonelline HCl	isoxsuprine HCl	buflomedil HCl
Number of transients per subspectrum	64	BCP: 128 DE: 480	BCP: 1080 DE: 17000	720
Number of sub-spectra	20	4	BCP: 7 DE: 5	12
Frequency stepsize (kHz)	90	90	BCP: 90 DE: 200	90
Recycle delay (s)	1	BCP: 10 DE: 15	2.5	5
Total experimental time for all sub-spectra (minutes)	20	BCP: 85 DE: 480	BCP: 315 DE: 3542	720
Method of summation of entire powder pattern (sky = skyline projected, coadd = coaddition of subspectra)	sky	sky	BCP: sky DE: coadd	sky
WURST refocusing pulse length (μs)	50	50	50	50
WURST refocusing pulse power (kHz)	22	25	BCP: 20 DE: 24	20
WURST CP sweep range (kHz)	500	500	500	350
WURST refocusing sweep range (kHz)	400	450	BCP: 400 DE: 3000	400
Number of echoes acquired	100	100	BCP: 200 DE: 360	200
CPMG echo length (per echo, μs)	100	100	BCP: 100 DE: 55	100
Spikelet Separation (kHz)	10	10	BCP: 10 DE: 18	10
^{1}H decoupling power (kHz)	40	40	40	53
^{1}H CP rf power (kHz)	40	40	40	40
^{14}N CP rf power (kHz)	22	22	22	22
Contact time (ms)	10	10	12.5	12.5

Table C2. Experimental parameters employed for BCP and DE comparison sub-spectra.

	α-glycine	trigonelline	isoxsuprine HCl	buflomedil HCl
Number of transients	128	480	8640	1792
Transmitter frequency (ν_{Tx}, MHz)	29.045	29.045	29.005	29.405
Recycle delay (s)	5	BCP: 15 DE: 45	2.5	BCP: 5 DE: 10
Experimental time (minutes)	11	BCP: 120 DE: 360	360	BCP: 150 DE: 300
WURST refocusing pulse length (μs)	50	50	50	50
WURST refocusing pulse power (kHz)	22	25	20	20
WURST refocusing sweep range (kHz)	400	450	400	400
Number of echoes acquired	100	100	200	50
CPMG echo length (per echo, μs)	100	100	100	100
Spikelet Separation (kHz)	10	10	10	10
^{1}H decoupling power (kHz)	40	40	40	53
^{1}H CP rf power (kHz)	40	40	40	40
^{14}N CP rf power (kHz)	22	22	22	22
Contact time (ms)	10	10	12.5	12.5
CP sweep range (kHz)	500	500	500	350

The conventional CP experiment shown in **Fig. 4.1B** was also recorded using 64 scans, with a 10 ms contact time and a Hartmann-Hahn match with rf power levels of 40 kHz on the ^{1}H channel, and ca. 22 kHz on the ^{14}N channel; QCPMG enhancement was applied to the experiment with rectangular pulses and conditions closely matching those listed for the BRAIN-CP/WURST-QCPMG (BCP) experiments in Table C2 (100 echoes of 100 μs each were recorded).

^{14}N T_2 anisotropy in Buflomedil HCl:

There appears to be a variation of the ^{14}N T_2 relaxation constant across the powder pattern under the experimental conditions applied in this study. We note first that this effect is unrelated to the CP preparation of the magnetization, and is a phenomenon of the WURST-CPMG echo train portion of the experiment. In section A1 and A2 of Figure C1, we show the time domain data (the echo train) recorded with the transmitter located at two positions within the powder pattern. The different effective T_2 relaxation constant is readily apparent from the different decay rate of the echo trains measured at these two frequencies. The relative height of the two sub-spectra generated by Fourier transforming (FT) of either the first echo (section B of Figure C1) or the entire echo train (section C1 of Figure C1) of each FID is noticeably different. The spectrum from FT of the first echo is only marginally affected by the T_2 constant, and therefore produces an accurate relative intensity for the two sub-spectra. However, the S/N enhancement produced by multi-echo acquisition is larger for the transmitter position corresponding to the green FID, yielding an inaccurate relative intensity for the two sub-spectra. Collation of the entire powder pattern without consideration of this T_2 anisotropy therefore yields a distorted spectrum, as shown in section C2 of Figure C1. However, it is relatively easy to use a line broadening (LB) filter to make the echo train data at every transmitter position have the same effective T_2 relaxation constant. This data processing method is demonstrated for the same two transmitter positions in section D1 of Figure C1, where the relative intensities are now seen to match the accurate values found in the single-echo FT results of section C1. Treatment of the entire collection of sub-spectra in this manner produces the nearly ideal spectrum shown in section D2, which is enhanced by the echo-train acquisition, but is free of effects from T_2 anisotropy.

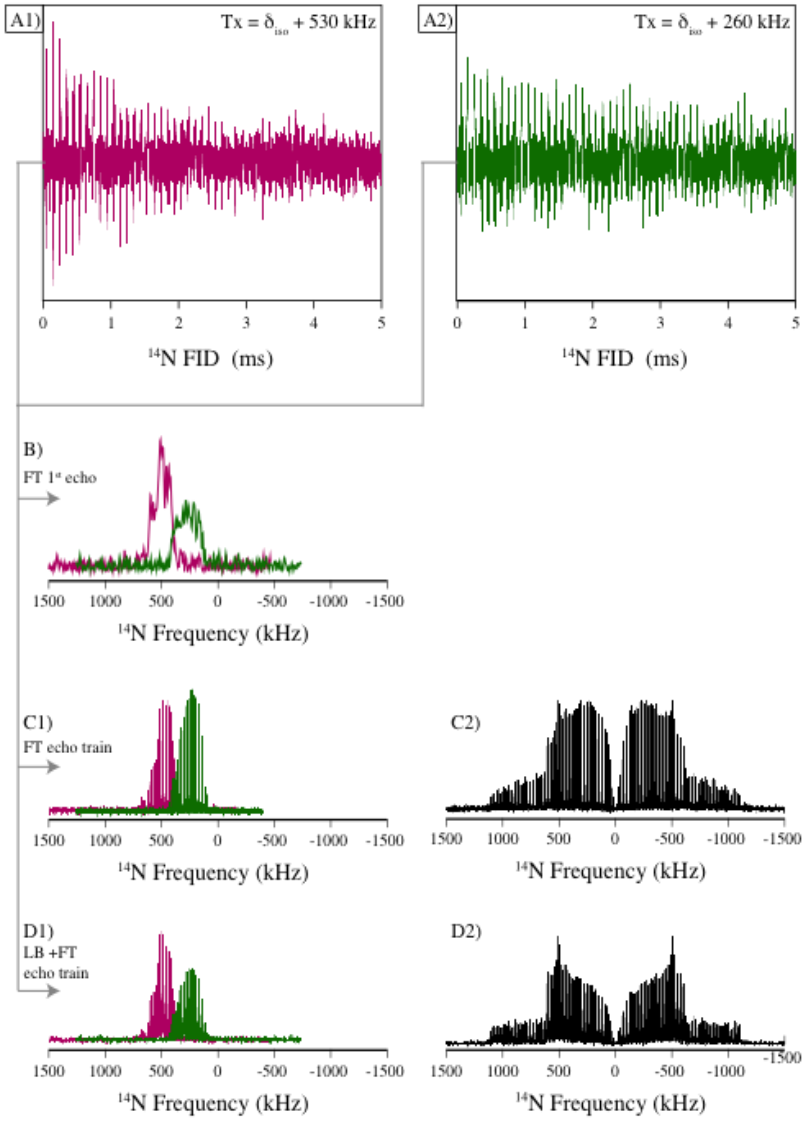

Figure C1: ^{14}N NMR data for Buflomedil HCl. *Section A1/A2*: Time domain data recorded at the two transmitter positions shown, using the BRAIN-CP/WURST-CPMG pulse sequence. *Section B:* Sub-spectra produced by Fourier transform (FT) of the first echo of the two FIDs shown in A1 (in fuchsia) and A2 (in green), displayed in magnitude mode. *Section C1/C2:* Sub-spectra produced by Fourier transform (FT) of each entire echo train shown in A1 (in fuchsia) and A2 (in green), are displayed in magnitude mode in C1. Analogous processing applied to all other sub-spectra produces the total pattern shown in C2, via skyline projection. *Section D1/D2:* Sub-spectra produced by Fourier transform (FT) of each entire echo train shown in A1 (in fuchsia) and A2 (in green), after application of 500 Hz of Gaussian line broadening (LB) via exponential multiplication are displayed in magnitude mode in D1. Analogous processing applied to all other sub-spectra produces the total pattern shown in D2, via skyline projection.

Appendix D: Supplementary Tables and Figures for Chapter 5

Table D1. Experimental parameters for DE ^{14}N NMR experiments used to collect the spectra in **Fig. 2.1**.

	α-glycine	tyrosine
Number of transients per sub-spectrum	256	21600
Number of sub-spectra	8	5
Transmitter frequency step (kHz)	150	150
^{14}N Recycle delay (s)	1	1
Experimental time per spectrum (hours)	0.5	31.2
Spectral window width (kHz)	2000	2000
Dwell time (μs)	0.5	0.5
Number of Meiboom-Gill Loops (*N*)	200	200
Acquisition window, τ_{window} (μs)	100	100
Spin echo time, τ_{echo} (μs)	210	210
Acquisition time, τ_{acq} (ms)	42	42
WURST pulse length (μs)	50	50
WURST sweep range (kHz)	2000	3000
WURST pulse power (kHz)	28	28
^{1}H decoupling power (kHz)	40	40

Table D2. Experimental parameters for DE ^{14}N NMR experiments used to investigate the interplay between S/N and spectral resolution.

	α-glycine			
Number of transients per sub-spectrum	1024			
Number of sub-spectra	6			
Transmitter frequency step (kHz)	152			
^{14}N Recycle delay (s)	0.5			
Experimental time per spectrum (minutes)	51.2			
Spectral window width (kHz)	2000			
Dwell time (μs)	0.5			
Acquisition window, τ_{window} (μs)	900	400	150	25
Spin-echo time, τ_{echo} (μs)	1000	500	250	125
Number of Meiboom-Gill Loops (*N*)	50	100	200	400
Acquisition time per scan, τ_{acq} (ms)	50			
Spikelet Separation (kHz)	1	2	4	8
WURST pulse length (μs)	50			
WURST sweep range (kHz)	750			
WURST pulse power (kHz)	28			
^{1}H decoupling power (kHz)	50			

Table D3. Experimental parameters for DE ^{14}N NMR experiments on glycine HCl used to investigate the effect of the dwell time of the pulse (*dwp*) on the spectral quality and its relation to the Nyquist dwell.

	Glycine HCl		
Number of transients per sub-spectrum		2048	
Transmitter frequency (ν_{Tx}, MHz)		28.624	
Transmitter offset from Larmor (kHz)		−250	
^{14}N Recycle delay (s)		0.5	
Experimental time (hours/sub-spectrum)		0.3	
Spectral window width (kHz)		2000	
Dwell time (μs)		0.5	
Acquisition window, τ_{window} (μs)		100	
Spin echo time, τ_{echo} (μs)		210	
Number of Meiboom-Gill Loops (*N*)		100	
Acquisition time, τ_{acq} (ms)		21	
WURST sweep range (Δ, kHz)	500	1000	2000
WURST pulse length (μs)		50	
WURST number of points (*np*)	100 63 50 32 25 16	500 250 125 100 63 50 32	500 250 125 100 63
Dwell time of the pulse (*dwp*, ns)	500 ≈800 1000 ≈1600 2000 3125	100 200 400 500 ≈800 1000 ≈1600	100 200 400 500 ≈800
WURST pulse power (kHz)		28	
^{1}H decoupling power (kHz)		40	

Table D4. Experimental parameters for DE ^{14}N NMR experiments on glycine HCl used to investigate the effect of the linear sweep rate (*R*) on the spectral quality.

	Glycine HCl	
Number of transients per sub-spectrum	2048	
Transmitter frequency (MHz)	28.624	
Transmitter offset from Larmor (kHz)	−250	
^{14}N Recycle delay (s)	0.5	
Experimental time (hours/sub-spectrum)	0.3	
Spectral window width (kHz)	2000	
Dwell time (μs)	0.5	
Acquisition window, τ_{window} (μs)	100	
Spin echo time, τ_{echo} (μs)	178−310	210
Number of Meiboom-Gill Loops (*N*)	100	150
Acquisition time per scan, τ_{acq} (ms)	17.8−31	31.5
WURST sweep range (SR, kHz)	750	250 375 500 750 1000 1500 2000 3000 4000 6000
WURST pulse length (μs)	150 100 75 50 37 25 18	50
Dwell time of pulse (*dwp*, ns)	100	
WURST pulse power (kHz)	28	
^{1}H decoupling power (kHz)	40	

Table D5. Experimental parameters for DE ^{14}N NMR experiments used to demonstrate how a common *R* value may be maintained.

	Glycine HCl	α-Glycine
Number of transients per sub-spectrum	2048	
Transmitter frequency (MHz)	28.624	
Transmitter offset from Larmor (kHz)	−250	
^{14}N Recycle delay (s)	0.5	
Experimental time (hours/sub-spectrum)	0.3	
Spectral window width (kHz)	2000	
Dwell time (μs)	0.5	
Acquisition window, τ_{window} (μs)	100	
Spin echo time, τ_{echo} (μs)	210−360	
Number of Meiboom-Gill Loops (*N*)	50	
Acquisition time per scan, τ_{acq} (ms)	10.5−18	
WURST sweep range (SR, kHz)	500 750 1000 1250 1500 2000	
WURST pulse length (μs)	50 75 100 125 150 200	
Dwell time of pulse (*dwp*, ns)	100	
WURST pulse power (kHz)	28	
^{1}H decoupling power (kHz)	40	

Table D6. Experimental parameters for DE ^{14}N NMR experiments acquired at $\Delta\nu_{T_x}$ = ±275 kHz and $\Delta\nu_{T_x}$ = ±715 kHz for the 'two sub-spectrum' strategy.

	α-glycine	Glycyl glycine	4-hydroxy-*L*-proline-d_2
Number of transients per sub-spectrum	2048	2048	1432
Number of sub-spectra	2	2	2
$\Delta\nu_{T_{x1}}$ (kHz)	+275	−275	−275
$\Delta\nu_{T_{x2}}$ (kHz)	+715	−715	−715
^{14}N Recycle delay (s)	1	1	20
Total experimental time (hours)	2	2	15.9
Spectral window width (kHz)	2000	2000	2000
Dwell time (μs)	0.5	0.5	0.5
Acquisition window, τ_{window} (μs)	100	100	100
Spin echo time, τ_{echo} (μs)	260	260	235
Number of Meiboom-Gill Loops (*N*)	125	125	125
Acquisition time per scan, τ_{acq} (ms)	32.5	32.5	29.4
WURST pulse length (μs)	100	100	75
WURST sweep range (kHz)	1000	1000	750
WURST pulse power (kHz)	28	28	28
^{1}H decoupling power (kHz)	40	40	40

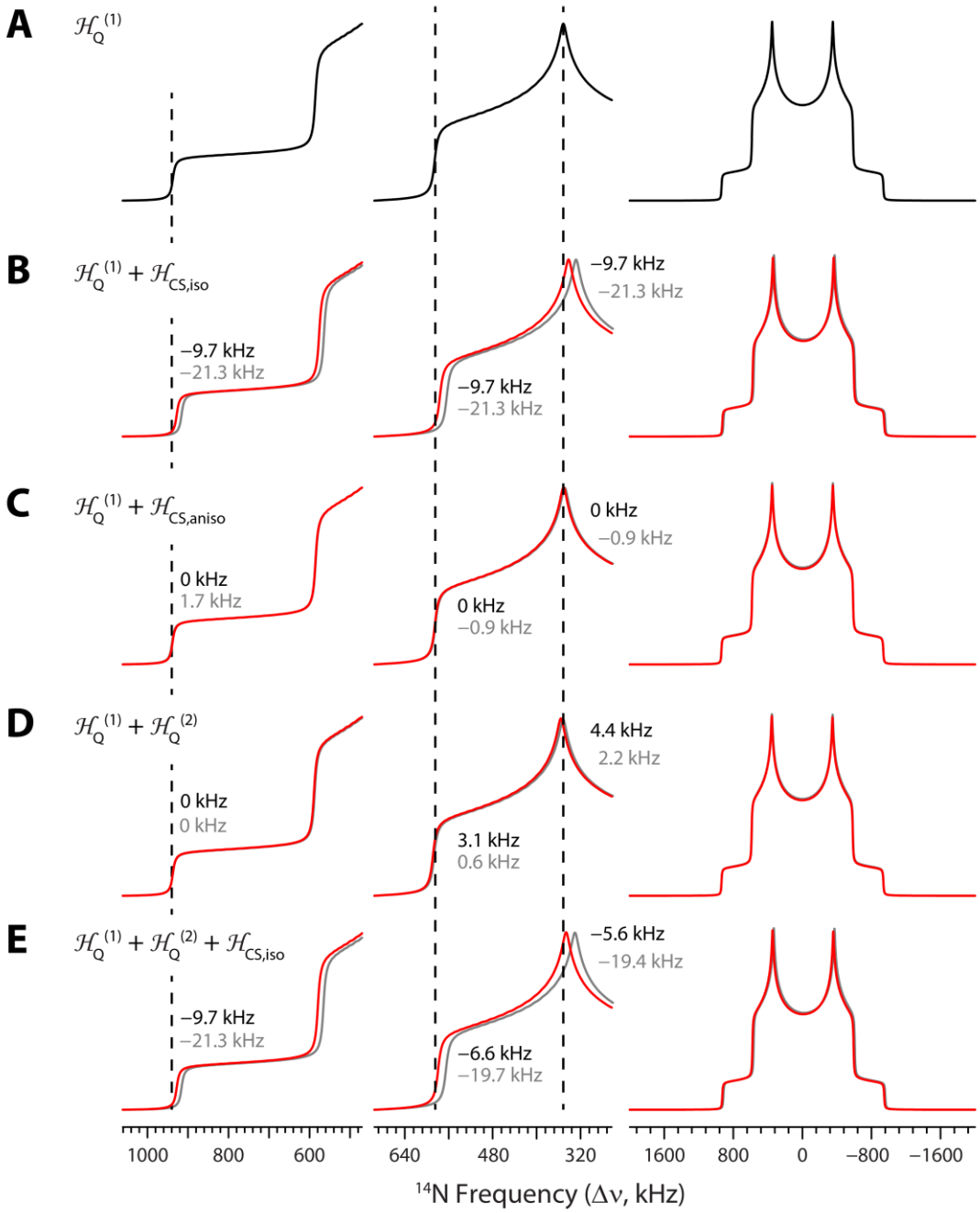

Figure D1. (a) Analytical simulation of a ^{14}N powder pattern dominated by the FOQI with C_Q = 1.25 MHz and η_Q = 0.25 (black trace). Simulations showing the influences of the nitrogen CS tensor and the SOQI are shown in (b) – (e) at two magnetic fields (red – 9.4 T, grey – 21.1 T). Vertical dashed lines mark the locations of the horn, shoulder, and foot discontinuities to first order. The frequencies shifts of the discontinuities are listed next to each of the dashed lines (black text – 9.4 T, grey text – 21.1 T). The most shielded component of the CS tensor, δ_{33}, is coincident with the largest component of the EFG tensor, V_{33}. The CS tensor is defined with a span of 30 ppm (which encompasses the chemical shift range of RNH_3^+ groups in organic compounds), a skew of 0, and δ_{iso} = −330 ppm.

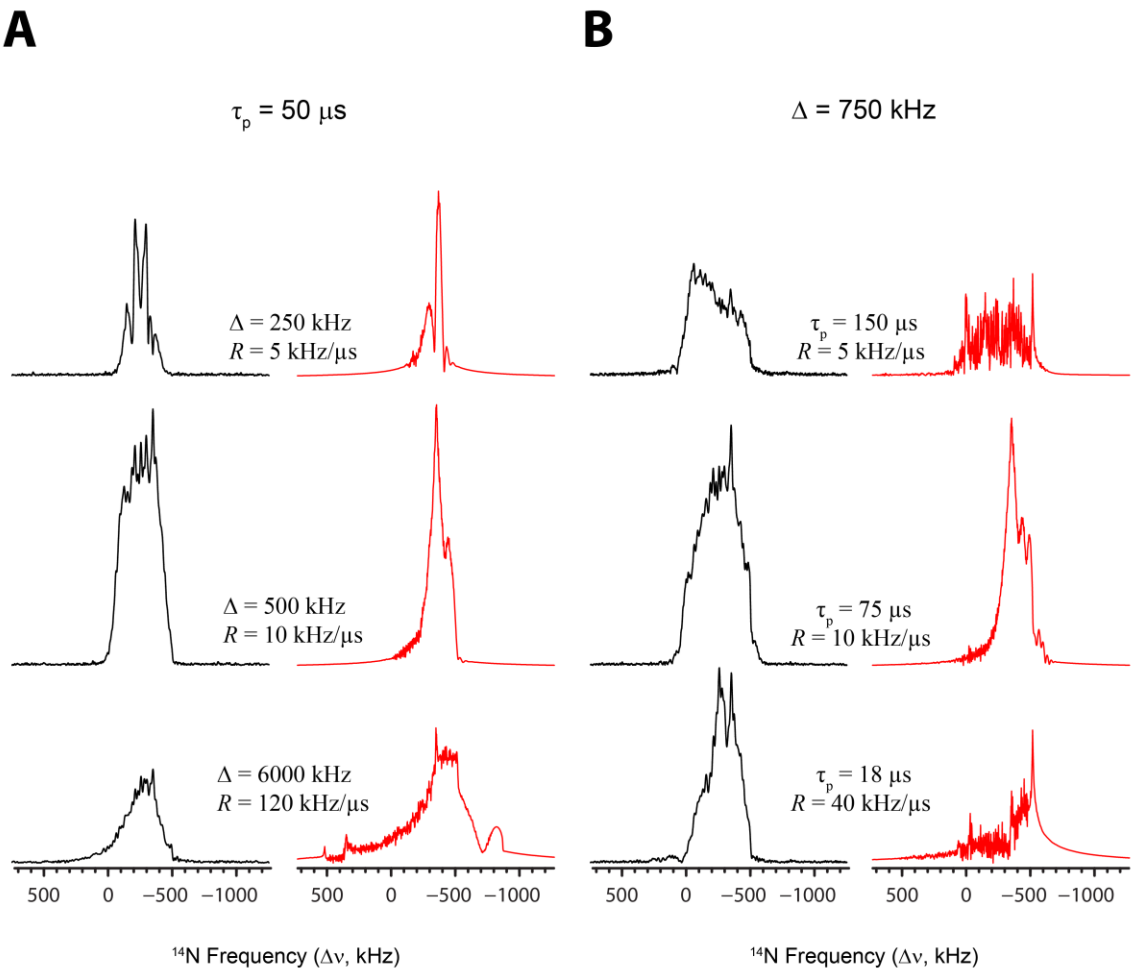

Figure D2. Three sub-spectra from each of the columns in **Figure 5.8** (black, left) with their associated SIMPSON simulations (red, right). Each column features sub-spectra resulting from the slowest R value (top), R = 10 kHz/us (middle), and the fastest R value. Numerical simulations were performed with SIMPSON 4.1.5 on a personal Macintosh computer using a 1.7 GHz Intel Core i7 processor. A WURST-echo pulse sequence was simulated in all cases, using WURST-80 pulses having the same pulse parameters (e.g., pulse widths, RF field strengths, pulse dwell times, frequency-sweep ranges) as those employed in the corresponding experiments. A spectral width of 5.0 MHz was used and 2048 points were used to define the spin echo. The average over the powder was calculated using 28656 (α, β) crystallites according to the Zaremba-Conroy-Wolfsberg distribution.[1-3]

(1) Zaremba, S. . Ann. di Mat. Pura ed Appl. 1966, 73, 293.
(2) Conroy, S. J. Chem. Phys. 1967, 47, 5307.
(3) Cheng, V. B.; Suzukawa, H. H.; Wolfsberg, M. J. Chem. Phys. 1973, 59, 3993.

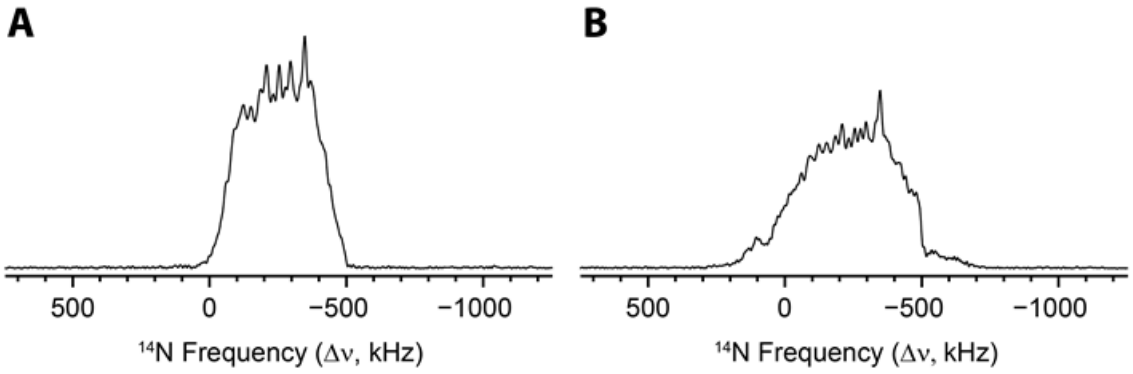

Figure D3. ^{14}N sub-spectra of glycine HCl acquired at $\Delta\nu_{Tx} = -250$ kHz with an acquisition time of $\tau_{acq} \approx 49$ ms. In A) $\Delta = 500$ kHz, $\tau_p = 50$ μs, and $N = 185$, while in B) $\Delta = 1000$ kHz, $\tau_p = 100$ μs, and $N = 135$. In both cases $\tau_{window} = 100$ μs. Although the S/N in A is higher than in B, it is outweighed by the broader excitation in B, which is nearly double. Both sub-spectra have approximately equal integrated intensity.

Appendix E: Supplementary Tables and Figures for Chapter 6

Table E1. WURST-CPMG acquisition parameters for spectra acquired at 9.4 T.

Pharmaceutical	**Bupi**	**Bupi II**	**Scop**
Number of sub-spectra acquired	5	5	9
Number of scans per sub-spectrum	28000	28000	7568
Transmitter offset per piece (kHz)	200	200	90
Recycle Delay (s)	1.0	1.0	2.0
Meiboom-Gill loops [N]	360	360	120
Real points per Loop	110	110	110
Acquisition length (number of points)	39600	39600	13200
Dwell (μs)	0.5	0.5	0.5
Sweep of WURST pulse (kHz)	3000	3000	450
WURST pulse width (μs)	50	50	50
Sweep rate of WURST pulse (MHz/ms)	60	60	9
^{1}H decoupling rf (kHz)	40	40	72
Total Experimental Time (hours)	38.9	38.9	37.9

Table E2. WURST-CPMG acquisition parameters for spectra acquired at 21.1 T. Note spectra were not mirrored.

Pharmaceutical	**Bupi**	**Bupi II**
Number of sub-spectra acquired	2	4
Number of scans per sub-spectrum	15001	15001
Transmitter offset per piece (kHz)	800	400
Recycle Delay (s)	1.0	1.0
Meiboom-Gill loops [N]	70	70
Real points per Loop	120	120
Acquisition length (number of points)	35044	35044
Dwell (μs)	2	2
Sweep of WURST pulse (kHz)	2000	2000
WURST pulse width (μs)	30	30
Sweep rate of WURST pulse (MHz/ms)	66.67	66.67
^{1}H decoupling rf (kHz)	30	30
Total Experimental Time (hours)	8.4	16.8

Table E3. BRAIN-CP-WCPMG acquisition parameters for spectra acquired at 9.4 T.

Parmaceutical	**Aceb**	**Alpr**	**Isop**	**Bupi**	**Bupi II**	**Nica**	**Rani**
Number of sub-spectra acquired	17	22	4	20*	10	11	25
Number of scans per sub-spectrum	608	2048	5200	2048	1024	736	1488
Recycle Delay (s)	7.0	1.0	2.5	5.0	5.0	10.0	2.5
WURST refocusing pulse length (μs)	50	50	50	50	50	50	50
WURST refocusing pulse power (kHz)	27	27	28	27	26	26	25
WURST refocusing sweep range (kHz)	400	400	500	450	400	400	450
Number of echos acquired	200	120	50	120	60	60	60
CPMG echo length (per echo, μs)	55	55	100	55	55	55	100
^{1}H decoupling power (kHz)	72	72	58	72	40	82	40
^{1}H CP rf power (kHz)	30	30	30	30	40	33	25
^{14}N CP rf power (kHz)	22	22.5	22	23	24	23	14
Contact time (ms)	10	10	7.5	5	7.5	20	20
CP sweep range (kHz)	500	500	500	450	500	500	500
Total Experimental Time	20.1	12.5	14.7	57*	14.2	22.5	26

*Too many sub-spectra were collected due to strong S/N from the underlying planar nitrogen site.

Table E4. $^{1}H\{^{15}N\}$ idHETCOR acquisition parameters for spectra acquired at 14.1 T.

Parmaceutical	**Aceb**	**Alpr**	**Isop**	**Bupi**	**Bupi II**	**Dibu**	**Nica**	**Rani**	**Scop**
Number of transients in direct dimension	8	80	120	32	32	16	96	16	8
Number of t_1 increments	64	128	128	256	256	400	128	512	512
t_1 increment (μs)	25	25	25	50	50	25	12.5	25	50
^{1}H Recycle delay (s)	10	3	2.5	4.5	4.5	6.5	6.5	3	10
CP contact time τ_{CP} (ms)	3	3	3	3	3	3	3	3	3
^{1}H π/2 pulse rf (kHz)	125	125	125	125	125	125	125	125	125
^{1}H CP pulse rf (kHz)	100	100	100	100	100	100	100	100	100
^{15}N π/2 pulse rf (kHz)	50	50	50	50	50	50	50	50	50
^{15}N CP pulse rf (kHz)	60	60	60	60	60	60	60	60	60
Rotary resonance time τ_{RR} (ms)	20	10	10	10	10	20	20	20	40
^{1}H rf for rotary resonance (kHz)	20	20	20	20	20	20	20	20	20
^{1}H decoupling power (kHz)	10	10	10	10	10	10	10	10	10
^{15}N decoupling power (kHz)	10	10	10	10	10	10	10	10	10
Total experimental time (hours)	2.8	17.2	21.5	20.6	20.6	23.3	44.6	13.9	22.9

Table E5. Acquisition parameters for DNP-enhanced $^{15}N\{^{1}H\}$CP/MAS spectra acquired at 9.4 T

Pharmaceutical	**Aceb**	**Nica**
Nuber of transients	12288	6144
^{1}H Recycle delay (s)	2.5	2.5
Contact time (ms)	4	4
^{1}H $\pi/2$ pulse rf (kHz)	100	100
^{1}H CP pulse rf (kHz)	107	107
^{15}N CP pulse rf (kHz)	87	87
^{1}H SPINAL64 decoupling power (kHz)	100	100
Total experimental time (hours)	8.5	4.3

Table E6. Calculated nitrogen EFG and NMS tensor values.

API	Site	EFG			NMS		
		V_{11} (a.u.)	V_{22} (a.u.)	V_{33} (a.u.)	σ_{11} (ppm)	σ_{22} (ppm)	σ_{33} (ppm)
Scop	$RR'R''NH^+$	0.0885	0.1941	−0.2826	150.18	177.30	179.64
Alpr	$RR'NH_2^+$	−0.0584	−0.2605	0.3189	126.24	161.57	175.54
Isop	$RR'NH_2^+$	−0.0171	−0.2079	0.2250	151.70	167.14	186.25
Aceb	$RR'NH_2^+$	0.0164	0.2122	−0.2286	123.03	158.82	187.34
	RR′NH	0.2103	0.4960	−0.7063	−36.34	131.03	161.22
Dibu	$RR'R''NH^+$	0.1308	0.1844	−0.3152	153.07	163.27	179.48
	RR′NH	0.2203	0.5077	−0.7280	−9.08	144.87	161.74
	RR′N	0.3897	0.4401	−0.8298	−256.30	−73.10	231.77
Nica	$RR'R''NH^+$	0.1039	0.1683	−0.2722	157.74	174.85	178.35
	RR′NH	0.2086	0.4103	−0.6189	−19.10	100.01	144.05
	RNO_2	0.0916	0.1365	−0.2281	−263.68	−194.11	25.04
Rani	$RR'R''NH^+$	0.1296	0.1823	−0.3119	168.01	173.07	188.12
	RR′NH	0.2482	0.5464	−0.7946	74.14	171.52	185.45
	RR′NH	0.1808	0.5853	−0.7661	60.19	147.27	192.28
	RNO_2	−0.0870	−0.1875	0.2745	−213.06	−169.49	42.75
Bupi	$RR'R''NH^+$	0.0863	0.1558	−0.2421	148.38	165.18	173.26
	RR′NH	0.1987	0.4669	−0.6656	−6.85	130.67	145.51
Bupi II	$RR'R''NH^+$	0.1316	0.1888	−0.3204	157.03	161.71	170.06
	RR′NH	0.1963	0.5074	−0.7038	−12.37	122.80	145.37

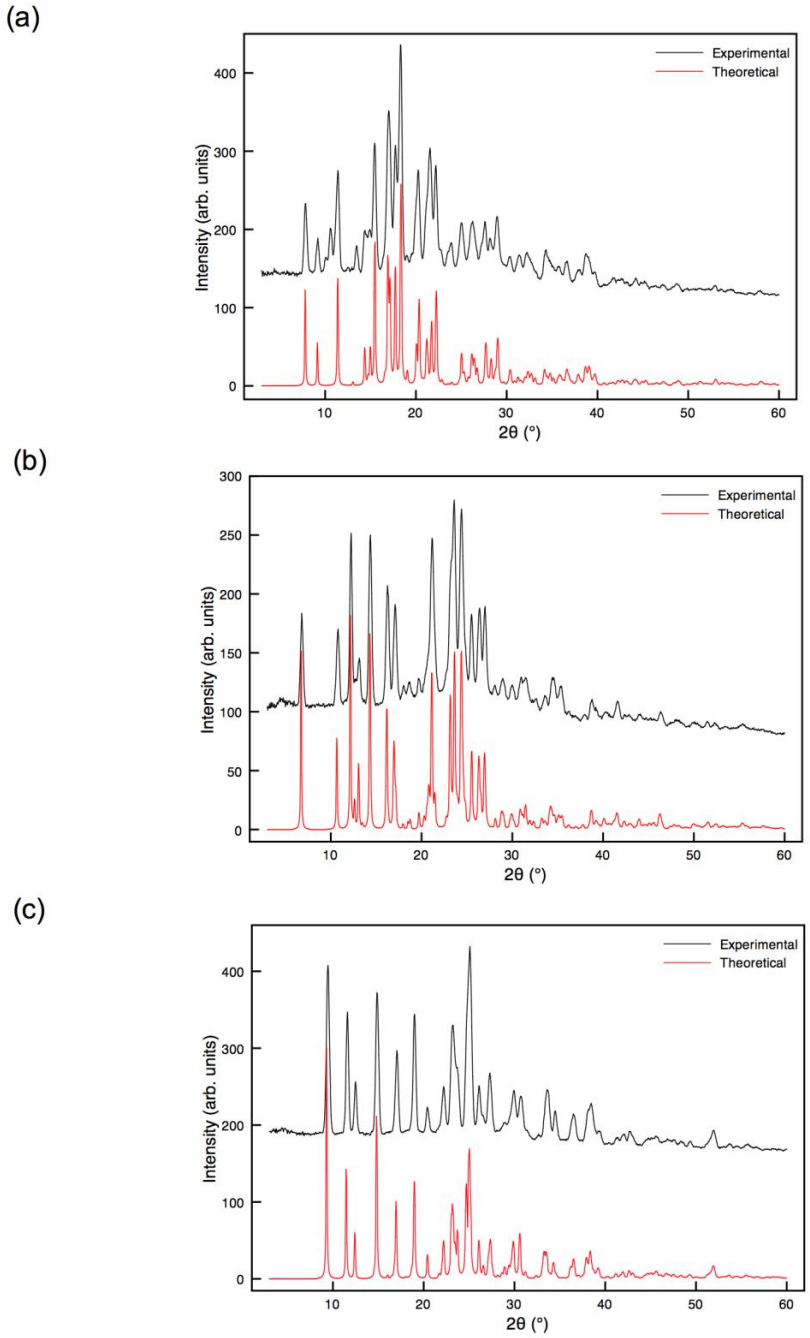

Figure E1. Powder X-ray diffraction patterns for (a) **Scop**, (b) **Alpr**, and (c) **Isop**. Additional peaks in the experimental diffraction pattern of **Scop** are attributed to the hydrated form, which is present as an impurity.

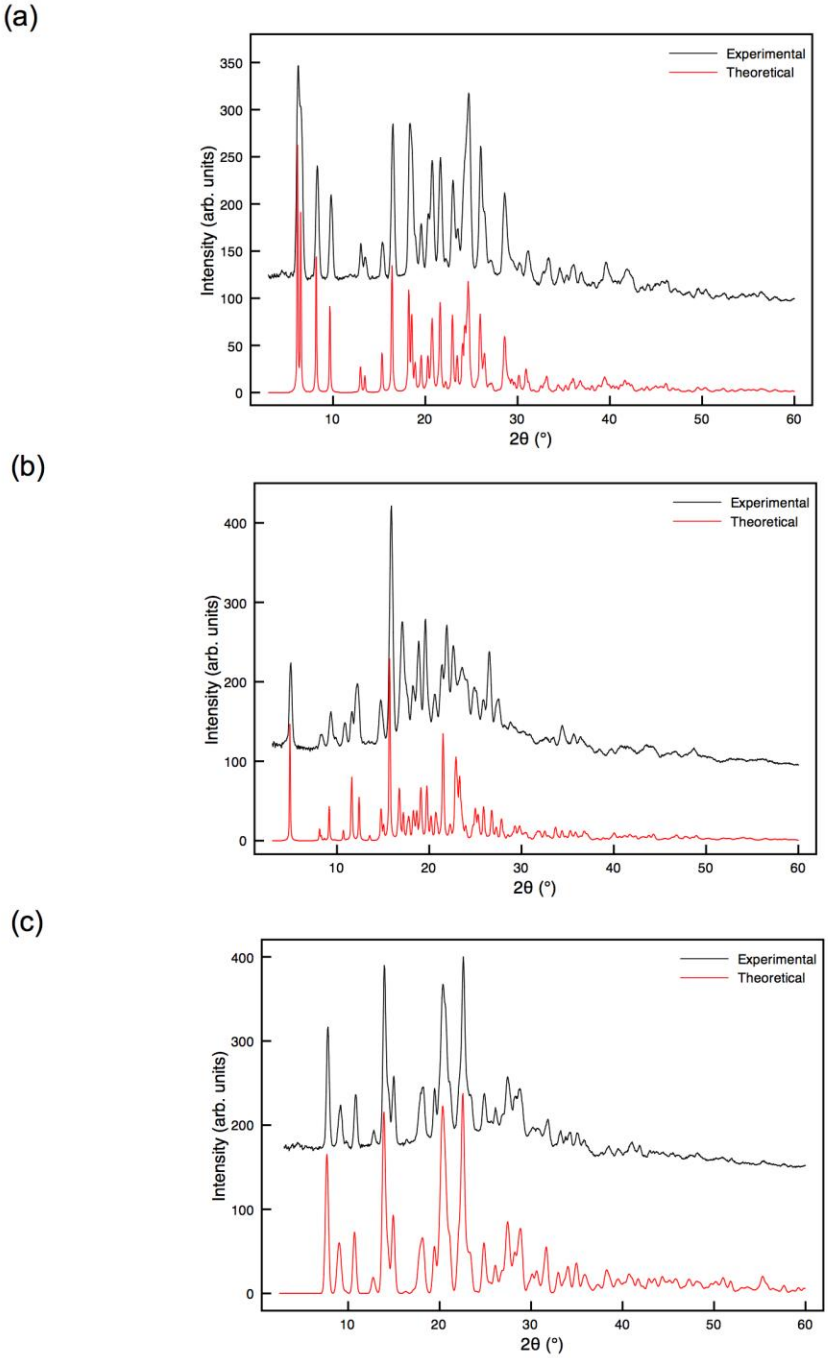

Figure E2. Powder X-ray diffraction patterns for (a) **Aceb**, (b) **Dibu**, and (c) **Nica**.

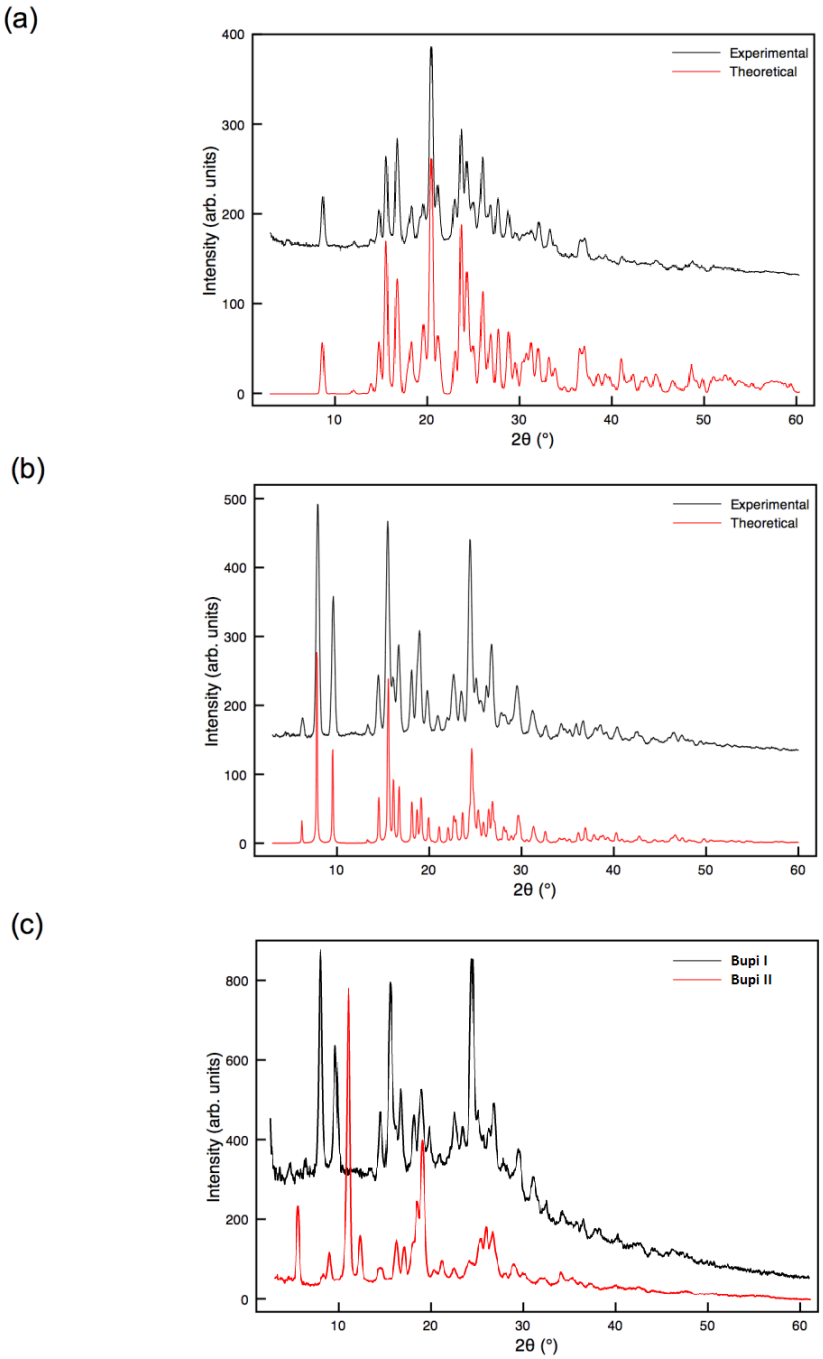

Figure E3. Powder X-ray diffraction patterns for (a) **Rani**, (b) **Bupi**, and (c) **Bupi I** (top) compared to **Bupi II (bottom)**.

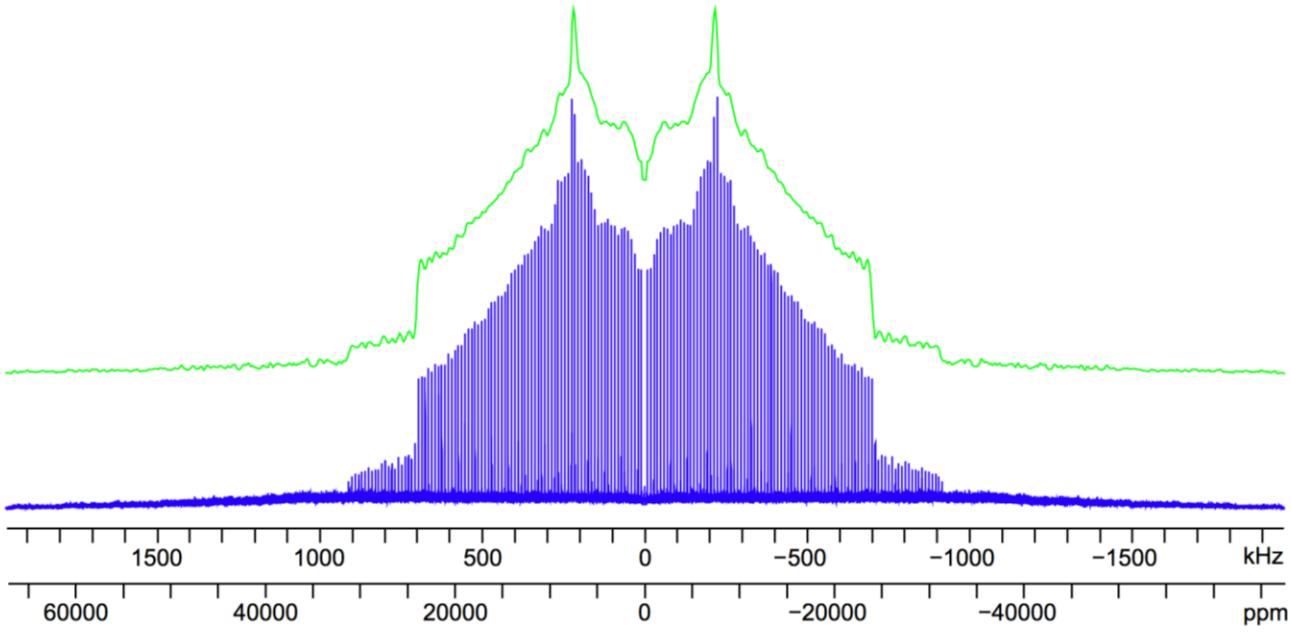

Figure E4. Static ^{14}N SSNMR spectrum acquired for glycine. The FID of the spectrum shown in blue was processed in the usual way, producing a series of narrow lines called *spikelets*. The FID of the spectrum shown in green was processed using an alternative method in which the echo train was coadded into a single echo. When both spectra are compared, the powder pattern has the same overall shape.

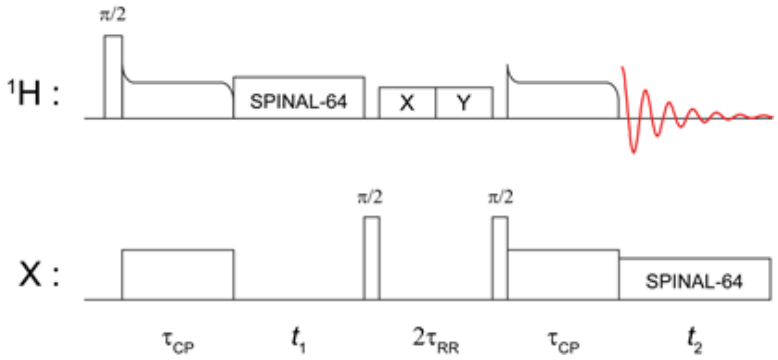

Figure E5. Schematic representation of the pulse sequence for ^{1}H detected HETCOR experiments under fast MAS. τ_{CP} is the cross polarization contact time and τ_{RR} is the rotary resonance recoupling time. States-TTPI detection[1] was used through appropriate phase cycling of the first $\pi/2$ pulses on the X channel.

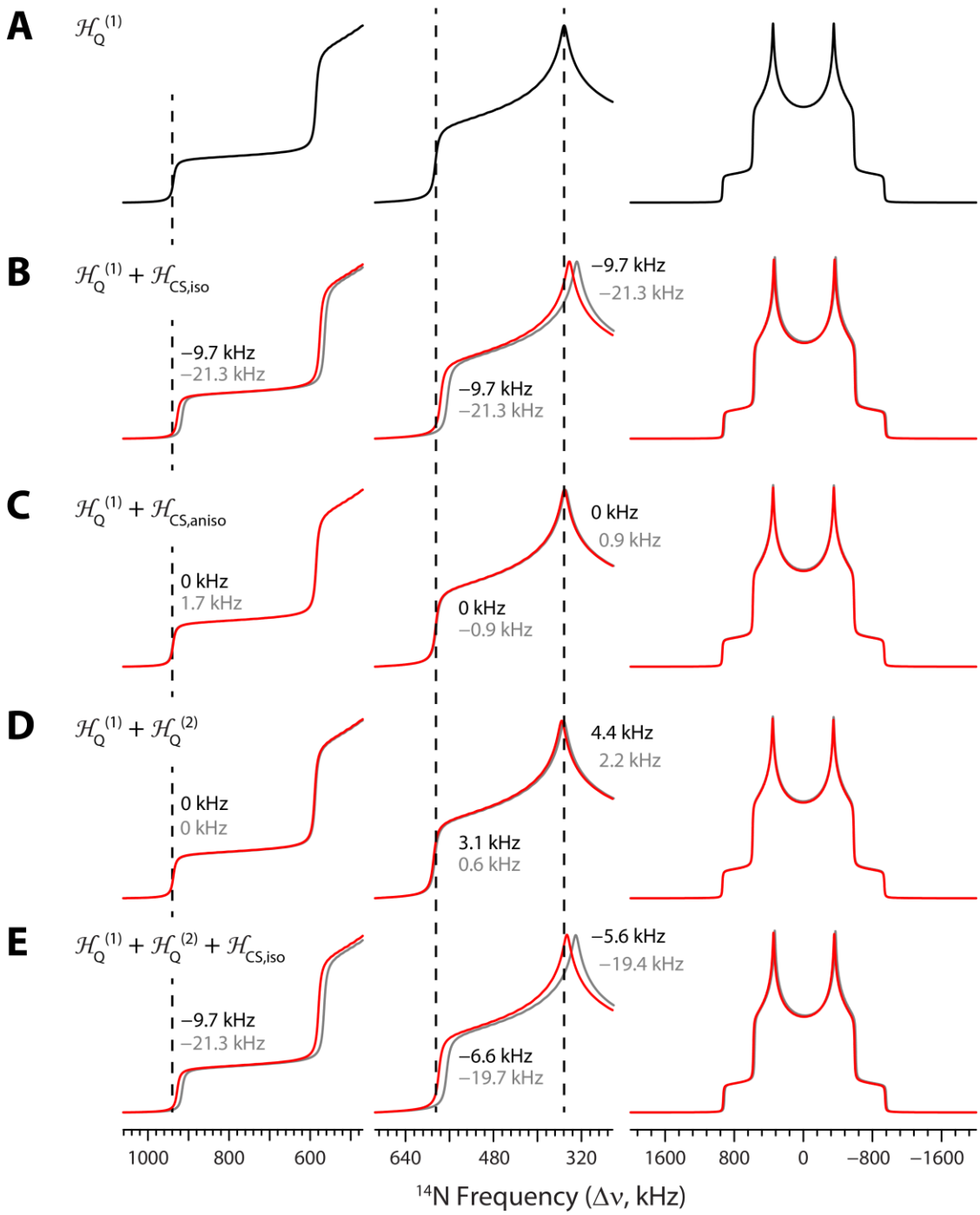

Figure E6. (A) Analytical simulation of a FOQI ^{14}N powder pattern with C_Q = 1.25 MHz and η_Q = 0.25 (black trace). Simulations showing the influences of the CSA (isotropic and anisotropic) and the SOQI are shown in (B) – (E) at two magnetic fields (red – 9.4 T, grey – 21.1 T). Vertical dashed lines mark the locations of the horn, shoulder, and foot discontinuities to first order. The frequencies shifts of the discontinuities are listed next to each of the dashed lines (black text – 9.4 T, grey text – 21.1 T). The CS tensor is assumed to be coincident with the EFG tensor, with a span of 30 ppm, a skew of 0, and δ_{iso} = −330 ppm.

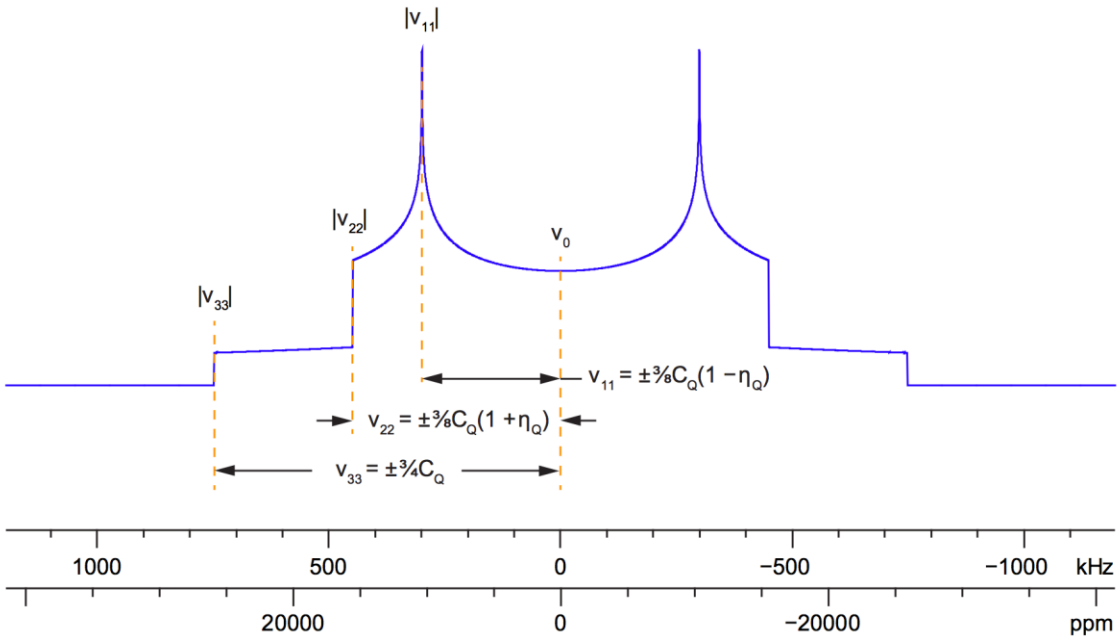

Figure E7. Analytical simulation of an idealized ^{14}N powder pattern dominated by the first-order quadrupolar interaction. Owing to the fact that the EFG tensor is traceless, the frequencies of all three discontinuities are closley related; thus, knowledge of the frequencies of any two of the discontinuities allows for accurate determination of the quadrupolar parameters.

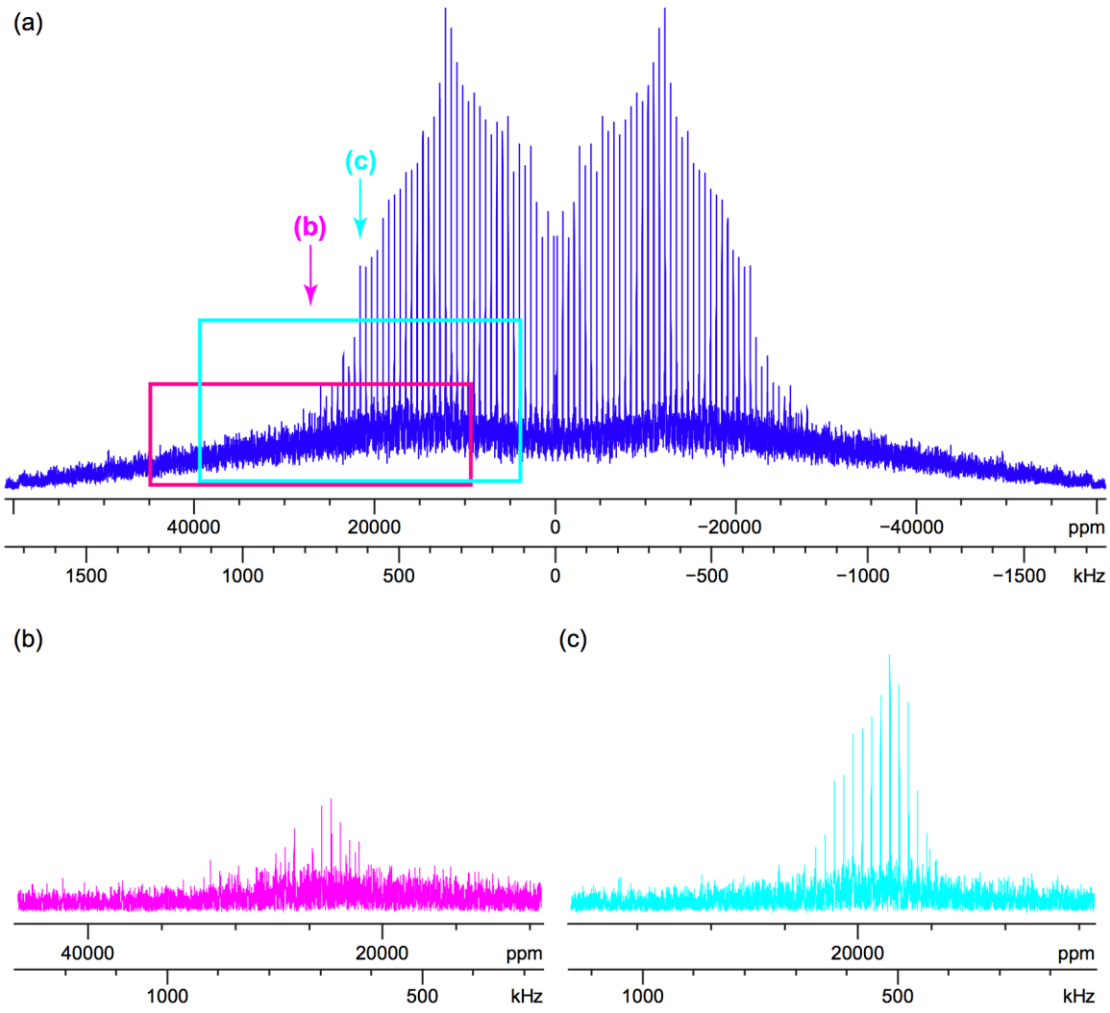

Figure E8. (A) Static ^{14}N SSNMR spectrum (9.4 T using WURST-CPMG) acquired for **Scop** and corresponding sub-spectra acquired at transmitter frequencies of (B) 29.681 MHz and (C) 29.499 MHz. As the transmitter frequency is increased the signal is reduced and it is not possible to acquire the region of the spectrum corresponding to the "foot" discontinuity. However, as demonstrated in **Figure E7**, it is possible to extract the quadrupolar parameters using the two known discontinuities.

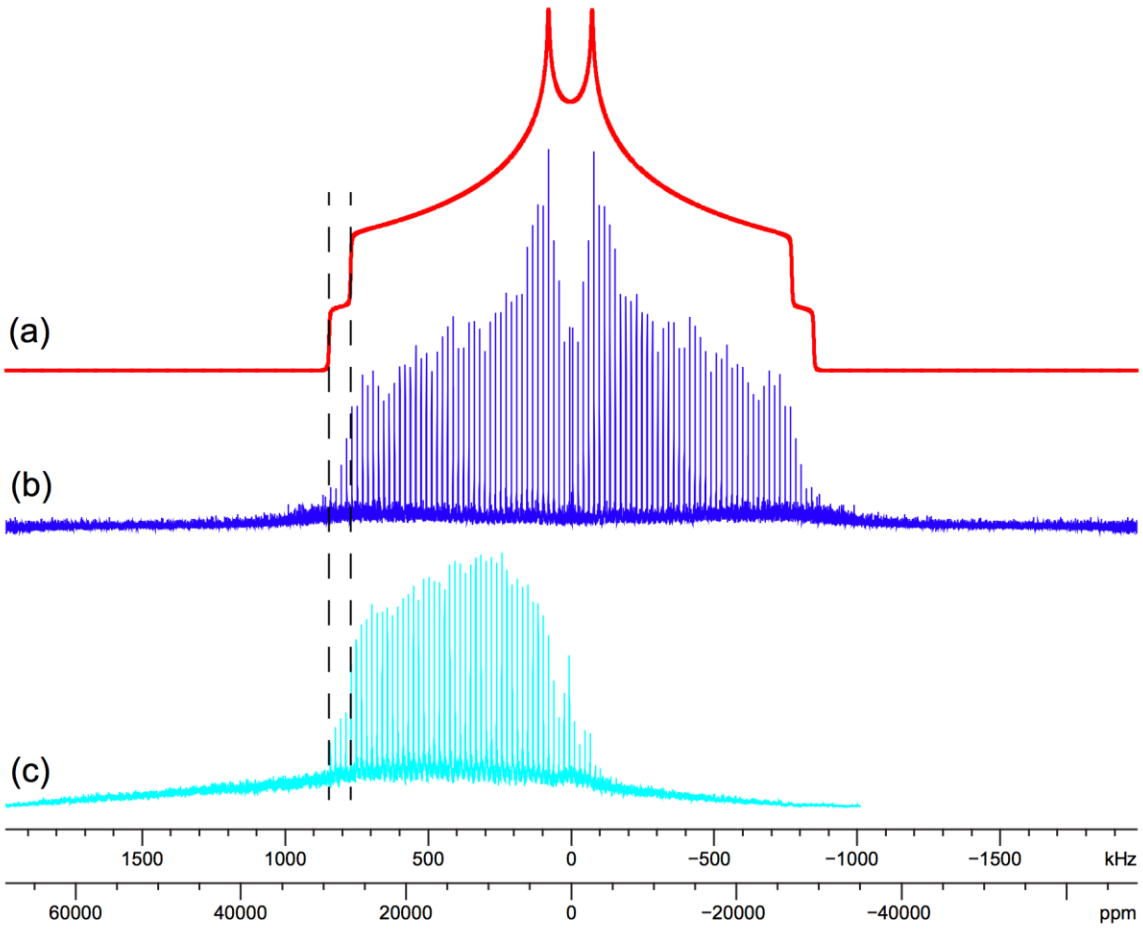

Figure E9. (a) Analytical simulation of the ^{14}N powder pattern acquired for **Alpr**. The simulation was achieved using the skyline projected and coadded spectra shown in (b) and (c), respectively. Using the skyline projected spectrum, the position of the "horn" discontinuity was accurately determined and using the coadded spectrum the "shoulder" and "foot" discontinuities were determined. It is noted that, due to the higher S/N of coadded spectra, features such as the shoulder and foot discontinuities are easier to observe and, hence, simulate. Also shown for clarity are dashed lines, highlighting the agreement between the experimental spectrum and the analytical simulation.

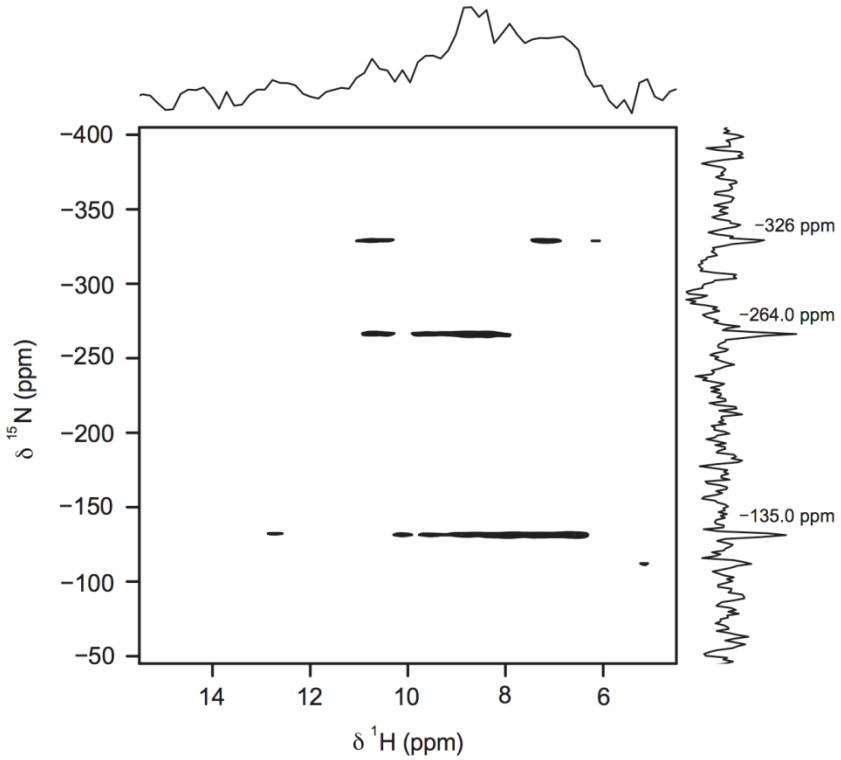

Figure E10. $^{1}H\{^{15}N\}$ idHETCOR spectrum (14.1 T) of **Dibu**. The spectrum was acquired using ν_{rot} = 40 kHz, $\nu_{RF}(^{1}H)$ = 125 kHz during short pulses, $\nu_{RF}(^{1}H)$ = 60 kHz during tangential ramped CP, $\nu_{RF}(^{1}H)$ = 10 kHz during SPINAL-64 decoupling, $\nu_{RF}(^{1}H)$ = 20 kHz during τ_{RR}, $\nu_{RF}(^{15}N)$ = 50 kHz during short pulses, $\nu_{RF}(^{15}N)$ = 60 kHz during CP, $\nu_{RF}(^{15}N)$ = 10 kHz during SPINAL-64 decoupling, τ_{CP} = 10 ms and τ_{RR} = 20 ms. The spectrum is the result of averaging 16 transients with τ_{RD} = 6.5 s for each of the 400 t_1 increments of 25.0 μs.

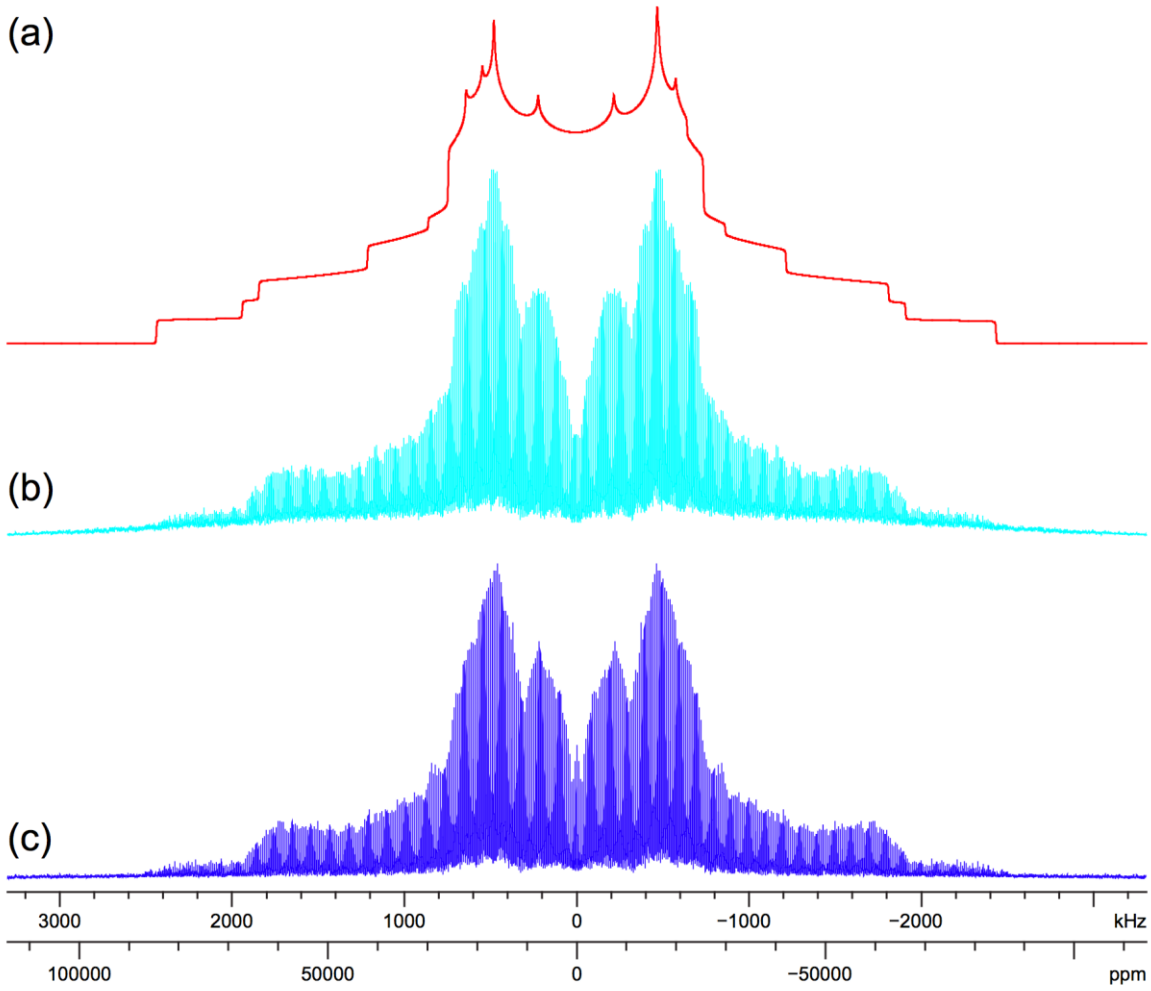

Figure E11. (a) Analytical simulation of the ^{14}N powder pattern acquired for **Rani** with four distinct sites; C_Q = 1.15, 1.62, 3.25 and 3.25, and η_Q = 0.49, 0.22, 0.5 and 0.58. The four site simulation was achieved using the coadded spectrum shown in (b) to accurately determine the shoulder and foot discontinuities of the outer sites. Additional refinement of the quadrupolar parameters for each site was achieved by fitting the horn discontinuities, using the skyline projected spectrum shown in (c).

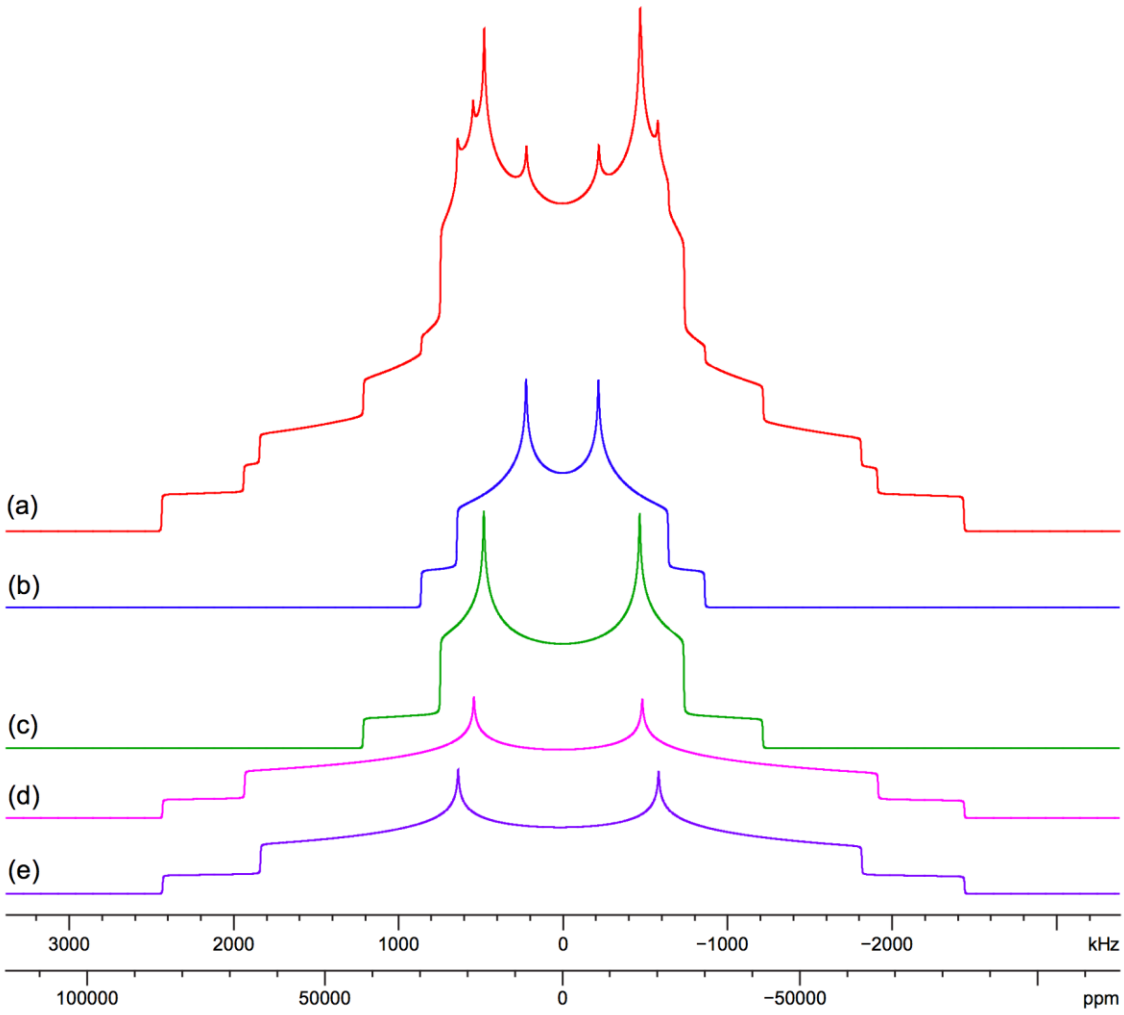

Figure E12. Deconvolution of the ^{14}N SSNMR powder pattern acquired for **Rani**. (a) The analytical simulation obtained upon summation of all four sites, (b) simulation of the RNO_2 site, with C_Q = 1.15 MHz and η_Q = 0.49, (c) simulation of the RR′R″NH$^+$ site, with C_Q = 1.62 MHz and η_Q = 0.22, and (d, e) simulation of the two RR′NH sites, with C_Q = 3.25 and 3.25 MHz and η_Q = 0.58 and 0.50, respectively.

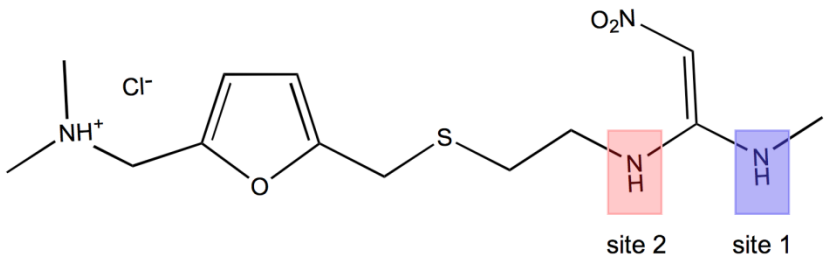

Figure E13. Schematic representation of **Rani** indicating assignments for the different planar nitrogen environments.

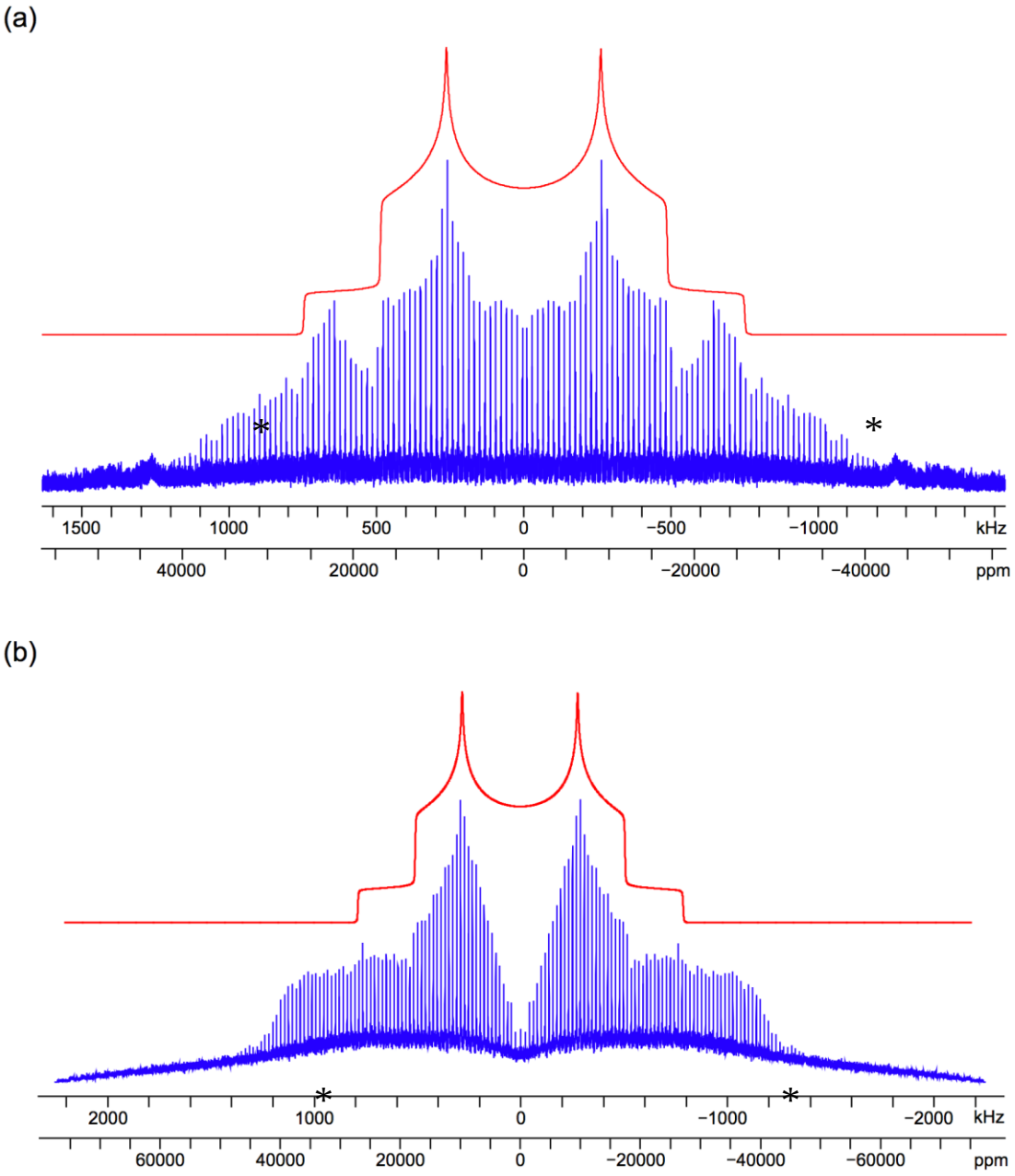

Figure E14. Static ^{14}N SSNMR spectra (9.4 T) acquired for **Bupi** using (a) DE and (b) BCP. Signal arising from the planar RR′NH site is denoted by *. The favourable relaxation characteristics (i.e., short $T_1(^{14}\text{N})$ and long $T_2^{\text{eff}}(^{14}\text{N})$) of the planar nitrogen site allow its detection with the use of both DE and BCP ^{14}N experiments at moderate magnetic fields.

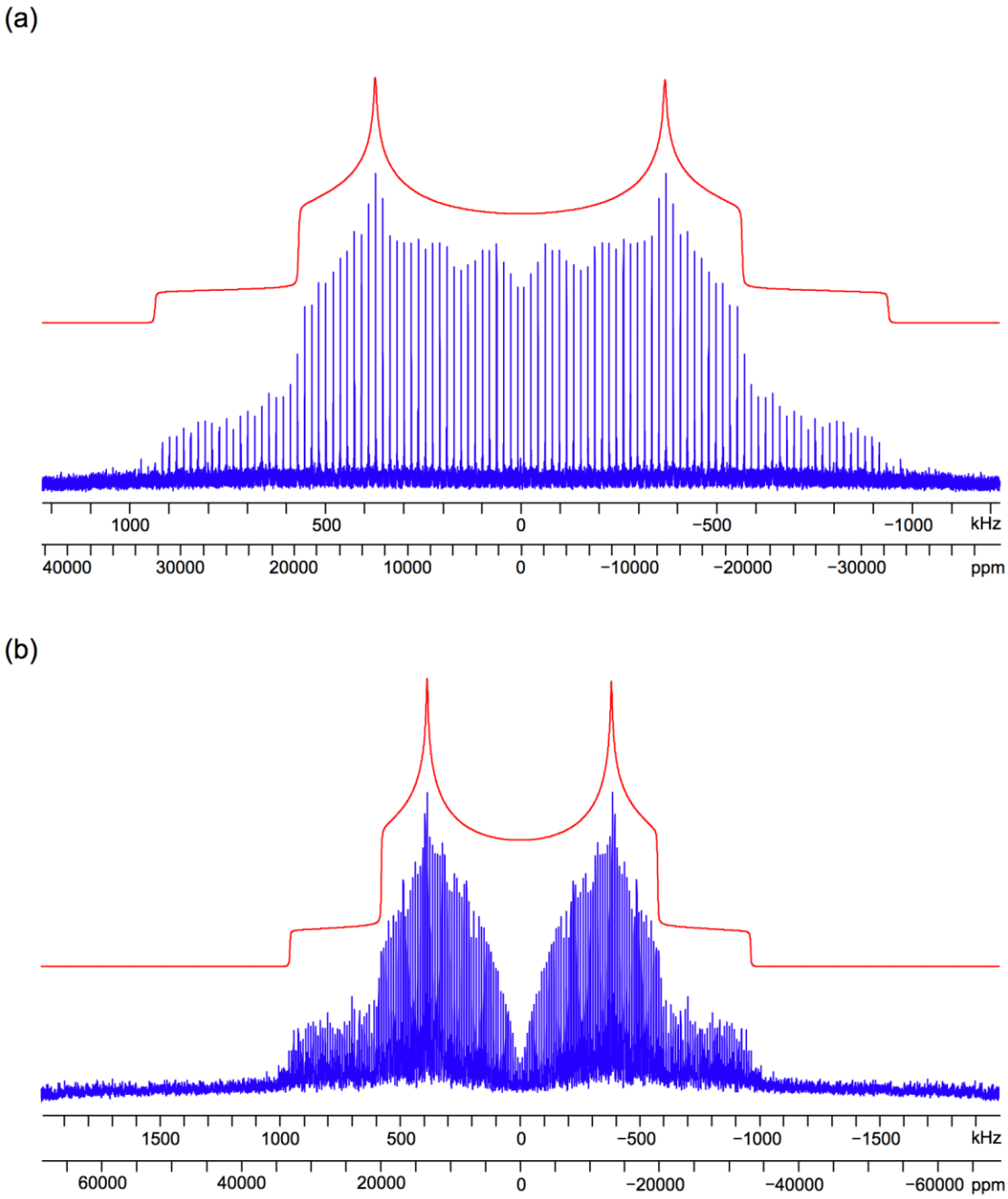

Figure E15. Static ^{14}N SSNMR spectra (9.4 T) acquired for **Bupi II** using (a) DE and (b) BCP.

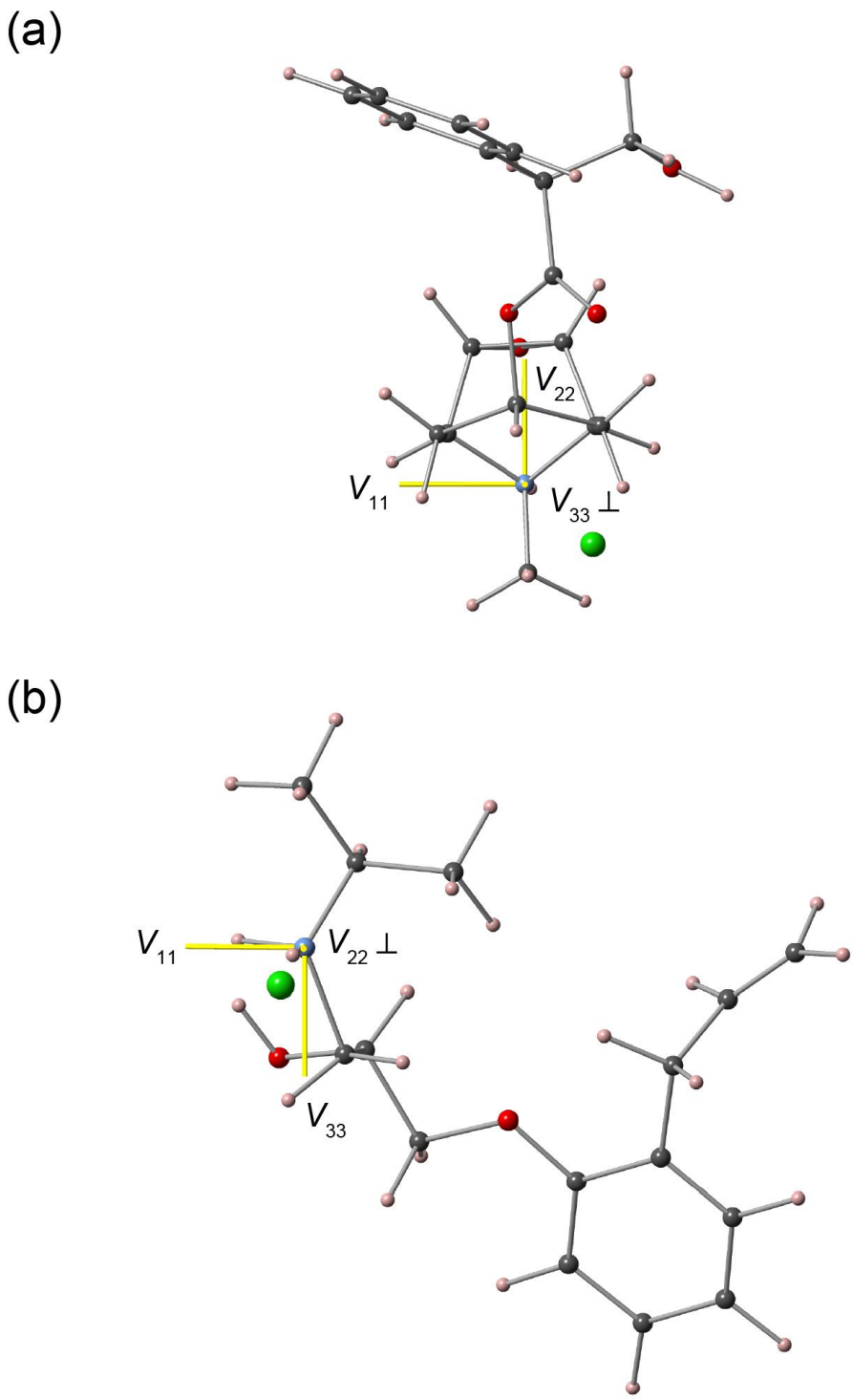

Figure E16. ^{14}N EFG tensor orientation of full molecules of (a) **Scop** and (b) **Alpr**

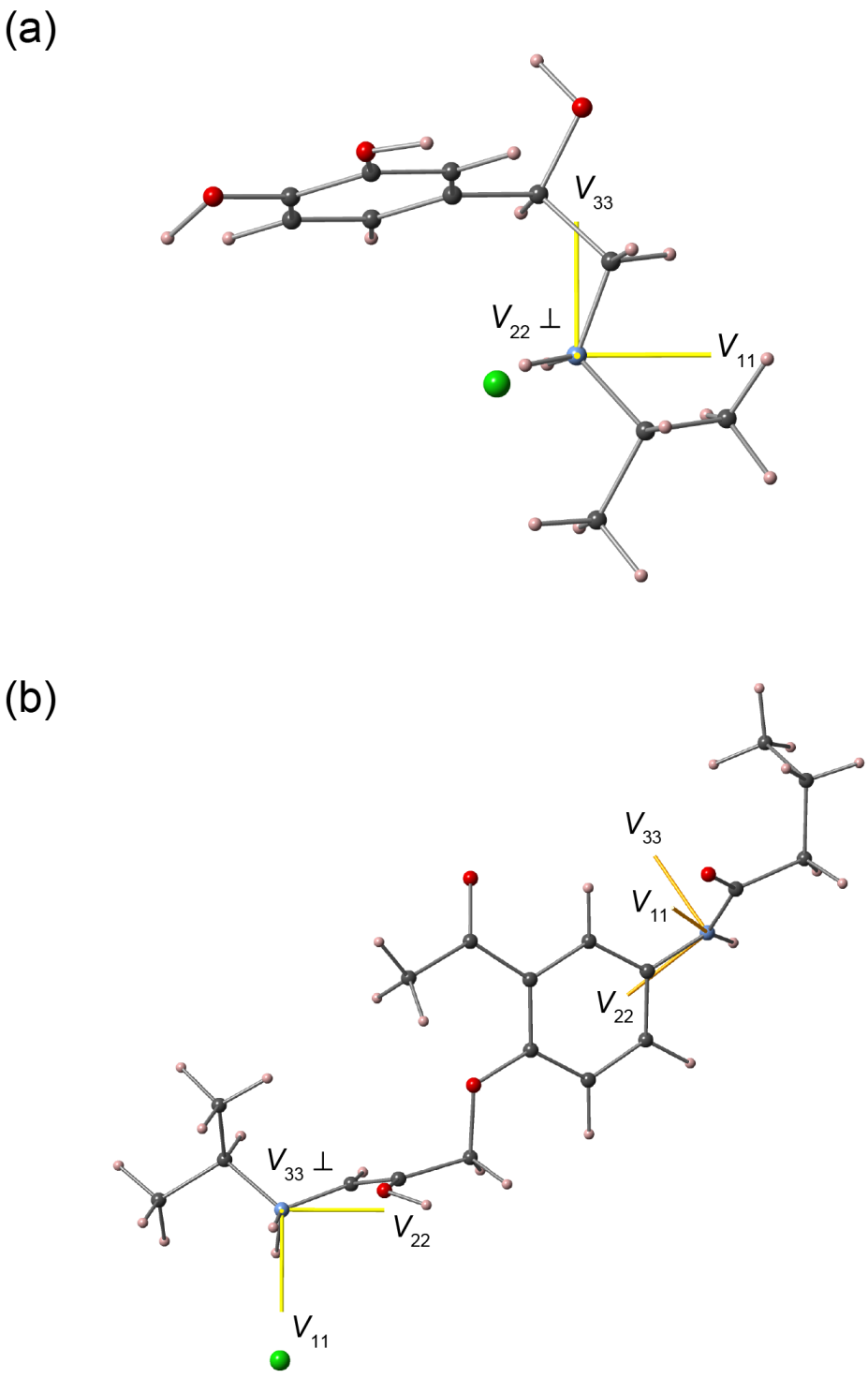

Figure E17. ^{14}N EFG tensor orientation of full molecules of (a) **Isop** and (b) **Aceb**

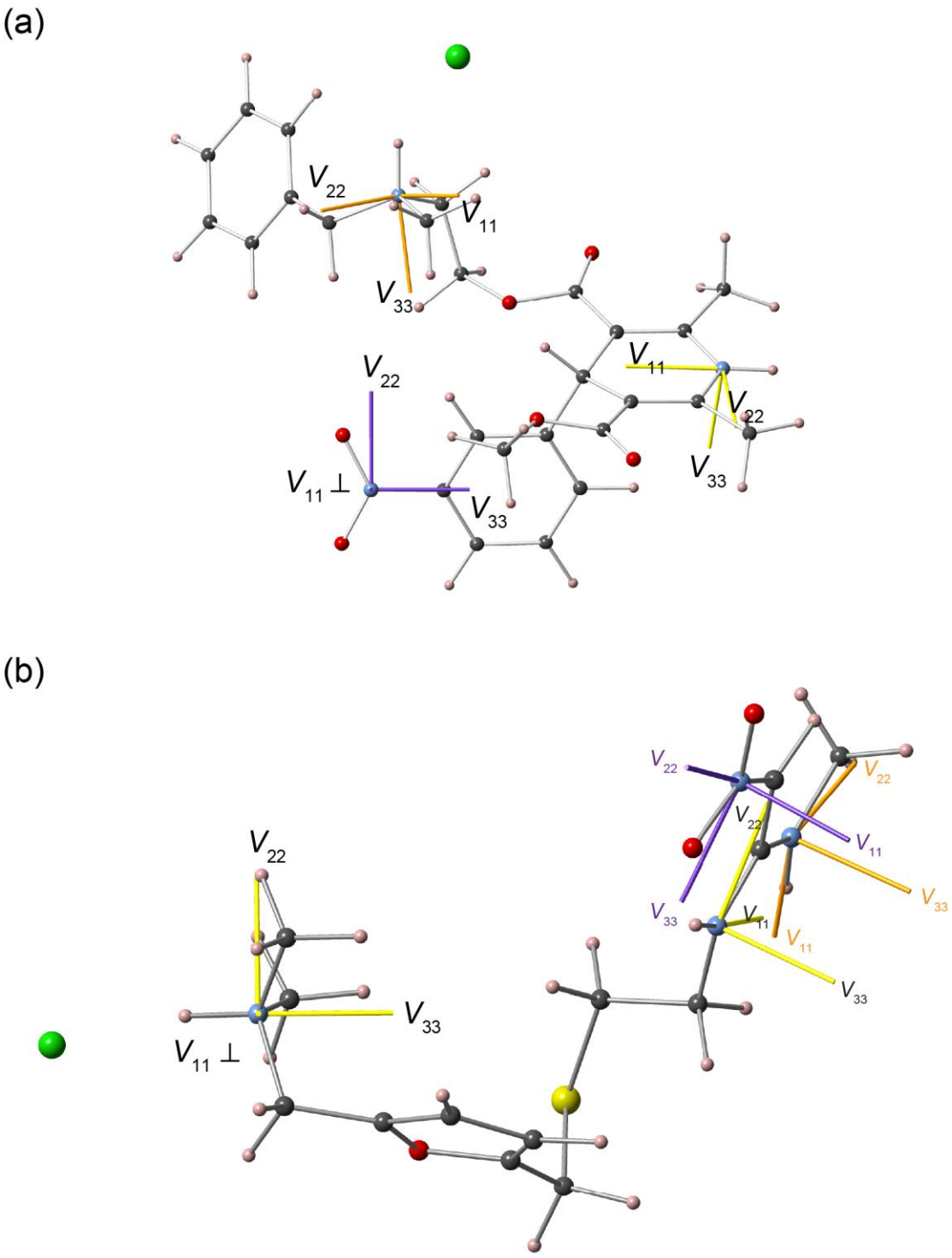

Figure E18. ^{14}N EFG tensor orientation of full molecules of (a) **Nica** and (b) **Rani**

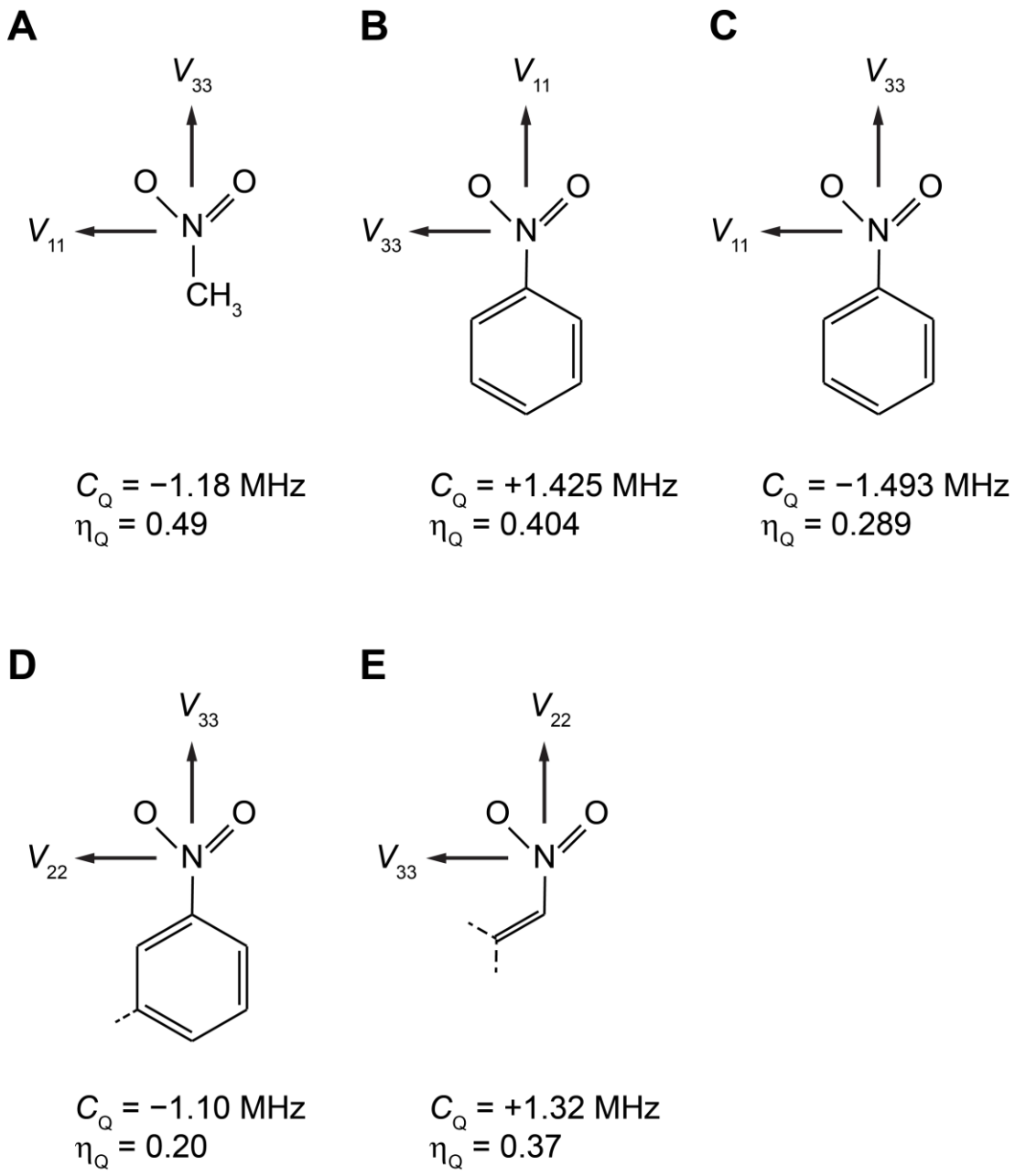

Figure E19. Summary of ^{14}N EFG tensor orinetations and quadrupolar parameters in NO_2 for a) nitromethane,[2] b) nitrobenzene,[3] c) nitrobenzene,[4] d) **Nica** [this work], and e) **Rani** [this work]. In each case, only two of three principal axis components are shown, the third lies perpendicular to the O-N-O plane.

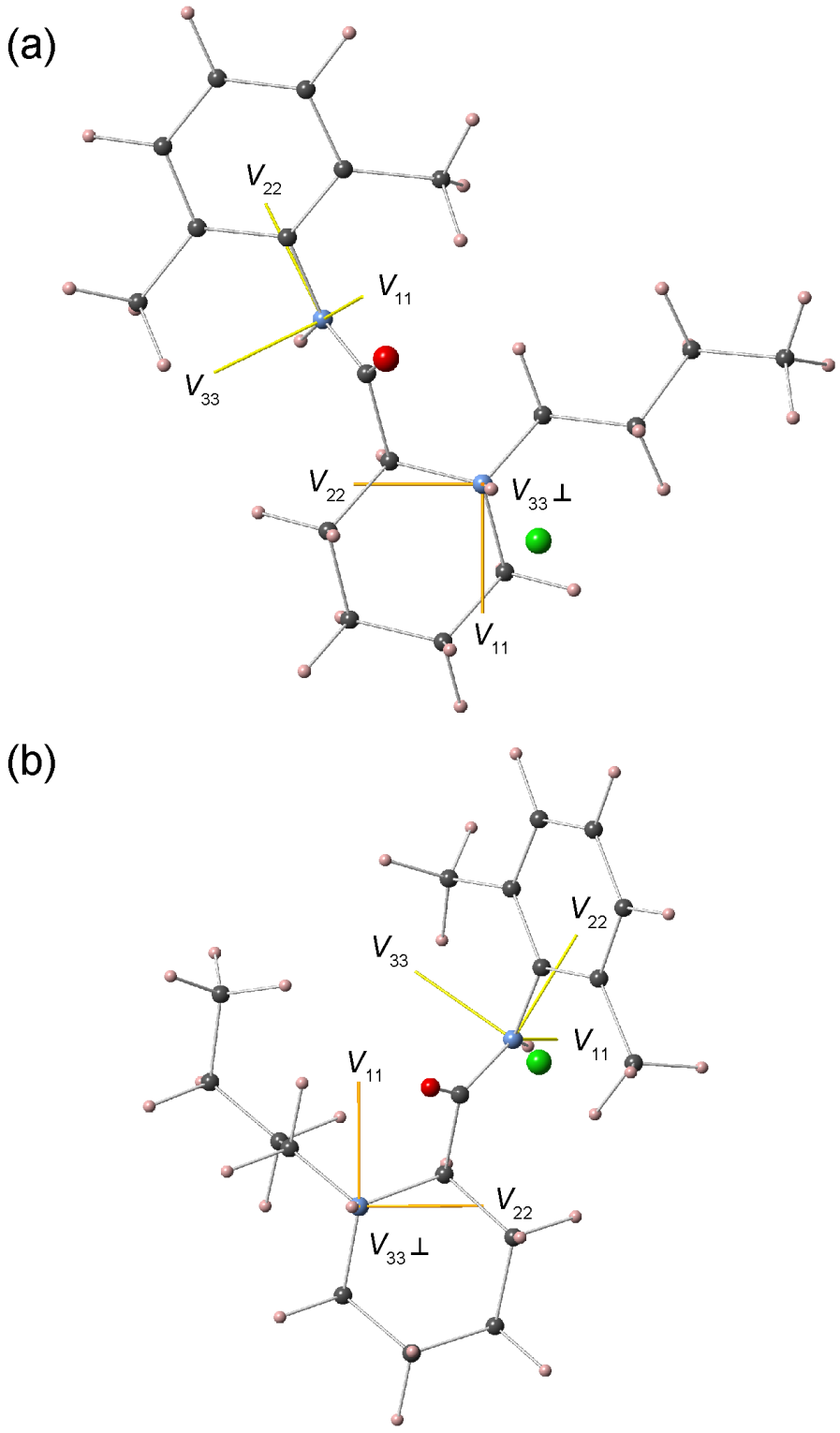

Figure E20. ^{14}N EFG tensor orientation of full molecules of (a) **Bupi** and (b) **Bupi II**

References

1. Marion, D.; Ikura, M.; Tschudin, R.; Bax, A. *J. Magn. Reson.* **1989**, *85*, 393.
2. Cox, A. P.; Waring, S.; Motgenstern, K. *Nature* **1971**, *229*, 22.
3. Subbarao, S. N.; Bray, P. J. *J. Chem. Phys.* **1977**, *67*, 3947.
4. Harris, R. K.; Jonsen, P.; Packer, K. J. *Magn. Reson. Chem.* **1985**, *23*, 565.

Vita Auctoris

Stanislav L. Veinberg was born in Moscow, Russia. He graduated from Belle River District High School in Belle River, Ontario in June of 2006, and the University of Windsor in May 2010 with a B. Sc. (Honours) in Chemistry and Physics. He is currently a Ph.D. candidate at the University of Windsor and is planning on graduating in June of 2016.

Publications:

2) Veinberg, S.L., Friedl, Z.W., Harris, K.J., O'Dell, L.A., and Schurko, R.W. Ultra-wideline ^{14}N Solid-State NMR as a Method of Differentiating Polymorphs: Glycine as a Case Study. CrystEngComm. **2015**, 17, 5225–5236. DOI: 10.1039/C5CE00060B.

1) Harris, K.J., Veinberg, S.L., Mireault, C.R., Lupulescu, A., Frydman, L., and Schurko, R.W. Rapid Acquisition of ^{14}N Solid-State NMR Spectra Using Broadband Cross Polarization. *Chem. Eur. J.* **2013**, *19*, 16469-16475. DOI: 10.1002/chem.201301862.